REPORT DOCUMENTATION PAGE

Public reporting burden for this collection of information is estimated to average 1 hour per response, including the time for re
maintaining the data needed, and completing and reviewing this collection of information. Send comments regarding this bur
including suggestions for reducing this burden to Department of Defense, Washington Headquarters Services, Directorate for .
Highway, Suite 1204, Arlington, VA 22202-4302. Respondents should be aware that notwithstanding any other provision of law, no person shall be sub,.
collection of information if it does not display a currently valid OMB control number. **PLEASE DO NOT RETURN YOUR FORM TO THE ABOVE ADDRESS.**

1. REPORT DATE (DD-MM-YYYY) 10-31-2007	2. REPORT TYPE FINAL REPORT	3. DATES COVERED (From - To) 07-01-2002 TO 09-30-2007

4. TITLE AND SUBTITLE	5a. CONTRACT NUMBER
MULTI-DISCIPLINARY RESARCH FOR HIGH ENERGY CHEMICAL LASERS	F49620-02-1-0357
CLOSED-CYCLE ELECTRICOIL TECHNOLOGY	5b. GRANT NUMBER
	5c. PROGRAM ELEMENT NUMBER

6. AUTHOR(S)	5d. PROJECT NUMBER
WAYNE C. SOLOMON	5e. TASK NUMBER
	5f. WORK UNIT NUMBER

7. PERFORMING ORGANIZATION NAME(S) AND ADDRESS(ES)	8. PERFORMING ORGANIZATION REPORT
UNIVERSITY OF ILLINOIS 302A TALBOT LABORATORY, MC-236 URBANA, ILLINOIS 61801	

9. SPONSORING / MONITORING AGENCY NAME(S) AND ADDRESS(ES)	10. SPONSOR/MONITOR'S ACRONYM(S)
AFOSR/PKA AF OFFICE OF SCIENTIFIC RESEARCH 875 N. RANDOLPH ST., RM. 3112 ARLINGTON, VA 22203	USAF, AFRL, AFOSR
Dr Michael Berman/NA	11. SPONSOR/MONITOR'S REPORT NUMBER(S)

12. DISTRIBUTION / AVAILABILITY STATEMENT

Approved for public release; distribution unlimited.

13. SUPPLEMENTARY NOTES

14. ABSTRACT The program was initiated in July 2002. Work during this grant resulted over 50 publications in several major breakthroughs by the MRI team: (1) the first measurement of *laser gain* in a discharge driven oxygen-iodine system was demonstrated in a supersonic flowing cavity; (2) the first measurement of positive gain in a discharge driven oxygen-iodine system was then demonstrated in a subsonic flow tube; (3) the first continuous wave (cw) discharge driven oxygen-iodine *laser* was demonstrated; (4) Laser gain and power were increased by almost two orders of magnitude (5) key measurements were made related to ElectricOIL specific kinetics; (6) critical new understanding of the electrodynamic phenomena in a pulse-sustainer type of discharge was attained using a detailed plasma discharge model; and (7) experiments with a pulse-sustainer discharge concept support the intriguing results from the new electrodynamics models. (8) Atomic Iodine was found to play a crucial role in the chemistry of the system when injected into the cavity; it was necessary to titrate the excess O atoms to achieve good gains. Based upon electrodynamic model predictions a laser system model was utilized to predict the scalability of the system; results indicate that theoretical electrical efficiencies of 40% into $O_2(^1\Delta)$ may be achievable at very high powers. High pressure experiments with stabilized RF discharges are beginning to approach this theoretical limit.

15. SUBJECT TERMS
AFOSR Final Report, Closed-Cycle ElectricOIL Technology

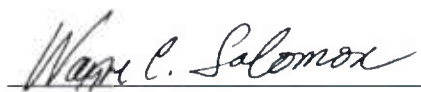| 16. SECURITY CLASSIFICATION OF:			17. LIMITATION OF ABSTRACT	18. NUMBER OF PAGES	19a. NAME OF RESPONSIBLE PERSON MICHAEL R. BERMAN
a. REPORT UNCLASSIFIED	b. ABSTRACT UNCLASSIFIED	c. THIS PAGE UNCLASSIFIED	SAR		19b. TELEPHONE NUMBER (include area code) (703) 696-7781

Standard Form 298 (Rev. 8-98)

AFOSR Final Report
Closed-Cycle ElectricOIL Technology
AFOSR Contract No. F49620-02-1-0357

9/1/2005 through 9/31/2007

Aerospace Engineering Department
University of Illinois at Urbana-Champaign
Urbana, IL 61801

Report Number: AE 05-03
UILU ENG 05-05-03

Prepared/Submitted:

Wayne C. Solomon

Wayne C. Solomon

31 October 2007
Date

20071212113

EXECUTIVE SUMMARY

Program Objectives

A team consisting of the University of Illinois at Urbana-Champaign (UIUC, the lead institution), Iowa State University, Emory University (EU), the Air Force Institute of Technology (AFIT), CU Aerospace (CUA), Physical Sciences Inc (PSI), has completed a multidisciplinary research program for a high energy closed-cycle laser that is derived from the Electrically assisted Oxygen Iodine Laser (ElectricOIL) (EOIL) technology currently being developed by UIUC and CUA. This program places emphasis on basic research at University institutions targeted at understanding(research) and improving EOIL technology, the education of a future generation of Masters and Ph.D. students, and the ultimate development of closed-cycle hybrid ElectricOIL (EOIL) system.

Advanced iodine laser technology logically requires novel all gas phase generation techniques for an iodine energy donor and, quite likely, the injection of atomic rather than molecular iodine. Our overall concept of the closed-cycle ElectricOIL consists of several basic elements. The key is a continuous closed flow loop of oxygen (or oxygen donor) and a buffer gas(es) that are driven by a single-stage turbo-pump. A second key element is the energy donor for excited iodine, $O_2(^1\Delta)$, which is created by a combination of some type of pulsed discharge and an RF discharge generator surrounding the flow tube. The third element is an iodine flow system that injects very small amounts of molecular/atomic iodine into the laser cavity region for lasing. Fourth, an optimally designed laser cavity/resonator. Fifth, in the closed-cycle version, a heat exchanger is required to cool the flow and remove iodine from the flow loop upstream of the turbo-pump. As the iodine flow rate is miniscule relative to the other gases and cumulative operational times are likely to be only a few hours for military systems, it will be possible to simply flow iodine from one reservoir and trap it in another. The principal advantage of the hybrid EOIL system is trading a small fixed mass in electrical generation (already on-board) and heat exchanger hardware for the massive chemical fluid supply, large tankage, and pressure recovery systems associated with current open loop COIL devices. The disadvantages are minimal at this point.

The primary objectives of this program are as follows:
1. *Understanding of discharge physics leading to production and destruction of excited states of oxygen;*
2. *Research for advanced discharge methodologies and corresponding power conditioning equipment that optimize production of singlet-delta oxygen;*
3. *Establishment of primary and secondary kinetic processes involved in the electric discharge generation of singlet oxygen and the dissociation of iodine in electro-chemical environments;*
4. *Development of complex EOIL electrodynamic discharge models;*
5. *Development of advanced diagnostic techniques to better understand the ElectricOIL device;*
6. *Demonstration of the first laboratory versions of the ElectricOIL hybrid- iodine laser;*
7. *Enhanced production and injection of atomic iodine into the laser cavity;*
8. *Design of scaling experiments for next generation of EOIL technology.*

Program Overview

The program was initiated in July 2002. Work under this grant resulted in several major breakthroughs by the MRI team: (1) the first measurement of *laser gain* in a discharge driven oxygen-iodine supersonic cavity was demonstrated in 2004 at UIUC (2) the first measurement of positive gain in a discharge driven oxygen-iodine system was also demonstrated in a subsonic flow tube; at PSI (3) *the first continuous wave (cw) discharge driven oxygen-iodine laser* was produced and power was increased by almost *two orders of magnitude to over 5 watts* during the period; (4) key measurements were made related to ElectricOIL specific kinetics; (5) Experiments with low power pulse-sustainer discharges support the intriguing results from the modeling; (6) Additional understanding of the electrodynamic phenomena in a pulse-sustainer type of discharge was attained using a detailed plasma discharge model; (7) A new high pressure Transverse RF discharge unit was successfully operated at pressures up to 100 torr; and (8) atomic oxygen was found to play a crucial role in the chemistry of the system in the presence of iodine; (9) Laser performance with atomic iodine look promising. It was deemed necessary to scavenge a portion of the excess O atoms to achieve positive gain. Catalytic amounts of NO were found to be beneficial to the performance of the discharge, significantly boosting the production of $O_2(^1\Delta)$. The electrodynamics simulation models were developed to search the parameter space for appropriate experimental conditions under which more advanced versions of the rf-discharge system could be effective in production rates of Based upon electrodynamic model predictions a laser system model was utilized to predict the scalability of the system; results indicate that electrical efficiencies into of 40% into $O_2(^1\Delta)$ may be achievable at very high powers.

During the past two years the electrodynamics models were improved, a 2-D model was developed and a number of parametric verification studies were conducted at UIUC. The models were adapted to detail the parameter space for appropriate experimental conditions under which more advanced versions of discharge systems that could be effective in increasing production of $O_2(^1\Delta)$ [also referred to as $O_2(a)$].

A mix of RF, microwave and pulse-sustainer discharges were studied during the research in order to better define the optimal parameter space for a new, more powerful, discharge unit being designed and tested. A number of upgrades to the discharge diagnostics were completed and a large number of fundamental electrical measurements were made. Much more sensitive $O_2(^1\Delta)$ and $O_2(^1\Sigma)$ [also referred to as $O_2(b)$] spectral measurements were evolved and verified. Our increasing ability to correlate electrical and spectral properties gives us direct connectivity to the theory. Careful iodine gain measurement systems were used to evaluate a variety of experimental parameters by workers at CU Aerospace and PSI. The researchers at Emory University have conducted a series of studies of key fundamental kinetic rates for discharge generated species. Work on advanced plasma and laser diagnostics has been quite successful by several members of the team. The workers at AFIT have devised new techniques to understand the plasma chemistry in oxygen discharges and are involved in studying the fate of discharge species within the discharge.

Coupling of discharge theory, post-discharge kinetics modeling and comparison with diagnostics measurement was continued with improvements in both. Yields of $O_2(^1\Delta)$ were realized (up to

28% at low pressures and 16% at moderate pressures and measured efficiencies into $O_2(^1\Delta)$ exceeded 30% when comparing to theory Gain was realized in both subsonic and supersonic flows. Having achieved this milestone, we procured sets of high reflectivity 1" mirrors and replaced the diagnostics flow cavity in the supersonic flow system with a supersonic laser cavity. Guided by the set of careful gain measurements, our first tests of the system provided laser oscillation at <100 mWatts. Subsequent testing of the improved flow system provided a very stable >5watt 1.314 micron Iodine laser which operated over the wide of powers, temperatures, pressures, and velocities. As a result, we have, in hand, the first example of a hybrid electric laser, ElectricOIL [EOIL], operating at a very important wavelength.

Our theorists and electrical engineers have been devising a series of pulse-sustainer discharge and high pressure RF experiments to allow us to exploit the recent technology breakthroughs as expeditiously as possible. The theory indicates that a pulse-sustainer system is a good way to operate the discharge so as to maximize the $O_2(^1\Delta)$ yield while at the same time minimizing the content of energy sapping species such as oxygen atoms. The critical parameters for both discharges have been mapped out. More recently, experiments are in concert with the theory and provide substantially increased yields of $O_2(^1\Delta)$ at significantly higher pressures. Our program for the intended applications will emphasize the establishment of scaling laws and scientific basis for production of an efficiently packagable high power hybrid laser system.

Table of Contents

1. INTRODUCTION

1.1 Significance of Closed-Cycle Electrically Assisted Hybrid Laser Systems to DoD

Evolving military and terrorist threats require systems that can rapidly and surgically deliver both lethal and non-lethal force. High energy laser systems offer attractive capabilities in both these areas, but they have yet to be packaged in tactical systems with sufficient average powers for many of the envisioned missions. In the 90's weapon laser research shifted from electric to gas dynamic and chemical lasers. Since that time, advances have occurred in military power generation and conditioning which have pointed to "all-electric" programs for aircraft, ground vehicles, and ships and have fueled a resurgence of interest in electric lasers (including semiconductor diode lasers, and photolytically pumped devices) to take unique advantage of these excess electrical capabilities. Since lasers are, in general, relatively inefficient at energy conversion, huge amounts of waste heat are generated and must be dealt with in real time to enable high average power systems with mission-relevant duty cycles. While progress has been made in getting waste heat out of solid state, fiber, and diode lasers, their scaling to high average powers continues to be a challenge. In contrast, the scaling of oxygen-iodine chemical lasers has been repeatedly demonstrated. The proposed electrical initiation and pumping techniques for oxygen-iodine hybrid systems do not alter the fundamental scaling behavior of such devices. Electrically-assisted, closed-cycle gas lasers offer several advantages: excellent beam quality and short wavelength for enhanced lethalities, good atmospheric propagation, and proven scalability to militarily-useful average powers.

A number of Army, Navy, and Air Force mission needs could be met with 100 kW or higher average power Tactical HELs. The HEL average power required also increases rapidly with increased engagement distances, and if multiple targets must be dealt with simultaneously to stay within mission timelines, again arguing for high average power systems. As described below for representative military missions across the Services, while low average powers are useful for some missions, the most robust and versatile tactical HEL systems will be required to deliver high average powers, at least 100 kW, for times on the order of minutes, before regenerating or "reloading."

Airborne HELs such as ABL (employing lighter weight ElectricOIL's) could provide attractive capabilities for several Air Force mission areas, tactical ballistic missile defense, including aircraft self defense, high value asset defense, ground target attack, battlefield illumination for 24-hour imaging, and control of space. Lasers with only Watts of average power can deceive previous generations of IR SAMs. However, new imaging seekers, with Focal Plane Arrays (FPA), can only be countered by blinding or destroying most of the FPA, readouts, or processing electronics, requiring hundreds of Watts or more. In general, for next generation air-to-air and cruise missiles, side aspect fluences of 2 kW/cm^2 are needed if engagements are limited to about a second, to deal with multiple simultaneous launches. This translates to HEL average powers of >50 kW for slant ranges of about 10 km. Another attractive mission for a tactical airborne HEL is space control, attacking LEO satellites to "deny," "degrade," or "damage" them. A single tactical aircraft with a >50 kW HEL could "deny" or "degrade" LEO satellites.

The Navy mission area that has been the focus of HEL interest is ship self-defense against a wide range of missions including sea-skimming cruise missiles. With the current emphasis on littoral

(near shore) operations, with ships usually operating independently, the need has been for self-defense systems onboard the defended ship. Many effects make this difficult but, self-defense from the platform requires the beam to propagate through a restricted channel in the air, so that any absorption of the beam by the air (which is wavelength dependent) will heat the air, reduce the local density and index of refraction and lead to thermal "blooming" of the beam. These challenges are less of an issue if the CONOPS allows for off-board defense, using an airborne HEL for capital ship defense.

While the THEL Deuterium Fluoride system (chemical laser) has demonstrated an ability to destroy small missiles, it will be challenging to make such a system portable enough to meet Army needs for highly mobile forces. A scaleable, closed-cycle, electrically-aided oxygen-iodine laser would be a much lower weight option for both advanced ground-based HEL applications and for future airborne HEL systems, including follow-ons to a closed-cycle COIL currently being developed for an Advanced Tactical Laser (ATL). Electrically aided oxygen-iodine lasers could provide a convenient option for both future ATL and THEL systems. The HEL power required for a mobile unit could be on the order of >50 kW, for a number of Army missions. Airborne options would also reduce the limitations of thermal blooming for certain wavelengths, such as for oxygen-iodine lasers.

1.1.1 Technical Objectives
This program places emphasis on basic research at University institutions targeted at understanding and improving ElectricOIL technology [Carroll, 2001; King, 2001], the education of a future generation of Masters and Ph.D. students, and the ultimate development of the closed-cycle ElectricOIL system. *The primary technical objective of this work is to investigate the details of electric gas generation methodology(plasma physics and chemistry) for producing both electronically excited oxygen and electronically excited atomic iodine from discharge generated species for incorporation into either a re-circulating lasing system or an open cycle flow.*

1.2 ElectricOIL
Dramatic changes to gain generator research and technologies are needed to allow COIL systems towards total elimination of massive liquid phase laser fuel and pressure recovery systems by use of closed-cycle operations and achieve their full potential as efficient producers of 1.3 μm laser beams. These include: 1) *radically new $O_2(^1\Delta)$ generator subsystems (ElectricOIL) which are amenable to closed-cycle operation; and* 2) *tailor a complex kinetic model which can harness the full potential inherent in the generated plasma fluids.* The current programs address both issues by means of innovative technologies in the generation of excited states molecular oxygen and atomic states of iodine as well as demonstrating the essential science needed for closed-cycle operation of an ElectricOIL device.

The classic chemical oxygen-iodine laser (COIL) system [McDermott, 1978] operates on the $I(^2P_{1/2}) \rightarrow I(^2P_{3/2})$ [hereafter denoted as I* and I, respectively] electronic transition of the iodine atom at 1315 nm. The population inversion is produced by the near resonant energy transfer between the metastable excited singlet oxygen molecule, $O_2(a^1\Delta)$ [interchangeably denoted by $O_2(a)$ hereafter], and the iodine atom ground state I. Conventionally, a two phase (gas-liquid) chemistry singlet oxygen generator (SOG) produces the $O_2(a)$. There are many system issues

having to do with weight, safety and the ability to rapidly modulate the production of the $O_2(a)$ which have motivated investigations into methods to produce significant amounts of $O_2(a)$ using flowing electric discharges. Early attempts to implement electric discharges to generate $O_2(a)$ and transfer energy to i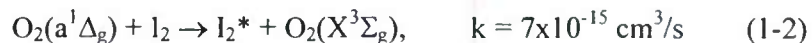odine to make a laser by Zalesskii [Zalesskii, 1975] and Fournier [Fournier, 1980] were unsuccessful. Several investigations have been conducted into the possibility of a continuous flow hybrid electrically powered oxygen-iodine laser with electric discharges to produce the $O_2(a)$ [Carroll, 2003a; Carroll, 2003b; Schmiedberger, 2001; Hill, 2001; Ionin, 2003; Rakhimova, 2003]. These studies have shown that flowing electric discharges through oxygen containing mixtures, typically diluted with a rare gas, can produce useful quantities of $O_2(a)$. Recent studies have demonstrated $O_2(a)$ yields greater than 15% using electric discharges [Schmiedberger, 2001; Hill, 2001; Rakhimova, 2003], and modeling results [Carroll, 2003a; Hill, 2001; Ionin, 2003; Stafford, 2004] have indicated that such laboratory systems may produce a viable laser. In this report we detail our AFOSR investigation that led to our recently reported measurements of gain [Carroll, 2004] and *the first successful laser oscillation* on the I* → I electronic transition of the iodine atom at 1315 nm pumped by resonance excitation transfer from $O_2(a)$ produced in an electric discharge.
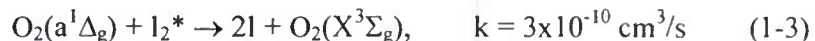
1.2.1 Theory

The role of the $O_2(^1\Delta_g)$ state is essential for the pumping of the upper state of the Iodine laser via:

$$O_2(a^1\Delta_g) + I(^2P_{3/2}) \rightarrow O_2(x^3\Sigma_g) + I(^2P_{1/2}) \tag{1-1}$$
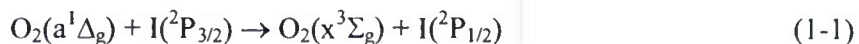
While Eqn. (1-1) leads directly to the upper laser level, several of the $O_2(a^1\Delta_g)$ molecules required to dissociate the molecular iodine under typical COIL conditions.

$$O_2(a^1\Delta_g) + I_2 \rightarrow I_2^* + O_2(X^3\Sigma_g), \qquad k = 7x10^{-15} \text{ cm}^3/\text{s} \tag{1-2}$$

followed by:

$$O_2(a^1\Delta_g) + I_2^* \rightarrow 2I + O_2(X^3\Sigma_g), \qquad k = 3x10^{-10} \text{ cm}^3/\text{s} \tag{1-3}$$

Details and identity of I_2^* are being determined as part of this grant and are being explored under this grant. Estimates are that approximately 5 $O_2(a^1\Delta_g)$, referred to as the "a" state in parts of this report, molecules are used in this process for each iodine molecule. However the $O_2(b^1\Sigma_g)$ state, referred to as the "b" state in parts of this report, can dissociate I_2 in one step:

$$O_2(b^1\Sigma) + I_2 \rightarrow 2I + O_2(X^3\Sigma_g), \qquad k = 4x10^{-12} \text{ cm}^3/\text{s} \tag{1-4}$$

and thus the densities of the $O_2(b^1\Delta_g)$ molecules produced in the EOIL discharge reduce the number of $O_2(a^1\Delta_g)$ molecules necessary for use in Eqn. (1-1). Additionally, oxygen atoms at the appropriate densities can participate in the dissociation step as we will show later. In the ElectricOIL concept, because of significant quantities of the $O_2(b^1\Sigma_g)$ state are produced, under certain conditions $O_2(b^1\Sigma_g)$ can assist in the dissociation process in a more significant way than in the classic COIL. Regardless, the molecular iodine must be dissociated, either with a discharge or by a neutral chemistry route Eqn. (1-3) enhanced by Eqn. (1-4). The advanced ElectricOIL system [Carroll, 2001] could also incorporate a pre-dissociation scheme for the iodine prior to injection into the $O_2(a^1\Delta_g)$ flow; O-atoms may play the a major role as will be seen later.

The justification for the use of an electrical discharge for the production of $O_2(^1\Delta)$ and $O_2(^1\Sigma)$ states is provided by Fig. 1-1. These are global predictions from a Boltzmann Equation solver (by Prof. M. Kushner, Iowa State) that tracks the fraction of electrical power utilized for each electron energy loss process. Shown here is the fraction used to excite the $O_2(^1\Delta)$ state (0.977 eV/exc.) for pure O_2 and mixtures of O_2 with Helium and Argon. In the pure O_2 case nearly 50% of the electrical power can be used to produce $O_2(^1\Delta_g)$ molecules at an E/N of about $9x10^{-17}$ volt-cm^2. In the 3:1 He:O_2 case roughly 42% of the electrical power can be used to produce $O_2(^1\Delta_g)$ molecules at an E/N of about $5x10^{-17}$ volt-cm^2 (also of interest is the significant amount of energy channeling into the "b" state, Fig. 1-2, which may augment "a" state numbers to total over 60%). In the 3:1 Ar:O_2 case about 60% of the electrical power can be used to produce $O_2(^1\Delta_g)$ molecules at an E/N of about $4x10^{-17}$ volt-cm^2. Elastic losses to low atomic weight Helium rob power to $O_2(^1\Delta_g)$, whereas Argon should be beneficial because it has a higher atomic weight and hence its elastic losses are lower. From Fig. 1-1 it is clear that Argon diluent provides a significant benefit if the E/N can be lowered to the optimal level(very recent experiments with a dipolar exciter rf discharge tend to verify this calculation)
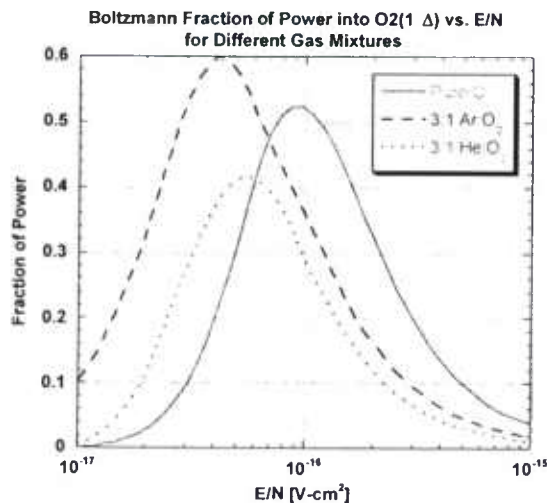
Figure 1–1. Results of Boltzmann Calculation for pure O_2, a 3:1 mix of Ar:O_2, and a 4:1 mix of He:O_2.

Note, the efficiency and yield of $O_2(^1\Delta_g)$ molecules are critically dependent on the field E to neutral gas density N, or E/N, with the dependence of the use of electrical power shown in Fig. 1-1. Although these graphs show a clear maximum at E/N ~ 10^{-16} V-cm^2 for pure oxygen, there is no guarantee that the discharge will, in fact, operate at that value. Fortunately, experiments with a simple DC pre-discharge (upstream from the RF one) indicated an E/N of ~1.5 - $2.0x10^{-16}$ V-cm^2 and obeyed the simple scaling laws for the positive column. Thus we feel that this is a reasonable estimate for spatially averaged value for several of the capacitive and inductive discharges used in our experiments. In an inductive discharge, the field is a maximum at the walls and zero on the axis. Previous calculations suggest an effective E/N of $1.2x10^{-16}$ V-cm^2 at 4.2 Torr and 300 Watts [Verdeyen, 2002]. Calculations of E/N for our recent capacitive discharge work indicates an E/N of around $2.5x10^{-16}$ V-cm^2 at 2.0 Torr of pure oxygen and around $0.8x10^{-16}$ V-cm^2 at 2.0 Torr partial pressure of oxygen mixed with 6.0 Torr partial pressure of Argon.

Figure 1–2.   Excitation Cross-Section for $O_2(a^1\Delta)$ and $O_2(^1\Sigma)$. [Masek, et al. (1977) Czech. J. Phys. B, 27, 888]

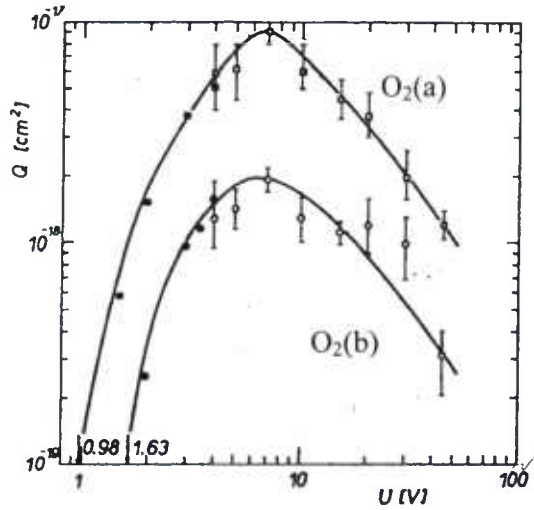For illustrative purposes, if we consider the aforementioned inductive case and assume that 45% of the baseline 300 Watts of RF power is used for the production of $O_2(^1\Delta_g)$ in a cylindrical tube (R=2.54 cm and length of 10 cm) with a volume of 200 cm³ at 4.2 torr of pure O_2, then the production rate for $O_2(^1\Delta_g)$ is:

$$\frac{d[^1\Delta_g]}{dt} = +\frac{135\,W}{Vol. = 200cm^3} \times \frac{1}{0.9775eV} \times \frac{1}{1.6\times10^{-19}\,J/eV} = 4.27\times10^{18}\,cm^{-3}/s \qquad (1\text{-}5)$$

For conditions used in Verdeyen *et al.* [Verdeyen, 2002], the flow velocity is approximately 2×10^3cm/s and thus the lifetime of the molecules in the discharge region is 5 ms. Thus, this elementary analysis would predict an exit density of $O_2(^1\Delta_g)$ of 2.13×10^{16} cm⁻³ or a yield of 16.4%. Given the simplicity of the expression, it is in reasonable agreement with our measured yields of ≈15-16% for several inductive discharges.

A similar calculation can be done for the $O_2(^1\Sigma_g)$ density, and it yields a smaller density by about a factor of $3\times1.66 = 4.98$. The factor of 3 arises because of using only ~15% of the power (as opposed to 45% for $a^1\Delta_g$) and the factor of 1.66 because it costs 1.627 eV to produce the $b^1\Sigma_g$ state as opposed to 0.9775 eV for the $a^1\Delta_g$ state. The origin of the factor of 3-4 is a consequence of the fact that the cross-section for electron impact production of $a^1\Delta_g$ is at least 4 times that for $b^1\Sigma_g$ for virtually all electron energies of significance, Fig. 1-2. This ratio is in reasonable agreement with current experimental results and later we will show that the early lab models have approximately this amount energy in the flow but that a roughly half this amount is needed to get the laser over threshold and a good amount is lost downstream in-part due to the limited size of the small cavity optics. The inductive configurations have the advantage of being able to be reconfigured rapidly as we improve the discharge units. They have the disadvantage of being relatively inefficient.

1.2.2 Peak Yield and Optimum E/N calculations
Using the non-equilibrium plasmadynamics capability of the newly developed BLAZE-IV model (Palla, 2007), physics critical to the improvement of ElectricOIL devices have been studied. For

the purposes of this study $O_2(a^1\Delta)$ yield is defined as the ratio of the $O_2(a^1\Delta)$ state to all states of the O_2 molecule.

$$\text{Yield} \equiv \frac{[O_2(a^1\Delta)]}{[O_2(^3X)]+[O_2(a^1\Delta)]+[O_2(b^1\Sigma)]+\frac{3}{2}[O_3]+\frac{1}{2}[O]} \qquad (1\text{-}6)$$

Calculations indicate that in a high-yield discharge, the equilibrium yield value is dominated by the equilibrium achieved between the inelastic electron impact excitation of $O_2(^3X)$ to $O_2(a^1\Delta)$ and its super-elastic reverse. Calculations indicate that this yield equilibrium may exhibit dependence on a range of discharge parameters.

To illustrate this effect, calculations were performed for a O_2:He:NO = 3:16:0.15 mmol/s discharge at 12.5 Torr. All ElectricOIL calculations utilized a discretization of the electron energy used in the solution of the Boltzmann equation into 100 cells with a constant energy cell width over the range 0 to 25 eV. As the yield equilibrium in this case is, to first order, dominated by an equilibrium between electron impact events, total electron number density may be factored out, therefore making the resulting calculated yield equilibrium independent of power deposition, assuming E/N may be held fixed, independent of applied power. It should be noted however, that applied power may strongly impact discharge gas temperature and electric field strength (in addition to other flow parameters) and therefore may indirectly influence the electron energy distribution function and any resulting equilibrium achieved between competing electron impact events. The $O_2(a^1\Delta)$ yield equilibrium in this case is characterized by the simplified net fraction of power deposited into $O_2(a^1\Delta)$. The simplified net fraction of power deposited into $O_2(a^1\Delta)$ is defined as the ratio of net power deposited into $O_2(a^1\Delta)$ [power deposited by electron impact excitation of $O_2(^3X)$ to $O_2(a^1\Delta)$ less power lost via the super-elastic reverse] to the net power deposited into the flow via all elastic and inelastic processes. When the simplified net fraction of power deposited into $O_2(a^1\Delta)$ is plotted versus the ratio of the electric field to gas number density for discharge start-up conditions (initially zero yield), the positive peak of the resulting curve may be considered the optimum E/N value for the net positive production of $O_2(a^1\Delta)$ in the modeled electric discharge. Calculations indicate that for this discharge start-up condition (Y = 0.0) the optimum E/N value for the production of $O_2(a^1\Delta)$ for the modeled discharge is approximately 3.9 Td, Fig. 1-3.

However, when the same study is performed for an operating discharge (non-zero yield, Y > 0, and concentrations of other states typical to an operating discharge) the location of the peak shifts to higher E/N values. For example, with a O_2:He:NO=3:16:0.15 mmol/s gas mixture at 12.5 Torr having an $O_2(a^1\Delta)$ yield of 0%, the peak fractional power deposition is 0.445 at 3.9 Td for these flow conditions, whereas at a yield of 0.3 the peak fractional power deposition is approximately 0.025 at 13.2 Td. Therefore, the above calculations were performed for a range of $O_2(a^1\Delta)$ yields from 0.0 to 0.3875. It was found that for yields above approximately 0.3875, at the above discharge conditions, the power deposition curves approached zero or below, indicating that for these conditions the maximum achievable yield is near 0.3875. This value is close to the achievable yield limit of 0.4 that may be predicted analytically based on an equilibrium energy distribution and the statistical weights of 2 and 3 that are used for the states $O_2(^3X)$ and $O_2(a^1\Delta)$ in the calculation of the collision cross-section for the super-elastic de-excitation of $O_2(a^1\Delta)$ to $O_2(^3X)$. In addition, the calculations indicate that the optimum operating E/N for production of $O_2(a^1\Delta)$ remains generally stable between 3.9 Td and 7.5 Td for

equilibrium yields in the range of 0.0 to 0.25, before shifting to higher values. This indicates that as a discharge stabilizes at an operating yield greater that zero, the optimum operating E/N may not be constant for certain operating conditions. It should be noted however, that even for the described discharge, the optimum yield may likely be tuned to higher values using other means such as the attenuation of temperature effects and other possibly detrimental conditions. Furthermore, discharge produced $O_2(b^1\Sigma)$ can be converted to $O_2(a^1\Delta)$ in the post-discharge region, and it may be possible to catalytically convert O atoms into $O_2(a^1\Delta)$, thereby further increasing the $O_2(a^1\Delta)$ yield.
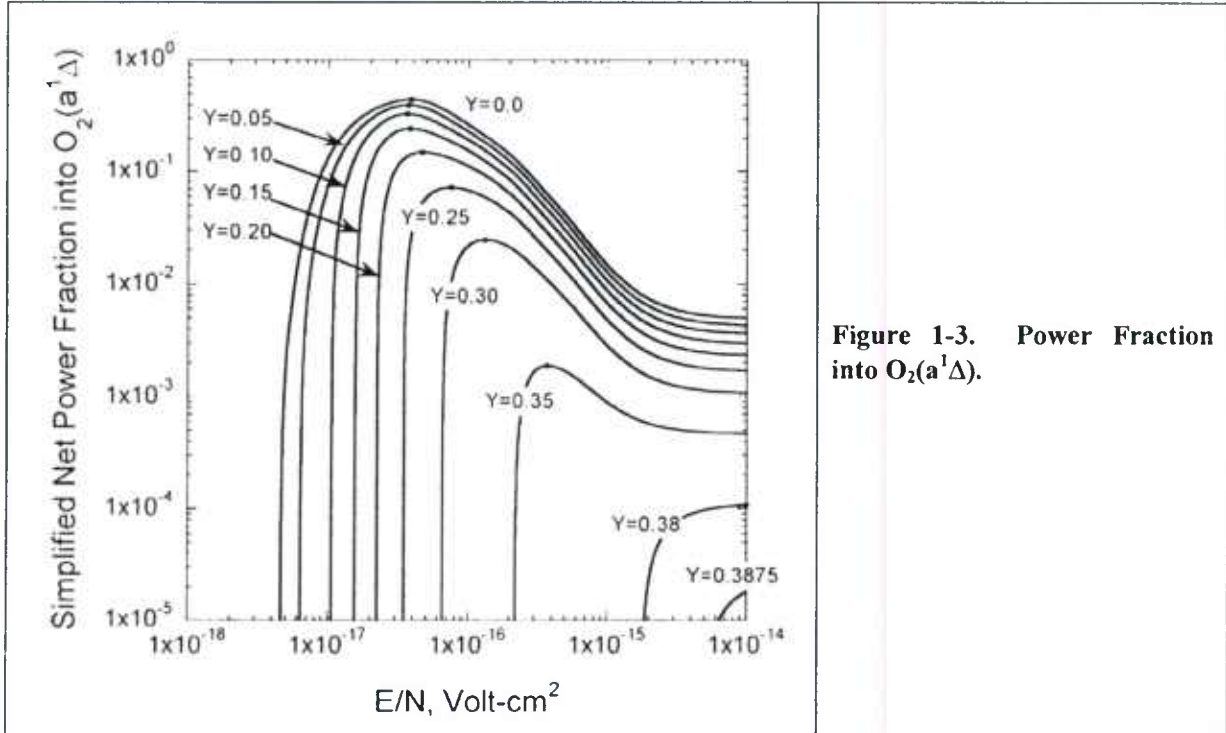

Figure 1-3. Power Fraction into $O_2(a^1\Delta)$.

2. EXPERIMENTAL ACCOMPLISHMENTS

2.1 Gain and Lasing Experiments with an RF Discharge
2.1.1 Experimental Setup

A block diagram of a typical discharge tube setup is shown in Fig. 2-1. A radio frequency (rf) discharge between two internal hollow cathode electrodes (each 13 cm long) operating at 13.56 MHz was used as the excitation source. The plasma zone is approximately 4.9 cm in diameter and 25 cm long. Details of the performance of a similar electric discharge with capacitive external electrodes can be found in Carroll *et al.* [Carroll, 2003b]. The subsonic diagnostic duct has four windows through which simultaneous measurements are made of the optical emission from $O_2(a)$ at 1268 nm, $O_2(b^1\Sigma)$ [denoted $O_2(b)$ hereafter] at 762 nm, I* at 1315 nm, and the gain/absorption proportional to $\{[I^*] - 0.5 \cdot [I]\}$. An early generation Optical Multi-channel Analyzer with a low-resolution monochromator or a germanium detector was used for the emission measurements at 1268 nm and 1315 nm. The emission of $O_2(b)$ at 762 nm was measured with a CCD camera and low resolution monochromator. A variety of Micro-Motion CMF and Omega FMA mass flow meters were used to accurately measure the flow rates of the gases. Capacitance manometers from MKS and Leybold measured pressures in the subsonic and supersonic flow regions. The supersonic diagnostic cavity is a Mach 2 nozzle with view port windows.
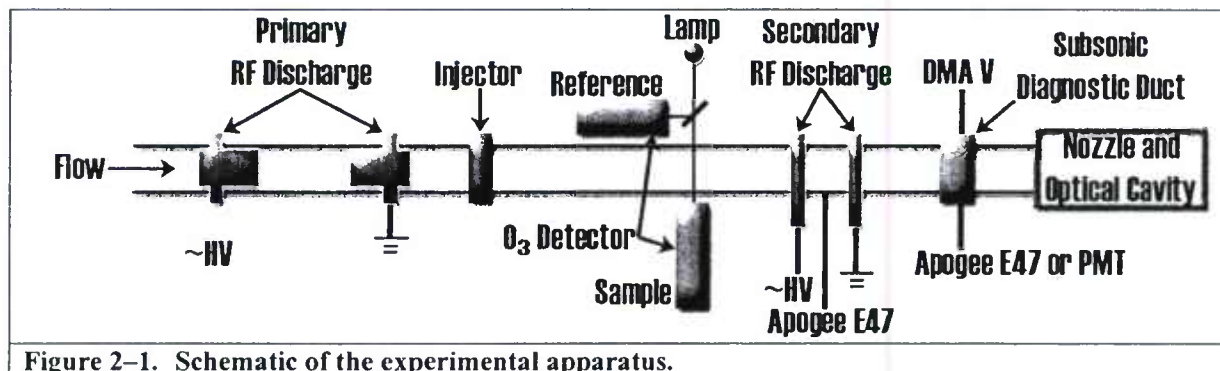
Figure 2–1. Schematic of the experimental apparatus.

Measurements of gain (or absorption) were made with an early version of the Iodine-Scan diagnostic (ISD), developed by PSI [Davis, 1996]. Since the ISD uses a narrow band diode laser, the measured lineshapes can also be used to determine the local temperature from the Voigt profile. Wedged anti-reflection coated windows were used on the sides of both the subsonic diagnostic section and the supersonic cavity for the gain diagnostic to minimize etalon effects. A 2-pass configuration (10 cm pathlength) was used in the subsonic section and a 4-pass configuration (20 cm pathlength) in the supersonic section. Preliminary yield measurements of $O_2(a)$ were made from the gain diagnostic and relative I* to $O_2(a)$ spectral intensity measurements based upon the techniques originally developed by Hager [Hager, 2002], and Davis and Rawlins [Rawlins, 2003], see Sections 2.1.2 and 2.2.1.

2.1.2 Recent Experimental Results with RF Discharges

During the course of this research, it was determined that electric discharge stability and temperature control are critical parameters to obtaining laser gain. Electric rf discharges sustained in moderate pressures (many to 10s of torr) of oxygen are prone to instabilities. The

discharge production of O atoms, O_3 and other excited species adds higher levels of complexity to the downstream kinetics when the iodine donor species are added to the flow, which are not encountered in a purely chemical generation system. The critical aspect of temperature control results from the equilibrium of the pumping reaction,

$$O_2(a) + I \leftrightarrow O_2 + I^* \tag{2-1}$$

where the forward rate is 7.8 x 10^{-11} cm^3/molecule-s [Derwent, 1972], and the backward rate is 1.04 x 10^{-10} exp(-403/T) cm^3/molecule-s [Perram, 1988], with the equilibrium rate constant ratio of the forward to backward reactions being K_{eq}=0.75 exp(403/T)] [Perram, 1988], where T is the gas temperature. The threshold yield, Y_{th}, of $O_2(a)$ for positive I* to I inversion as a function of temperature can be written as Y_{th}=1/[1+1.5 exp(403/T)] [Hon, 1996]. Note that the backward rate is slower, K_{eq} larger, and Y_{th} lower as T is decreased.

We had previously been unsuccessful in attaining laser gain (as had other groups, see Section 1.2) despite having achieved yields of $O_2(a)$ with an electric discharge that were, in principle, high enough to do so. Last year, we conducted experiments that have led to the attainment of gain and lasing, and we describe these below. We measured absorption in the supersonic region with temperatures of approximately 240 K, despite having yields estimated at 15%, which should have been well over the required threshold yield, Y_{th}, of $O_2(a)$ required for positive gain. To solve the puzzle, we began a rigorous investigation of the effects of iodine in the subsonic flowing region without the added complication of the supersonic cavity. To perform these experiments we moved the iodine injection point upstream (by approximately 20 cm) from a diagnostic section added into the subsonic flow tube, Fig. 2-1; previously we had been injecting the iodine just upstream of the nozzle throat as in traditional COIL geometries.

We made simultaneous measurements of the optical emission from $O_2(a)$ at 1268 nm, $O_2(b)$ at 762 nm, I* at 1315 nm, and the absorption through the optical windows in the subsonic diagnostic section, Fig. 2-2. Two important things are immediately apparent from these data. First, for the zero iodine case there is a peak in the 1268 signal that begins at around 500 W. (Note that rf system power is presented; electrical measurements indicate that approximately 80-90% of the system power is actually absorbed by the plasma for the O_2:He=1:4 mixtures in these experiments.) The drop in signal at higher powers is believed to be a consequence of instabilities and thermal constriction that visibly develop in the rf discharges employed under these flow conditions. We are presently investigating the discharge stability issues in an effort to improve the performance and yield of the discharge. We are presently investigating an advanced Intermediate Frequency Pulse-Sustainer (IFPS) power electronics unit that is found to significantly reduce the discharge instability and permit more efficient energy coupling into the desired $O_2(a)$ state (see Section 6). The second and more troubling observation from Fig. 2-2 is that when very small amounts of molecular iodine were added to the flow, the level of $O_2(a)$ emission dropped dramatically. The flow rate of O_2 was 4 mmol/s with 500 W of rf power, and approximately 0.6 mmol/s of $O_2(a)$. The iodine flow rate was approximately 0.006 mmol/s, i.e., only 1% of the $O_2(a)$ concentration. Given that the molecular iodine was only 1% of the $O_2(a)$ and that the O atoms will rapidly dissociate it [Carroll, 2003a], the dramatic drop in 1268 signal could not be explained by a classic COIL iodine dissociation process. Further, the concentration of atomic iodine was far too low to explain a significant drop in $O_2(a)$ from the pumping reaction. These facts lead us to the suggestion that whatever phenomenon is causing this dramatic drop in the energy source, $O_2(a)$, is also a reason why we (and others) had previously

been unsuccessful in attaining gain with electrically pumped systems. Further, while measurements of high yields of $O_2(a)$ in pristine high velocity environments of rare gas diluents are encouraging, the issue of greater significance is the yield of $O_2(a)$ in the presence of iodine.
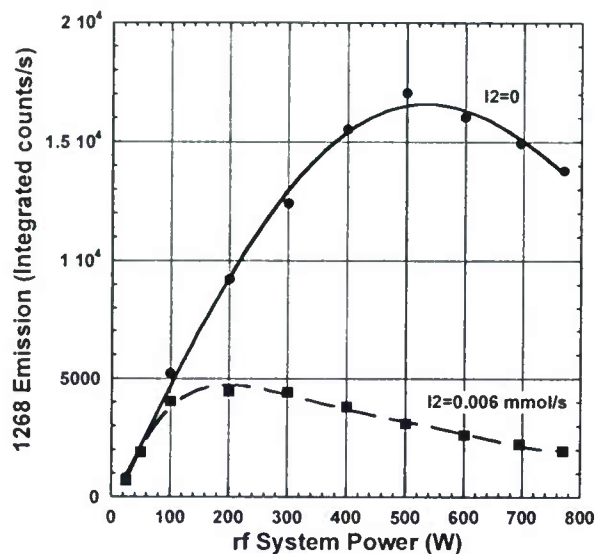

Figure 2–2. O2(a) emission at 1268 nm with and without iodine at the subsonic diagnostic port as a function of system power, for a flow of 4 mmol/s of O2 mixed with 16 mmol/s of He at a pressure of 10 torr.

Given the successful history of conventional COIL where the change in yield in the presence of iodine is negligibly small, we clearly have a different system to deal with. The character with this electrically pumped system is related to products of the discharge that are not present in classic COIL, i.e., products other than $O_2(a)$ and $O_2(b)$. Since the loss behavior occurs only with iodine present, it is believed that the loss is through the I* channel, i.e., energy transfers through I* from $O_2(a)$ to some other species. The potential candidates are: O atoms, O_3 *(recent measurements of rate constants involving* O_3 *seem to rule out this route)*, charged species, ultra-violet (UV) or vacuum ultra-violet (VUV) radiation. All could play a deleterious role and none appear in classic COIL. The most obvious candidates are high densities of atomic oxygen as it is present in number densities on the order of the $O_2(a)$. Modeling predicts and recent measurements establish that O_3 is in quantities of two to three orders of magnitude lower than $O_2(a)$ [Carroll, 2003a; Stafford, 2004], and the charged species become negligible within a few cm downstream of the exit of the discharge [Stafford, 2004], so these candidates are less likely to be the major cause of the observed $O_2(a)$ loss. As such, we focused in on oxygen atoms as being the major contributor to the deleterious loss of $O_2(a)$ with iodine present.

Oxygen atoms play a positive role as well as a potential deleterious role in the kinetics downstream of the discharge region with iodine present. Their positive role is that they rapidly dissociate molecular iodine through processes (2-2) and (2-3):

$$I_2 + O \rightarrow IO + I \tag{2-2}$$

$$IO + O \rightarrow O_2 + I. \tag{2-3}$$

The rates for reactions (2-2) and (2-3) are 1.4×10^{-10} cm^3/molecule-s [Payne, 1998], and 1.5×10^{-10} cm^3/molecule-s [Payne, 1998], respectively. A potential deleterious role of oxygen atoms was first postulated by Heaven [Heaven, 2001] to be,

$$I^* + O \rightarrow I + O. \tag{2-4}$$

Han et al. [Han, 2004] have recently measured this rate to have an upper bound of 2×10^{-12} cm^3/molecule-s; this is considerably smaller (an order of magnitude or more) than both the forward and backward rates of reaction (1) and hence this reaction was originally thought to be of limited importance in reasonably fast flowing systems such as our set up. However, of the candidate processes listed for the dramatic loss of $O_2(a)$ in the presence of iodine, atomic oxygen seemed the most likely culprit and the rate for equation 4 is likely near 1×10^{-11}.

We established the O atom production from the discharge as a function of power into the discharge by titrating with NO_2 using a well established technique first developed by Kaufman [Kaufman, 1958]. We found an approximately linear dependence of O atom production with discharge power, which is consistent with modeling work in the range in which we are operating [Stafford, 2004].

We then added NO_2 upstream of the iodine ring injector and monitored the emission at 1268, 1315 and 762 nm at the subsonic diagnostic section. Figures 2-3 and 2-4 show the dramatic changes that occur as the flow rate of NO_2 is increased. Note that as NO_2 was added the pressure in the discharge region was maintained at approximately 10 torr by adjusting a downstream flow rate of Ar, see Fig. 2-1. Figure 2-3 clearly shows how increasing the NO_2 flow raises the 1268 signal in the presence of iodine progressively to approximate the signal with no iodine in the flow, i.e., by scavenging O atoms from the flow there is a progressively lesser effect from process 4. However, the situation is more complex than just that. Note that the point where we are almost back to the nominal 1268 signal occurs at an NO_2 flow rate of 1.0 mmol/s, yet the O atom flow at 770 W is only approximately 0.59 mmol/s. This result was unexpected since the NO_2 flow rate is well beyond the full titration point, i.e. where $[NO_2] = [O]$ at the highest system power level. Since our mixing appears to be visibly complete within a few cm and the $O+NO_2$ reaction rate is fairly fast, approximately 1×10^{-11} cm^3/molecule-s at room temperature [Atkinson, 1997], we did not understand why we must significantly over-titrate the atomic oxygen to regain the majority of the $O_2(a)$ signal; we recently showed that it was largely a mixing effect when we observed a more reasonable result by measurements take further downsteam and that there may be some other process(es) occurring that we have not yet identified nor understood.

Figure 2-4 illustrates the progressive rise in the I* emission with increasing NO_2 flow rate. This rise is consistent with the increasing $O_2(a)$ signal shown in Fig. 2-4. It is of considerable interest that the location of the peak signal shifts to higher powers with higher NO_2 flow rates.

A dramatic increase of the $O_2(b)$ emission was also observed when NO_2 was added (not shown for brevity). We believe that this is due to a combination of atomic iodine formed by reactions with O atoms along with reaction (1) to produce I* followed by the process $I^* + O_2(a) \rightarrow I + O_2(b)$, which has a reaction rate of 1.0×10^{-13} cm^3/molecule-s [Heidner, 1983]. While this is a negligible loss to $O_2(a)$ it is a significant production rate of $O_2(b)$.
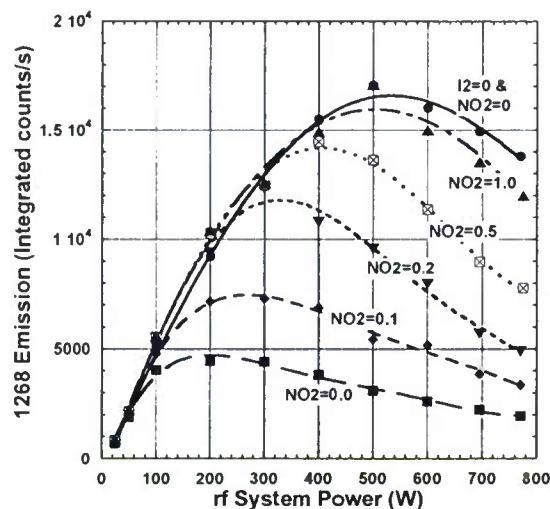
17

Figure 2–3. O$_2$(a) emission at 1268 nm with and without iodine at the subsonic diagnostic port as a function of system power and the NO$_2$ flow rate (in mmol/s), for a flow of 4 mmol/s of O$_2$ mixed with 16 mmol/s of He at a pressure of 10 torr.
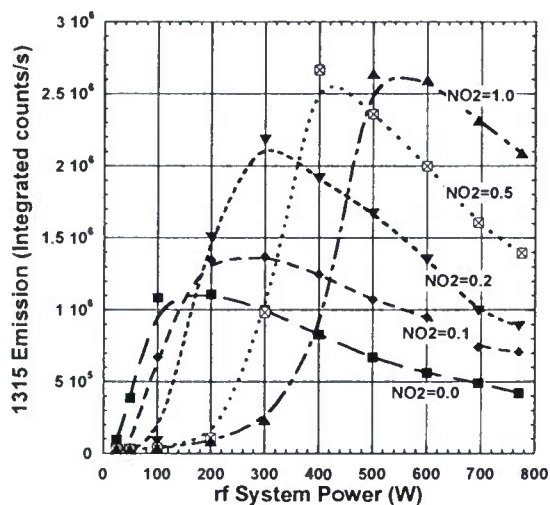

Figure 2–4. I* emission at 1315 nm at the subsonic diagnostic port as a function of system power and the NO$_2$ flow rate (in mmol/s), for a flow of 4 mmol/s of O$_2$ mixed with 16 mmol/s of He at a pressure of 10 torr.

In an effort to establish a better estimate for the rate constant for reaction (2-4), the emissions of O$_2$(a) and I* were monitored as a function of the distance from the plane of the I$_2$ injection and is presented in Fig. 2-5. The data show that the two signals decay by a significant amount with a simple exponential decay. Both appear to have the same approximate spatial decay rate, which is an indication of the near equilibrium between O$_2$(a) and I* via the forward and backward rates associated with reaction (2-1).

The data illustrated in Fig. 2-5 coupled with measurements of the oxygen atom concentration and the initial O$_2$(a) concentration determined by the technique outlined by Rawlins et al. [Rawlins, 2003] one can obtain a first order estimate of the rate coefficient for the deactivation of I* to I from Eq. (2-5),

$$k_4 = \frac{[O_2(a)]_0}{[O]_0[I^*]_0} \cdot \frac{u_f}{L}. \qquad (2\text{-}5)$$

Here, u_f is the flow velocity and the subscript "0" indicates the concentration of the various species at the plane of iodine injection (with the assumption that the molecular iodine is

dissociated immediately by the O atoms) with spatial variation of $O_2(a)$ and I^* being $\exp(-z/L)$ in agreement with Fig. 2-5. For the 10 torr case illustrated in Fig. 2-5 having an estimated $O_2(a)$ yield of 15% (at the I_2 injection point), a temperature of 375 K from the gain diagnostic and hence an equilibrium constant $K_{eq}=2.19$, an oxygen atom density of 3.72×10^{15} cm^{-3}, an $O_2(a)$ density of 6.70×10^{15} cm^{-3}, $[I]+[I^*]$ of 1.86×10^{14} cm^{-3} and thus $[I^*]$ of 4.60×10^{13} cm^{-3} [from K_{eq} and an $O_2(a)$ yield of 15%], a flow velocity of 2633 cm/s and L of 30.5 cm from Fig. 2-5 gives

$$k_4 = 3.4 \times 10^{-12} \text{ cm}^3/\text{molecule-s,} \qquad (2-6)$$

which is higher than the upper bound of 2×10^{-12} cm^3/molecule-s given by Han et al. [Han, 2004]. The simple exponential deactivation of $O_2(a)$ and I^* suggests a simple process as expressed by reaction (2-4).
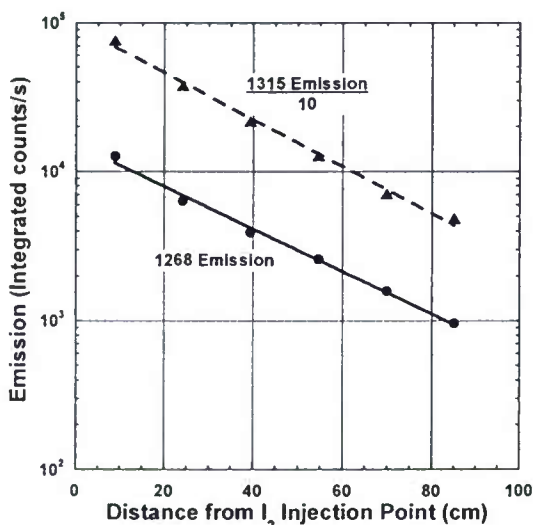

Figure 2–5. $O_2(a)$ (1268 nm) and I^* (1315 nm) emission versus distance from the I_2 injection point for a primary discharge flow of 4 mmol/s of O_2 mixed with 16 mmol/s of He at a pressure of 10 torr. A secondary flow of 0.008 mmol/s of I_2 and 2 mmol/s of He was injected at x=0. The rf power was 400 W. (Note that the 1315 signal has been divided by a factor of 10.)
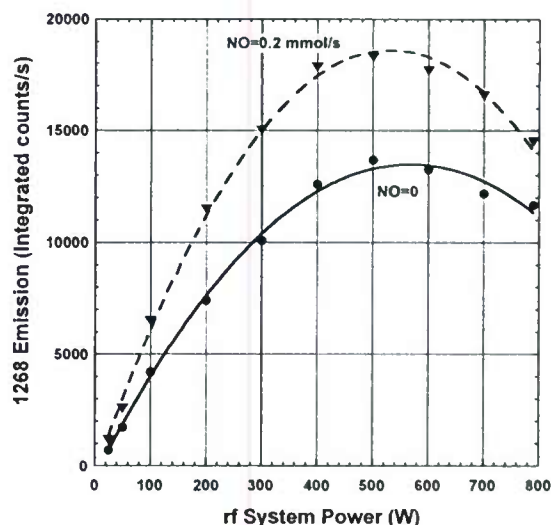
Figure 2–6. $O_2(a)$ emission at 1268 nm with and without NO at the subsonic diagnostic port as a function of system power, for a flow of 5 mmol/s of O_2 mixed with 20 mmol/s of He at a pressure of 10 torr

Other possible quenchers of I^* that have been considered are NO_2, NO, IO, and O_3. The I^*+NO_2 rate was measured to have an upper bound of 8.5×10^{-14} cm^3/molecule-s [Han, 2004], and the rate by NO is 1.2×10^{-13} cm^3/molecule-s [Heaven, 2004], but neither of these rates is large enough to compete with the I^*+O quenching rate. The IO self removal reaction $IO + IO \rightarrow 2I + O_2$ is fast, 8.2×10^{-11} cm^3/molecule-s [Han, 2004], but the predicted densities are too low for IO to play any significant role in quenching I^*. The quenching rate of ozone has recently been measured as being slow and based upon predicted concentrations, the quenching rate with ozone would have to be two orders of magnitude larger than the quenching rate of O for the ozone reaction to compete. It is still possible that the sum of the effects of all competing reactions is

adding up to a level that competes with the O atoms; further modeling studies need to be conducted to validate or refute this possibility.

As discussed in prior works [Zalesskii, 1975; Fournier, 1980; Carroll, 2003a; Carroll, 2003b; Hill, 2001; Ionin, 2003; Rakhimova, 2003] it is important to lower the parameter E/N such that it is close(r) to the optimal excitation cross-section value to attain maximal yields of $O_2(a)$. One way to lower E/N is to introduce a gas with a lower ionization threshold. NO has an ionization threshold of 9.26 eV, which is significantly lower than 12.07 eV threshold of O_2. Experiments were conducted by adding NO to the flow. It was found that NO additions of 1-10% of the O_2 flow rate produced the largest increases in the production of $O_2(a)$ and typically >4% was optimal. Figure 2-6 shows the significant improvement (~33%) attained with a 4% (0.2 mmol/s) addition of NO in a flow of 5 mmol/s of O_2 mixed with 20 mmol/s of He at 10 torr total pressure (Recently NO has been shown to have a catalytic role in the reaction set in addition to it's role in lowering E/N).

Several flow conditions were found that resulted in laser gain using the configuration shown in Fig. 2-1. A typical set of conditions is 4 mmol/s of O_2 mixed with 16 mmol/s of He and 0.2 mmol/s of NO flowing through a 400 W rf discharge. An additional 0.2 mmol/s of NO_2 was added downstream to scavenge some of the excess O atoms, followed by injection of a secondary stream of 0.008 mmol/s of I_2 with 2.0 mmol/s of secondary He diluent. To raise the pressure for more ideal nozzle performance with our vacuum system, 20 mmol/s of Ar was injected further downstream. The pressures in the subsonic diagnostic duct and in the supersonic diagnostic cavity were 10.6 torr and 1.6 torr, respectively.

Absorption in the subsonic region for these conditions was –0.009% cm^{-1}, with a temperature of 400 K, and an $O_2(a)$ yield of 15% (as computed from the gain/spectral technique outlined by Rawlins *et al.* [Rawlins, 2003]). Based on these measurements, positive gain could be expected if the gas temperature were sufficiently reduced. As such, gain measurements in the supersonic cavity were made for the above flow conditions as shown in Figs. 2-7 and 2-8. At a low power of 100 W of rf discharge power and a yield of approximately 5% only absorption was observed. Upon raising the discharge power to 400 W, positive gain of ≈0.002% cm^{-1} was measured. The measured lineshapes were corrected for homogeneous broadening due to He, Ar, and O_2 to obtain the Doppler width according to the procedure outlined by Whiting [Whiting, 1968]. From the resulting Doppler width, we obtain a temperature estimate of ≈210 K at 100 W and ≈240 K at 400 W in the supersonic region. *These were the first measurements of positive gain in a continuously flowing iodine system with $O_2(a)$ being provided by an electric discharge [Carroll, 2004].* Interestingly, the first measurement of positive gain on a classic liquid chemistry COIL system was also on the order of 0.001%/cm [Pritt, 1977]. Note the signal-to-noise with the existing Iodine Scan diagnostic; PSI's new BRD gain diagnostic (discussed further in Section 5.1) improves the signal-to-noise by approximately a factor of 10 and will greatly improve the accuracy of our data.
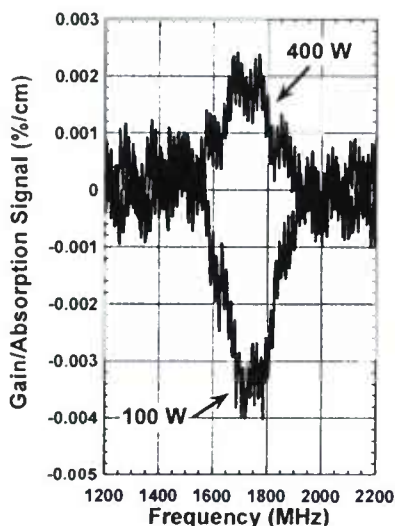
Figure 2–7. Gain in the supersonic cavity as a function of frequency. Positive gain was observed at 400 W rf discharge power and absorption observed at 100 W.
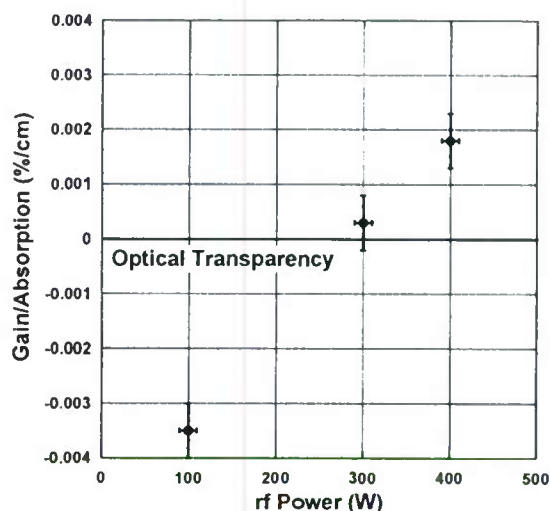
Figure 2–8. Gain in the supersonic cavity as a function of rf discharge power.

By adding pre-cooled Ar upstream of the nozzle throat and raising the upstream pressure to 13 torr we were able to make further improvements to the gain by lowering the total temperature and increasing the density. Figure 2-9 shows both a positive gain trace in the supersonic cavity and the corresponding absorption trace in the subsonic cavity. The flow conditions were the same for this case as discussed above with the exception of raising the Ar flow rate to 38 mmol/s of Ar to raise the upstream total pressure to 13 torr. The gain in the supersonic cavity was measured to be ≈at 400 W of rf discharge power. From Fig. 2-9, including a correction for homogeneous broadening, we estimate temperatures of ≈220 K in the supersonic cavity and ≈375 K in the subsonic region.

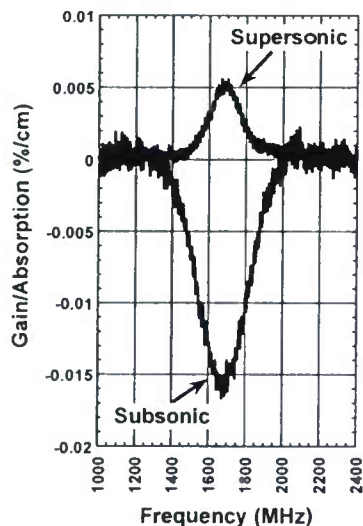**Figure 2–9.** Absorption in the subsonic diagnostic section and gain in the supersonic cavity as a function of frequency at 400 W rf discharge power with cooled N_2 injected upstream of the throat. Positive gain was observed in the supersonic section and absorption in the subsonic section.

21

Laser power measurements were made with a Scientech Astral™ model AC2500/AC25H calorimeter attached to a Scientech Vector™ model S310 readout. The laser power measurements were made at the same position as the gain in the supersonic laser cavity. The gain measurements were made first and then the vacuum mirror mounts (VMM) were put in place with mirrors for the laser power tests. Two very high reflectivity mirrors with 1 m radius of curvature were purchased through Los Gatos Research, Inc. (LGR). LGR characterized the mirrors by cavity-ring-down spectroscopy to have a reflectivity, R, of 99.990% ± 0.001%. A measurement of mirror transmission, T, and absorption/scattering, AS, was unavailable, but historically a large fraction of the remainder of 1-R is in AS losses for high reflectivity mirrors. The mirrors were separated by approximately 38 cm. An Infrared (IR) Detection Card from New Focus, Model 5842, with response between 800-1600 nm, was also used to verify the laser action.

Several flow conditions were found that resulted in lasing using the configuration shown in Fig. 2-1. A typical set of conditions was 3.0 mmol/s of O_2 mixed with 16.0 mmol/s of He and 0.15 mmol/s of NO flowing through a 450 W rf discharge. The pressures in the subsonic diagnostic duct and in the supersonic diagnostic cavity were 12.6 Torr and 1.55 Torr, respectively. For these conditions, no additional NO_2 was necessary to scavenge excess O atoms. A secondary stream of approximately 0.008 mmol/s of I_2 with 1.0 mmol/s of secondary He diluent was injected approximately 50 cm downstream from the exit of the discharge. A tertiary flow of 54.5 mmol/s of cold N_2 gas ($\approx$120 K) was injected further downstream to lower the temperature and to raise the pressure for better nozzle performance with our vacuum system. The total outcoupled cw laser power was 205 mW. (Note that the first measurement of laser action on a classic liquid chemistry COIL system produced 4 mW [McDermott, 1978].) An image of the 205 mW laser beam from the IR card is shown in Fig. 2-10. Simultaneous measurements of $O_2(a)$ yield and laser power as a function of rf power input were made, Fig. 2-11; the laser is seen to turn on at 260 Watts of rf power when the $O_2(a)$ concentration gets high enough to get the gain above the resonator threshold level. Note: in this early data there is a roll off in laser power beyond 450 W that is larger than the drop in $O_2(a)$ yield; we believe that this is a consequence of two factors: (1) the drop in singlet-delta yield, and (2) the fact that progressively more O atoms are created at higher powers and that the NO flow rate was optimized for 450 W rather than the higher power levels.

CW Laser Power & O2(a) Yield vs. RF Power
(O2:He:NO=3:16:0.15, 12.6 Torr)
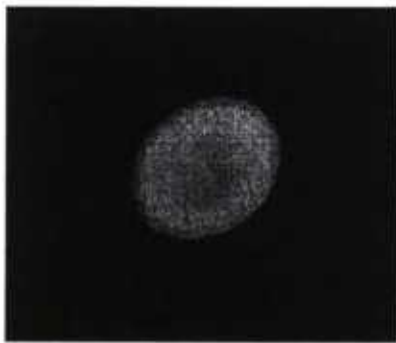
Figure 2–10. ElectricOIL laser beam with 205 mW of cw outcoupled power. The beam size at the output mirror is approximately 1.9 cm.
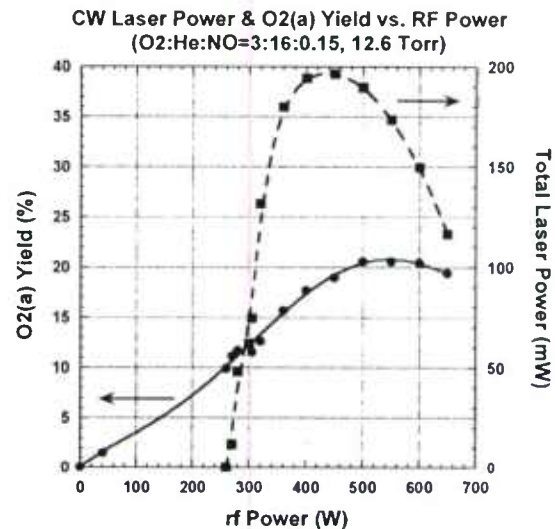
Figure 2–11. CW laser power and O2(a) yield as a function of rf discharge power.

Tests were performed to demonstrate the stability of the ElectricOIL laser. Figure 2-12 illustrates the relatively steady power output over a 35-minute test; the total power output was 205 mW ± 10 mW. Another experiment was performed where the laser was cycled on and off over 33 minutes; Figure 2-13 illustrates the high degree of cycle-to-cycle repeatability of the system. It should be noted that these are the first lasing demonstrations this new cw electric hybrid laser system and that we anticipate dramatic improvements in efficiency in the coming work period.

CW Laser Power vs. Time
(O2:He:NO=3:16:0.15, 12.6 Torr)

Cycled Laser Power vs. Time
(O2:He:NO=3:16:0.15, 12.6 Torr)
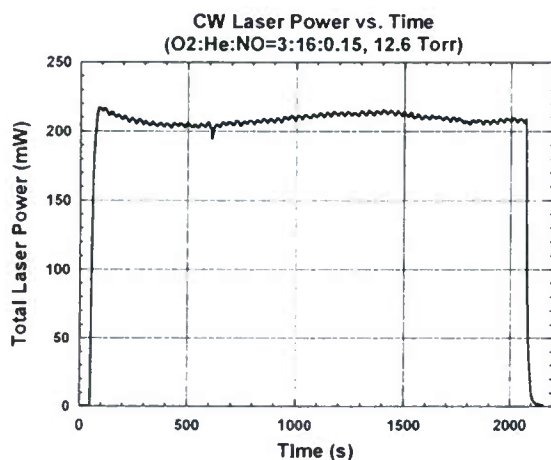
Figure 2–12. ElectricOIL CW laser power as a function of time.
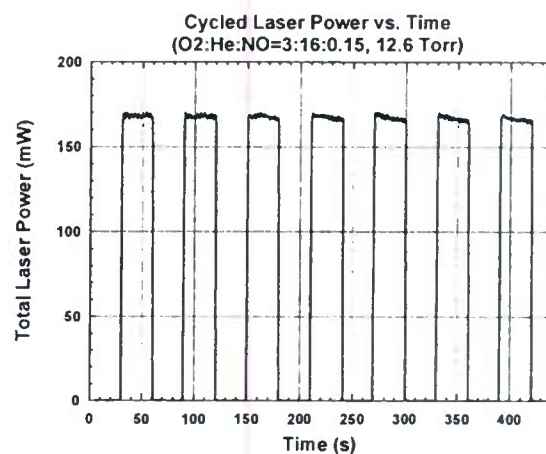
Figure 2–13. ElectricOIL CW cycled laser power as a function of time showing steady cycle-to-cycle power.

More recent measurements employing several of the more advanced transverse discharges gave successive improvements in both the laser gain and power. Figure 2-14 shows one configuration

of an advanced cavity/discharge unit. In recent measurements the gain of the laser was increased in a transverse rf discharge unit coupled to a closer coupled cavity. With this improvement pressures were increased and more stable discharges are achieved allowing power densities in the flow to increase dramatically. After incorporating an iodine dissociator from another program the gain increased from less than .005% cm^{-1} to 0.1% cm^{-1} at pressures up to 48 torr, Fig. 2-15. Extracted power also increased from the milliwatt range in the earlier measurements to over 6 watts. These measurements, made during the final months of the grant, are highly encouraging and we are pursuing new discharge technologies to increase the yields which should begin to make even better performance in the near future.
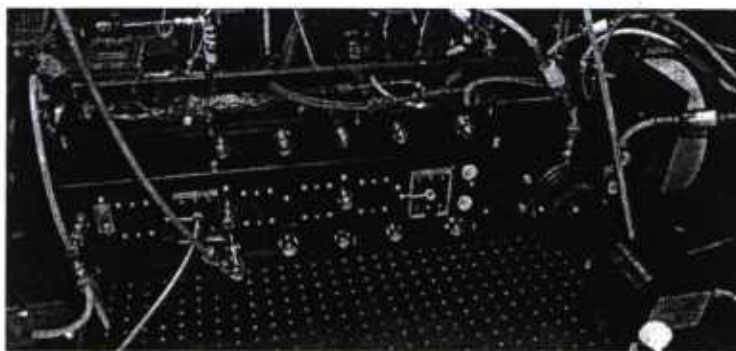
Figure 2-14. Advanced cavity discharge unit.

Figure 2-15. Changes in discharge and cavity configurations show successive increases in laser gain.

Figure 2-16. Subsonic laser cavity with Mach = 0.8 nozzle installed.

Work was initiated to demonstrate laser gain in a subsonic version of the laser. This mode is important since this might be preferable for closed-cycle operation. Figure 2-16 shows the

subsonic nozzle control volume and laser cavity. Only a few measurements were made, but performance was quite acceptable and comparable to a similar supersonic case, Fig. 2-17. It is important to understand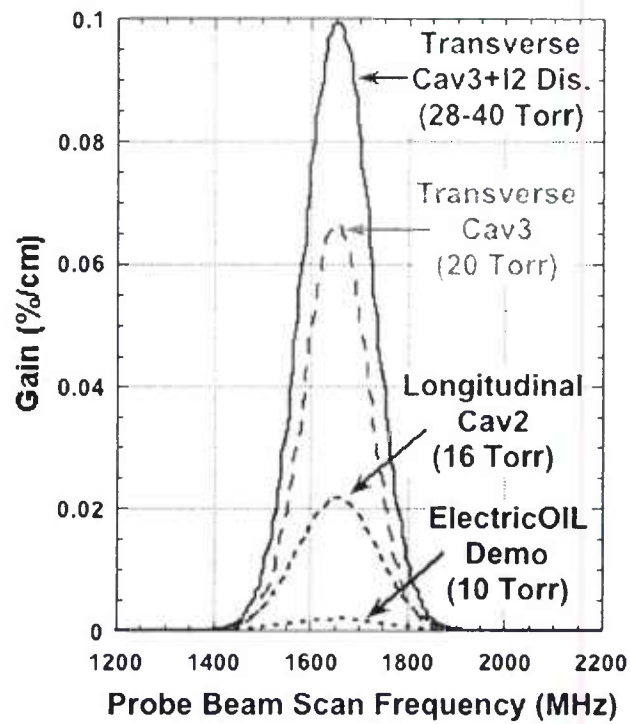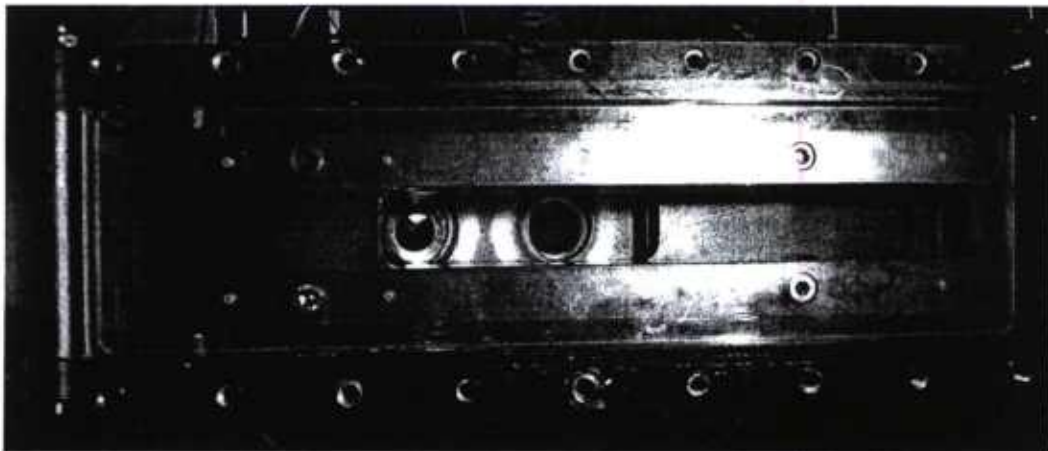 that if it is operated in a closed cycle configuration a heat exchanger section would need to be added to make the system perform adequately.
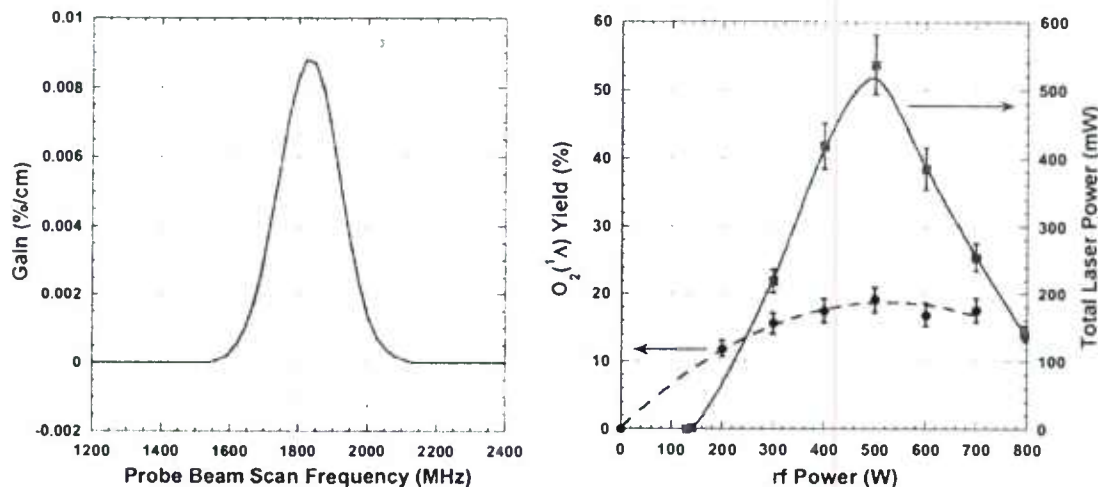
Figure 2-17. Performance of subsonic EOIL laser at UIUC/CU Aerospace.

2.1.3 Experimental Studies in Scaling EOIL Lasers

Experiments and modeling by Rakhimova, 2005, 2006 and Braginsky 2005, 2006, 2007, have shown that $O_2(a)$ generation in transverse RF discharges is significantly enhanced by exciting the discharge at higher frequencies than the typical 13.56 MHz. Rakhimova, 2005, suggested that increased frequency led to a narrowing of the sheath region in which $O_2(a)$ production is ineffective and allowed operating the discharge in the homogeneous α-mode to higher energy inputs. In various works by this group [Braginsky, 2005], three such operating regimes are identified as energy is deposited in the plasma:

I- the homogeneous mode (α-mode): energy is deposited approximately uniformly across the tube diameter

II- the transition mode (γ-mode): plasma jets form outside the electrode gap but most of the energy is deposited within the electrode gap.

III- the inhomogeneous mode: plasma jets and surface wave discharge propagates outside the electrode gap and a large portion of the energy dissipation occurs outside of the gap.

The α or γ-mode is more favorable because it results in more efficient energy deposition into $O_2(a)$. However, the maximum $O_2(a)$ production occurs at energy depositions in which the discharge is in γ-mode. This description of operational mode for flowing RF discharges is consistent with the designations found in non-flowing RF systems first noted by Levitskii, 1958. Raizer provides numerous examples of this type of behavior in a variety of gas mixtures at moderate pressures (10-100 Torr).

An important characteristic of α-mode RF transverse capacitive discharges is the "normal current density." In the condition where energy deposition is low and the discharge does not fill the electrode gap, as the current is raised, the discharge volume grows such that the current density remains nearly constant; this constant density is the "normal current density", sometimes denoted $j_{n\alpha}$ (see Raizer). From work by Yatsenko with He and Air discharges, the following trends can be expected: (1) $j_{n\alpha}$ varies with mixture, (2) $j_{n\alpha}$ increases with pressure, (3) j_n increases with gap. Carroll et al. [Carroll, 2004 & 2005] suggested that the increase in $O_2(a)$ production from the presence of NO in the discharge gas mixture that they first observed [Carroll, 2005; Zimmerman, HPLA 2006] is due to a lower ionization potential of NO thereby enhancing the electron number density in the discharge which resulted in better discharge stability and increased pumping of the $O_2(a)$. Braginsky, 2005 et al. expand on this idea by suggesting that the beneficial influence (in the α-mode) from of the more easily ionized gas mixture containing NO additionally results in the plasma occupying more volume within the gap, thus lowering the normal current density.

Vidaud, 1988 experimented with α to γ transition and found that transition voltage increases with increasing pressure, and decreases with increasing frequency. Odrobina modeled the transition between α and γ mode and showed that increasing the applied frequency led to a decrease in the sheath depth and delayed the transition to higher energy deposition, consistent with Rakhimova's conclusions for the flowing system; Odrobina, 1996, also found that transition voltage decreased as frequency increased, consistent with Vidaud's observations.

In 2-D modeling work, Rakhimova, 2006, showed that when the discharge frequency was increased from 13.56 to 81 MHz for an energy deposition range of 50-400 J/mmol, the discharge spatial structure changed dramatically. The case modeled was 10 Torr of pure oxygen in a transverse discharge with 14-mm gap and 30-cm electrode length. At 13.56 MHz, the discharge glow filled the electrode gap, and the power was uniformly deposited. In the 81 MHz case, the discharge did not fully occupy the discharge gap, and the discharge operated in normal current density mode. In the modeling result, the length occupied by the 81 MHz discharge increased with energy deposition, which was in good agreement with visual observation of the experiment. Also, the electron density, and specific energy input (per unit volume) in the 81 MHz case were twice as high as the 13.56 MHz case.

In this report, behaviors of typical ElectricOIL transverse RF discharges in O_2:He:NO mixtures are discussed, showing the influence of frequency on $O_2(a)$ and oxygen atom production in the pressure range of 5-100 Torr. The transition between α and γ modes is described, and the influence of frequency on discharge structure and electron density is established via experimental measurements of discharge intensity. It is shown that increased yield can be obtained at moderate pressures (20-30 Torr) by increasing the excitation frequency and reducing the discharge gap, following the behaviors observed and modeled by Rakhimova and Braginsky for pure oxygen and O_2:NO mixture.

2.1.4 Recent ElectricOIL Transverse RF Discharge Studies
Several experiments have led to the conclusion that $O_2(a)$ production in transverse RF discharge geometries is a strong function of excitation frequency, gap and pressure. The investigations discussed here made use of transverse discharges in various quartz tube geometries in the

pressure range 5-100 Torr. The excitation frequencies examined were 13.56, 27, and 60 MHz. The general trends observed are as follows:

i) At the low end of the pressure range, increasing the excitation frequency (from 13.56 MHz) leads to increased $O_2(a)$ production.
ii) At high pressures increasing the excitation frequency (from 13.56 MHz) is detrimental to $O_2(a)$ production.
iii) For fixed geometry, power input, and frequency, there is an optimal operating pressure at which the $O_2(a)$ yield is maximized. As the frequency is increased, the optimal pressure decreases. As the discharge gap decreases, the optimal pressure increases.
iv) $O_2(a)$ yield is maximized by operating at low pressure and high frequency.
v) The excitation frequency has a significant impact on the spatial characteristic behavior of the discharge with measurements suggesting that increasing frequency leads to higher electron density, and operation in α-mode to higher energy deposition (similar to Rakhimova *et al*'s results). This leads to higher power densities and higher dissociation fractions.

For purposes of this report, the results from four transverse capacitive RF discharge geometries will be discussed. These are summarized in Table 2-1. All four discharges use 25.4-cm long copper plates or foil as electrodes. The term "clamshell" is used to describe a set of transverse foil electrodes which conform to the outer radius of the tube.

Table 2-1. Transverse RF Discharge Geometries.

#	Flow Tube, Electrodes	Max. Internal Gap [cm]	Internal Volume [cm^3]	Wall thickness [cm]
1	Circular, "Clamshell"	4.9 cm	479	0.25
2	Circular, Parallel Plate	4.9 cm	479	0.25
3	Rectangular, Parallel Plate	3.0 cm	465	0.30
4	Circular, Parallel Plate	2.0 cm	77.4	0.15

2.1.4.1 α to γ Transition in a 13.56 MHz Discharge in O_2:He Mixture

To show the transition between α to γ modes in a typical ElectricOIL discharge setup, the current-voltage-characteristic (CVC) was taken for discharge geometry #3 (rectangular) at the baseline flow rate of 10:33 O_2:He at ~21 Torr without, and with a trace NO flow rate of 0.15 mmol/s. As seen in Figure 2-18, at low input powers, the discharge operates in normal mode or α -mode. As power is increased, the current increases, and there is a transition in the neighborhood of 1.7-1.9 A, after which the voltage and current both increase with increased power input. As will be shown later, this transition point occurs at nearly the same RF power input where the plates are nearly filled with plasma, and that beyond this power, the electron density (and therefore current density) increases throughout the electrode gap region. The trace NO flow rate has little effect on the transition point which occurs at approximately 350 W RF. However the production of $O_2(a)$ increases significantly. Figure 2-19 shows [$O_2(a)$] determined from 1268-nm emission measured 58 cm downstream of the electrode gap for the cases in Fig. 2-18. In the α-mode, [$O_2(a)$] increases linearly with RF power; as more power is added, there is a transition to γ-mode and the slope in [$O_2(a)$] vs. RF decreases. The addition of NO results in an

increase of the slope in [O₂(a)] vs. RF in the α-mode; because the CVC is not substantially affected by the addition of trace NO, it appears that the beneficial increase in $O_2(a)$ is due primarily to a kinetic effect and not due to the influence of the lower ionization potential of NO. Figure 2-20 shows the influence of pressure on the CVC for 10:33 mmol/s O_2:He. As pressure is increased, the transition voltages and currents increase. For the 32 Torr case in Fig. 2-20, it was trivial to operate the discharge in either α or γ-mode at powers near 500 W, and a significant amount of overlap in the two modes is observed in the CVC. Similar hysteretic behaviors near transition were observed in work by Vidaud.
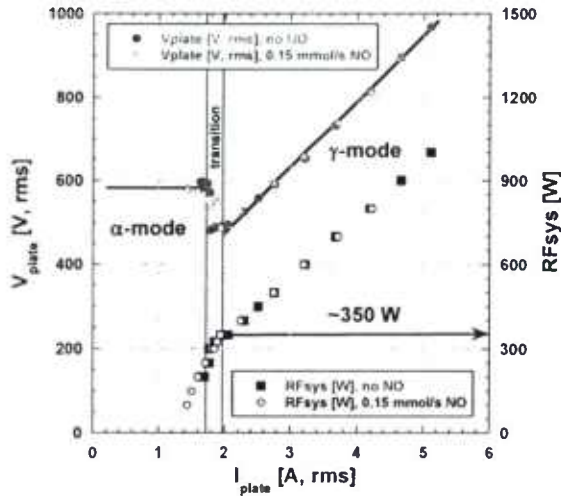
Figure 2-18. Current-voltage characteristic and current power characteristic in discharge geometry #3 for 10:33 O_2:He at ~21 Torr +/- 0.15 mmol/s NO. The transition to γ-mode occurs at ~350 W RF input in either case.

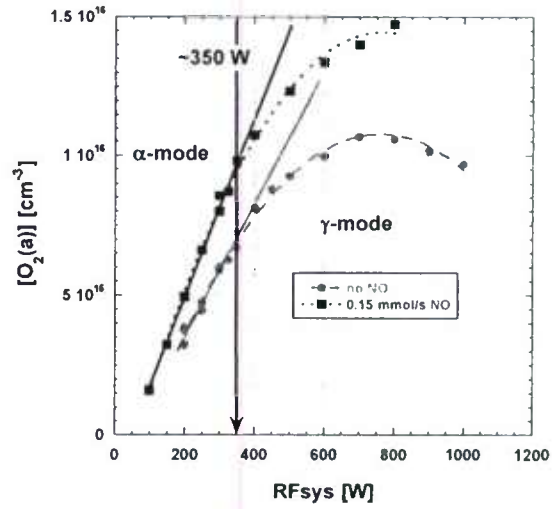**Figure 2-19.** [O₂(a)] measured 58 cm downstream of discharge geometry #3 for 10:33 O_2:He at ~21 Torr +/- 0.15 mmol/s NO. The transition to γ-mode occurs at ~350 W RF input in either case.
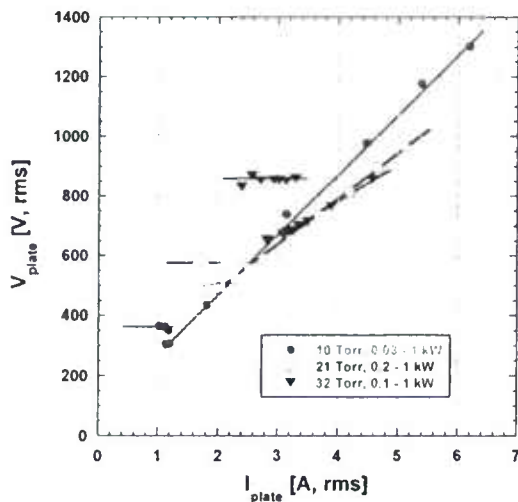

Figure 2-20. Current-voltage characteristic in discharge geometry #3 for 10:33 O_2:He with varied pressure. The transition voltage and current increase with increasing pressure.

2.1.4.2 Decay of O_2(a) and Oxygen Atoms in the Discharge Afterglow

At higher operating pressures, the O_2(a) decays significantly with distance from the electrode gap. Figure 2-21 shows the decay of O_2(a) yield in the afterglow of discharge geometry #1 for operation at 800 W in a mixture of 10:33:0.15 mmol/s O_2:He:NO at 20, 30 and 50 Torr. Here the "O_2(a) Yield" is defined as $[O_2(a)]/[O_2]_{input}$(T,P), where $[O_2]_{input}$(T,P) is the total input O_2 density evaluated at the local measured temperature and pressure. The exit yields for these cases are ~16% at 20 Torr, ~14% at 30 Torr, and ~6% at 50 Torr; the slope of yield with distance is similar for the three pressures. Figure 2-22 shows the decay of the oxygen atom yield with distance for the cases shown in Fig. 2-21; the oxygen atom yields were determined from O-NO recombination measurement at 580-nm.
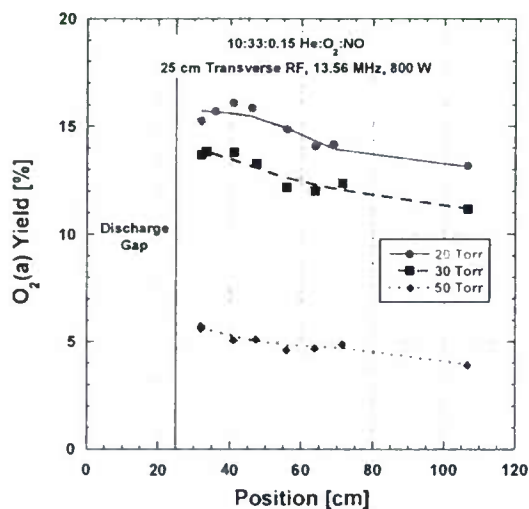
Figure 2-21. O_2(a) yield vs. position downstream of discharge geometry #1 for 10:33:0.15 mmol/s O_2:He:NO at 20, 30 and 50 Torr.
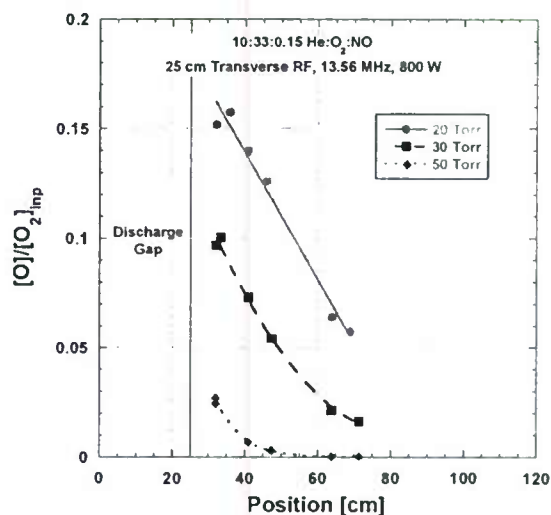
Figure 2-22. Oxygen atom yield vs. position downstream of discharge geometry #1 for 10:33:0.15 mmol/s O_2:He:NO at 20, 30 and 50 Torr.

2.1.4.3 Influence of Frequency on O_2(a) Production in Transverse RF Discharge

Figures 2-23 and 2-24 show O_2(a) yield as a function of pressure without and with NO for 13.56 MHz and 60 MHz in discharge geometry #3 (rectangular tube). These measurements were made 89 cm downstream of the discharge gap in a 50-mm I.D. circular flow channel, and therefore the curves are lower than the exit yield due to increasing O_2(a) decay as pressure is increased. It was necessary to make measurements at this downstream location in order to have direct yield comparisons over the range of discharge tube geometries; the transition between the smaller diameter tubes and the 50-mm I.D. (well-calibrated) diagnostic block volume results in a subsonic jetting effect (highly visible via O-NO recombination emission) which confuses interpretation of the measured 1268-nm intensity due to axial variations of flow parameters. The influence of frequency on O_2(a) production is substantial, Figs. 2-23 and 2-24, and has no characteristic dependence on trace NO content. At 5 Torr (low pressure), the yield increases by more than a factor of two when frequency is increased from 13.56 to 60 MHz, reaching a maximum of 18%; near 20 Torr, the production level of O_2(a) is nearly identical at the two frequencies; at pressures greater than 20 Torr, the use of the higher frequency results in strong

reduction in $O_2(a)$ levels and it is better to use a 13.56 MHz discharge at pressure > 20 Torr for this particular geometry. This data suggests a strong coupling between the influences of discharge pressure and excitation frequency on discharge behavior. Rahkimova et al. observed improved $O_2(a)$ yield at 30 Torr by increasing excitation frequency from 13.56 MHz to 81 and 160 MHz, but this may be explained by the fact that they took their 80 MHz data with a ½" (14 mm) diameter discharge tube and the 160 MHz data with a ¼" (7 mm) discharge tube, which allowed extension of $O_2(a)$ production efficiency to higher pressures.
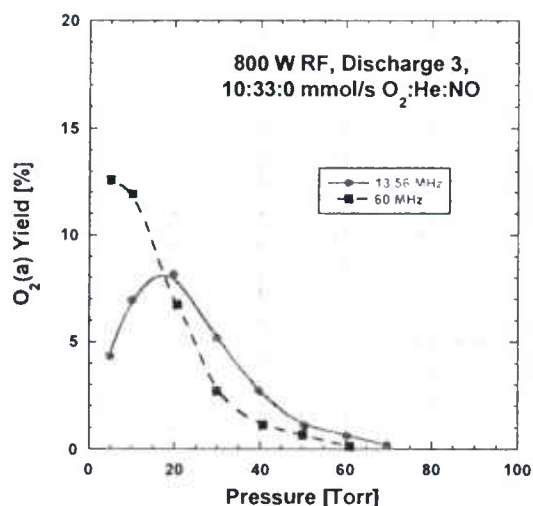
Figure 2-23. $O_2(a)$ yield as a function of pressure for varied excitation frequency in discharge geometry #3 (rectangular). Data measured 89 cm from discharge exit.
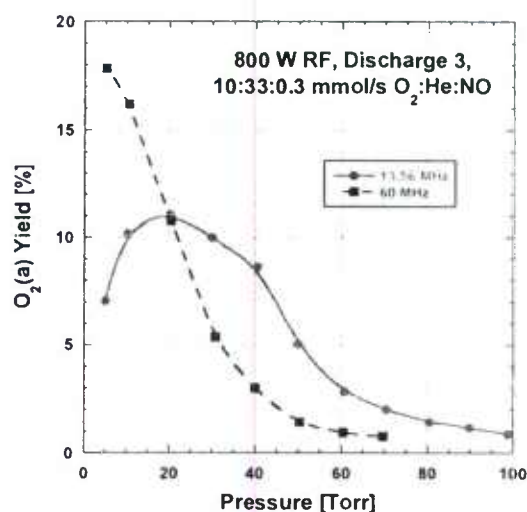
Figure 2-24. $O_2(a)$ yield as a function of pressure for varied excitation frequency in discharge geometry #3 (rectangular) with NO addition. Data measured 89 cm from discharge exit.
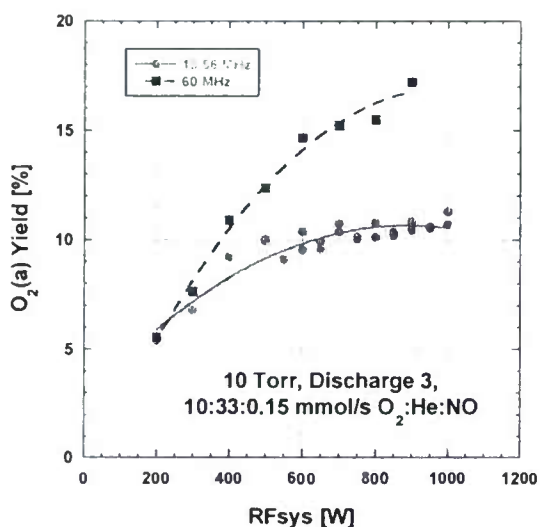
Figure 2-25. O₂(a) yield as a function of RF input power at 10 Torr for varied excitation frequency in discharge geometry #3 (rectangular). Data measured 89 cm from discharge exit.
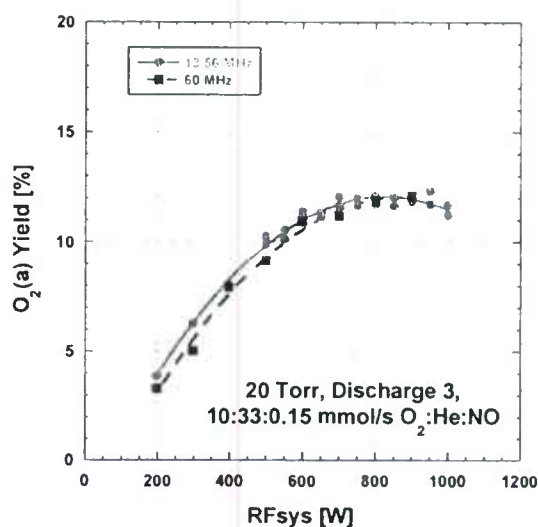
Figure 2-26. O₂(a) yield as a function of RF input power at 20 Torr for varied excitation frequency in discharge geometry #3 (rectangular). Data measured 89 cm from discharge exit.

Figures 2-25 and 2-26 show the influence of excitation frequency on $O_2(a)$ yield as a function of power in discharge geometry #3 for 10:33:0.15 mmol/s O_2:He:NO at 10 and 20 Torr. The $O_2(a)$ production is similar for the two frequencies at 20 Torr; at 10 Torr, the slope of yield with power is significantly increased. Given the similarity seen in Fig. 2-26, one might expect the discharge characteristics to also be similar. However, this is not the case, and the two discharges behave quite differently at the two frequencies. As will be shown, the 60 MHz case operates in α-mode while the 13.56 MHz case is in γ-mode.

The modal behavior of the discharge can be observed qualitatively by visual inspection of the various discharge glow emissions and the air-glow (O-NO → NO₂* → NO₂ + h□) in the various cases with NO added to the flow. Figure 2-27 shows photographs of discharge geometry #2 (circular cross-section, parallel plate electrodes) driven at 13.56 MHz with a flow mixture of 10:33:0.15 O₂:He:NO at 20 and 50 Torr for a variety of power levels. As the power is increased, the fraction of the plate gap occupied by the plasma emission is increased. For the 20 Torr case, with power increasing from 0.2 to 1 kW, transition of the discharge from α to γ-mode is observed; when the pressure is increased to 50 Torr, α-mode is maintained up to 1 kW.
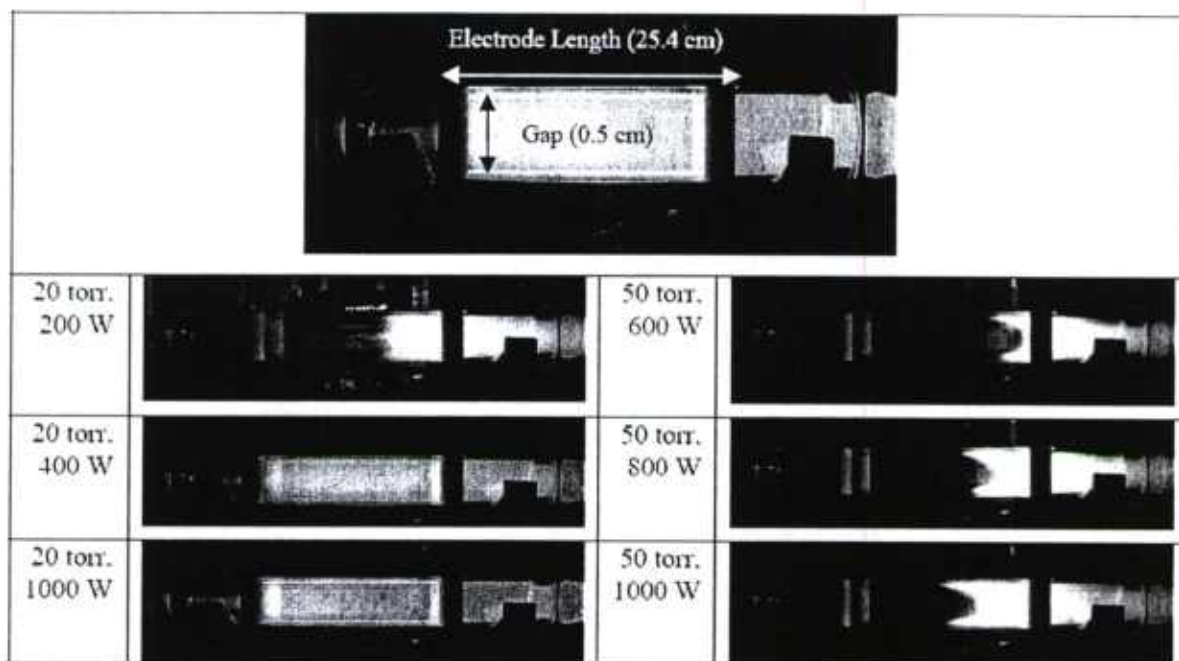
Figure 2-27. Photographs of discharge glow in geometry #2 (circular) at 13.56 MHz. The flow mixture was 10:33:0.15 mmol/s O_2:He:NO.

This visualization is a good qualitative technique for discerning the volume occupied by the plasma between the plates, but it does not directly describe the discharge characteristics (n_e, T_e or E/N). Also, it does not allow the influence of trace NO on the plasma volume to be deduced. In order to determine the influence of frequency on the discharge characteristics, $O_2(A^3\Sigma \rightarrow X^3\Sigma)$ and $O_2(c^1\Sigma \rightarrow X^3\Sigma)$ transitions were monitored (Herzberg I and II band groups). A 404.7 nm filter with an 11-nm bandwidth was used, capturing a number of transitions in each band group. For fixed mixture and pressure, and assuming that the pumping rate is unaffected by frequency (i.e. EEDF is similar) the intensity of this state should be proportional to the electron density.

The 404.7 nm intensity measurement as a function of position and power from discharge geometry #3, comparing 13.56 and 60 MHz at 20 Torr, is shown in Fig. 2-28a. Figure 2-28b shows some cross-sections of this data for fixed power and pressure. The intensity was deduced from the average of the filtered emission from three evenly spaced span-wise rows of 1/8" holes in the grounded electrode. In the 13.56 MHz case at high power, the visible plasma fills the electrode gap and the intensity is relatively constant, falling off with distance as the gas is heated through the discharge. For the same input conditions at 60 MHz, the intensity increases greatly at nearly the mid-point of the electrode gap and reaches a level in excess of the 13.56 MHz case. This data indicates that increasing the frequency from 13.56 MHz results in both higher electron density and higher current density (since the visible plasma is confined downstream at higher frequency). In the lower pressure case (10 Torr), this effect results in enhanced $O_2(a)$ production. At 20 Torr, there is no benefit in $O_2(a)$ production for increased frequency, although the influence of frequency on discharge character is similar. The significant increase in electron density and decrease in plasma volume with frequency agrees well with Rakhimova *et al*'s modeling result[2] which showed that increasing the frequency allows the discharge to operate in α-mode to higher energy deposition. Clearly, operating discharge geometry #3 at higher

frequency results in α-mode operation at a higher current density for a given energy deposition, and transition is delayed to higher energy depositions.

The increase in frequency also results in a significant increase in oxygen atom production due to the larger power density. The oxygen atom content determined by O-NO recombination emission at 580-nm is shown in Fig. 2-29 as a function of (a) RF input power and (b) pressure. At the measurement position (46 cm from the exit), the oxygen atoms are nearly completely recombined for pressures of 30 Torr and greater. Figure 2-29a shows significantly higher O atom yield at 10 Torr with the 60 MHz discharge, which is consistent with higher energy coupling into the O_2 as seen in Fig. 2-24 for the $O_2(a)$. At 20 Torr the O atom yields are more similar for the two frequencies.

(a)   (b)
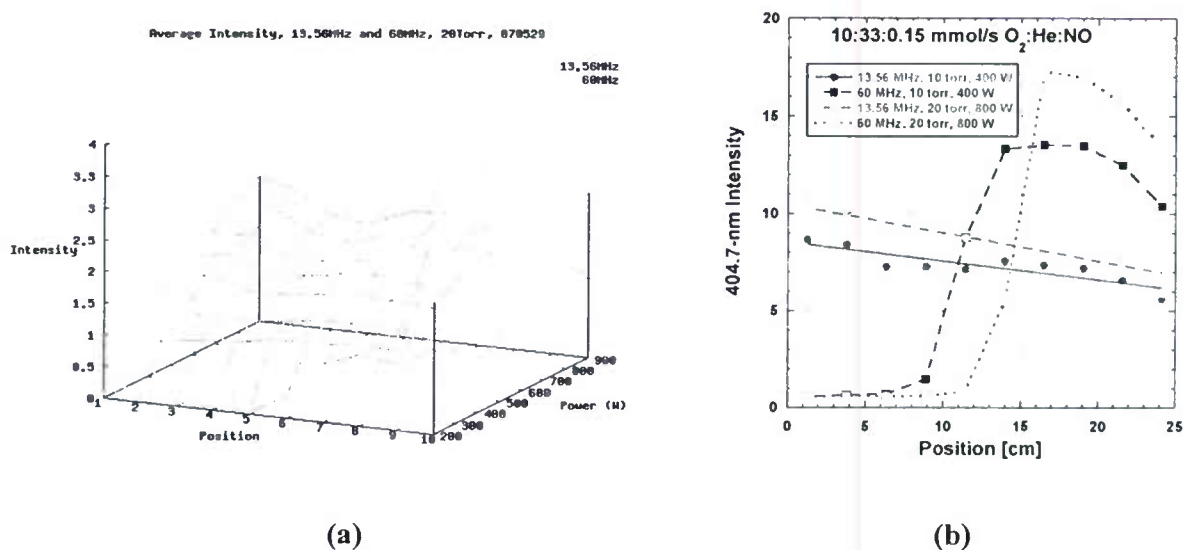
Figure 2-28. 404.7-nm intensity as a function of position and RF input power for varied excitation frequency in discharge geometry #3 (rectangular): (a) Intensity = f(position, RF input) for 10:33:0.15 mmol/s O_2:He:NO at 20 Torr, (b) Intensity = f(position) for 10:33:0.15 mmol/s O_2:He:NO at 10 and 20 Torr with 40W/Torr input RF power.
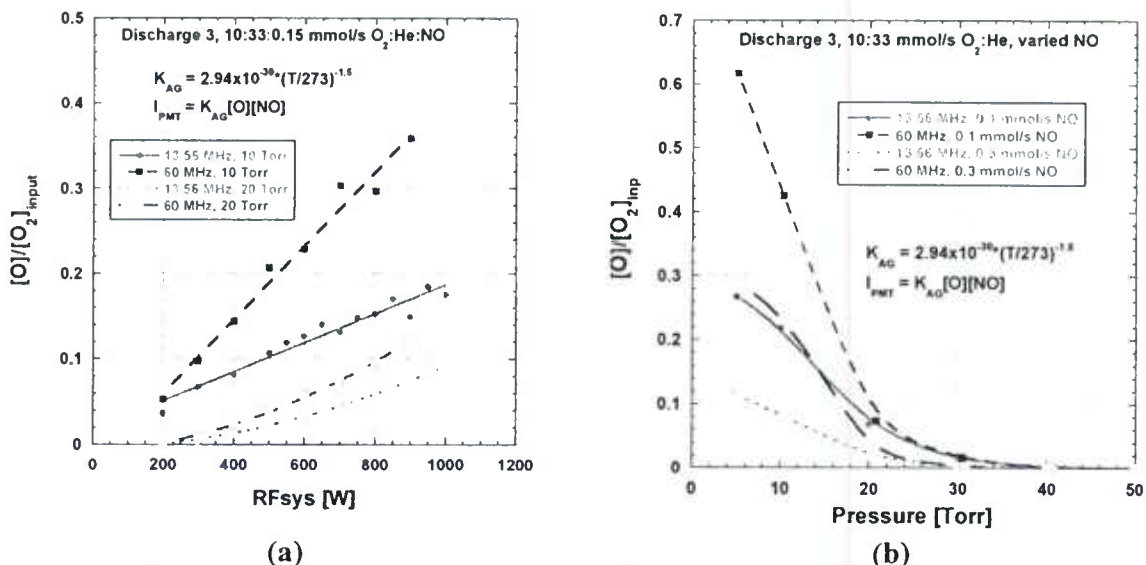
Figure 2-29. The influence of frequency and oxygen atom production. The airglow emission due to O-NO recombination was measured 46 cm downstream using a PMT filtered at 580 nm: (a) oxygen atom yield vs. RF input power for varied frequency and pressure, and (b) oxygen atom yield vs. pressure for varied frequency and NO content.

Decreasing the discharge gap led to enhanced $O_2(a)$ production at mid-range pressures (20-30 Torr). Figures 2-30 and 2-31 summarize data taken with discharge configuration #4 (circular, small diameter). Although the behavior with pressure and frequency is similar to that seen in Figs. 2-23 and 2-24, the use of a smaller discharge gap resulted in an extension of the benefit of frequency to higher pressures. At an operating pressure of 20 Torr, increasing the excitation frequency from 13.56 MHz to 60 MHz doubled the $O_2(a)$ production. This result is consistent with Rakhimova *et al*'s work in which it was necessary to decrease the tube diameter as the frequency increased to maximize $O_2(a)$ production. The increased frequency led to similar changes in oxygen atom production; Figure 2-33 shows the actinometry measurements comparing oxygen atom yield at 800 W RF in discharge geometries #3 and #4 for 13.56 and 60 MHz. The significant increase in power density (W/cm^3) between geometries #3 and #4 results in a substantial increase in the dissociation. For geometry #3, the higher power volume at 60 MHz compared to that at 13.56 MHz results in the slope of dissociation fraction increasing by a nearly factor of 6; in the smaller diameter tube (geometry #4) the slope of the O atom production at 13.56 and 60 MHz is similar, which is likely due to the power densities being similar in this case, see Fig. 2-32.

The spatial behavior of the discharge in the smaller diameter tube is quite different than the results seen for the 5 cm I.D. tube; as seen in Fig. 2-33, the visible plasma fills the electrode gap completely for 50 Torr and 800 W RF, and appears to operate in homogeneous α-mode up to this power input (compare Fig. 2-33 with Fig. 2-27).
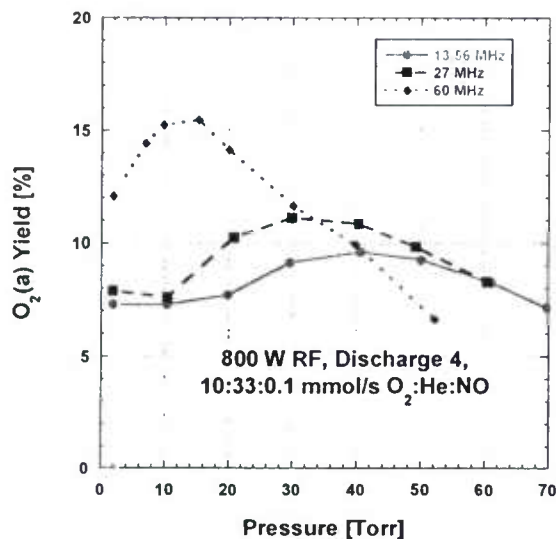
Figure 2-30. O₂(a) yield as a function of pressure for varied excitation frequency at 800 W in discharge geometry #4 (circular, small diameter). Data measured 89 cm downstream from the discharge exit.
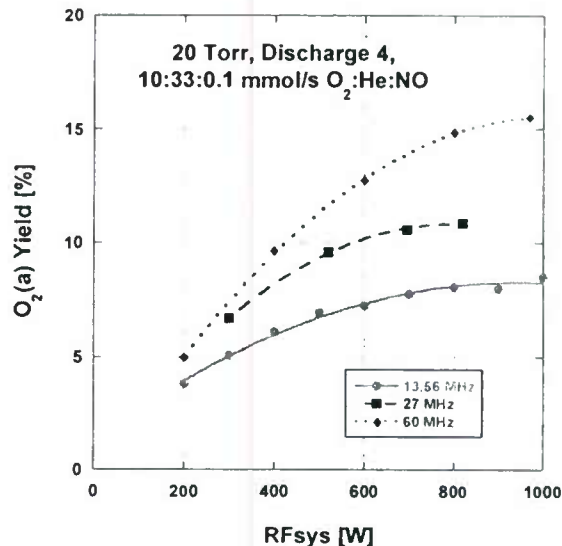
Figure 2-31. O₂(a) yield as a function of power for varied excitation frequency at 20 Torr in discharge geometry #4 (circular, small diameter). Data measured 89 cm downstream from the discharge exit.
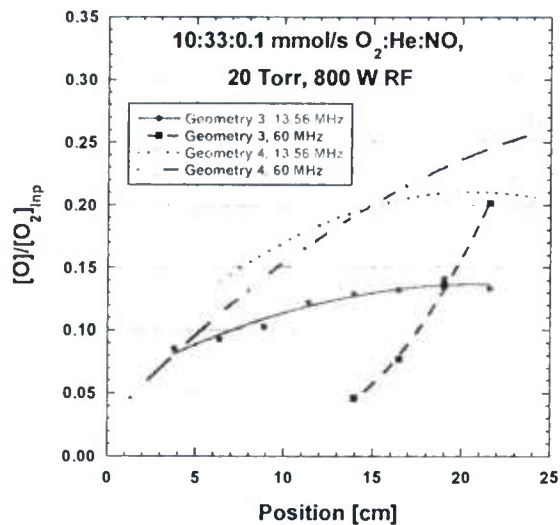
Figure 2-32. Argon actinometry results for oxygen atom yield in discharge geometries #3 (3.0 cm electrode gap) and #4 (2.0 cm electrode gap). Measurements made inside the discharge region.

50 Torr. 300 W	
50 Torr. 400 W	
50 Torr. 800 W	
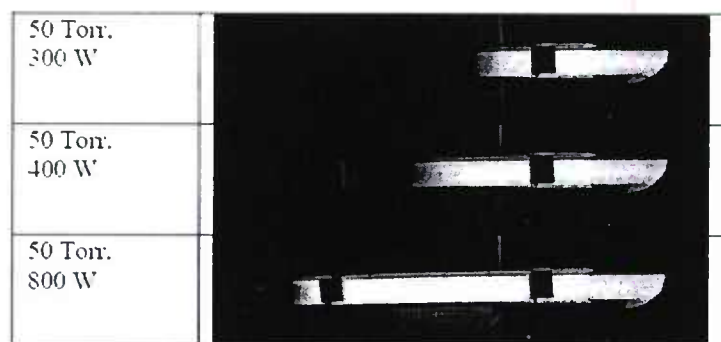
Figure 2-33. Photographs of discharge glow in geometry #4 (circular, small diameter) at 13.56 MHz. The flow mixture was 10:33:0.15 mmol/s O_2:He:NO.

2.1.4.4 Temperature, Yield, and Voltage Data for eV/molecule Scaled Conditions

An important issue for any oxygen-iodine laser system is temperature. In anticipation that our research and development efforts will proceed towards progressively higher power systems, we experimentally determined the effects of RF power on gas flow temperature. To perform a broad range of measurements we chose five different flow pressures having a fixed input gas flow velocity of approximately 1520 cm/s and a fixed O_2:He ratio of approximately 3:7. The inside diameter of the quartz flow tube was 4.9 cm and the transverse discharge was 25.4 cm long (geometry #1) excited at 13.56 MHz. The test matrix is shown in Table 2-2 and in Fig. 2-34. The measurements show that the gas flow temperature remains quite reasonable (< 650 K) at high pressures even for RF powers of nearly 2 kW. For a fixed eV/molecule, the temperature of the flow increases with pressure, which we believe is a consequence of increased quenching and recombination kinetics (e.g. three-body processes) that naturally occur at higher pressure and release excited state energy into the flow as heat. The O_2(a) yield for the cases in Table 2-2 are given in Fig. 2-35. With this large diameter discharge tube, the O_2(a) yield falls off dramatically with pressure, with the best yields occurring in the lower pressure range (3-20 Torr). Figure 2-36 plots the driven plate voltage as a function of RF input power for the cases in Table 2-2. For approximately the same energy input range, there is an obvious shift from γ-mode (V_{plate} increases with power), to α-mode (V_{plate} ~ const. with power) as pressure increases.

Table 2-2. Experimental test matrix for measurements of gas flow temperature as a function of pressure, flow rate, and discharge RF power for a fixed inlet gas flow velocity of approximately 1520 cm/s. Temperature measurements were made 27.9 cm downstream from the exit of the discharge.

Total Pressure (Torr)	O_2 Flow Rate (mmol/s)	He Flow Rate (mmol/s)	RF Powers (W)	eV/molecule	Gas Flow Temperature (K)
3.1	1.3	3.2	39, 77, 115, 150	0.32 – 1.22	314 – 323
10.5	4.5	10.4	130, 260, 390, 500	0.30 – 1.16	367 – 433
20	8.9	20.5	260, 520, 775	0.30 – 0.90	402 – 473
30	13.7	31.3	390, 779, 1147	0.30 – 0.89	350 – 527
51	22.3	52.7	649, 1298, 1949	0.30 – 0.91	451 – 638
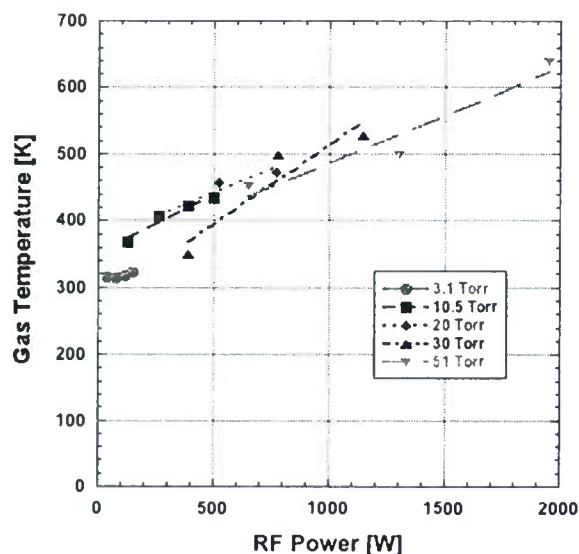
Figure 2-34. Experimental measurements of gas flow temperature as a function of pressure, flow rate, and discharge RF power for a fixed inlet gas flow velocity of approximately 1520 cm/s. Temperature measurements were made 27.9 cm downstream from the exit of the discharge.
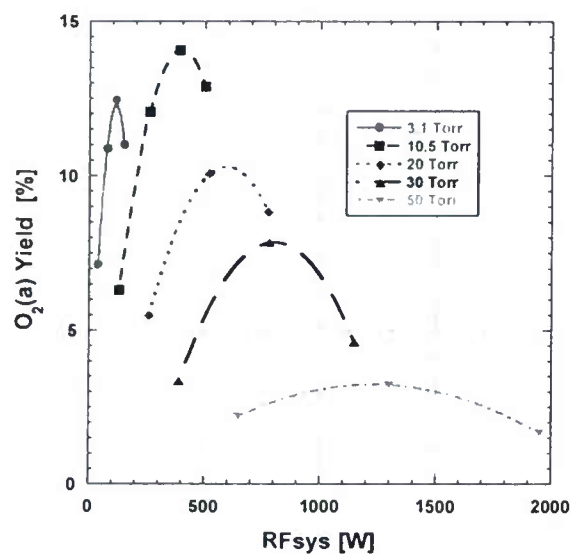
Figure 2-35. Experimental measurements of $O_2(a)$ as a function of pressure, flow rate, and discharge RF power for a fixed inlet gas flow velocity of approximately 1520 cm/s. 1268-nm emission measurements were made 27.9 cm downstream from the exit of the discharge. The data fits are not necessarily indicative of the actual trend.
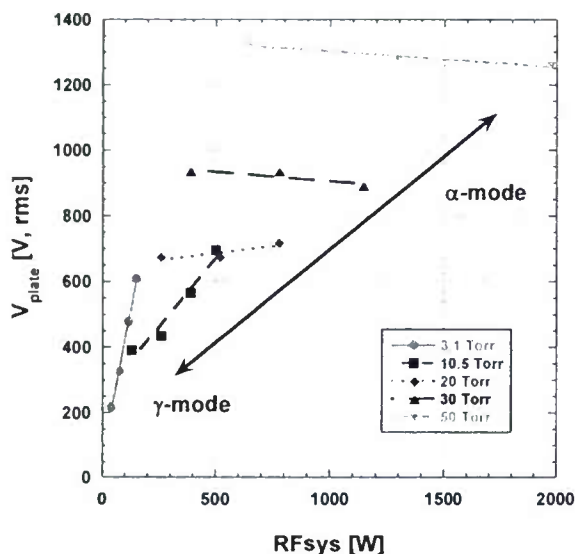
Figure 2-36. Measurements of driven plate voltage as a function of pressure, flow rate, and discharge RF power for a fixed inlet gas flow velocity of approximately 1520 cm/s. The double arrow indicates the transition of the discharge from γ-mode to α-mode as pressure is increased.

2.1.4.5 Conclusions

The region of high yield operation was extended to higher pressures by following the *pd* scaling laws exemplified by Rakhimova et. al., showing improved operation by decreasing the tube diameter while increasing the excitation frequency. The transition between α and γ modes was established by CVC (current-voltage-characteristic) measurements; measurements of $O_2(a)$ in afterglow clearly indicate the reduction in $O_2(a)$ production efficiency after transition, with maximum production occurring in γ-mode. The addition of trace NO leads to no clear change in the CVC, but results in a large increase in $O_2(a)$ yield.

The increase in transition power deposition with increasing pressure was observed for typical laser flow rates, with the transition corresponding to the point at which the plasma fills the electrode gap; the transition voltage and current increased with pressure. Therefore, at a given power level (sufficiently high for γ-mode operation at low pressure), as pressure is increased, there is a critical operating pressure at which transition to α-mode will occur.

The level of $O_2(a)$ produced for a given discharge geometry, mixture, energy deposition, and excitation frequency is a strong function of pressure. At low pressure, γ-mode operation, increasing the excitation frequency trends toward α-mode operation, which leads to higher production efficiency of $O_2(a)$ for a given energy deposition. At mid range to high pressures beyond the critical pressure, where the discharge is in α-mode, increasing the frequency leads to further constriction of the discharge to high normal current density, which results in higher dissociation and lower $O_2(a)$ yield in the afterglow, perhaps due to increased quenching.

When the discharge diameter (and volume) is decreased, at the same power input, the 13.56 MHz discharge operates in γ-mode over a larger pressure range. As a result increasing the discharge frequency in the smaller volume discharge (geometry #4) is effective in increasing $O_2(a)$ production at higher pressures compared to the larger volume case (geometry #3).

Based on these results, it is the goal of future work to pursue a transverse RF discharge design in which more efficient $O_2(a)$ production is achieved by maintaining the α-mode to high power inputs. Increasing the excitation frequency at low pressures has allowed maintenance of α-mode to higher energy depositions, resulting in enhancement of the $O_2(a)$ yield. In the high pressure case, which is more desirable for ElectricOIL operation, the influence of frequency is reversed, and it is necessary to decrease the discharge gap in order to exploit the benefit of higher frequency operation, or to operate at lower frequency. In any case, operation of the discharge at higher specific power (power per volume) results in increased oxygen atom production leading to higher quenching of $O_2(a)$. Therefore, if it is necessary to reduce the gap to maintain favorable $O_2(a)$ production at higher pressure, this should be accomplished by reducing the transverse gap while maintaining the volume between the electrodes such that low power density is maintained

2.2 Advanced Diagnostics and Kinetics of Oxygen-Iodine Laser Systems (Conducted by PSI)
2.2.1 Advanced Diagnostics and kinetics measurements at PSI
The potential for gas-phase electric discharge generation of $O_2(a^1\Delta)$ to produce $I(^2P_{1/2}) \rightarrow I(^2P_{3/2})$ lasing offers substantial improvements in efficiency and weight limitations of closed-cycle systems.

A major mechanistic difference between the discharge and chemical methods is the discharge's prolific production of O from the electron-impact dissociation of the O_2 feedstock. O reacts rapidly with I_2 to form IO, which in turn reacts rapidly with O to form I [Payne, 1998], so that essentially no $O_2(a^1\Delta)$ is consumed in I_2 dissociation. Previous kinetics investigations of the oxygen-iodine system using discharge-generated $O_2(a^1\Delta)$ employed catalytic recombination of O, [Derwent, 1972; Heidner 1983] and thus did not examine conditions relevant to a discharge-driven laser system. As a result, very little is known about the abundances and effects of the discharge effluent species relevant to I^* excitation. Recently, Carroll and coworkers reported the first observations of $I^* \rightarrow I$ gain [Carroll, 2004] and lasing [Carroll, 2005a] from discharge-generated $O_2(a^1\Delta)$ and O, using supersonic expansion to achieve positive gain at low temperatures [Carroll, 2005b]. PSI has recently reported similar observations of $I^* \rightarrow I$ gain in a subsonic, microwave-discharge flow reactor near room temperature [Rawlins, 2005]. In the present paper, they describe results from a series of kinetics investigations of the production of $O_2(a^1\Delta)$ and O by a conventional microwave discharge at a few torr, and of the subsequent interactions with I_2 reagent near room temperature. The experiments are based on a multispecies measurement approach, using a suite of high-sensitivity optical emission and absorption diagnostics to determine time-resolved, absolute species concentrations for $O_2(a^1\Delta)$, O, I_2, I^*, and I, as well as small-signal gain and temperature [Rawlins, 2003; Rawlins, 2004].

For typical O concentrations produced in a flow reactor by a microwave discharge at a few torr, I_2 is promptly dissociated upon addition to the flow, and the near-resonant $O_2(a^1\Delta) + I$ energy exchange is expected to attain a steady state which is essentially an equilibrium:

$$O_2(a) + I = O_2(X) + I^* \tag{2-6}$$

$$\frac{[I^*]}{[I]} = K_{eq}\frac{[O_2(a)]}{[O_2(X)]} \ , \ K_{eq} = 0.75\exp(402/T) \tag{2-7}$$

This expression holds if the quenching of I^* by O is negligible, i.e. $k_{I^*+O}[O] \leq k_{I^*+O2}[O_2(X)]/10$. For the experimental conditions given below, this corresponds to $k_{I^*+O} < 6 \times 10^{-12}$ cm^3/molecule-s, and is consistent with $k_{I^*+O} \leq 2 \times 10^{-12}$ cm^3/molecule-s recently measured by Heaven and coworkers [Han, 2004]. Thus the $[O_2(a)]/[O_2(X)]$ ratio required to achieve the threshold for positive gain, $[I^*]/[I] = 0.5$, should be given by the equilibrium expression and decreases with temperature. $[O_2(X)]$ is given by

$$[O_2(X)] = [O_2]_o - [O_2(a)] - [O]/2 \tag{2-8}$$

where $[O_2]_o$ is the total O_2 concentration, and the yield of $O_2(a)$ is defined as $[O_2(a)]/[O_2]_o$. The value of $[O_2]_o$ is determined from the mole fraction of O_2 admitted to the discharge, and the pressure and temperature of the $O_2(a) + I$ reaction zone. For 15% dissociation of the initial O_2, the expected threshold $O_2(a)$ yields are 0.126 and 0.167 at 300 K and 400 K, respectively. As [O] decreases toward zero, these values approach upper bounds of 0.149 at 300 K and 0.196 at 400 K. Thus, according to Eq. (2-8), $O_2(a)$ yields in excess of 0.2 should give rise to positive $I^* \rightarrow I$ optical gain upon addition of I_2 near room temperature.

$O_2(a)$ can be generated efficiently in a variety of electric discharge types and configurations. In the experiments, here, we have used a conventional, electrodeless microwave discharge at 2450 MHz with a tuned, resonant cavity of the Evenson design [Fehsenfeld, 1965]. This type of cavity operates on gas flows through a 13-mm o.d. pyrex or quartz tube, at typical pressures from about 0.5 torr to about 20 torr, and externally applied powers up to ~120 W. The chemistry of low-pressure, resonant-cavity microwave discharges is described by Kaufman [Kaufman, 1969]. The externally applied electric field strength is nominally ~30 V/cm. The electron number density is in the 10^{11} to 10^{12} cm^{-3} range, and is limited primarily by wall losses and dissociative recombination. The wall loss is accentuated by the Debye shielding effect, which confines most of the ion-pair production to an axisymmetric annular region near the inner surface of the glass tube. The gas temperature within the discharge is usually about 500 to 600 K for an air-cooled pyrex tube. For 3 torr, 500 K, and ~70 W discharge power, the electric field parameter E/N is ~(5 to 10) $\times 10^{-16}$ V cm^2, or 50-100 Td (where E is the electric field strength and N is the total number density). The characteristic electron energy (electron diffusion/mobility ratio) ranges from ~2 eV for a diatomic gas to ~8 eV for a monatomic rare gas like argon. The electron energy distributions follow a non-Boltzmann distribution, i.e. the high-energy tail of the distribution is suppressed due to inelastic collisions with the gas molecules. Ionization levels are typically low, diffusion is ambipolar, and the ions and electrons recombine promptly upon leaving the active discharge.

We have previously published model calculations of excitation rates in O_2/Ar discharges [Rawlins, 1987]. The rate coefficients for the electron-impact excitation processes are given by the convolution integral of the energy-dependent excitation cross sections and the electron energy distribution. To calculate these, we used a computer code [Morgan, 1990] which solves the Boltzmann transport equation [Frost, 1969]. The code treats all the inelastic processes occurring in the active discharge, to evaluate the steady-state electron energy distributions and reaction rate coefficients as functions of E/N and O_2 mole fraction in Ar or He. The electron-

impact cross section data are taken from the data base discussed extensively by Phelps and co-workers [Lawton, 1978; Tachibana, 1981; Phelps]. The calculations and data base are discussed in detail in [Rawlins, 1987].

The effects of E/N and O_2 mole fraction on the computed electron energy distributions are shown in Fig. 2-37. With either increasing E/N or decreasing O_2 fraction, the fraction of high-energy electrons increases, signifying increasing electron "temperature." The increases in the high-energy component of the electron energy distribution result in larger overlap integrals with the key electronic excitation cross sections, illustrated in Figure 2-38. The 10 Td distribution provides power-efficient $O_2(a)$ excitation, in that very little power is expended on O_2 dissociation; however the poor overlap with the ionization cross section results in a very low ionization rate and consequently low electron number density. The 100 Td distribution gives greater overlap with both the $O_2(a)$ excitation cross section and the O_2 ionization cross section, but at the expense of increased O_2 dissociation. The $O_2(a)$ excitation rate is given by the product $k_{exc}[e^-][O_2]$. Both k_{exc} and $[e^-]$, and hence the yield of $O_2(a)$, can be considerably enhanced through use of larger E/N and/or lower O_2 mole fraction to achieve more energetic electron energy distributions.
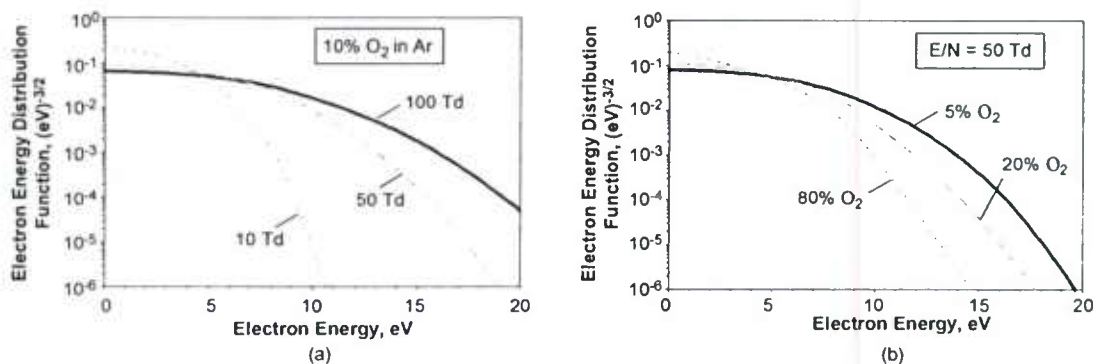
Figure 2–37. Computed electron energy distribution functions in discharge-excited O_2/Ar mixtures: (a) Effect of variations in E/N for 10% O_2 in Ar; (b) Effect of variations in O_2 mole fraction for E/N = 50 Td.
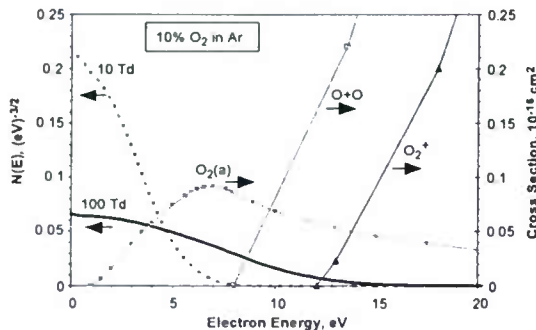
Figure 2–38. Illustration of overlap of electron energy distributions with electron impact excitation cross sections for $O_2(a)$ excitation, O_2 dissociation to form O + O, and O_2 ionization to form O_2^+. The electron energy distributions are computed for E/N = 10 and 100 Td, in 10% O_2/Ar. Cross section values were taken from Ref. 20.

The computed dependences of the rate coefficients for $O_2(a)$ excitation, O_2 dissociation, and O_2 ionization on O_2 mole fraction in Ar are shown in Figure 2-39 for E/N = 50 Td. The excitation rate coefficient increases modestly with decreasing O_2 fraction. However, the O_2 ionization rate coefficient increases by almost two orders of magnitude from 80% O_2 to 5% O_2, signifying a

large increase in the ion pair production rate and in the electron number density. The Ar ionization rate coefficient, which has a higher energy threshold, is even more sensitive to the O_2 fraction, and becomes an important contributor for the dilute mixtures. For the discharge configuration and flow rates used in the experiments reported here, the gas residence time in the discharge is ~0.2 ms. This corresponds to an effective $O_2(a)$ "loss" rate which is faster than the collisional losses within the discharge for our anticipated electron number densities. To zeroth order, we can approximate the $O_2(a)$ production as

$$[O_2(a)] \ . \ k_{exc}[e^-][O_2]\tau \ , \tag{2-9}$$

where τ denotes the gas residence time in the discharge. The $O_2(a)$ yield is then simply ~$k_{exc}[e^-]\tau$, and is thus highly dependent on the electron energy distribution via E/N and O_2 fraction. Of course, a quantitative treatment requires inclusion of the $O_2(a)$ losses due to collisions with electrons (superelastic quenching, dissociation), as well as the effects of dissociative attachment of electrons with O_2 and the subsequent role of O^- [Franklin, 2001; Stafford, 2004]. (Note that deactivation of $O_2(a)$ by collisions with the reactor walls and with neutral discharge species in and downstream of the discharge is negligible for our experimental conditions.) This analysis, coupled with continuing measurements with different residence times, is in progress.
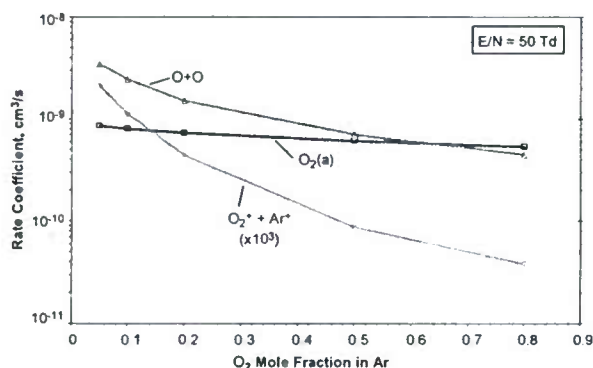
Figure 2–39. Effect of variations in O_2 mole fraction on computed electron-impact rate coefficients for $O_2(a)$ excitation, O_2 dissociation, and total ionization for discharge-excited O_2/Ar mixtures, E/N = 50 Td.

The experiments were performed in a conventional discharge-flow reactor shown in Figure 2-40. The primary flow was a mixture of 5% to 80% O_2 in Ar at 1.5 and 3 torr. The gas passed through a 2450 MHz microwave discharge excited by an Evenson-style resonant cavity [Fehsenfeld, 1965] at 40 to 120 W power, with an approximate residence time of 0.2 ms in the active discharge. Flow velocities in the main flow tube (5 cm o.d.) were 1100-1300 cm/s. For investigations of I^* excitation, I_2 was added at trace concentrations by passing Ar over a bed of iodine crystals at room temperature and through a ¼-inch (o.d.) pyrex sliding injector. I_2 flow rates were determined by optical absorption using a light-emitting diode filtered at 488 nm [Davis, 1979]. Initial I_2 concentrations in the flow reactor were (5 to 12) x 10^{12} molecules/cm³. Additional reagents, NO and NO_2, were added through a fixed loop injector 16 cm (~13 ms) upstream of the optical port. Typical flow times from the discharge exit to the optical cell were ~20 ms. Typical concentrations of O and $O_2(a)$ were on the order of 10 molecules/cm³.
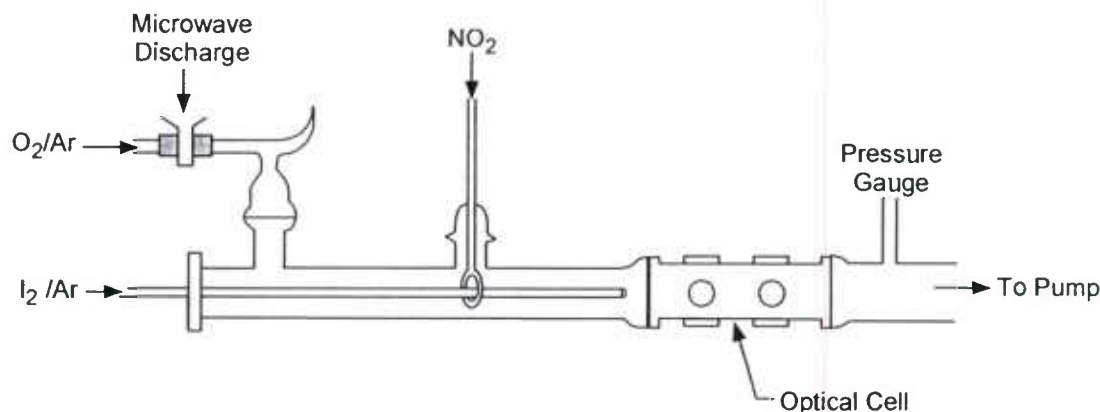
Figure 2–40. Schematic diagram of discharge-flow reactor apparatus.

The optical measurements were performed concurrently along two orthogonal sight paths at the first window station of the optical cell. Absorption and gain on the $I(^2P_{3/2}, F=4) - I(^2P_{1/2}, F=3)$ hyperfine transition were observed by a narrow-band (<10 MHz full width at half maximum) frequency-scanning diode laser at 1.315 μm, in a fiber-coupled, dual-beam configuration [Rawlins, 2003; Rawlins, 2004, Davis, 1996]. The measurements used a single pass of the laser beam across the 5.6 cm diameter of the optical cell. A balanced ratiometric detection circuit [Allen 1995] provided noise cancellation and ultra-high sensitivity. Analysis of the Doppler-broadened line shapes gave gas temperatures of 330-350 K. Division of the negative absorbance, $-\ln(I_o/I)$, by the path length gives the small-signal gain in cm^{-1}; division of this quantity by the stimulated emission cross section gives the quantity $[I^*] - [I]/2$. We also attempted to make the measurements with a multipass (~40 passes) Herriott cell arrangement, however we observed discrepancies between the single-pass and multipass results that were apparently due to the effects of radial concentration gradients in I and/or I* across the off-axis lines of sight of the multipass beam path. Such radial gradients occur for species which are efficiently removed or deactivated at the reactor wall, as expected for I* and possibly for I as well.

Emission spectra from $O_2(a^1\Delta_g \rightarrow X^3\Sigma_g^-, 1270$ nm) and $I(^2P_{1/2} \rightarrow {}^2P_{3/2}, 1315$ nm) were observed with a liquid-nitrogen-cooled InGaAs array spectrometer at 0.5 nm resolution [Rawlins, 2003; Rawlins, 2004]. The emission was collected by an optical fiber mounted on the entrance slit. The field of view was collimated and apertured to view only the opposing window, with no reflecting surfaces. The instrument was calibrated for absolute spectral responsivity to ∀1% accuracy using a NIST traceable blackbody source. All windows were antireflection-coated for 1.3 μm, and the windows for the emission measurements were purged with a small flow of Ar to prevent deposition of iodine oxides. O concentrations were determined to ±5% accuracy using the O + NO titration method [Kaufman, 1958; Kaufman, 1961; Piper, 1989], where the continuum air-afterglow emission from the O + NO interaction was viewed by a calibrated, bandpass-filtered photomultiplier at 580 nm. NO used in these determinations was purified of higher oxides by passage through an Ascarite trap (NaOH supported on asbestos) followed by an alcohol/liquid nitrogen slush trap, was diluted in He, and was stored in a Pyrex vacuum bulb.
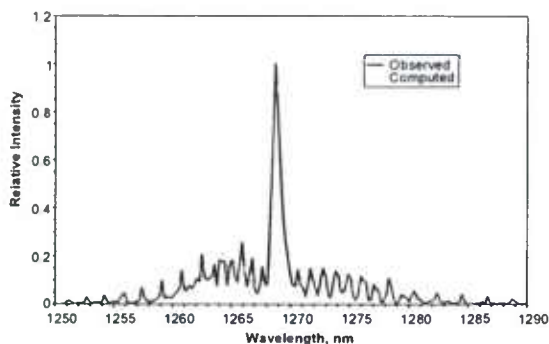
Figure 2–41. Observed and best-fit computed spectra for $O_2(a \rightarrow X)$ emission: microwave discharge of O_2 at 2.6 torr, spectral resolution 0.5 nm, rotational temperature 350 K.

The emission spectra of $O_2(a \rightarrow X)$ and $I^* \rightarrow I$ were corrected for detector baselines and were converted into absolute column intensities, photons/cm^2-s-sr-nm, using the spectral responsivities determined by blackbody calibrations of the full spectrometer optical collection system. An example $O_2(a \rightarrow X)$ spectrum is shown in Fig. 2-41, together with a spectrum computed by a least squares spectral fitting procedure. The spectral fitting analysis gives a rotational temperature of 350 K, in excellent agreement with temperatures determined from the $I \rightarrow I^*$ absorption line widths when I_2 is injected. In addition, the analysis confirms that all of the observed emission is due to the (0,0) band of the $a \rightarrow X$ system, i.e. there is no observable vibrational excitation of the $O_2(a)$ 20 ms downstream of the discharge. Consequently, $O_2(a)$ concentrations can be accurately determined by integration of the spectra and application of the Einstein A-coefficient for the band. Both the spectral fitting and band-integral methods are based on the fundamental principle relating emission intensity and upper state number density [Herzberg, 1951]:

$$(4\pi/P) \int I(\lambda)d\lambda = N_u A_{ul}, \qquad (2\text{-}10)$$

where P is the path length across the viewing volume (5.6 cm), $I(\lambda)$ denotes the set of spectral column intensities over the entire band, 4π is the solid angle (in sr) for isotropic, optically thin molecular emission, N_u is the number density of the upper or emitting state, and A_{ul} is the Einstein coefficient for the transition. From the responsivity calibrations, the product $N_u A_{ul}$ is determined to a relative uncertainty of about $\pm 2\%$. Although the Einstein coefficient for the $O_2(a \rightarrow X)$ transition has been the subject of considerable controversy and uncertainty in the past, recent determinations by two independent groups and three independent methods indicate a value of 2.2 x 10^{-4} s^{-1} with an overall relative uncertainty of $\pm 10\%$ [Newman, 1999; Lafferty, 1998]. The net relative uncertainty of our $[O_2(a)]$ determination is then a systematic error of $\pm 10\%$.

In separate measurements, we confirmed ~100% fractional dissociation of I_2 in the $O + I_2$ and $O + IO$ reaction sequence [Rawlins, 2003]:

$$O + I_2 \rightarrow IO + I \qquad (2\text{-}11)$$

$$O + IO \rightarrow O_2 + I \qquad (2\text{-}12)$$

For the O concentrations in our experiments, we have seen prompt, complete dissociation of I_2 by O, essentially as rapidly as the injected I_2 can be mixed into the main flow.

2.2.1.1 O and $O_2(a)$ Yields

Workers at PSI have determined atomic oxygen and $O_2(a)$ yields for our Evenson-cavity microwave discharge-flow reactor (Figure 2-40) as a function of power and O_2 mole fraction in argon diluent. The measurements were performed at two pressures, 1.5 and 3 torr, and linear flow velocities of about 1300 cm/s. In these measurements, we took care to maintain constant linear flow velocity as the pressure and O_2 mole fraction were changed, in order to ensure a constant residence time of ~0.2 ms in the active discharge. Thus the observed variations in O and $O_2(a)$ yields reflect variations in their respective electron-impact dissociation/excitation rate coefficients and the electron number density (i.e. ionization rate) with changing electron energy distributions. Variations with discharge power at constant pressure and O_2 mole fraction should reflect primarily changes in the electric field strength and electron number density within the discharge.

Typical observed O-atom concentrations were in the range (0.7 to 2) x 10^{15} molecules/cm^3. Measurements of the air-afterglow intensity along the length of the flow tube confirmed that there was negligible loss of O due to heterogeneous and homogeneous recombination, as we expected. Atomic oxygen yields, expressed as $[O]/[O_2]_o$, are plotted as a function of discharge power in Figure 2-42; the power dependence was observed for 1.5 torr, 5.4% O_2 and 3 torr, 5.1% O_2. The air-afterglow determinations were highly reproducible, to within 5% or less. The curves are quadratic fits to the data. The atomic oxygen yield increases a factor of 1.6 to 2.3 for a factor of 3 increase in the discharge power. The variation of O yield with initial O_2 mole fraction for 1.5 and 3 torr, at 70 W discharge power, is shown in Figure 2-43. In this case, the O yield variation is approximately inverse-first order in O_2 mole fraction, approaching 0.4 (20% O_2 dissociation) at 5% O_2 and 1.5 torr. The observed O yields exhibit small variations from day to day, apparently due to slight variations in the details of the discharge cavity configuration, tuning, and air cooling. The increase in O yield with decreasing O_2 mole fraction and decreasing pressure is consistent with our expectations based on the discharge physics outlined above.
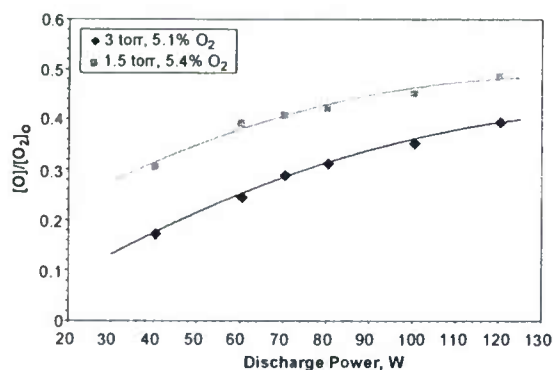
Figure 2–42. Dependence of atomic oxygen yield on microwave discharge power for 1.5 and 3 torr, ~5% O_2 in Ar.
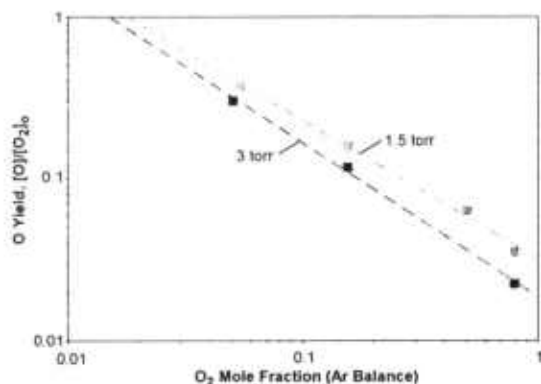
Figure 2–43. Dependence of atomic oxygen yield on O_2 mole fraction and total pressure: Ar diluent, 70 W discharge power, 1.5 and 3 torr.

Observed $O_2(a)$ yields as functions of O_2 mole fraction (1.5 and 3 torr) and discharge power (1.5 torr) are plotted in Figures 2-44 and 2-45, respectively. The observed $O_2(a)$ concentrations were (0.5 to 2) x 10^{15} molecules/cm^3. Measurements of the $O_2(a)$ emission intensity along the length of the flow tube confirmed that there were no significant wall or quenching losses, as expected. (O and $O_2(a)$ have similar accommodation coefficients on untreated pyrex, ~10^{-4} per collision [Black, 1981; Marinelli, 1988].) Day to day variations in the discharge behavior are illustrated in Figure 2-45. As in the case of O, the $O_2(a)$ yields increase with decreasing pressure, and increase markedly with decreasing O_2 mole fraction. For 5% O_2 at 1.5 torr and discharge powers of 70 W or more, we routinely observe $O_2(a)$ yields in excess of 20%. These yields are well above the equilibrium threshold for inversion of the I^* population.
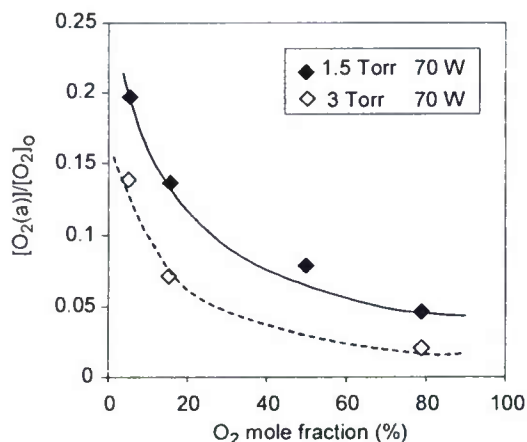
Figure 2–44. Dependence of $O_2(a)$ yield on O_2 mole fraction and total pressure: Ar diluent, 70 W discharge power, 1.5 and 3 torr.
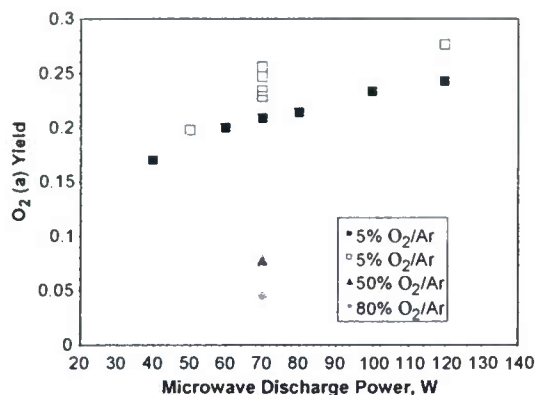
Figure 2–45. Dependence of $O_2(a)$ yield on microwave discharge power for 1.5 torr and three O_2/Ar mixtures. The two data sets for 5% O_2/Ar were observed on separate, consecutive days, and indicate day to day variability in the discharge operation.

For some of the experiments, we used the near-infrared spectrometer to observe $O_2(b)$ emission spectra, $O_2(b^1\Sigma_g^+ \rightarrow X^3\Sigma_g^-)$, centered at 760 nm. $O_2(b)$ is produced in the discharge by electron-impact excitation of $O_2(X)$, with an excitation rate coefficient which is a factor of ~4 smaller than that for $O_2(a)$ excitation [Rawlins, 1987], and is also formed from quenching of discharge-excited $O(^1D)$ by O_2 [Stafford, 2004; Lee, 1978]. However, unlike $O_2(a)$, $O_2(b)$ is rapidly quenched by the walls and, to some extent, by O-atoms [Slanger, 1979], so that its concentration in the reaction zone of the flow tube is very small. Accordingly, our measurements typically show the $O_2(b)$ concentration at the measurement cell is some two orders of magnitude below that of $O_2(a)$ and is therefore insignificant (work at CU Aerospace has shown significant conversion of $O_2(b)$ to $O_2(a)$ in RF discharges). Similarly, vibrationally excited $O_2(v)$ is produced rapidly in the discharge, however it is deactivated by collisions with O and with the reactor walls downstream of the discharge [Rawlins, 1987; Gelb, 1982]. The same expectation applies to the other discharge-produced metastables of O, O_2, and Ar. We expect O_3 to be present in the discharge effluent flow, but at low concentrations. Most of the O_3 reaching the reaction zone is formed downstream of the discharge by three-body recombination of O and O_2. For this process, we estimate $[O_3] < 10^{12}$ molecules/cm^3 in the flow reactor for our experimental conditions. Thus the primary discharge-produced species in the effluent flow are expected to be O and $O_2(a)$.

As discussed above, the observed increases in O and $O_2(a)$ production with decreasing pressure and O_2 mole fraction result from a combination of increasing electron-impact rate coefficients and increasing electron number densities, both of which result from increasing electron "temperatures" in the discharge. Much of the mole fraction effect appears to be due to greatly increased ionization rates at low mole fractions. The mole fraction effect is more pronounced for O than for $O_2(a)$, reflecting the larger energy threshold for O_2 dissociation than for $O_2(a)$ excitation. This is illustrated by the computed rate coefficients plotted in Figure 2-39, where the rate coefficient for O_2 dissociation is a steeper function of O_2 mole fraction than that for $O_2(a)$ excitation. All of these trends are consistent with O_2/Ar discharge model predictions previously published by Rawlins et al, [Rawlins, 1982]. However, we note that our observed O production, relative to that for $O_2(a)$, is considerably less than that implied by the O_2 dissociation cross sections compiled by Phelps [Lawton, 1978; Phelps]. Figure 2-46 shows our observed $[O_2(a)]/[O]$ values, compared to the computed ratios of $O_2(a)$ and O production rates given by $k_{exc}/2k_{diss}$. Since $O_2(a)$ probably suffers additional electron-induced loss processes in the discharge that O does not experience, this simple ratio of the production rates provides an upper

bound to the predicted concentration ratio downstream of the discharge. The data show surprisingly little pressure dependence, and a relative variation with O_2 mole fraction which is consistent with the curves for 50-100 Td. However, the observed ratios are much larger than the predicted upper bounds. Since the $O_2(a)$ excitation cross section appears to be reasonably well determined [Tachibana, 1981], we infer that the O_2 dissociation cross sections give a substantial overprediction of O formation, by perhaps as much as an order of magnitude. The O_2 dissociation cross section reported by Cosby [Cosby, 1993] is smaller and tends to underpredict the O production. Clearly, this aspect of the O_2/Ar discharge modeling needs closer attention and comparison to experimental data.
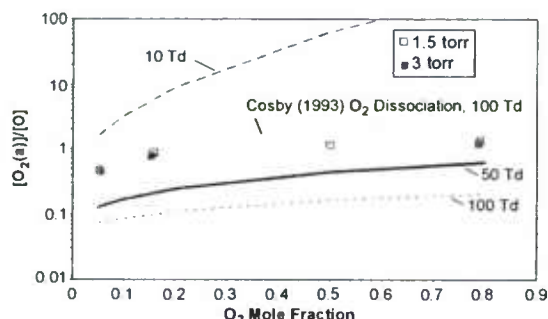
Figure 2–46. $[O_2(a)]/[O]$ ratios observed at 1.5 and 3 torr, compared to computed upper bounds as described in the text.

To investigate the kinetics of I^* excitation, we injected I_2 into the discharge effluent in the flow reactor at several distances from the observation port, to give systematic variations in the reaction time. I_2 was diluted in He and was injected at initial concentrations of (0.5 to 1.3) x 10^{13} molecules/cm^3, so that [O] and [$O_2(a)$] were well in excess. The discharge conditions were (5 to 80)% O_2 in Ar at 1.5 and 3 torr and 40-120 W, however we emphasized 5% O_2 at 1.5 torr and 70-120 W where the $O_2(a)$ yields were highest. For these conditions, the lifetime of I_2 against reaction with O is <<0.1 ms, so the rate of I_2 dissociation is limited by mixing of the injectant gas with the main flow stream. All of the I_2 dissociation occurs through the reactions of I_2 and IO with O. This takes place so rapidly that the multi-step $O_2(a)$ + I_2 energy transfer sequence, which is the usual I_2 dissociation mechanism in the absence of O (as in COIL reactors) [Heidner, 1983], does not occur, and no $O_2(a)$ can be consumed by this path. The reacting mixture then consists of excess O and $O_2(a)$, with much smaller concentrations of I and I^*; this mixture flows down the reactor from the reagent inlet to the observation port. These expectations are borne out by observations of the emission spectra of $O_2(a{\rightarrow}X)$, $O_2(b{\rightarrow}X)$, and $I^*{\rightarrow}I$, with no detectable emission from the $I_2(A^3\Pi{\rightarrow}X^1\Sigma)$ or $I_2(B^3\Pi{\rightarrow}X^1\Sigma)$ bands, which would be excited in the multi-step $O_2(a)$ + I_2 energy transfer sequence [Heidner, 1983]. We observed a faint, visible $I_2(B{\rightarrow}X)$ flame immediately downstream of the injector, which extended only for about 1-2 cm as the I_2 was consumed.

Addition of small concentrations of I_2 gave rise to strong I^* emission at 1315 nm and net $I{\rightarrow}I^*$ absorption of the scanning diode laser beam (negative small-signal gain). We observed net absorption even for cases where the initial $O_2(a)$ yield was well above the equilibrium threshold for positive gain. This occurs in part because the addition of I_2 results in significant depletion of [$O_2(a)$], even though the injected I_2 concentrations are ~100 times smaller than those of $O_2(a)$. In addition, we observed net absorption even when the depleted $O_2(a)$ yield was observed to be essentially at the threshold, where the medium should be near transparency. These results

indicate a complex quenching effect which calls into question the equilibrium description of I^* excitation given by (2-6) and (2-7).
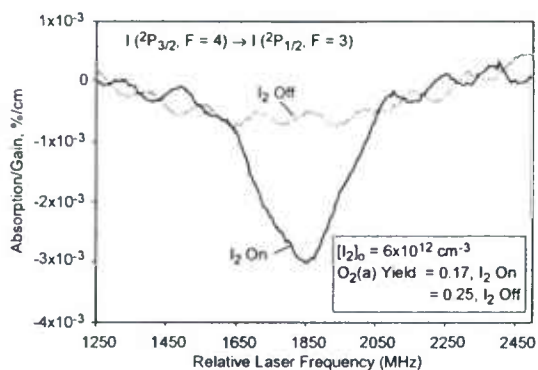
Figure 2–47. Single-pass tunable diode laser scans of atomic iodine line in net absorption, with and without the addition of I_2: 5% O_2/Ar, 70 W, 1.5 torr, 13 ms reaction time.
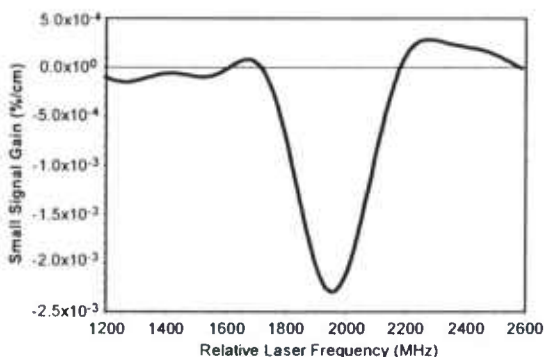
Figure 2–48. Processed tunable diode laser scan from the data in Figure 11, 5% O_2/Ar, 70 W, 1.5 torr, 13 ms reaction time.

Example traces of the scanning laser absorption/gain measurement are shown in Figure 2-47, for cases with and without the addition of I_2 at 1.5 torr, 5% O_2 in Ar, 70 W power, 350 K. Prior to the injection of I_2, the $O_2(a)$ yield measured from the near-infrared emission was 0.25 ([$O_2(a)$] = 5.2×10^{14} molecules/cm^3), and the upper curve was observed, corresponding to zero gas-phase absorption. Upon injection of I_2 at an initial concentration of 6×10^{12} molecules/cm^3, with a reaction time of 12 ms from the injector to the observation port, the observed $O_2(a)$ yield promptly diminished to 0.17 ([$O_2(a)$] = 3.5×10^{14} molecules/cm^3) and a clear absorption signal was observed, corresponding to a net negative small-signal gain of -2.3×10^{-3} %/cm at line center. For these measurements, the laser was scanned repeatedly across the transition at 50 Hz, and 1000 scans were averaged for each of the traces shown. The traces are clearly affected by etalons in the optical system (e.g. due to non-wedged windows and to reflections between the beam launch and collection optics) which are commonly observed at these very low signal levels. Accordingly, we processed the averaged absorption spectra by fast Fourier transform filtering and subtracting the baseline spectra observed with the I_2 flow off. The processed absorption signal from Figure 2-47 is shown in Figure 2-48. For this measurement, the small-signal gain gives a value of [I^*]-[I]/2 = -3.5×10^{12} molecules/ cm^3, while the I^* emission observed by the near-infrared spectrometer gives [I^*] = 1.7×10^{12} molecules/cm^3. Combination of these values gives [I] = 1.04×10^{13} molecules/cm^3, and [I^*]/[I] = 0.16. In addition, ([I^*]+[I])/2 = 6.05×10^{12} molecules/cm^3, in excellent agreement with the initial injected I_2 concentration. This consistency check also confirms the accuracy of the emission diagnostic. However, for the measured O yield (0.3) and the $O_2(a)$ yield observed in the presence of iodine, the equilibrium

relationship gives a predicted ratio $[I^*]/[I] = 0.6$, i.e. just above the inversion threshold of 0.5. This would correspond to an expected positive gain of 7×10^{-4} %/cm, which clearly disagrees with the measurements.

Carroll et al [Carroll, 2004; Carroll, 2005b] also encountered $O_2(a)$ losses upon addition of I_2 to O_2/He discharge effluent streams in a supersonic discharge-flow system. They surmised that the effect was due to a global process whose net effect was rapid quenching of I^* by O. To negate this effect, they added NO_2 to the subsonic flow upstream of the iodine injection and the supersonic nozzle. The titration reaction

$$O + NO_2 \rightarrow NO + O_2 \qquad (2\text{-}13)$$

efficiently reduces [O]: if $[NO_2]_{added} < [O]$, then $[O]_{final} = [O]_{initial} - [NO_2]_{added}$; if $[NO_2]_{added} >$ [O], then all of the O is removed [Kaufman, 1958; Kaufman, 1961]. In addition, some of the NO combines with the remaining O to produce air-afterglow emission, providing a convenient and quantitative means to monitor the progress of the titration. As the NO_2 flow rate is increased from zero, the air afterglow intensity increases, passes through a maximum at $[NO_2]_o =$ $[O]_{initial}/2$, and then decreases until it reaches zero at $[NO_2]_o \geq [O]_{initial}$. (However, we note that, for $[NO_2]_o \approx [O]_{initial}$, the reaction rate becomes second order, and it can take several ms to reduce [O] by two orders of magnitude.) When Carroll et al. [Carroll, 2004; Carroll, 2005b] added NO_2 to their discharge effluent, they observed recovery of the $O_2(a)$ yield to its prior level, and concomitant increases in the $[I^*]/[I]$ ratio, including positive small-signal gain at reduced temperature in their supersonic flow section.
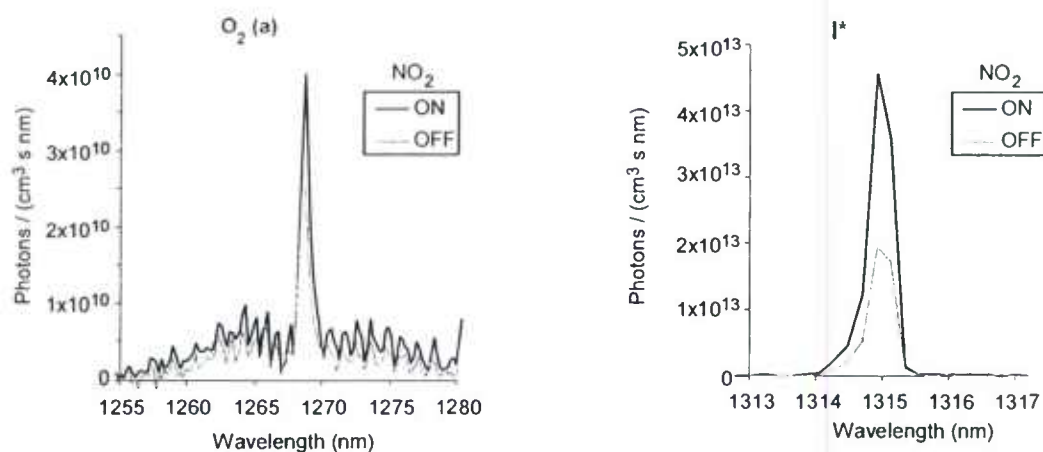
Figure 2–49. Effect of NO_2 addition on observed $O_2(a \rightarrow X)$ and $I^* \rightarrow I$ emission intensities: 5% O_2/Ar, 110 W, 1.5 torr, $[NO_2]_{added} = 0.95[O]_o$, $[O]/[O]_o = 1/20$. With NO_2 off: $O_2(a)$ yield = 0.15, $[I^*]/[I] = 0.13$. With NO_2 on: $O_2(a)$ yield = 0.25, $[I^*]/[I] = 0.36$.

Accordingly, we added NO_2 through a fixed loop injector upstream of the I_2 injector, at flow rates giving $[NO_2]_o \sim [O]_{initial}$ as monitored via the air-afterglow intensity. These experiments used 5% O_2 in Ar at 1.5 torr, 350 K, and $[I_2]_o = 6 \times 10^{12}$ molecules/cm^3. As shown by the emission spectra in Fig. 2-49, we observed essentially complete recovery of the initial $O_2(a)$ and a large increase in the I^* excitation. This was accompanied by decreased laser absorption, approaching transparency. However, as indicated in the figure, the resulting $[I^*]/[I]$ values were still below the inversion threshold of 0.5. With increasing $[NO_2]_{added}$, the remaining [O] became

less than $2[I_2]_o$, so that O was the limiting reagent and I_2 was no longer fully dissociated. This resulted in decreasing $[I^*]$ and $[I]$, however the ratio $[I^*]/[I]$ continued to increase. For the overtitrated condition $[O] \sim [I_2]_o$ and 7 ms reaction time, we observed ~50% dissociation of I_2, and the positive gain spectrum shown in Fig. 2-50. As in Fig. 2-48, this spectrum was processed by averaging 250 scans (~5 s), fast Fourier transform filtering, and subtraction of the baseline spectrum. Also shown in the figure is a Gaussian fit to the lineshape. The line-center small-signal gain for this case was $+8 \times 10^{-5}$ %/cm. The concentration determinations gave $O_2(a)$ yield = 0.25, $[I^*] = 2 \times 10^{12}$ molecules/cm^3, $[I] = 3.8 \times 10^{12}$ molecules/cm^3, and $[I^*]/[I] = 0.53$. Despite the extensive suppression of $[O]$ in this measurement, the observed gain is well below the predicted value of 6×10^{-4} %/cm ($[I^*]/[I] = 0.7$) given by the equilibrium relationship. Nevertheless, these experiments demonstrate the feasibility of attaining positive gain on the $I^* \rightarrow I$ laser transition using $O_2(a)$ generated in a conventional, low-power microwave discharge in subsonic flow.
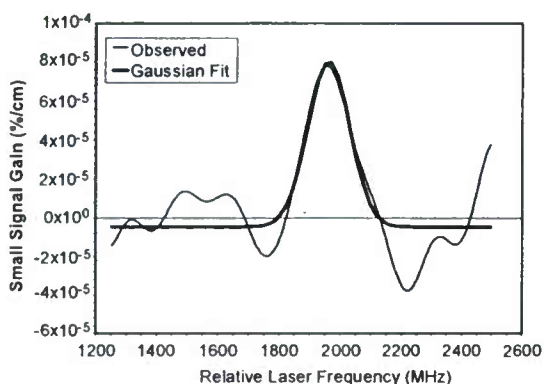
Figure 2–50. Processed tunable diode laser scan of atomic iodine line, showing net positive gain: 5% O2/Ar, 70 W, 1.5 torr, 7 ms reaction time, NO2 added, $[O] \cong [I2]o = 6 \times 1012$ cm-3, O2(a) yield = 0.25. A Gaussian fit to the data is also shown.

We have also obtained kinetic data on the loss of $O_2(a)$ caused by the injection of trace amounts of I_2. The $O_2(a)$ loss factor, $[O_2(a)]_o/[O_2(a)]$, increases with reaction time and with $[O]$, with pseudo-first order loss rates on the order of 50 to 100 s^{-1}. Given the species and concentrations in the reactor, this loss cannot be caused by direct quenching of $O_2(a)$. However, the observed loss of $O_2(a)$ can occur through quenching of I^*, apparently by O. As the I^* concentration produced in Reaction (2-14) [see also Reaction (2-6)] is depleted by quenching, $O_2(a)$ is converted to $O_2(X)$ as the equilibrium shifts. Carroll et al. [Carroll, 2004; Carroll, 2005b] also observed this effect, and analyzed their data to infer an apparent $O + I^*$ quenching rate coefficient of 3.5×10^{-12} cm^3/molecule-s (updated to 8×10^{-12} in more recent analysis). This is considerably smaller than the directly measured value of 8×10^{-12} cm^3/molecule-s reported by Heaven and coworkers for the isolated elementary reaction [Heaven, 2005].

We analyze the kinetics of $O_2(a)$ loss by I^* quenching as follows. For simplicity, let the dissociation of I_2 by reactions of O with I_2 and IO be essentially instantaneous on our reaction time scale. The excitation and quenching of I^* can be described by three reactions:

$$O_2(a) + I \rightarrow O_2(X) + I^* \qquad (2\text{-}14)$$
$$O_2(X) + I^* \rightarrow O_2(a) + I \qquad (2\text{-}15)$$
$$O + I^* \rightarrow O + I \qquad (2\text{-}16)$$
$$d[O_2(a)]/dt = k_{-1}[O_2(X)][I^*] - k_1[O_2(a)][I] \qquad (2\text{-}17)$$

Equating the instantaneous production and loss rates of I* (steady state approximation) gives the pseudo-first-order loss rate for $O_2(a)$:

$$\frac{d(\ell n[O_2(a)])}{dt} = -\frac{k_1 k_2 [I][O]}{k_{-1}[O_2] + k_2[O]} \tag{2-18}$$

This equation can be applied to observed $O_2(a)$ loss rates for known [I], [O], and [O_2] to determine the value of k_2. Note that, since [I] > [I*], the variation of [I] with reaction time due to I* quenching is small. A plot of the measured $O_2(a)$ loss is shown in Figure 2-51, observed by adding I_2 through the sliding injector at different distances from the observation port. The measurements were made for 5.5% O_2 in Ar at 1.58 torr and 330 K, with a discharge power of 70 W and a flow velocity of 1280 cm/s. [I] was determined from the combination of I* emission and I→I* absorption measurements as described above: [I] = $(7.9 \pm 1.0) \times 10^{12}$ molecules/cm^3. The initial, unquenched [$O_2(a)$] was 6×10^{14} cm^{-3}. The slope of the line through the data points gives a pseudo-first-order $O_2(a)$ loss rate of (97 ± 15) s^{-1}. Solution of the above rate law for k_2 gives $k_2 = (1.3 \pm 0.3(1\sigma)) \times 10^{-11}$ cm^3/molecule-s. This is much larger than the upper bound measured for the elementary O + I* quenching reaction [Han, 2004], indicating that our measurement represents a global overall process consisting of several elementary reactions.
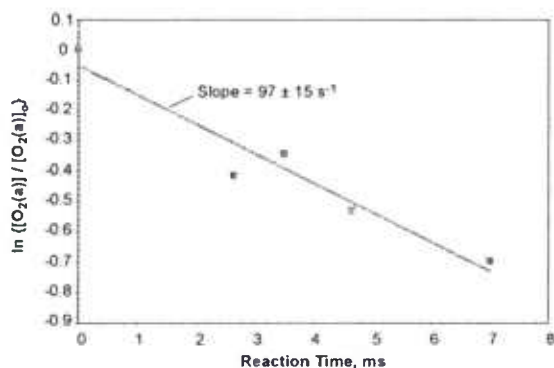
Figure 2–51. $O_2(a)$ decay and first-order loss rate upon addition of I_2: $[I_2]_0 = 4.7 \times 10^{12}$ cm^{-3}, 5.5% O_2/Ar, 70 W, 1.58 torr, $[O_2(a)]_0 = 6 \times 10^{14}$ cm^{-3}.

Using the techniques described above, we have determined [I*]/[I] ratios for a range of reaction times and for discharge conditions giving a wide range of $[O_2(a)]/[O_2(X)]$ ratios. The experimental conditions included: 1.5 torr, 5% and 50% O_2; 3 torr, 80% O_2; discharge power 40-120 W; reaction times 3-12 ms; and initial I_2 concentrations $(0.5-1.3) \times 10^{13}$ molecules/cm^3. Figure 16 summarizes the data in the form of a plot of [I*]/[I] vs. $[O_2(a)]/[O_2(X)]$. Also shown on the plot is the equilibrium relationship from Equation (2-7), for 340 K. The experimental data span a range in $[O_2(a)]/[O_2(X)]$ of 0.05 to 0.3, and all of the measured [I*]/[I] values lie below the equilibrium values. The discrepancy between the data and Equation (2-7) increases with increasing $[O_2(a)]/[O_2(X)]$, except for the case with NO_2 added. The observed trend does not appear to be strongly influenced by discharge power or reaction time. Possibly the data for the higher I_2 concentrations, all at $[O_2(a)]/[O_2(X)] \leq 0.15$ and 9 ms reaction time, trend closer to the line, however there are not enough data with different I_2 concentrations to conclude this with certainty. More systematic measurements are needed, particularly for dependence on [I_2]. However, it is clear from these data that the mechanism for I* excitation and deactivation in discharged O_2 effluent streams is much more complex than previously thought.

Our observations of the microwave discharge yields of $O_2(a)$ and O, and of their trends with discharge conditions, are qualitatively consistent with predictions based on the chemical physics of the discharge. These data warrant more quantitative comparisons with discharge model predictions, which are in progress in our laboratory and will be reported elsewhere. Our preliminary analysis indicates that the calculated yields are most sensitive to the rate of electron loss to the walls associated with Debye shielding, and to the dissociation rates of $O_2(X)$ and $O_2(a)$. In addition, the effects of dissociative attachment and the O^- ion need to be carefully evaluated. For example, it appears that the role of O^- as an $O_2(a)$ sink is considerably muted if we consider the relatively low rate coefficient measured by Upschulte et al. [Upschulte, 1994] for the collisional detachment reaction:

$$O^- + O_2(a) \rightarrow O_3 + e^-, \quad k = 2.7 \times 10^{-11} \, cm^3/s \qquad (2\text{-}19)$$

This value is an order of magnitude smaller than has been used in many previous discharge modeling calculations. It also appears inevitable that increased $O_2(a)$ production will be accompanied by increased O production, which benefits I_2 dissociation but interferes with I^* excitation as discussed below. Our data suggest that the O production is considerably less than predicted from commonly accepted dissociation cross sections, and this point requires further examination. The so-called "mercury mirror" technique [Derwent, 1972; Heidner, 1983; Upschulte, 1994] provides an effective means for catalytic removal of O in small-volume discharge-flow systems, however this approach has an inherently limited surface/volume ratio and short coating lifetime, and is not practical for larger scale, high-throughput systems required to demonstrate lasing and power scaling.

The attainment of positive $I^* \rightarrow I$ gain from discharge-generated $O_2(a)$ in subsonic flow is a necessary step in the eventual development of a recyclable, electrically pumped iodine laser system. Our results confirm and complement recent observations of gain in supersonic flow by Carroll et al [Carroll, 2004; Carroll, 2005b]. In addition, we have observed significant unexpected kinetic limitations: (1) an O-related quenching process that reduces $O_2(a)$ yield in the presence of trace amounts of added I_2, and (2) an unknown mechanism which suppresses $[I^*]/[I]$ for a given $O_2(a)$ yield.

The first process is consistent with a global reaction of the form $I^* + O \rightarrow I + O$, which results in net deactivation of $O_2(a)$. However, the global rate coefficient to account for our data is $\sim 10^{-11}$ cm^3/s, much larger than the upper bound of $< 2 \times 10^{-12}$ cm^3/s measured for the isolated elementary $O + I^*$ reaction [Han, 2004]. Our value is also larger than that of 3.4×10^{-12} cm^3/s determined by Carroll et al [Carroll, 2005b]. for the equivalent global process at 10 torr and much larger I_2 concentrations, $[I_2] \sim 10^{14}$ molecules/cm^3. This suggests the possibility of an overall quenching mechanism containing an inverse dependence on total-I concentration.

	P torr	% O₂	I₂ cm⁻³	Power W	Rxn Time ms
Δ	3	80%	1 14 (13)	60-120	9.0
■	1 5	50%	1 25 (13)	40-120	9.0
□	1 6	5.5%	4.7 (12)	70	2.7-7.0
✕	1 5	5%	5 2 (12)	120	7.6
◇	1 5	5%	6.0 (12)	70	13
✕	1 5	5%	6.0 (12)	70	7.0
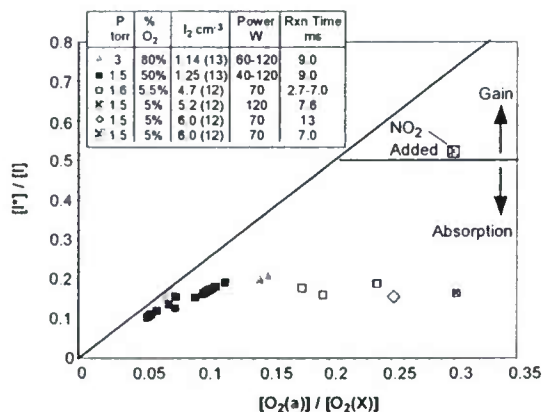
Figure 2–52. Observed dependence of $[I^*]/[I]$ on $[O_2(a)]/[O_2(X)]$, compared to the equilibrium relationship. Inversion of the atomic iodine state populations and positive gain occur for $[I^*]/[I] > 0.5$.

The second process is revealed by the difficulty of achieving positive gain even with 20-25% $O_2(a)$ yields, once the $O_2(a)$ loss mechanism was suppressed by reduction of [O]. The discrepancies between the observed and equilibrium $[I^*]/[I]$ values shown in Figure 2-52 are too large to be accounted for by uncertainties in the experimental data or in the Einstein coefficients. Our present data base is sufficient to establish the discrepancy, but more systematic dependencies on [O], $[I_2]$, and reaction time need to be examined in order to clearly identify the reaction mechanism responsible. In the following discussion, we consider some candidate hypotheses.

As discussed above, the expected active constituents of the oxygen discharge effluent stream are primarily $O_2(a)$ and O, with much smaller (and supposedly insignificant) amounts of O_3, $O_2(X,v)$, $O_2(b)$, and the more energetic (~4.5 eV) O_2 metastables. Thus the mechanistic possibilities are quite limited, unless one of the trace species is actually present at much larger concentration than expected from the known chemistry. We note that the energy of I^*, which lies 783 cal/mole below that of $O_2(a,v=0)$, is 183 cal/mole *above* that of $O_2(X,v=5)$ [Krupenie, 1972]. This near-resonant relationship, $0.27kT$ at 350 K, suggests the possibility of a rapid energy exchange process, accompanied by O-atom deactivation of $O_2(X,v=5)$:

$$I^* + O_2(X,v=0) \rightarrow I + O_2(X,v=5) \tag{2-20}$$

$$O + O_2(X,v=5) \rightarrow O + O_2(X,v=0 \text{ to } 4) \tag{2-21}$$
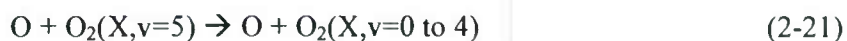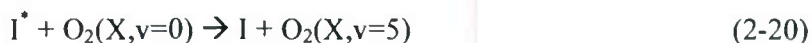
The forward step of Reaction (2-20) is basically an exoergic branch of the $I^* + O_2$ quenching reaction, and the near-resonant forward and reverse reactions would proceed towards $K_{eq} \sim 1$, altering the overall equilibrium towards lower $[I^*]/[I]$ ratios. The deactivation of $O_2(X,v=5)$ by O is likely to be efficient, $k \sim 10^{-11}$ cm³/s [Rawlins, 1987; Gelb, 1982], resulting in net loss of I^*. At low total-I concentrations, Reaction (2-21) removes $O_2(X,v=5)$ more rapidly than it can be converted back to I^* by Reaction (2-20). At large total-I concentrations and/or low [O], Reaction (2-20) competes effectively against Reaction (2-21), and I^* loss is reduced. Thus this mechanism incorporates an inverse dependence on total-I concentrations as suggested above. We note that, in the regime [O] >> [I], Reaction (2-20) can be neglected, and the sum of Reactions (2-20) and (2-21) gives the net global reaction

$$I^* + O \rightarrow I + O \tag{2-22}$$

as inferred in our experiments and by Carroll et al [Carroll, 2005b].

In order to examine the effect of this mechanism for our experimental conditions, we performed kinetics modeling calculations using the elementary reaction set in Table 2-3. The rate coefficient values in the table were taken from the literature, except for k_4, which was adjusted to give an $O_2(a)$ loss rate similar to our observation. The calculations were performed for 5% O_2 in Ar at 1.5 torr, 350 K, with initial $O_2(a)$ and O yields of 0.23 and 0.3, respectively, and $[I_2]_o = 6$ x 10^{12} molecules/cm^3. Calculations were performed with and without reduction of [O] by the NO_2 titration reaction. The predicted behavior of small-signal gain with reaction time is shown in Figure 2-53. The curves in Figure 2-53a were calculated for the conventional mechanism, i.e. by omitting Reactions 4 and 5 in Table 2-3 and setting $k_6 = 1$ x 10^{-11} cm^3/s as inferred from our $O_2(a)$ loss data. This calculation indicates substantial positive gain upon suppression of [O] by a factor of 20, and is clearly incompatible with our measurements. The curves in Figure 2-30b were calculated for the full reaction set in Table 2-3, assuming $k_4 = 7$ x 10^{-12} cm^3/s. These curves illustrate the progressive increases in the small-signal gain as [O] is reduced, first by a factor of 20 and then by a factor of 100 so that $[O]_o = [I_2]_o$ as in the experiments. At the lowest [O], the gain at our typical measurement time of 7 ms is small and positive, ~1 x 10^{-4} %/cm, as we observe. With no O suppression, the computed first-order $O_2(a)$ loss rate at 7 ms is 118 s^{-1}, and the I_2 dissociation is 100%, also in agreement with the observations. With O suppression to $[O]_o = [I_2]_o$, the $O_2(a)$ loss rate at 7 ms is

Table 2-3. Hypothetical Reaction Mechanism

	k (350 K), cm^3/s	Reference
$O+I_2 \xrightarrow{\ 1\ } IO+I$	1.5 (-10)	5
$O+IO \xrightarrow{\ 2\ } O_2+I$	1.4 (-10)	5
$O_2(a)+I \xrightarrow{\ 3\ } O_2+I^*$	$K_{EQ} k_{-3}$	2
$O_2+I^* \xrightarrow{\ -3\ } O_2(a)+I$	3.3 x 10^{-11} - k_4	2
$O_2+I^* \xrightarrow{\ 4\ } O_2(v=5)+I$	k_4	
$O_2(v=5)+I \xrightarrow{\ -4\ } O_2+I^*$	$k_{-4} = k_4$	
$O_2(v=5)+O \xrightarrow{\ 5\ } O_2+O$	~ 1 (-11)	15, 39
$O+I^* \xrightarrow{\ 6\ } O+I$	~ 1 (-12)	12

33 s^{-1}, and the I_2 dissociation is 67%, both larger than measured. In addition, the computed [O] is rapidly removed by excess I_2, and is $<10^{11}$ molecules/cm^3 at >6 ms. We stress that, at this writing, the reaction mechanism in Table 2-3 represents a preliminary and unproven hypothesis, which is qualitatively consistent with our data for a very specific set of experimental conditions. More comprehensive measurements and comparative modeling will be required to fully test this hypothetical reaction mechanism.
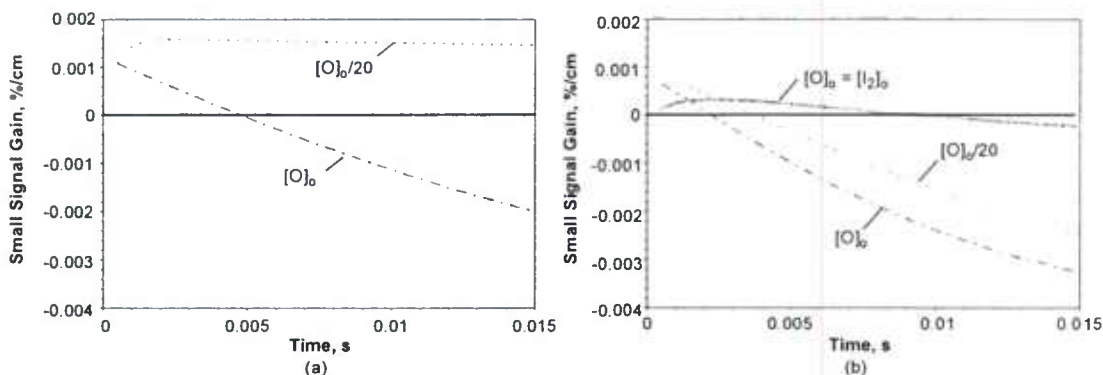
Figure 2–53. Dependence of small-signal gain on reaction time, computed for the reaction mechanism given in Table 1, 5% O_2/Ar, 1.5 torr, 350 K, initial $O_2(a)$ yield = 0.23, initial O yield = 0.3: (a) $k_4 = k_{-4} = k_5 = 0$, $k_6 = 1 \times 10^{-11}$ cm^3/s; (b) rate coefficients as given in Table 1 with $k_4 = 7 \times 10^{-12}$ cm^3/s.

Possible contributions from O_3 and $O_2(v)$ seem unlikely but should be considered. If present in sufficient quantities, O_3 could alter the $[I^*]/[I]$ ratios through the reaction

$$O_3 + I \rightarrow IO + O_2 , \tag{2-23}$$

which may proceed with a larger rate coefficient for I^* than for I. This reaction would not deplete total I since the O + IO reaction would promptly regenerate I. If O_3 is formed only by three-body recombination of O and O_2, it is straightforward to calculate that its concentration in the flow reactor will be $<10^{12}$ molecules/cm^3 and therefore is negligible. However, Copeland and co-workers [Copeland, 1994, Knutsen, 1994] have shown that one of the 4.5 eV metastables of O_2, $O_2(A^3\Sigma,v)$, can react efficiently with $O_2(X)$ to form O_3:

$$O_2(A^3\Sigma_u^+,v) + O_2(X^3\Sigma_g^-) \rightarrow O_3 + O, \quad k \cong 3 \times 10^{-11} \; cm^3/s \tag{2-24}$$
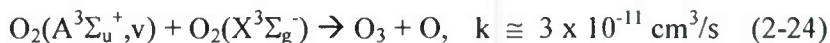
This reactive property may also apply to the other nested 4.5 eV states, $O_2(A'^3\Delta_u)$ and $O_2(c^1\Sigma_u^-)$. $O_2(c)$ is excited in the discharge by electron impact with a rate coefficient of ~6 x 10^{-10} cm^3/s [Rawlins, 1987], and we expect similar values for the other states. For our flow velocities, the $O_2(A,A',c)$ that exits the active discharge is quenched by O and O_2 within tens of microseconds, and much of this quenching could proceed through the potentially reactive channel with O_2. The O_3 concentrations formed by this mechanism could conceivably exceed 10^{13} molecules/cm^3, and thus could be a factor if the $I^* + O_3$ reaction occurs with a near-gas-kinetic rate coefficient. This question can be directly addressed through measurements of O_3 concentrations in the flow reactor (very recent measurements of O_3 in one of the RF discharges at UIUC showed only the small amounts predicted by theory to be present. When NO was added to the flow, O_3 was virtually undetectable.)

Similarly, interference from vibrationally excited $O_2(v)$ must also be considered. $O_2(v)$ is formed efficiently in the discharge by electron impact excitation, $k \sim 10^{-9}$ cm^3/s [Rawlins, 1987], however it should be rapidly quenched by O and walls downstream of the discharge. When O is reduced by the O + NO_2 titration reaction, $O_2(v)$ from the discharge and/or from the titration reaction,

$$O + NO_2 \rightarrow NO + O_2(v) , \tag{2-25}$$

may persist into the $O_2(a) + I$ reaction zone:

$$O_2(a,v) + I \rightarrow I^* + O_2(X,v) \ . \tag{2-26}$$

The primary effect would be to reduce the energy defect between the right-hand and left-hand sides of the reaction, thus lowering the equilibrium constant and the $[I^*]/[I]$ ratio for a given $O_2(a)$ yield. This would limit the small-signal gain observed with suppressed $[O]$. We would expect to observe evidence of vibrationally excited $O_2(a,v)$ in the emission spectra, however there is no clear evidence for this in our spectral data. This can be addressed by further experiments varying the flow times from the discharge and the NO_2 injector.

We have used a microwave discharge-flow reactor and a comprehensive optical diagnostic suite to characterize the kinetics of I^* excitation and small-signal gain by electrically generated $O_2(a)$. The diagnostic suite provided independent measures of the concentrations of $O_2(a)$, $O_2(b)$, O, I_2, I^*, and I, all as functions of reaction time. Using discharge modeling predictions of the relevant electron-impact excitation and ionization rate coefficients, we identified and experimentally quantified a range of discharge conditions (low O_2 mole fractions, high E/N) giving $O_2(a)$ yields of 0.2 to 0.3. The results also indicate O yields of comparable magnitude, which are much smaller relative to the $O_2(a)$ yields than predicted from commonly accepted O_2 dissociation cross sections. Upon addition of the I_2 reagent at low concentrations, we found that the $O_2(a)$ concentration was reduced via an unexpected I^* quenching mechanism involving O produced in the discharge. When we reduced the O concentration by a factor of ~100 through titration with NO_2, we observed positive small-signal gain, in a subsonic flow at ~350 K. This observation is an important step in determining the feasibility of a microwave-driven hybrid electric oxygen-iodine laser. However, for all experimental conditions, we consistently observed small-signal gains which were much lower than expected from the conventional $O_2(a)/I^*$ equilibrium description. These results indicate the existence of one or more multi-step reaction mechanisms for quenching of I^* in the discharge effluent flow stream which have not previously been identified.

The discovery of an unknown I^* deactivation mechanism does not significantly impact the feasibility of an efficient hybrid electric oxygen-iodine laser, but rather prompts more systematic fundamental investigations to provide data and models required for scaling and optimizing the system. Indeed, our observation of positive gain in subsonic flow [Rawlins, 2005] was preceded by positive gain observations and successful laser power extraction in supersonic flow [Carroll, 2004; Carroll, 2005b]. The small-signal gain observed in our subsonic flow experiments scales to 0.02%/cm for $[I_2]_o \sim 10^{15}$ cm^{-3}, indicating the potential for a viable subsonic laser. The combination of these emerging experimental results verifies the potential of the hybrid laser concept. We are continuing to pursue coupled kinetics experiments and modeling over a broader range of experimental parameters, both for the oxygen discharge kinetics and for the I^* excitation chemistry.

PSI will continue to evaluate this and other possible mechanisms through kinetics modeling calculations and comparisons with experimental measurements during the next reporting period. Additional possibilities to consider and test include reactions involving discharge-generated ozone. The capability of our flow reactor for systematic kinetics investigations under well-controlled conditions and low reagent concentrations is well suited for this purpose.

2.2.1.2 Conclusions from diagnostics studies in microwave systems

PSI has applied the diagnostics for $O_2(a)$, I^*, O, and small-signal gain on the PSI flow reactor at a high level of sensitivity and accuracy, and have assisted with implementation of these methods at UIUC as well. PSI characterized the yields of $O_2(a)$ and O generated by microwave discharge of O_2/Ar mixtures, and demonstrated that large yields of both species can be obtained at low O_2 mole fractions. They applied these results to the investigation of I^* excitation by discharge-generated $O_2(a)$, and we were able to observe positive small-signal gain upon reduction of O concentrations by titration with NO_2. Our preliminary kinetics experiments indicate the presence of previously unknown reactions which reduce the efficiency of I^* excitation for these conditions. PSI has conjectured a hypothetical reaction mechanism to account for these effects, and we plan to continue this line of investigation in more detail.

During the next reporting period, PSI plans to continue with diagnostic development and kinetics experiments. They are working on systems for high-sensitivity optical absorption measurements of I_2 dissociation and O_3 formation in both the PSI and UIUC flow reactors. They also plan a more detailed investigation of the kinetics of the discharge-initiated oxygen-iodine energy transfer mechanism in the PSI flow reactor, in order to more fully characterize and understand the loss phenomena. This will be highly relevant to eventual engineering efforts to design and scale up to prototype discharge-driven laser systems. PSI plans to submit several related papers for publication during the next year.

2.2.2 Experiments with Double Microwave Discharge at AFIT
2.2.2.1 Key Kinetic Processes

The production of $O_2(a^1\Delta, b^1\Sigma)$ by plasma electrons is important in ionospheric chemistry, glow discharges for microelectronic processing, and in the ElectricOIL system. Several kinetic models for such discharges exist [Dai, 1996; Lee, 1994; Stafford, 2004]. The models must include several key elements: (1) electron excitation and de-excitation of singlet oxygen, (2) atomic oxygen production from direct electron impact and multiple step dissociation from O_2^+ and O_2^*, (3) intermediate kinetics including O_2^+ and vibrationally excited O_2 production, and (4) collisional cascading to $O_2(a)$ from O_2 states with energies of $1.5 - 5$ eV . A short summary of some of these key reactions is provided in Table 2-4 and is extracted from the complete table show before. The cross-sections for electron interactions with ground state molecular oxygen are rather well established [Dai, 1996; Rapp, 1965]. The rate coefficients depend on electron energy distributions and the rates listed in Table 2-4 represent conditions typical of RF discharges [Dai, 1996]. Tailoring the E/N ratio of the discharge is critical to maximizing the singlet oxygen yield. Note that the dominant process in the electron energy range of importance (0-20 eV) is dissociation. Indeed, large atomic oxygen concentrations, as high as 40%, can be obtained [Ivanov, 1999] at low pressures, and computations and discharge measurements at UIUC essentially confirm these data, Fig. 2-54. (It should be noted that at higher pressures and higher dilutions we have observed significantly reduced flows of oxygen atoms in laser flows.)

59

Table 2-4. Key Oxygen Discharge Kinetic Processes.

Reaction	Process	Rate Coefficient, k_i (cm³/particle-s)
2-13	$O_2 + e^- \rightarrow O_2(a) + e^-$	5×10^{-10}
2-14	$O_2 + e^- \rightarrow O_2(b) + e^-$	---
2-15	$O_2(a) + e^- \rightarrow O_2 + e^-$	1.5×10^{-9}
2-16	$O_2(a) + e^- \rightarrow O + O + e^-$	$< 1.4 \times 10^{-9}$
2-17	$O_2(a) + e^- \rightarrow O_2(b) + e^-$	---
2-18	$O_2 + e^- \rightarrow O + O + e^-$	9×10^{-9}
2-19	$O_2 + e^- \rightarrow O + O^-$	4×10^{-11}
2-20	$O_2 + e^- \rightarrow O_2^+ + e^- + e^-$	2×10^{-9}
2-21	$O_2^+ + e^- \rightarrow O + O$	2×10^{-7}
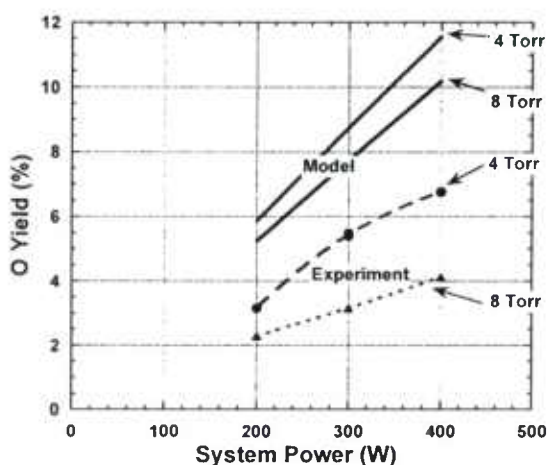
Figure 2–54. Oxygen atom experimental data and modeling predictions as a function of pressure by UIUC. The oxygen flow rate run through the discharge was 5 mmol/s mixed 20 mmol/s of helium.

As the singlet oxygen concentration increases, electron – excited state interaction becomes increasingly important. The yield of $O_2(a)$ is in part limited by super-elastic collisions, reaction (2-15), where the electron gains kinetic energy equivalent the molecular oxygen internal excitation, and by dissociation of singlet oxygen, reaction (2-16). The rate for the superelastic reaction (2-15) is constrained by detail balance and the rate for the excitation reaction (2-13). The cross-sections for the dissociative reaction (2-16) are more difficult to measure and are not well established. In fact, the rate coefficient provided in Table 2-1 includes a significant contribution from vibrationally excited O_2.

The scaling of $O_2(a)$ yield is limited by the electron - singlet state interactions and the rates for these processes are poorly established. AFIT is currently in process of the study reactions (2-15) and (2-16) both theoretically and experimentally.

The cross-section for excitation of the $O_2(b)$ state from $O_2(a)$ of reaction (2-17) is an order of magnitude greater than the corresponding excitation from $O_2(X)$, reaction (2-14). The cross-section for reaction (2-17) at an electron energy of 4.5 eV is large, 23×10^{-18} cm² [Hall, 1975], and comparable to the $O_2(a)$ production from reaction (2-13). In the traditional Chemical Oxygen-Iodine Laser, the concentration of $O_2(b)$ is small. However, in the ElectricOIL laser, a significant $O_2(b)$ concentration is obtained. As much as 20% of the discharge electrical power

results in the production of $O_2(b)$ [King, 2001] within the discharge. A significant increase in $O_2(a)$ yield may be achieved by selectively deactivating $O_2(b)$ to $O_2(a)$. Small concentrations of organics added to the flow have been shown to increase $O_2(a)$ emission at the expense of $O_2(b)$ [Mikheyev, 1999].

2.2.2.2 Selective Energy Transfer from $O_2(b^1\Sigma)$ to $O_2(a^1\Delta)$

One key to recovering energy stored in higher lying states such as $O_2(b)$ to excite atomic iodine via the laser pumping reaction Eqn. (2-1) is to transfer the energy to $O_2(a)$ without losing significant energy via the quenching to $O_2(X)$. Thus, the collision partner M must posses a rapid rate for reaction (2-22), Table 2-2, with a large branching ratio, $\phi = k_{21}/(k_{21}+k_{22})$. In addition, the collision partner must not efficiently deactivate $O_2(a)$ via reaction (2-24).

Table 2-5. Kinetics for Relaxation of $O_2(b) \to O_2(a)$.

Reaction	Process
2-22	$O_2(b) + M \to O_2(a) + M$
2-23	$O_2(b) + M \to O_2(X) + M$
2-24	$O_2(a) + M \to O_2(X) + M$

There is some promise for such a collision partner, as the spin is conserved in reaction (2-22) but not in reactions (2-23) and (2-24). Furthermore, if M is a molecular specie with vibrational energy spacing near the $O_2(b) - O_2(a)$ energy difference, a resonant E-V process will likely enhance the rate for reaction (2-22). An investigation of such potential collision processes is being conducted by workers at AFIT.

2.2.2.3 Experimental Apparatus

A two element microwave discharge apparatus was developed, as shown in Figure 2-55. The first discharge produces a flow of $O_2(a)$, $O_2(b)$, and atomic oxygen, as well as vibrationally excited states of oxygen, which then serve as the initial condition to the second discharge. The conditions can be changed by either varying the power of the first discharge or placing silver wool between the two discharges to control the O atom concentration. By looking into these changes and monitoring the output of the second discharge, one can determine the effects on the rates of electron and singlet oxygen interactions.
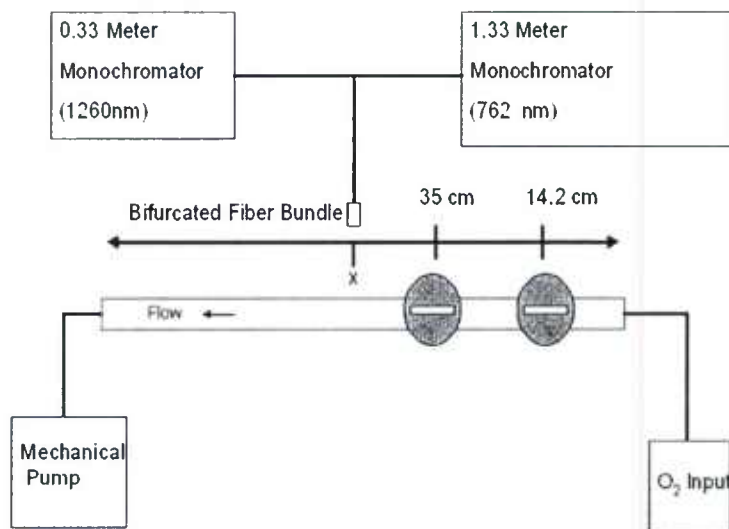
Figure 2–55. **Double microwave discharge flow tube with spectrally-resolved emission diagnostics.**

The ½" flow tube provides a typical flow velocity of 800 cm/s. Two similar Evenson-type microwave cavities with 120 W Opthos power supplies were employed to produce the oxygen discharges. The two discharges are separated by 20.8 cm and optical access is largely obscured for 4 cm around each discharge. Pressure (1-5 torr) and flow rates were monitored with MKS 600- series capacitance manometers and Sierra capacitance-based flow controllers.

The principal diagnostics include both $O_2(a)$ and $O_2(b)$ spectra as a function of flow distance, x. The optical emissions were collected with a fiber bundle and focusing probe providing approximately 0.5 cm spatial resolution in the flow direction. The $O_2(b)$ emission is resolved by a 1.3 m monochromator with ICCD camera detection, providing ~ 0.01 nm spectral resolution. The weaker $O_2(a)$ emission is resolved by a 0.3 m monochromator and an InGaAs array providing ~ 1.7 nm spectral resolution.

2.2.2.4 Experimental Results

The spectrally resolve emissions from $O_2(b-X)$ near 762 nm and $O_2(a-X)$ near 1.27 μm are shown in Figures 2-56 and 2-57. Nearly complete spectral isolation is achieved for the $O_2(b-X)$ emission, allowing for clear determination of rotational population distributions. Only the ^PP and ^PQ branches are illustrated in Figure 2-56, as the bandwidth of the spectrometer is insufficient to cover the other two rotational branches. The rotational spectrum of the $O_2(b\rightarrow X)$ emission is labeled as $^{\Delta K}\Delta J(K'')$ where K is the total angular momentum without electron spin, and J represents the total angular momentum (spin + rotation). The magnetic dipole selection rules, Hunds case (b), produces four branches: ^PP and ^PQ, beginning near 1320 cm^{-1} and extending to about 13020 cm^{-1}, and the ^RQ and ^RR lines from 13125 – 13165 cm^{-1}.
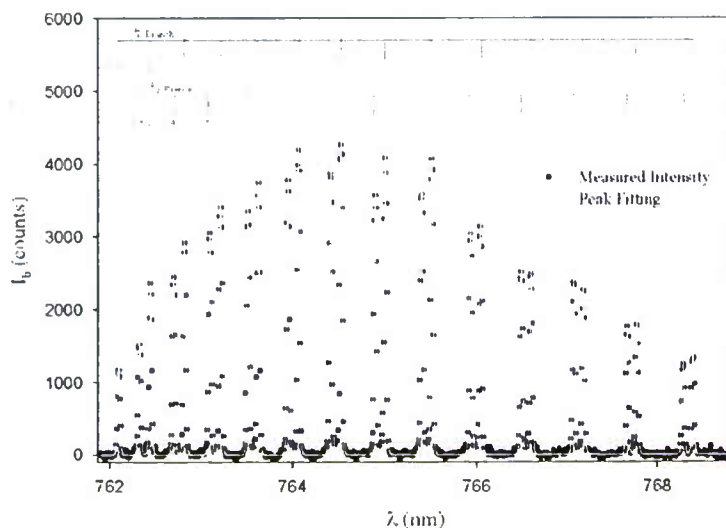
Figure 2–56. Portion of the rotationally resolved $O_2(b^1\Sigma \rightarrow X^3\Sigma)$ emission spectrum at 40.5 cm from a 100 watt microwave discharge operating at an oxygen pressure of 4.015 torr. The $O_2(b-X)$ rotational distribution is statistical with a temperature of 772 K.
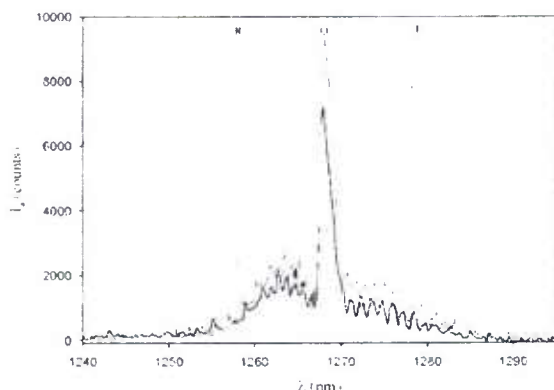
Figure 2–57. Emission spectrum for $O_2(a^1\Delta - X^3\Sigma)$ ($v'=0 \rightarrow v''=0$) band recorded just after the second discharge at x =40.5 cm for an oxygen pressure of 4.015 torr.

The $O_2(a \rightarrow X)$ emission intensity, I_a, defined as the total area under the spectra, is shown as a function of flow time in Figure 2-58. The dramatic increase in intensity just outside of the discharge is largely attributed to the declining temperature. However, a definite increase (~28%) in $O_2(a)$ is observed even after the temperature change is accounted for. We are unaware of any previous reports of singlet oxygen production downstream of the discharge, and the source of this emission is under active investigation. Possible explanations include: (1) relaxation to $O_2(a)$ from $O_2(b)$, or higher lying oxygen electronic states, (2) vibrational relaxation from $O_2(a, v>0)$, (3) atomic oxygen recombination, (4) ozone reactions, (5) thermal electron excitation, and (6) reactions involving $O(^1D)$.
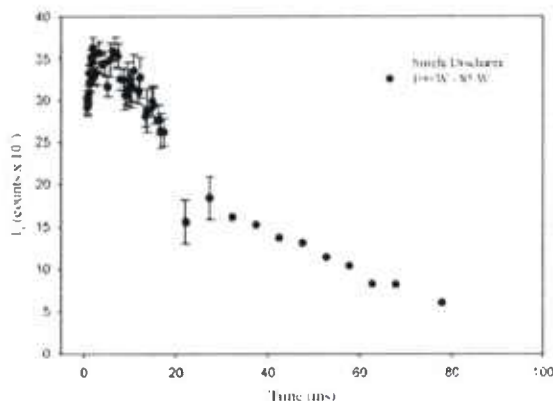
Figure 2–58. $O_2(a\text{-}X)$ emission intensity, corrected for temperature induced concentration variations, as a function of flow time outside the second discharge for two cases: (•) 1st discharge at 85 W, and (•) 1st discharge off.
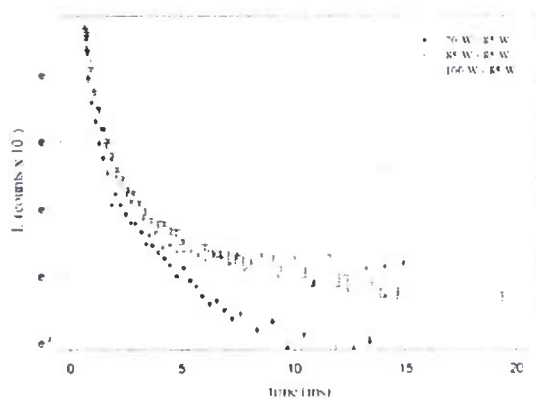
Figure 2–59. $O_2(b\text{-}X)$ emission intensity, corrected for temperature induced concentration variations, as a function of flow time outside the second 85 W discharge for three 1st discharge powers.

The flow tube kinetics of oxygen discharges have been studied extensively, but almost always under conditions where the $O_2(b)$ concentration is controlled by the pooling reaction:

$$O_2(a) + O_2(a)^- \rightarrow O_2(b) + O_2(X)^- \qquad (2\text{-}27)$$
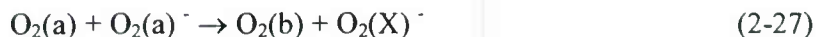
with rate coefficient, $k_{21} = 2.7 \times 10^{-17}$ cm^3/molecule-s. For a total $O_2(b)$ deactivation decay rate of Γ_b, the steady-state concentration is:

$$[O_2(b)] = \frac{k_{21}[O_2(a)]^2}{\Gamma_b} \qquad (2\text{-}28)$$

In Figure 2-53, the $O_2(b)$ and $O_2(a)$ intensities are correlated. The steady-state relation of equation (2-26) is demonstrated by the linear portion of the plot at the lower $O_2(b)$ concentrations. From the slope of the linear portion of the curve and the know pooling rate constant, an estimate for the $O_2(b)$ decay rate is established. The steady-state conditions are largely unaffected by the injection of excited oxygen into the discharge. A significant deviation from these conditions is observed just outside the discharge where the $O_2(b)$ concentration is much higher and, when excited oxygen is introduced to the second discharge, the $O_2(a)$ concentration increases. Note that the quantitative increase in $O_2(a)$ outside of the second discharge is consistent with the increase in steady-state $O_2(b)$ concentration far from the second discharge.
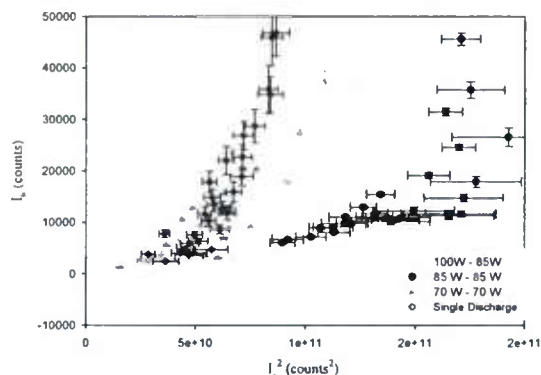
Figure 2–60. Emission intensities from $O_2(a)$ and $O_2(b)$ for discharge powers of ( ) 100 W- 85 W, ( ) 85 W – 85 W, ( ) 70 W– 70 W, and ( ) 0 W – 85 W. In (b) the scale is expanded to illustrate steady-state $O_2(b)$ concentrations.

Sets of data from double discharge experiments were extracted and plotted against the eV/particle data. It was found that maxima in the data for intensity and yield occurred between 1-5 eV. This is in agreement with some of the theoretical arguments presented later in this report. Since a few of these experimental yields approached the theoretical limits we believe that the theory is beginning to establish itself.
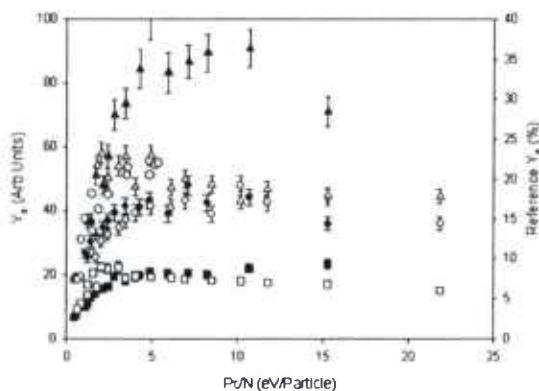
Figure 2–61. Arbitrary Intensity Units as a function of eV per particle.
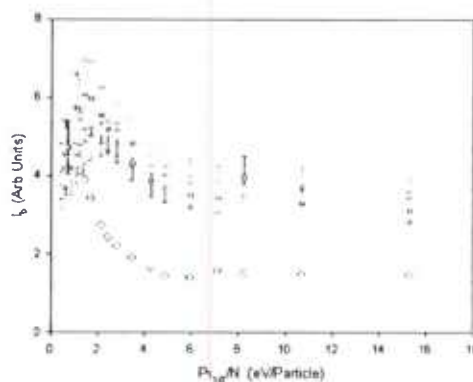
Figure 2–62. Relative yield data from double discharge as a function of eV per particle.

2.2.2.5 Preliminary Conclusions From Double Discharge Kinetic Study

The singlet oxygen, $O_2(a^1\Delta, b^1\Sigma)$, produced in a microwave discharge of pure molecular oxygen at modest flow rates provides an initial $O_2(b^1\Sigma)$ concentration that exceeds the steady-state concentration controlled by pooling by more than a factor of ten, reflecting significant discharge yields. When singlet molecular oxygen and atomic oxygen is introduced to the inlet of the second discharge, an increase in $O_2(a^1\Delta)$ is observed immediately outside of the discharge. The kinetic mechanism responsible for this production requires further study. If this production arises from relaxation from higher lying states, then a significant increase in singlet oxygen yield may be obtained if a selective relaxation collision partner were identified. Unfortunately, the sensitivity of singlet oxygen yields from a microwave discharge to the initial excited oxygen inlet conditions is low, suggesting a kinetic limitation to the microwave generator performance. Indeed, the production of $O_2(a, b)$ is likely countered by second order reactions whose rates increase as the singlet oxygen yield increases. In particular, the electron dissociation of $O_2(a, b)$

may be a critical limiting process. Uncovering this limitation is important to assessing the efficiency and scalability of the proposed ElectricOIL device.

2.3 Alternate Kinetic Paths With Plasma Discharge Products And Iodine (from Work at Emory U.)

Rate constant data for several key reactions are needed to guide the design and development of the ElectricOIL system. Many of the open questions concerning the reactions between the products from the discharge generator and the iodine atom precursor may be answered through experimental investigations of reaction kinetics. Table 2-6 lists several alternate kinetics paths between iodine and products from the plasma discharge that may be of importance in the post discharge fluids.

Table 2-6: Reactions used in the kinetic model of the $I_2/N_2/O_3$ + 266 nm photolysis system.

Reaction	Rate constant (cm^3 s^{-1})
$I+O_2(a)=I^*+O_2(X)$	$k = 7.6e-11$
$I^*+O_2(X)=I+O_2(a)$	$k = 2.6e-11$
$O(^1D)+N_2=O(^3P)+N_2$	$k = 2.6e-11$
$O(^3P)+I_2(X)=IO+I$	$k = 1.4e-10$
$O(^3P)+IO=O_2+I$	$k = 1.5e-10$
$I^*+O_3=I+O_3$	$k = 1.8e-12$
$I+O_3=IO+O_2$	$k = 9.6e-13$
$IO+IO=2 I+O_2$	$k = 8.0e-12$
$IO+IO= I+IO_2$	$k = 3.2e-11$
$I^*+I_2=I+I_2$	$k = 3.0e-11$
$I^*+O(^3P)=I+O(^3P)$	$k = 8.0e-12$
$O_2(a)+O_3=2O_2(X)+O$	$k = 4.0e-15$
$I^*+O_2(a)=I+O_2(b)$	$k = 2.20e-13$

2.3.1 Theoretical Approach and initial results: The quenching of I*

Theoretical methods for treating inelastic and reactive collisions have now reached the stage where quantitative predictions can be made for many small molecule reactions, provided that heavy atoms do not play an important role. The challenges faced in extending theory to molecules that involve heavy atoms are mostly associated with the increased density of electronic states and the need for adequate treatment of spin-orbit coupling. Methods for including spin-orbit coupling in electronic structure calculations and electronically non-adiabatic processes in nuclear dynamics are being investigated by several research groups. EU is participating in this effort through investigations of the I* + O = energy transfer process (a potential deactivation process for ElectricOIL) from a theoretical perspective [Kaledin, 1998; Kaledin, 2001]. It appears that there is a low-lying curve crossing indicating little or no temperature dependence for this reaction. Figures 2-42 and 2-43 show that high concentrations of $O(^3P)$ atoms are produced by discharge excitation. In one respect this may be beneficial, as O atoms will rapidly dissociate I_2, Table 2-6. This would reduce the need to inject atomic I, provided that I* is not rapidly quenched by O. It may be possible to estimate how efficient the quenching may be from inspection of the potential energy curves that correlate with the O+I* and O+I dissociation asymptotes, Fig. 2-63. Roszak et al. [Roszak, 2000] recently calculated a

sub-set of the relevant potential curves. Their results and ours show avoided curve crossings that are likely to facilitate quenching of I*. Clearly it will be of critical importance to measure the rate constant for the process of the I* + O reaction. Recent experimental studies at EU, see below, show this process to be moderate, so the oxygen atoms in ElectricOIL can be useful for I_2 dissociation.
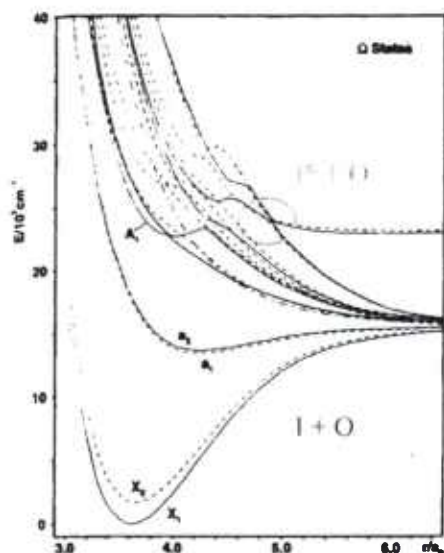
Figure 2–63. Potential energy curves for the lowest electronic states of IO radical calculated including spin orbit coupling.

A high-level quantum chemical method including spin-orbital coupling with Davidson correction is used to study the quenching mechanism of the I* + O system. The previous calculations performed have had some errors and we have performed a recalculation. The potential energy surfaces of 33 lowest (doublet and quartet) states that correlate to ^2P state of I and ^3P and ^1D states of O, have been calculated. Complex avoided crossing patters are found among 84 spin-orbital states, as illustrated for $\Omega=1/2$ states in Fig 2-63. Four important crossings between two spin-orbital states coming from two experimentally interested asymptotes, $I(^2P_{3/2})+O(^3P)$ and $I(^2P_{1/2})+O(^3P)$. Work continues to try to elucidate the nature of the curve crossings in this important system.

1. Ab initio potential energy surfaces of $O_2(X, a$ and $b) + O_2(X, a$ and b): Mechanism of quenching of O_2 (a).

Ab initio computational studies were carried out in order to explore the possible mechanisms of quenching of $O_2(a)$ by $O_2(X)$, the self-quenching of O_2 (a) and other energy transfer processes involving two O_2 molecules. All eighteen states arising from two O_2 molecules in the X, a and b states are considered. After scans at the SA-CASSCF (state-averaged complete active space self-consistent field) method to identify possible regions of crossing between states belonging to different asymptotes, CASPT2 (complete active state second order perturbation theory) high-symmetry optimization and low symmetry scans established that four different minima on the seams of crossing (MSXs), arising between the a+a manifold and the X+b manifold and responsible for self-quenching: O_2 (a) + O_2 (a) → $O_2(X)$ + $O_2(b)$, have coplanar C_{2h} or C_{2v} symmetries and are only 0.45 eV barrier relative to the a+a asymptote and energetically easily accessible. The rate constant for this process was estimated based on the Landau-Zener

formalism. The MSXs for quenching of O_2 $(a^1\Delta_g)$ by the ground state $O_2(X)$: O_2 (a) + $O_2(X) \rightarrow$ $O_2(X) + O_2(X)$ require higher energies to reach, and the process is not likely to be important.

2. Analytical potential functions for the self-quenching process: O_2 (a) + O_2 (a) $\rightarrow$ $O_2(X)$ + $O_2(b)$.

Ab initio potential energy surfaces of over 2000 gemeotries points of the $[O_2]_2$ system that connnect to the dissociation limits of O_2 (a) + O_2 (a) and $O_2(X)$ + $O_2(b)$ have been fit to various forms of analytical functions. The paper on the fitted potential surfaces is in preparation.

3. Electronic quenching conveyed on two crossed states: A 6-D time dependent wave packet study for the collision of two electronically excited $O_2(a^1\Delta_g)$ molecules.

We have performed a 6-dimension multiple state time dependent wave packet (TDWP) calculation to study the process of electronic quenching for the collision of

$$O_2(a^1\Delta_g) + O_2(a^1\Delta_g) \rightarrow O_2(b^1\Sigma_g^+) + O_2(X^3\Sigma_g^-). \tag{2-29}$$
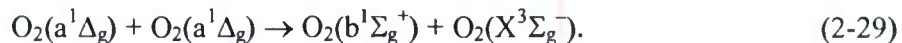
This involves two close-by electronic states, and a spin orbit coupling term, assumed to be constant in the preliminary calculation. The multiple state TDWP method is developed based on the legendary single state TDWP program (Dynasol) of Prof. John Z. H. Zhang. We exactly follow all procedures of the original Dynasol code, and add a coupling matrix, expressed in an analytical form, to include the effect of nonadiabatic couplings between two electronic states. A large basis set is used to expand the nuclear wavefunctions for both of the ground and excited electronic states. As shown in Fig. 2-64, a wave packet analysis shows the quenching process proceeds more efficiently in the repulsive part of the potential energy surface (PES), near the curve crossing regions. This enhanced quenching process can be explained by the fact that the wave packet tends to spend more time (less kinetic energy) in the repulsive part of the PES, which happened to be close to the region, where two PESs cross. The work is still in progress.
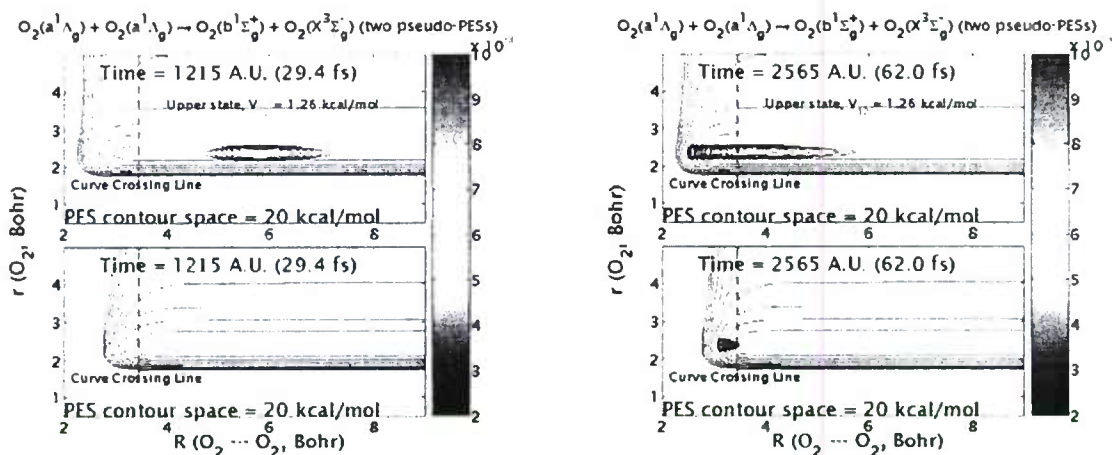
Fig. 2–64. Snapshots of time dependent wave packet propagated on two pseudo-PESs. (Left panel: T = 1215 au. Right panel: 2565 au.) The electronic quenching proceeds more efficiently on the repulsive part of the PES, close to the region where two PESs cross.

4. Theoretical study of dissociative attachment of oxygen molecule

We have theretically studied reactions associated with electron scattering by oxygen molecule. Here, we are specifically interested in dissociative attachment reaction.

$$O_2(X) + e \rightarrow O + O^-. \tag{2-30}$$

Although there is a theoretical work on this subject in 1967, it was based on crude approximations with empirically fitted parameters. In order to interpret the experimental results as well as to predict details on this reaction, we need to apply more sophisticated theory. In this work, we employ the R-matrix formulation for the dissociative attachment of electron, originally proposed in 1979. Since the R-matrix formulation for rigid molecule has been successfully applied to many electron-molecule scattering processes, the R-matrix theory for dissociative attachment can be expected to work fine as well. In this work, we used a modified version of UK R-matrix program suite, developed by Prof. Tennyson in University College London. First, we prepared molecular orbitals of neutral O_2 by state-averaged CASSCF calculations on different internuclear distances. Then, diffuse functions representing a continuum electron were placed at the middle point of O_2 bond, and augmented to neutral molecular orbitals to construct 19 electron R-matrix states inside an R-matrix sphere. Vibrational calculation on these R-matrix states gives cross sections for vibrational excitation as well as dissociative attachment cross sections. In Figure 2-65, we show a preliminary result for dissociative attachment cross sections for different initial O_2 vibrational states.
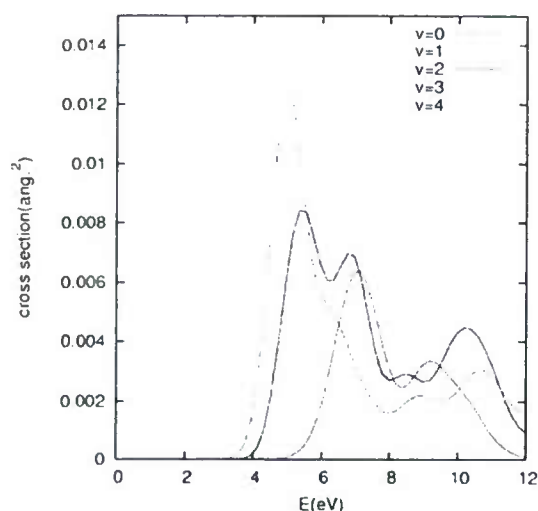
Figure 2–65. Dissociative attachment cross sections for different initial O_2 vibrational states.

2.3.2 Experimental: Kinetics of $O_2(a^1\Delta_g)$ and $I(^2P_{1/2})$ in the photochemistry of N_2O/I_2 mixtures

2.3.2.1 Introduction

Reactions between O atoms and iodine containing molecules have been characterized previously due to the participation of these processes in the chemistry of the atmosphere, [Bedjanian, 2003; Carlos 2005; Stutz, 1999]. Additional motivation for studies of these reactions has been provided recently by the demonstration of an oxygen-iodine laser (OIL) that is powered by electric discharge excitation of O_2 [Carroll, 2005a,b,c]. The central reaction in the OIL system is energy transfer from singlet oxygen to atomic iodine

$$O_2(a^1\Delta_g) + I(^2P_{3/2}) \rightarrow O_2(X^3\Sigma_g^-) + I(^2P_{1/2}) \tag{2-31}$$
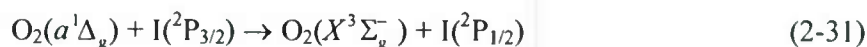
The laser operates on the $I(^2P_{1/2}) \rightarrow I(^2P_{3/2})$ transition at 1315 nm. In the following $I(^2P_{1/2})$, $I(^2P_{3/2})$ and $O_2(a^1\Delta_g)$ are designated by I*, I and $O_2(a)$ respectively. The chemical kinetics of the electric discharge OIL (EOIL) are significantly different from those of the better-known chemical oxygen-iodine laser (COIL) [Han, 2004; Heaven, 2001; Perram, 1995]. This difference arises due to the presence of O atoms in the flow from a discharge singlet oxygen generator. Oxygen atoms are not produced in the chemical generation of $O_2(a)$ but they are present in the flow from a conventional discharge to the extent that the concentrations of $O_2(a)$ and O are comparable [Palla, 2006]. The O atoms have a deleterious effect in the laser system and their removal by the reaction

$$O + NO_2 \rightarrow O_2 + NO \tag{2-32}$$

was the key to achieving lasing in EOIL. It was postulated that the most important negative effect of the O atoms was the quenching process

$$I* + O \rightarrow I + O \tag{2-33}$$

In a related earlier study, Zolotarev and co-workers [1989, 1991] concluded that the presence of O atoms was responsible for the low efficiency of an OIL system that was powered by photolysis of O_3.

Attempts to measure the rate constant for reaction (2-33) have resulted in values ranging from $<2 \times 10^{-12}$ to 1.2×10^{-11} cm^3 s^{-1}. Han et al.[2004] used photolysis of $CF_3I/X/N_2O$ and $I_2/X/N_2O$ mixtures (with $X=CO_2$ or N_2) to investigate reaction (2-33). The reaction scheme for the I_2 mixtures was as follows

$$N_2O + h\nu \rightarrow N_2 + O(^1D) \tag{2-34}$$
$$O(^1D) + X \rightarrow O(^3P) + X \tag{2-35}$$
$$O(^1D) + N_2O \rightarrow NO + NO \tag{2-36a}$$
$$\rightarrow N_2 + O_2(a, X) \tag{2-36b}$$
$$\rightarrow O(^3P) + N_2O \tag{2-36c}$$
$$O + I_2 \rightarrow I + IO \tag{2-37}$$
$$O + IO \rightarrow O_2 + I \tag{2-38}$$
$$O_2(a) + I \rightarrow O_2(X) + I^* \tag{2-39}$$

Reactions (2-37) and (2-38) have near gas kinetic rate constants ($k_7=1.4 \times 10^{-10}$, $k_8=1.5 \times 10^{-10}$ cm^3 s^{-1}) so I_2 was rapidly converted to I atoms in the presence of excess O. The kinetics of this system was followed by recording the time-resolved fluorescence from I*. Provided that the O atom concentration was sufficiently high, conditions could be achieved where the long-time fluorescence decay was dominated by reaction 3. Using this approach Han et al.[2004] obtained an upper bound for the rate constant of $k_3 < 2 \times 10^{-12}$ cm^3 s^{-1}. This was in conflict with the results from a flow tube study [Rawlins, 2005] and modeling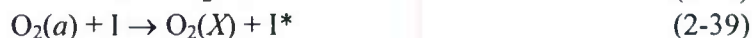 of EOIL[Palla, 2006] which indicated a rate constant near 10^{-11} cm^3 s^{-1}. Very recently, Azyazov et al.[2006] used photolysis of $O_3/N_2/I_2$ mixtures to examine reaction (2-33). They obtained a value of 1.2×10^{-11} cm^3 s^{-1}. The accumulated evidence suggests that there were problems with the previous N_2O photolysis experiments. However, if the $k_3 < 2 \times 10^{-12}$ cm^3 s^{-1} upper bound for the rate constant was correct it is possible that quenching processes that involved the products of O atom chemistry could give the appearance of rapid quenching by O. The present study was carried out in order to resolve this uncertainty and provide an accurate value of the rate constant for reaction 3. The kinetics of the $I_2/X/N_2O$ system were examined in greater detail by tracking multiple species (I*, I_2, and IO).

The yield of O atoms from N_2O photolysis is of central importance in using the $I_2/X/N_2O$ system to study quenching by O atoms. UV photolysis of N_2O has been widely used as a source of electronically excited oxygen atoms $O(^1D)$, and the photodissociation dynamics of N_2O is of fundamental interest. The reaction of the $O(^1D)$ photofragment with N_2O has three product channels, defined by equations (2-36a), (2-36b), and (2-36c) above. It has been extensively studied because one of the products, the NO molecule, plays a role in the depletion of ozone Marx et al.[1979] and Lam et al.[1981] reported branching ratios of 0.62 for channel (2-36a) and 0.38 for (2-36b) using photolysis at 184.9 and 206.2 nm. Nishida et al.[2004] measured the branching ratio of $O(^3P)$ formation in process (2-36) to be 0.04 using vacuum-ultraviolet laser induced fluorescence spectroscopy around 130 nm. The IUPAC subcommittee recommends the branching ratio for channel (2-36c) < 0.0086 based on an extensive literature review [Atkinson, 1997]

Spin-correlation rules and *ab initio* calculations [Gonzales, 2001] for $O(^1D) + N_2O(X^1\Sigma)$ predict that singlet oxygen is the product of reaction (2-36b), but there has been no direct experimental verification of this expectation. The experiments of Han et al.[2004] provide indirect evidence that $O_2(a)$ is formed. As noted above, they observed I* luminescence when $N_2O/CO_2/CF_3I$ or

$N_2O/N_2/CF_3I$ mixtures were photolyzed using at 193 nm light, and it was clear from the time-evolution that I* was being formed by secondary reactions. In attempts to improve the performance of the OIL powered by O_3 photolysis, Zolotarev et al. tested the use of N_2O, N_2 and/or CO_2 as reagents for the removal of $O(^1D)$, and the best results were obtained for N_2O. Zolotarev et al. concluded that an increase in laser power was achieved due to the fact that N_2O consumes oxygen atoms in process (2-36)and that $O_2(a)$ is produced by reaction 6b. Note that the yield of $O_2(a)$ from reaction (2-36b)is also of interest from the perspective of atmospheric chemistry. The O_2 a-X emission system is the most intense feature in the Earth's airglow spectrum, and under certain conditions reaction (2-36b)could contribute significantly to $O_2(a)$ formation.

To minimize the negative effect of $O(^3P)$ atoms on the performance of EOIL, NO_2 has been added into the post-discharge oxygen to scavenge excess of oxygen atoms[Carroll,2005]. In modeling this system Zimmermann et al.[2006] found that the improvement in the I* concentration could not be explained by the removal of O atoms alone. An additional source of $O_2(a)$ was needed to achieve agreement with the observed behavior. They speculated that the reaction

$$O(^3P) + NO_2 \rightarrow O_2(a) + NO \qquad (2\text{-}40)$$

may be a contributing factor. Production of $O_2(a)$ by this process had not been reported previously. In the present study we have searched for evidence of this reaction.

The measurements reported here began with an investigation of the yield of $O_2(a)$ in reaction (2-36b). In this work photolysis of O_3 was used as means to calibrate the detector used to measure $O_2(a)$ concentrations. The yield of $O_2(a)$ from reaction (2-36b) was then determined using photolysis of N_2O/Ar mixtures. Quenching of I* by $O(^3P)$ was examined using photolysis of $N_2O/CO_2/I_2/Ar$ mixtures. The kinetics of $I_2(X)$ removal and IO generation were used to characterize the O atom concentrations. Lastly, photolysis of NO_2 was used to search for evidence of reaction (2-40).

2.3.2.2 Discussion
It was found that the O_2 produced by the reaction of $O(^1D)$ with N_2O is almost entirely $O_2(a)$, as expected on the basis of spin correlation rules. Hence, the branching fraction for reaction 6b (0.38) is also the branching fraction for production of $O_2(a)$ from reaction 6. The relatively high yield of $O_2(a)$ raises the possibility that reaction 6 may contribute to the Earth's airglow. Confirmation that $O_2(a)$ is produced by $O(^1D)+N_2O$ also explains the results of Zolotarev et al. who found that adding N_2O to I_2/O_3 mixtures improved the performance of the photolysis initiated laser. It will be of interest to re-evaluate the potential of this type of device using the branching fraction and rate constant data determined in this study, See Table 2-7, below.

The rate constant for quenching of I* by $O(^3P)$ obtained in this work was in excellent agreement with the results from a study of $I_2/O_3/X$ photochemistry. It is also in agreement with estimates for k_3 obtained by modeling EOIL device performance. However, these results did not agree with earlier work from our laboratory, where studies of the $N_2O/I_2/X$ photochemistry yielded an upper bound for k_3 of $<2x10^{-12}$ cm^3 s^{-1}. It is difficult to pin point the problems with the earlier experiments, but it seems likely that the estimates of the O atom concentrations were in error. These densities were estimated on the basis of the absorbed energy, without the additional cross checks provided by observing the I_2 and IO kinetics.

The large rate constant for quenching of I* by $O(^3P)$ suggests that a Landau-Zener curve-crossing mechanism is involved. This is similar to the situation for quenching of I* by $Cl(^2P)$ which occurs with a room temperature rate constant of 1.5×10^{-11} cm^3 s^{-1} [Kamissarov, 2003] In the case of I*+Cl it was possible to identify the specific curve crossing that dominated the quenching process using the results from high-level theoretical calculations[Kamissarov, 2003] . Ab initio potential energy curves for I+O and I*+O were reported by Roszak et al. Figures 2 and 3 in their paper show several avoided crossings (which become curve crossings in a diabatic representation) that could be responsible for the fast quenching.

The deleterious effect of O atoms on the discharge driven oxygen iodine laser are clearly seen to be a consequence of the direct quenching of I* by O atoms. The addition of NO_2 to the post-discharge oxygen flow improves the laser by scavenging O, but there is no evidence to support the tentative suggestion that $O_2(a)$ is generated during the scavenging process. The present measurements show that the yield of $O_2(a)$ from $O+NO_2$ is insignificant. There is, however, another way in which removal of O atoms may benefit the laser. Vasiljeva,[2004] have reported that the three-body quenching process $O+O_2(a)+O_2 \rightarrow 2O_2+O$ occurs with a rate constant of approximately 10^{-32} cm^6 s^{-1}. Hence, removal of the O atoms may also decrease the rate of $O_2(a)$ deactivation.

Since I* is moderately quenched by O atoms we will need to assess the viability of methods for optimizing O from the flow prior to I_2/I injection. One possibility would be to add NO_2 to the flow that exits from the generator. This will remove O atoms [Clyne, 1979]. Quenching of I* by NO is known to be inefficient ($k=1.2 \times 10^{-13}$ cm^3 s^{-1}) [Grimley, 1978]. For partial removal of O atoms it would be advantageous to operate under conditions where $[NO_2]\sim[O]$. This would be viable provided that quenching of I* by NO_2 is slow. As this process has not yet been examined, we will use pulsed photolysis methods to measure the I*+NO_2 quenching rate constant.

Table 2-7. Rate constants used in the kinetic model for $N_2O/I_2/CO_2$ photochemistry at T=300 K.

Reaction	Rate constant cm^3/s	Ref
6a, $O(^1D)+N_2O \rightarrow NO+NO$	7.2×10^{-11}	21
6b, $O(^1D)+N_2O \rightarrow O_2(a)+N_2$	4.4×10^{-11}	21
6c, $O(^1D)+N_2O \rightarrow O(^3P)+N_2O$	1×10^{-12}	21
1, $I+O_2(a) \rightarrow I*+O_2(X)$	7.6×10^{-11}	10
17, $I*+O_2(X) \rightarrow I+O_2(a)$	2.7×10^{-11}	10
7, $O+I_2 \rightarrow I +IO$	1.4×10^{-10}	16
8, $O+IO \rightarrow O_2+I$	1.5×10^{-10}	16
3, $I*+O(^3P) \rightarrow I+O(^3P)$	1.2×10^{-11}	this work
5, $O(^1D)+CO_2 \rightarrow O(^3P)+CO_2$	1.3×10^{-10}	21
5, $O(^1D)+Ar \rightarrow O(^3P)+Ar$	5×10^{-13}	21
16, $I*+I_2 \rightarrow I+I_2$	3.8×10^{-11}	10
18, $IO+IO \rightarrow products$	9.9×10^{-11}	31
19, $IO+NO \rightarrow I+NO_2$	1.95×10^{-11}	31
$I*+O_2(a) \rightarrow I+O_2(b)$	1.1×10^{-13}	10
$I*+O_2(a) \rightarrow I+O_2(a)$	1.1×10^{-13}	10
$I*+N_2O \rightarrow I+N_2O$	2.1×10^{-15}	30

2, $O(^3P)+NO_2 \rightarrow NO+O_2$ 9.7×10^{-12} 21

Computational models show that injection of dissociated iodine into conventional COIL and ElectricOIL systems will improve the output power significantly. A similar effect can be obtained for ElectricOIL if O atoms can be tolerated in the laser cavity. We will further investigate the merits of these schemes through studies of reaction kinetics. The proposed study of I^*+NO_2 quenching is also relevant to ElectricOIL since NO_2 is being used to scavenge O atoms in the present UIUC/CUA experiments.

2.3.3. Comment on mechanism for dissociation of I_2 by $O_2(b)$ for COIL and EOIL Lasers

The problem of I_2 dissociation plays a role in both COIL and ElectricOIL Hybrid Lasers systems and needs to be elucidated (see mechanism below). Computational design optimization of these systems is limited by our inability to predict the dissociation kinetics for conditions that lie outside of the conventional operating range. A major problem is that $O_2(a, v=0) + I_2 \rightarrow O_2(X) + I_2(v>20)$ is too slow to be the initiation step as is usually assumed. Other issues do not bode well for the classic dissociation mechanism including the, now known, relatively rapid reaction of $O_2(b)$ with I_2.

7	O2 generator
8	walls
9	I2 nozzles
10	channel
11	platform
12	director
13	optical fiber
14	monochromator
15	PMT
16	amplifier
17	PC
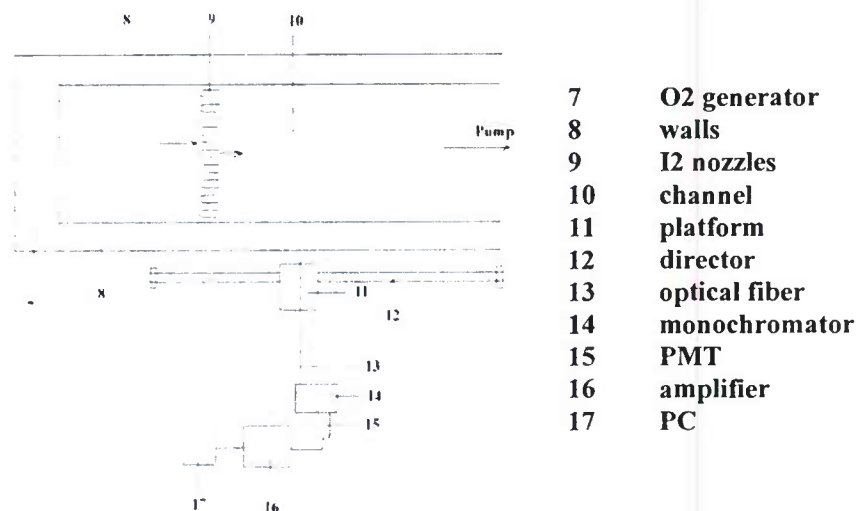
Figure 2–66. Low pressure Flow Cell and identifying Key.

Recent studies of the mechanism by which $O_2(a)$ dissociates I_2 indicate that metastable electronic states of I_2 (e.g., $I_2(A, A')$) are important intermediates [Kommisarov, 2001; Heaven, 2001b]. These metastables carry enough energy for $I_2(A, A')$ to be dissociated by a single collision with $O_2(a)$. Hence it may be possible to enhance the efficiency of ElectricOIL (and COIL) by injecting $I_2(A, A')$ into the primary flow. Electric discharges are very effective in generating $I_2(A, A')$ and have been used in spectroscopic studies of these metastables. By establishing a corona discharge at the mouth of an injector it may be possible to inject $I_2(A, A')$ with minimal losses due to wall deactivation processes (the discharge would penetrate a short distance into the primary flow). To see if this approach has any real merit we need to validate and further characterize the electronic excitation-dissociation model. We will begin by examining the deactivation of $I_2(A')$ by $O_2(X)$ and H_2O. The population of vibrationally excited $I_2(X)$ levels

will be monitored by laser excitation of the B-X and D-X transitions. These measurements will provide the information needed to assess the extent to which electronically metastable I_2 is involved in the dissociation process. Subsequently we will characterize the kinetics of $I_2(A)$. A tunable pulsed dye laser will be used to excite a specific ro-vibrational level of $I_2(A)$ via the A-X transition. After a fixed delay, pulses from a second tunable laser (probe) will be used to examine the population distributions in the A and A' states. The β-A and D'-A' transitions will be used for this purpose. The delay and gas pressures will be chosen such that the excited molecules will experience an average of one collision occurring during the delay between pump and probe lasers (near single collision conditions). The collision partners to be investigated are He, Ar, $O_2(X)$ and H_2O. These measurements will permit determination of the rate constants for transfer between the A and A' state vibrational manifolds, the rate constants for relaxation within the manifolds, and the total removal rate constants.

2.3.3.1 Energy Transfer Between $O_2(a, b)$ and I_2

Because of the importance of the energy transfer steps $O_2(a, b)$ to I_2 a separate study was conducted to examine some of the conventional mechanisms in use. The workers at Emory University excite the individual states of oxygen using direct laser excitation. The apparatus for the study is shown below in Fig. 2-67.
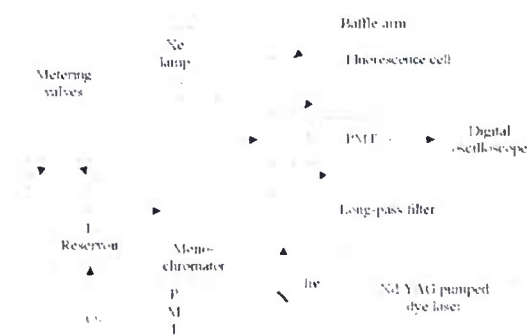
Figure 2–67.   Apparatus Used to Study the Quenching of $O_2(a)$ and $O_2(b)$.

The standard dissociation mechanism for I_2 in the presence of $O_2(a)$ is given below. EU choose to study the dissociation in the presence of both $O_2(b)$ and $O_2(b)$ since both are important in ElectricOIL. We are fairly sure that some of the rates in this scheme are inaccurate and because the kinetic model requires an upper bound on the rate constant for quenching of $O_2(a)$ by I_2 of 5×10^{-16} cm^3 s^{-1}. The standard model for I_2 dissociation in COIL assumes that the energy transfer process,

$$O_2(a)+I_2 \rightarrow O_2(X)+I_2(X,v>20), \tag{2-41}$$

occurs with a rate constant of $\mathbf{7\times10^{-15}}$ **cm^3 s^{-1}**. Clearly the upper bound for the quenching rate constant is inconsistent with the usually assumed energy transfer rate. The strong implication is that the $O_2(a)+I_2$ step must not be the initiation step in the chain dissociation process. Detailed rate constants for the pertinent processes are furnished in Table 2-8 and Table 2-9.

Standard Dissociation Model

$$O_2(a) + I_2 \rightarrow O_2(X) + I_2(v>20) \qquad\qquad \text{Initiation} \qquad (2\text{-}42)$$

$$O_2(a) + I \rightarrow O_2(X) + I^* \qquad \text{Energy transfer} \qquad (2\text{-}43)$$

$$I^* + I_2 \rightarrow I + I_2(v>20) \qquad \text{Chain propagation} \qquad (2\text{-}44)$$

$$I_2(v>20) + M \rightarrow I_2 + M \qquad \text{Deactivation} \qquad (2\text{-}45)$$
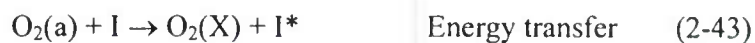
$$\text{Where M=He, } H_2O, O_2(X)$$

Table 2-8. Reactions used in the kinetic model of the $O_2(a)+ I_2(X)$ quenching measurements. † a in units of cm^3/s unless otherwise indicated

Reaction	Process	Rate Constant, $a^\dagger$
2-46	$I_2 + hv \rightarrow 2I$	1.4×10^{-10}
2-47	$I + I + O_2(X) \rightarrow O_2(a) + I_2$	$f10(3.7 \times 10^{-32})\ cm^6 s^{-1}$
2-48	$\rightarrow O_2(X) + I_2$	$(1\text{-}f10)\,(3.7 \times 10\text{-}32)\ cm^6 s^{-1}$
2-49	$O_2(a) + I \rightarrow O_2(X) + I^*$	7.8×10^{-11}
2-50	$O_2(X) + I^* \rightarrow O_2(a) + I$	2.6×10^{-11}
2-51	$I^* + I_2 \rightarrow I + I_2$	0.5×10^{-11}
2-52	$O_2(a) + O_2(X) \rightarrow 2O_2(X)$	8.2×10^{-19} (this work)
2-53	$O_2(a) + I_2 \rightarrow O2(X) + I_2$	$k12 < 5 \times 10^{-16}$
2-54	$O_2(a) \rightarrow O_2(X) + hv'$	$2 \times 10^{-4}\ s^{-1}$
2-55	$I^* \rightarrow I + hv''$	$7.8\ s^{-1}$

Table 2-9. Additional reactions used in the kinetic model of the $O_2(a) + I_2(X)$ quenching measurements.

No	Reaction	Rate constant cm^3/s
9	$O_2(b) + CO_2 \rightarrow O_2(a,v) + CO_2(v')$	4.2×10^{-13}
28	$I_2(A') + O_2(X) \rightarrow I_2(X) + O_2(a)$	6.3×10^{-12}
29.1	$I_2(A') + H_2O \rightarrow I_2(X) + H_2O$	3.4×10^{-12}
29.2	$I_2(A') + N_2 \rightarrow I_2(X) + N_2$	3.5×10^{-12}
29.3	$I_2(A') + CO_2 \rightarrow I_2(X) + CO_2$	8.5×10^{-13}
29.4	$I_2(A') + He \rightarrow I_2(X) + He$	9.4×10^{-15}
70	$O_2(v) + O_2 \rightarrow O_2(v\text{-}1) + O_2$	8.2×10^{-19}
71	$O_2(v) + H_2O \rightarrow O_2(v\text{-}1) + H_2O$	8.2×10^{-17}
72	$O_2(v) + He \rightarrow O_2(v\text{-}1) + He$	0
73	$O_2(v) + N_2 \rightarrow O_2(v\text{-}1) + N_2$	0
76	$O_2(X,2) + O_2(X,0) \rightarrow O_2(X,1) + O_2(X,1)$	1.3×10^{-13}
77	$O_2(X,3) + O_2(X,0) \rightarrow O_2(X,2) + O_2(X,1)$	1.9×10^{-13}
78	$O_2(X,4) + O_2(X,0) \rightarrow O_2(X,3) + O_2(X,1)$	2×10^{-13}
79	$O_2(a,1) + CO_2 \rightarrow O_2(a,0) + CO_2(v)$	1.8×10^{-14}
80	$O_2(a,2) + CO_2 \rightarrow O_2(a,1) + CO_2(v)$	4.4×10^{-14}
81	$O_2(a,3) + CO_2 \rightarrow O_2(a,2) + CO_2(v)$	1.0×10^{-13}
82	$O_2(b,1) + CO_2 \rightarrow O_2(b,0) + CO_2(v)$	1.2×10^{-12}
83	$O_2(b,2) + CO_2 \rightarrow O_2(b,1) + CO_2(v)$	1.7×10^{-12}
84	$O_2(b,3) + CO_2 \rightarrow O_2(b,2) + CO_2(v)$	1.6×10^{-12}
85	$O_2(X,1) + H_2O(000) \rightarrow O_2(X,0) + H_2O(010)$	1.7×10^{-12}
89	$O_2(a,1) + O_2(X,0) \rightarrow O_2(X,1) + O_2(a,0)$	5.6×10^{-11}
90	$O_2(a,2) + O_2(X,0) \rightarrow O_2(X,2) + O_2(a,0)$	3.6×10^{-11}
91	$O_2(b,1) + O_2(X,0) \rightarrow O_2(X,1) + O_2(b,0)$	1.52×10^{-11}
92	$O_2(b,2) + O_2(X,0) \rightarrow O_2(X,2) + O_2(b,0)$	1.7×10^{-12}
93	$O_2(b,3) + O_2(X,0) \rightarrow O_2(X,3) + O_2(b,0)$	1.5×10^{-13}
94	$H_2O(010) + H_2O \rightarrow H_2O(000) + H_2O$	5×10^{-11}
95	$O_2(a,1) + I_2(X) \rightarrow O_2(X) + I_2(A')$	2×10^{-12}
96	$O_2(a,2) + I_2(X) \rightarrow O_2(X) + I_2(A)$	3×10^{-11}
97	$O_2(a,3) + I_2(X) \rightarrow O_2(X) + I + I$	10^{-11}

The individual rates of energy transfer to I_2 are determined by quenching of the states in the presence of excess iodine. In the case of the "b" state the decay data are found in the following plots, Figs. 2-68 and 2-69. It was found that the energy transfer rates for "b" state into iodine molecule were a medium fast reaction and will need to be part of any mechanism which involves electrical generation. Thus,

$$O_2(b) + I_2 \rightarrow O_2(X)^* + I_2^*, \tag{2-46}$$

where $O_2(X)^*$ represents the sum of vibrationally excited oxygen and whatever is partitioned into the "a" state. Note that some of the energy is released in terms of vibrationally excited iodine.
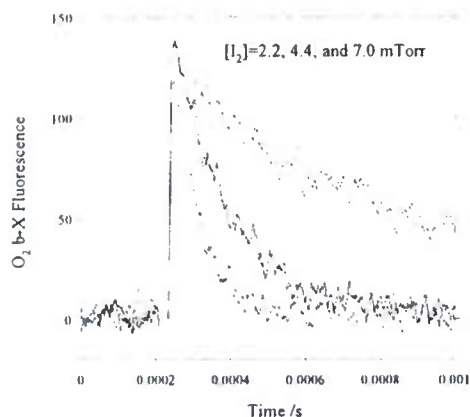
Figure 2–68. Curves for quenching of $O_2(b)$ by $I_2(X)$
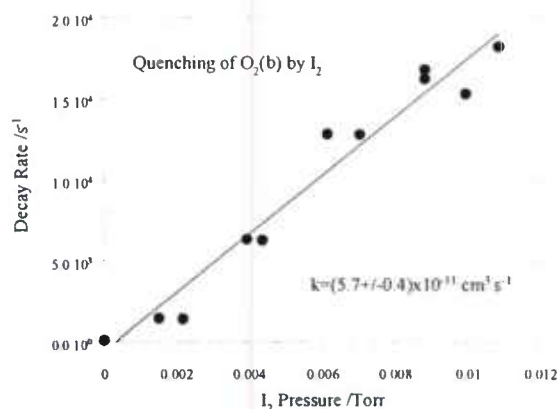
Figure 2–69. Quenching rate constant for $O_2(b)$ by $I_2(X)$.

A table containing our most recent estimates for the energy transfer among $O_2(a)$, and iodine species appears below (Table 2-8 and Table 2-9). The key point is that the rate constant for the first step in the excitation of iodine atom by $O_2(a)$ is probably too slow to be the first step in the dissociation of iodine molecules. This is most interesting, since most mechanisms use this as the initiation step for the transfer of energy into $I_2(X)$. Using the apparatus illustrated in Figure 2-70 The workers at Emory University measured the rate constant for energy transfer (See Fig. 2-71) and find it too slow. The rate constant, $k=5.7\times10^{-11}$ cm^3 s^{-1}, with the branching fraction of 0.4 (measured in this work) for energy transfer from $O_2(b)$ is sufficient to be the initiation step.
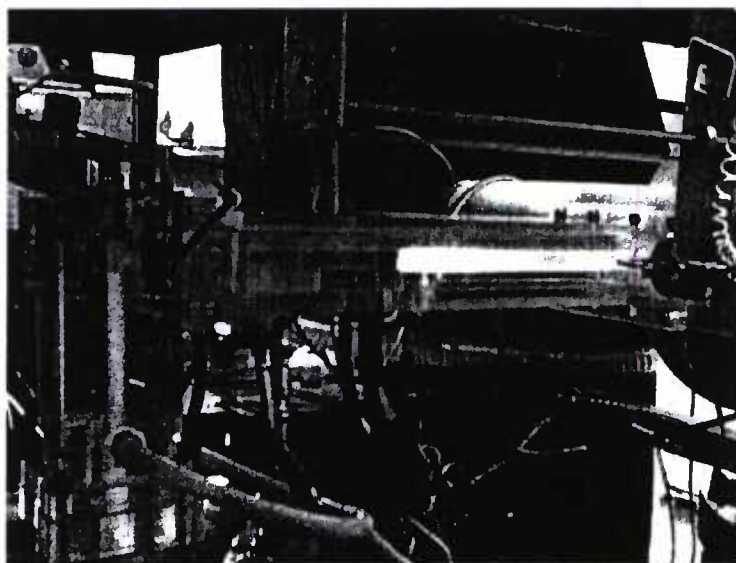
Figure 2–70. Emission Spectoscopy Measurements.
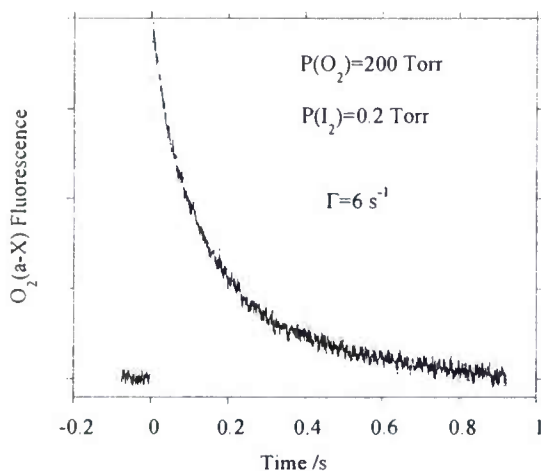
Figure 2–71. Rate measurement for quenching of $O_2(a)$ by I_2 of $7x10^{-15}[I_2]=45$ s^{-1} is too slow to be the initiation step.

However, recent work which show that initiation is unaffected by the presence of CO_2 which destroys $O_2(b)$, Fig. 2-72 and 2-73. So, this appears to rule out the principle species $O_2(b)$ as being, in the main, responsible for initiation.
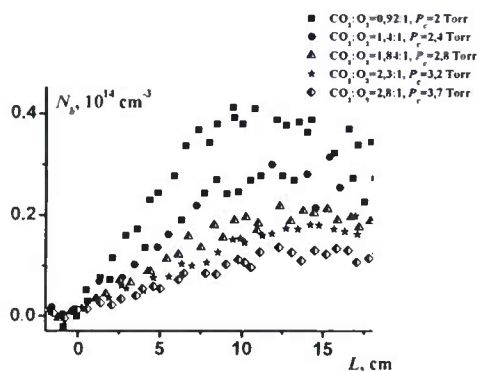
Figure 2–72. Quenching of $O_2(b)$ by CO2
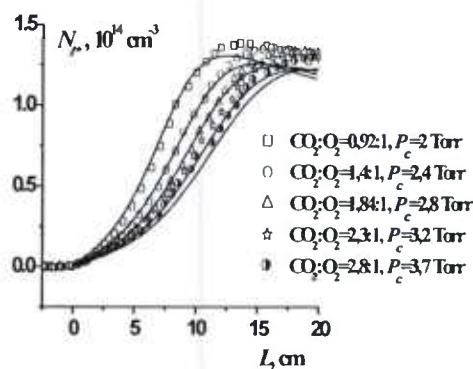
Figure 2–73. Quenching of I* by CO2

This fact seems to be confirmed when H_2O is added to the fluid stream, Fig. 2-74, where water deactivates the "b" state without affecting the I* distribution.
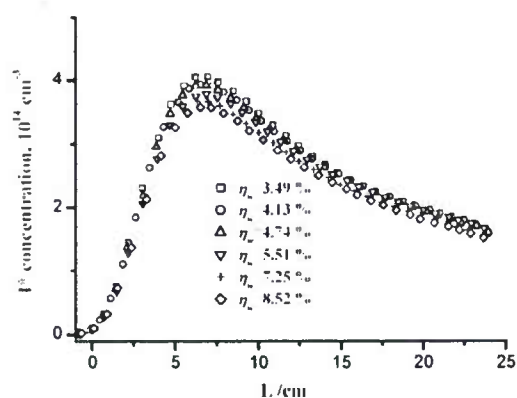
Figure 2–74. Quenching of I* by water

Kinetic modeling of the flow tube results also indicates that direct dissociation of I_2 by $O_2(b)$ cannot provide the primary dissociation channel, or the initiation of the chain sequence.

Taking into account all the facts, the Emory workers suggest a new chain initiation for the Iodine laser system as follows:

Initiation

$$O_2(a, v=2)+I_2 \rightarrow O_2 (X) + I_2(A')$$ (2-47)

Propagation

$$I^* + I_2 \rightarrow I + I_2 (v>10)$$ (2-48)

$$I_2 (v>10)+ O_2(a) \rightarrow I_2 (A',A)+ O_2(X)$$ (2-49)

Dissociation

$$I_2 (A',A)+ O_2(a) \rightarrow 2I+ O_2(X)$$ (2-50)
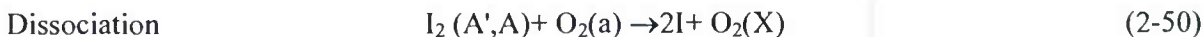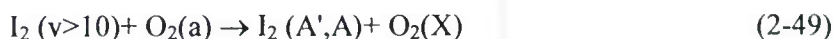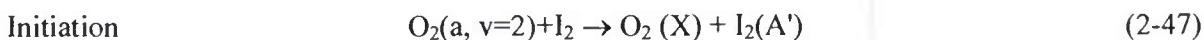
where the number of $O_2(a)$ molecules required to dissociate I_2 is 3 or greater.

These observations are consistent with all the observations of which we are aware and in particular explains the rather large number of molecules of $O_2(a)$ required in dissociation and pumping of the atomic iodine (Considerable modeling of data from COIL laser experiments should be done to confirm these findings).

Are electronically excited states of I_2 important in the dissociation mechanism? Let us consider the B states first since strong I_2 B-X emission is observed, and ask the question, "Is $I_2(B)$ a significant intermediate?" If one looks at the considerable quenching of the "B" state, Figure 2-75 and 2-76, one concludes that $I_2(B)$ it is probably not involved directly in the energy transfer scheme.
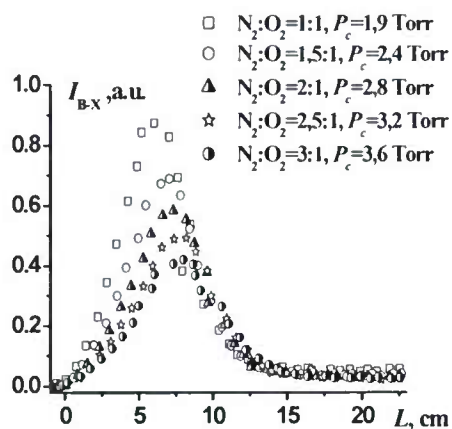
Figure 2–75. I_{B-x} Transition Quenching with N_2.
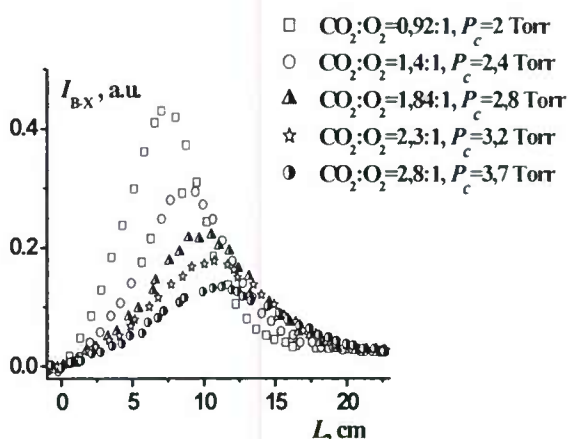
Figure 2–76. I_{B-x} Transition Transition Quenching with CO_2.

Involvement of low lying $I_2(A'_3P_2)$ and $I_2(A, _3P_1)$ electronic states has been considered by several investigators. Are the rate constants for quenching of $I_2(A', A)$ consistent with the dissociation rate data. Examination of the energy level diagrams for the various species, Figure 2-81, gives us guidance as to the most probable energetics of the system. It also reminds us that several vibrational levels of O_2 such as $O_2(a, v=2)$ are available during and subsequent to the energetically favorable BHP generation process. If we have ruled out the role of $O_2(b)$ and then one is pretty much left with higher vibrational levels of oxygen being the energy doners to the low lying electronic states of I_2.

These some of the $O_2(a, v)$ states are responsible for the well-known dimole radiation so we know that at least some of the upper vibrational levels of the "a" state are present. The spectra from two of these states are shown below in Figures 2-77 and 2-78.
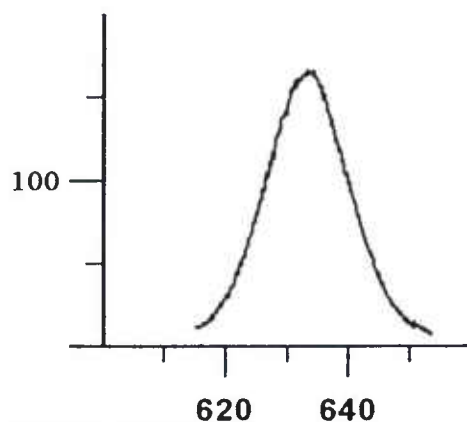
Figure 2–77. Dimolar radiation $O_2^*(v=0)$ $O_2^*(v=0) \rightarrow O_2(v=0)$ $O_2(v=0)$ $\lambda=634$ nm.
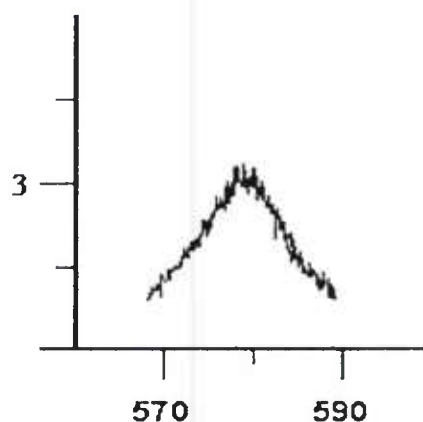
Figure 2–78. Dimolar spectra $O_2^*(v=1)$ $O_2^*(v=0) \rightarrow O_2(v=0)$ $O_2(v=0)$ $\lambda=579$ nm.

The ratio of intensities $I_{634}/I_{579} \approx 50$; leads to the following $K_{579}/K_{634} \approx 0.93$ equilibrium expression for the radiation from the "a" state dimmers. So, at least, the $O_2(a, v=2)1$ vibrational level is

81

available to excite the A and A' states of I_2. Other evidence from the "b"state spectra tell us that there is a distribution of vibrational states, and the assumption is that something similar is available in the $O_2(a, v)$ molecules.

Now reactions are also available to redistribute the vibrational energy,

$$O_2* + O_2* \rightarrow O_2**(v=2) + O_2(v') \qquad 2*10^{-17} \text{ cm3/s} \qquad (2-51)$$

$$O_2(v)+O_2(v') \leftrightarrow O_2(v-1)+ O_2(v'+1) \qquad \approx 10^{-13} \text{ cm3/s} \qquad (2-52)$$
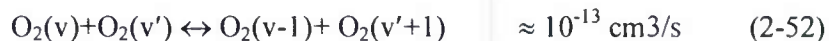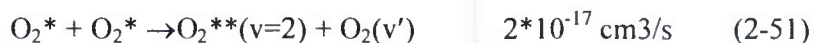
What is left to measure is the rates of collisional deactivation of the. The apparatus shown in Fig. 2-79 was used to estimate the collisional lifetimes of these states.
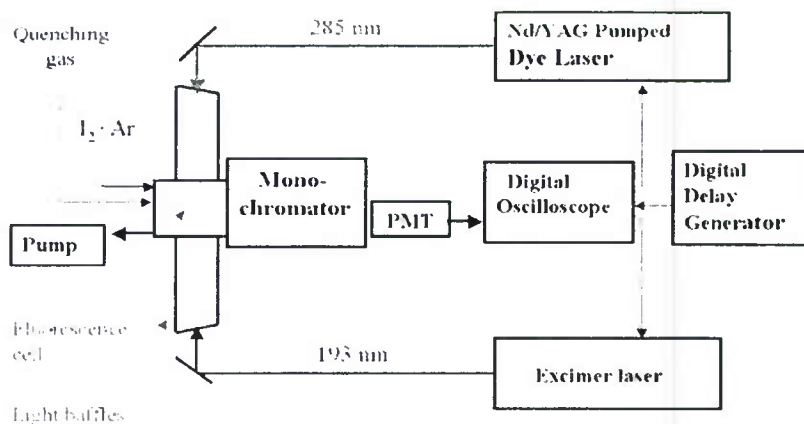
Figure 2–79. Schematic for measurement of deactivation times of I_2 "A" states.

The rate constants, shown in Fig 2-80, are only moderately fast so these intermediates are available for energy transfer with one of the "a" state molecules.
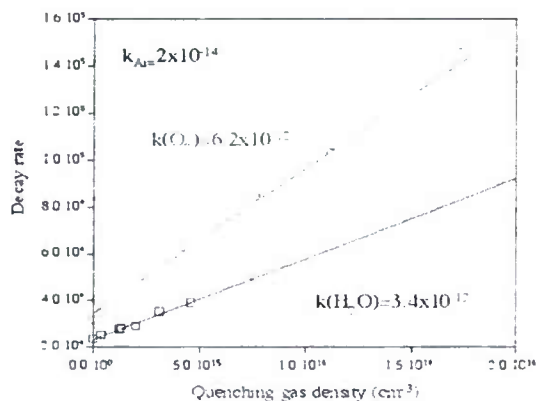
Figure 2–80. Quenching rate constants for the "A" state of I_2.

82
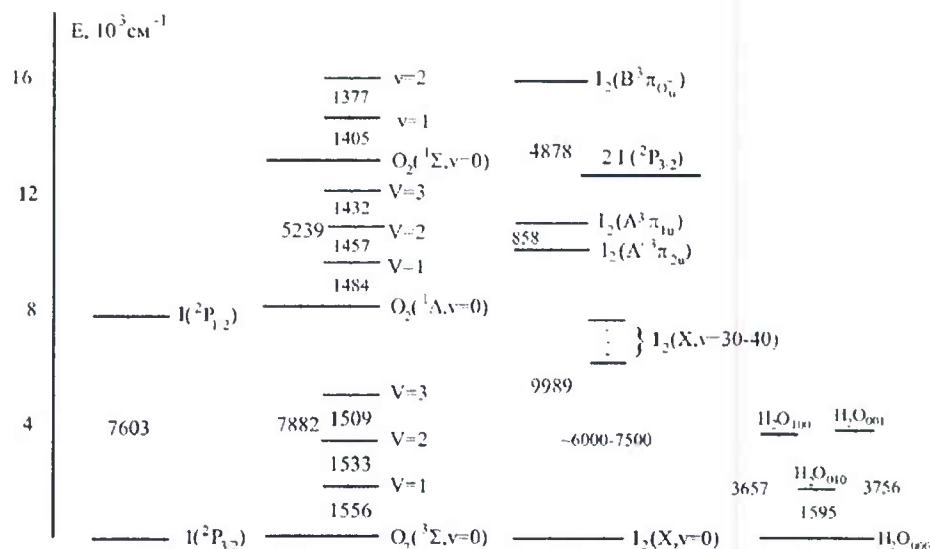
Figure 2–81. Relevant Energy Levels for I, I$_2$, O$_2$ showing potential energetic pathways

So the conclusions from this detailed study is that O$_2$(b) and I$_2$(B) do not play a role in the dissociation of I$_2$ into the atomic state. The relaxation kinetics of I$_2$(A',A) are consistent with the assignment of this species as the primary dissociation intermediate. A model that involves excitation of I$_2$(A',A) by O$_2$(a, v≥1) yields results that are in reasonable agreement with the flow tube experiments. Kinetic studies of energy transfer from O$_2$(a, v≥1) are needed to validate the proposed model.

In contrast with the standard mechanism, the model presented here does not assign a significant role to vibrationally excited I$_2$(X). However, the studies of Hall et al., Van Bentham and Davis, and Barnault et al. show that vibrationally excited I$_2$(X) is produced in I$_2$/O$_2$(a) mixtures. Van Bentham and Davis estimated that the [I$_2$(X, v>32)]/[I$_2$(X)] ratio was around 2.5x10^{-4} for a flow tube experiment where O$_2$(a) was generated using a microwave discharge. It is quite possible that energy transfer events of the type

$$I_2(X, v \geq 10) + O_2(a) \rightarrow I_2(A', A) + O_2(X) \tag{2-53}$$
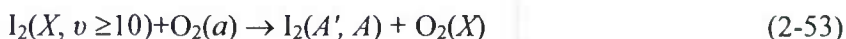
contribute to the excitation of I$_2$(A', A), as proposed by Barnault et al. Inclusion of these channels in the revised kinetic model will be explored in a future study. This may improve the agreement between the observed and simulated data in the region where the dissociation is accelerating.

Overall, the I$_2$ dissociation mechanism outlined here yields simulations that are in reasonably good agreement with our flow tube experiments. The obvious weakness of the model is that, like the standard package, it still contains many assumed values for unmeasured rate constants and branching fractions. The excitation probabilities for O$_2$ and I$_2$ vibrational levels in the proposed E-V processes are unknown. The values of the rate constant of key reactions (95)-(97) are, at present, just fitting parameters.

In addition to probing the dissociation mechanism, the present experimental results also have a significant practical implication. It was found that the presence of a moderate pressure of CO$_2$

does not inhibit the I_2 dissociation process under the conditions of a typical COIL device. This is consistent with the findings of Heaven, [2005], where it was demonstrated that CO_2 can be used effectively as an inexpensive carrier gas for COIL. This circumstance opens a new possibility for the development of both open- and closed-cycle COIL's that utilize cryogenic pumps.

Figure 2-82. Dependence of the I* concentration on the distance along the flow for $\eta_w=3$ %, $\eta_{I_2}=0.28$ %. The smooth curves are simulations for the $I_2(A',A)$ dissociation model.
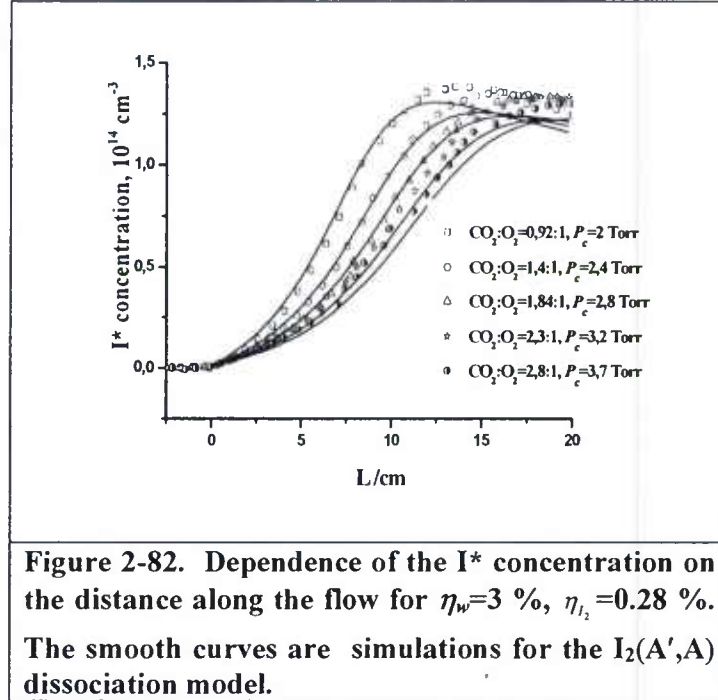
2.3.4 Quenching of $I(^2P_{1/2})$ by NO_2, N_2O_4 and N_2O

Carroll et al. were the first to demonstrate an oxygen-iodine laser (OIL) that utilizes an electric discharge to produce singlet oxygen molecules $O_2(a^1\Delta_g)$. One of the distinguishing features of discharge-driven singlet oxygen generators is that a substantial quantity of $O(^3P)$ is produced along with $O_2(a^1\Delta_g)$. It has been shown that $O(^3P)$ is detrimental to the laser due to the fast quenching process

$$I(^2P_{1/2}) + O(^3P) \rightarrow I(^2P_{3/2}) + O(^3P). \tag{2-54}$$
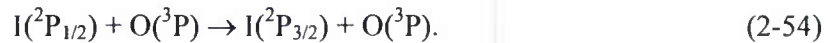
Recent determinations of the rate constant for this deactivation channel have established a value of $k_l=(1.2\pm0.2)\times10^{-11}$ cm^3 s^{-1}. In the following, $I(^2P_{1/2})$, $I(^2P_{3/2})$ and $O_2(a^1\Delta_g)$ are designated by I*, I and $O_2(a)$, respectively.

Reaction (2-54) results in a significant loss of I* for typical discharge generated oxygen atom concentrations. Due to the rapidly established equilibrium between I* and $O_2(a)$

$$I + O_2(a) \leftrightarrow I* + O_2 \tag{2-55}$$

quenching of I* also results in the deactivation of $O_2(a)$. Working with prototype electrically-driven oxygen iodine laser (EOIL) systems, Carroll et al. [2005] and Rawlins et al. [2005] found that production of I* was increased when NO_2 was added to the post-discharge flow upstream of the iodine injection. They concluded that this effect was due to consumption of the excess of oxygen atoms via the process

$$O(^3P) + NO_2 \rightarrow O_2 + NO. \qquad (2\text{-}56)$$

$(k_3 = (9.5 \pm 1.1) \times 10^{-12}, cm^3 s^{-1}$, [Bemand,1974]. The optimal concentration of NO_2 to be added to the flow is dependent, among other factors, on the rate constant for the quenching of I^* by NO_2

$$I^* + NO_2 \rightarrow I + NO_2 \qquad (2\text{-}57)$$

As NO_2 readily forms the N_2O_4 dimer, the quenching process

$$I^* + N_2O_4 \rightarrow I + N_2O_4 \qquad (2\text{-}58)$$

is also a matter for concern. There is only one report of an attempt to measure the rate constant for reaction (2-57). Han et al. obtained an upper bound at room temperature of $k_4 < 8.5 \times 10^{-14}$ cm^3 s^{-1}.

In order to determine an accurate value for the rate constant for deactivation of I^* by NO_2, we have reinvestigated this process at ambient temperature and extended our measurements to elevated temperatures. The temperature dependence study was motivated by two factors. First, the conditions in EOIL devices span a wide temperature range as the gas mixture travels from the discharge to the optical cavity. Immediately after the discharge the gas temperature can be greater than 700 K. Cooling to temperatures below 300 K by the time the gas reaches the cavity is desirable as this increases the gain [due to the effect of temperature on the equilibrium represented by reaction (2-55)]. Secondly, the equilibrium between NO_2 and N_2O_4 is temperature dependent, and measurements made over a range of temperatures were helpful in separating out the quenching contributions from reactions (2-57) and (2-58).

Quenching of I^* by N_2O was studied both for fundamental reasons, and because of the relevance to a particular type of photolytically-driven oxygen-iodine laser. Zolotarev et al. explored a laser scheme where photolysis of O_3 was used as the primary source of $O_2(a)$. In attempts to improve the performance of this system, Zolotarev et al. tested the use of N_2O, N_2 and/or CO_2 as reagents for the removal of the unwanted $O(^1D)$ photoproduct. The best results were obtained for N_2O, and Zolotarev et al. concluded that an increase in laser power was achieved due to the fact that N_2O consumes oxygen atoms in processes

$$O(^1D) + N_2O \rightarrow NO + NO \qquad (2\text{-}59a)$$
$$\rightarrow O_2(a\,^1\Delta_g, X\,^3\Sigma_g^-) + N_2 \qquad (2\text{-}59b)$$

where $O_2(a)$ is the dominant product of reaction (2-59b). Recently the branching fraction of electronically excited O_2 produced by channel (2-59b) was found to be >0.9. The optimal mole fraction of N_2O for the laser driven by O_3 photolysis depends on the rate at which I^* is quenched by N_2O

$$I^* + N_2O \rightarrow I + N_2O \qquad (2\text{-}60)$$

Han et al. reported a rate constant for reaction 6 at room temperature of $k_7 = 2.1 \times 10^{-15}$ cm^3 s^{-1}. This measurement, made using photolysis of CF_3I/N_2O mixtures at 266 nm, was approximately consistent with the results of Hathorn et al., who obtained a value of $k_7 = (1.3 \pm 0.2) \times 10^{-15}$ cm^{3}s^{-1}. In the present work we have extended the characterization of reaction (2-60) by performing the first measurements at elevated temperatures.

The present measurement of the room temperature rate constant for the quenching of I* by N_2O is in good agreement with the value reported by Hathorn et al. (($1.3\pm0.2)\times10^{-15}$ cm^3s^{-1}). The dependence of this rate constant on the temperature was too weak to be determined, indicating that the mechanism does not involve a barrier or facilitation through the formation of a long-lived collision complex. The rate constant for quenching by NO_2 was well below the upper bound reported by Han et al. In that earlier study the limiting factor was the presence of impurity O_2 in the NO_2 sample. The results obtained in this study indicate that the I* quenching characteristics of N_2O and NO_2 are quite similar. This is an interesting observation that deserves some further consideration.

The quenching rate constants (293 K) for NO, NO_2 and N_2O are 1.2×10^{-13}, 2.9×10^{-15} and 1.4×10^{-15} cm^3 s^{-1}, respectively. NO and NO_2 are open-shell species. Their interactions with iodine are such that INO and INO_2 are moderately stable molecules. In contrast, N_2O is a closed-shell molecule that interacts with I via weak van der Waals forces. Hence the large difference in the quenching rate constants for NO and N_2O is not surprising, but the low efficiency for quenching by NO_2 (compared to NO) was unexpected. It appears that long-range attractive forces facilitate quenching by NO, as Deakin and Husain reported a negative temperature dependence for this process (and they speculated that transient formation of INO was implicated). Grimley and Huston further suggested that the quenching was mediated by means of seams of intersection occurring between the potential energy surfaces that correlate with the I*+NO and I+NO dissociation asymptotes.

INO_2 is bound, and it is reasonable to expect that one or two of the surfaces that correlate with I*+NO_2 will also possess potential minima. However, the slow quenching of I* by NO_2 indicates that intersections between the I*+NO_2 and I+NO_2 potential energy surfaces do not occur within the energy range that is thermally accessible to collisions at $T\leq380$ K. The small and similar quenching rate constants for NO_2 and N_2O suggests that they deactivate I* by an energy transfer mechanism that does not involve potential surface intersections.

Quenching of I* by N_2O_4 was found to be a factor of 120 times more efficient than quenching by the monomer. Here it is of interest to note that the energy carried by I* (7603 cm^{-1}) exceeds the O_2N-NO_2 bond energy of about 4600 cm^{-1}. Consequently the channels

$$I^* + N_2O_4 \rightarrow I + NO_2 + NO_2 \qquad (2\text{-}61a)$$
$$\rightarrow INO_2 + NO_2 \qquad (2\text{-}61b)$$

could account for the faster deactivation by the dimer.

With regard to the discharge-driven oxygen-iodine laser, the quenching rate constant data indicate that both NO and NO_2 are relatively inefficient quenchers of I*. Their successful use as O atom scavengers has been demonstrated in low pressure laser systems, where the partial pressure of the NO or NO_2 added to the flow has been below 0.5 Torr. The quantity of NO or NO_2 that can be tolerated in the laser depends on both the partial pressures and the gas transit time between the I_2 injectors and the optical cavity. The rate constants provided by this study will facilitate further modeling for the design of higher power lasers, which will need to operate with much higher reagent densities than the devices explored to date.

3. ELECTRODYNAMIC DISCHARGE MODELING

In parallel to the experimental work there has been an ongoing computational effort to investigate the electrodynamics of ElectricOIL using plasma kinetics models. The purpose of this effort is the development of a predictive capability for the ElectricOIL discharge configurations. The objectives for the development of the discharge model are four-fold: *(1) Develop a kinetics package that appropriately models the reactions that occur within the discharge, (2) produce a discharge power deposition model that correctly models the discharge physics (RF, pulsed power, etc.), (3) use the results from higher fidelity modeling to guide experimental studies, and predict performance, and (4) develop a two-dimensional model that more realistically models the coupled fluid and electrodynamics.* Thus far, work with a quasi 1-D simulation has produced many interesting results, and has allowed study of discharge kinetics, optimization of input parameters, and scaling. Development of a full 1-D model including Navier-Stokes has captured some of the plasma dimensionality, predicting the upwind propagation of the plasma, and allowing an initial look at quasi-steady results for pulsed operation. Modeling work continues with the evolution of a 2-D simulation joining electrodynamics, chemistry and fluid dynamics models to fully simulate the complex ElectricOIL discharge. This model has been used to examine basic cases of the inductive, capacitive, and pulse-sustainer discharge configurations similar to laboratory efforts. The computational studies provided here show the developments in the discharge model and highlight the basic trends that have been observed.

3.1 Discussion of Important Discharge Kinetics

Discharge modeling has allowed the identification of key electrodynamic mechanisms that affect performance of the ElectricOIL system. The primary concerns are the production and loss mechanisms of $O_2(^1\Delta)$ which pumps the laser species. Secondary concerns are the production of other discharge species such as $O_2(^1\Sigma)$ and oxygen atoms. Additional topics are the effect of diluents, helium in particular, and the influence of discharge sensitizers such as NO, CO, or NO_2.

Table 3-1. Significant Reactions in the GlobalKin Kinetics Package.

#							Rates, cm³/molecule-s	Reference
1	e^-	+	$O_2(^3\Sigma)$	$\rightarrow$	$O_2(^1\Delta)$	+ e^-	$f(T_e)$	Phelps, 1985
2	e^-	+	$O_2(^3\Sigma)$	$\rightarrow$	$O_2(^1\Sigma)$	+ e^-	$f(T_e)$	Phelps, 1985
3	e^-	+	$O_2(^3\Sigma)$	$\rightarrow$	$O + O$	+ e^-	$f(T_e)$	Phelps, 1985
4	e^-	+	$O_2(^3\Sigma)$	$\rightarrow$	$O + O(^1D)$	+ e^-	$f(T_e)$	Phelps, 1985
5	$O_2(^1\Sigma)$	+	O	$\rightarrow$	$O_2(^1\Delta)$	+ O	$7.20e\text{-}14*(T_{gas})^{0.5}$	Atkinson, 1997
6	$O_2(^1\Sigma)$	+	O	$\rightarrow$	$O_2(^3\Sigma)$	+ O	$0.80e\text{-}14*(T_{gas})^{0.5}$	Atkinson, 1997
7	$O_2(^3\Sigma)$	+	$O(^1D)$	$\rightarrow$	$O_2(^1\Sigma)$	+ O	$2.56e\text{-}11*\exp(-67/T_{gas})$	Atkinson, 1997
8	e^-	+	$O_2(^1\Delta)$	$\rightarrow$	$O_2(^1\Sigma)$	+ e^-	$f(T_e)$	Hall, 1975
9	e^-	+	$O_2(^1\Delta)$	$\rightarrow$	$O + O$	+ e^-	$f(T_e)$	Shifted from ground state
10	e^-	+	$O_2(^1\Delta)$	$\rightarrow$	$O(^1D) + O$	+ e^-	$f(T_e)$	Shifted from ground state
11	e^-	+	$O_2(^1\Delta)$	$\rightarrow$	$O_2(^3\Sigma)$	+ e^-	$f(T_e)$	Superelastic from detailed balance
12	$O_2(^1\Delta)$	+	O	$\rightarrow$	O_2	+ O	$2.00e\text{-}16$	Herron, 2001
13	$O_2(^1\Delta)$	+	O_3	$\rightarrow$	$O_2 + O_2$	+ O	$5.20e\text{-}11*\exp(-2840/T_{gas})$	Atkinson, 1997
14	$O_2(^1\Delta)$	+	$O_2(^1\Delta)$	$\rightarrow$	O_2	+ O_2	$9.00e\text{-}17*\exp(-560/T_{gas})$	Herron, 2001
15	$O_2(^1\Delta)$	+	$O_2(^1\Delta)$	$\rightarrow$	$O_2(^1\Sigma)$	+ O_2	$9.00e\text{-}17*\exp(-560/T_{gas})$	Herron, 2001

Table 3-1 lists important mechanisms that are applied in the discharge models. Reactions 1 – 4 in Table 3-1 are the elastic electron impacts which produce the discharge species of interest: $O_2(^1\Delta)$, $O_2(^1\Sigma)$, atoms, and excited atoms. Reactions 5 – 7 are the interactions among atoms and excited states. These reactions are responsible for cycling energy back to the $O_2(^1\Delta)$ state from $O_2(^1\Sigma)$ and excited atoms. Reactions 8 – 11 are electron impacts with $O_2(^1\Delta)$. These mechanisms are responsible for most of the $O_2(^1\Delta)$ loss which occurs within the discharge. Including these mechanisms in the discharge model produces a large change in how power from the electron gas is deposited in the $O_2(^1\Delta)$ state. Note that reaction rates 9 and 10 are estimated by shifting the cross-sections for the corresponding ground state process by 0.98 eV, the threshold energy for $O_2(^1\Delta)$. Reactions 12 – 15 are afterglow reactions which transfer energy from $O_2(^1\Delta)$ through collisions with atoms and ozone, and also through pooling. Of the afterglow losses, the quenching by atoms dominates pooling and ozone quenching at typical operating conditions for ElectricOIL due to high atom concentrations and a fast rate. Pooling also plays a primary role in $O_2(^1\Delta)$ depletion and is expected to become more dominant at higher pressures and yields. Quenching by ozone is significant for typical cases, and should become more dominant at higher pressures with higher ozone production due to detachment reactions within the discharge ($O^- + O_2(^1\Delta) > O_3 + e$) and three-body association in the afterglow ($O + O_2 + M > O_3 + M$).

The use of diluents is a key factor in ElecticOIL performance. Due to the temperature dependence of the COIL pumping reaction, it is necessary to maintain a low temperature. One way to do this is by adding helium diluent to the discharge. This will increase the thermal conductivity of the gas-flow, and shift the equilibrium of the pumping reaction in favor of I*. A consequence of this is that the fraction of power available to excite $O_2(^1\Delta)$ within the discharge is lowered due to elastic collisions of the electron gas with helium. This result seems fairly

discouraging, but it is also important to consider the E/N at which the discharge will operate. Figure 3-1(a) shows the quasi 1-D solution for E/N as a function of position for varied helium diluent ratio. These E/N values are superimposed as operating lines onto Figures 3-1(b) and (c) which show the fraction of power into $O_2(^1\Delta)$ as a function of E/N for varied diluent ratio at 0% and 15% yield respectively. Going from pure O_2 to 1% O_2, the peak fraction of power into $O_2(^1\Delta)$ is greatly reduced from ~0.5 to ~0.05. For the conditions specified, the efficiency into $O_2(^1\Delta)$ given by the operating line is decreased as diluent is added. Additionally, comparing Fig 3-1(b) and (c), it is seen that the fraction of power into $O_2(^1\Delta)$ excitation is reduced as yield increases. This is due to the electronic loss mechanisms listed in Table 3-1 becoming dominant as $O_2(^1\Delta)$ concentration increases. From the results in Fig. 3-1 it is expected that although helium addition lowers E/N, it has little benefit toward power efficiency to $O_2(^1\Delta)$. Therefore, its primary benefit is due to thermal effects.
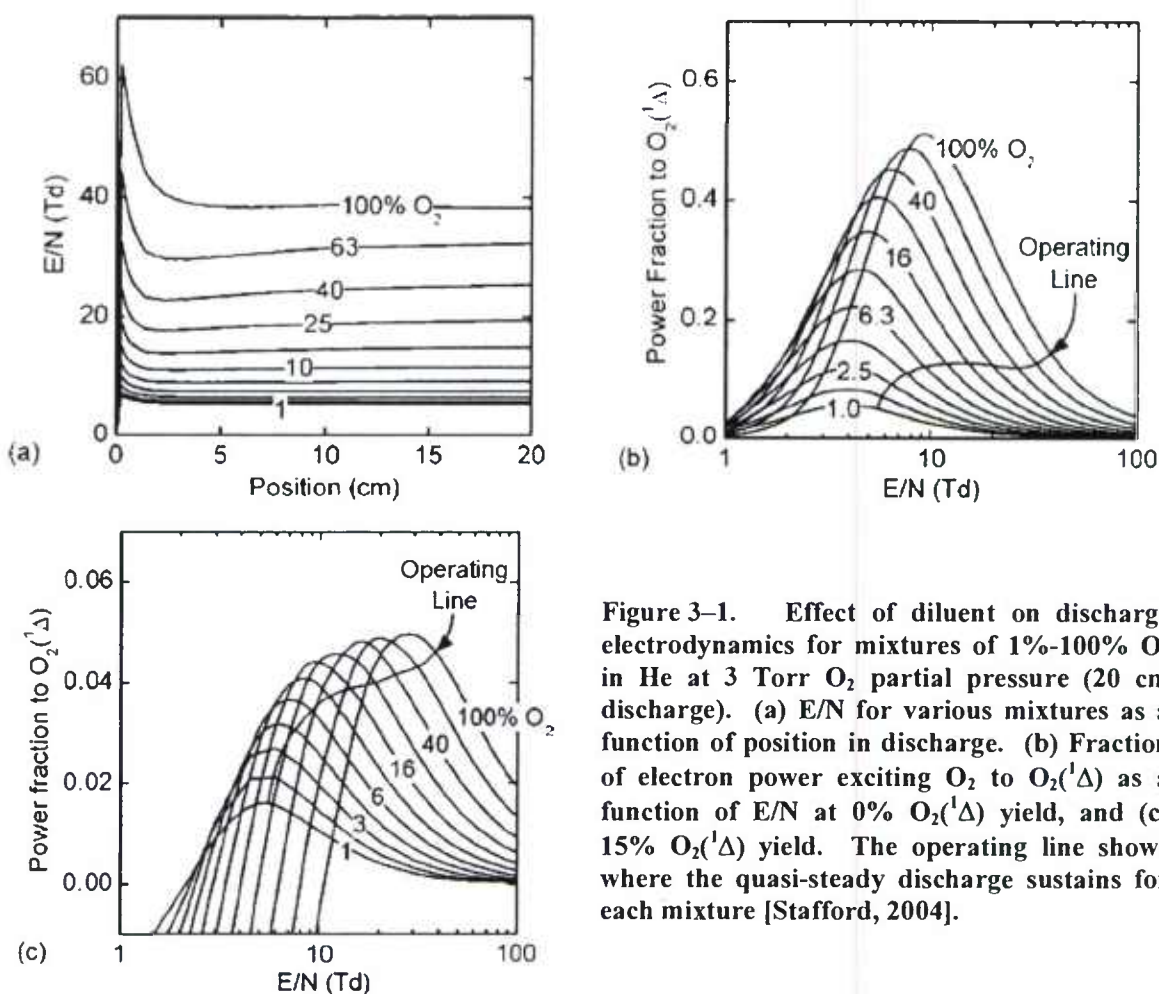
(a)

(b)

(c)

Figure 3–1.   Effect of diluent on discharge electrodynamics for mixtures of 1%-100% O_2 in He at 3 Torr O_2 partial pressure (20 cm discharge). (a) E/N for various mixtures as a function of position in discharge. (b) Fraction of electron power exciting O_2 to $O_2(^1\Delta)$ as a function of E/N at 0% $O_2(^1\Delta)$ yield, and (c) 15% $O_2(^1\Delta)$ yield. The operating line shows where the quasi-steady discharge sustains for each mixture [Stafford, 2004].

The modeling investigation has also led to understanding the discharge dynamics of various diluents (He, Ar) and sensitizers (CO, NO, NO_2), with primary respect to $O_2(^1\Delta)$ production. It was seen earlier in this section that elastic collisions with helium deprive $O_2(^1\Delta)$ of electron power, reducing the peak fraction of power for $O_2(^1\Delta)$ excitation (see Fig. 3-1). It is noted that the presence of Ar or CO has a similar effect. There are elastic losses associated with argon addition and vibrational-excitation losses associated with carbon-monoxide. The addition of argon or helium to the mixture causes the peak FOP to shift to lower E/N, while carbon-monoxide influences a shift to higher E/N. The kinetics modeling predicts that the elastic losses due to Ar are much lower than those associated with He. With the addition of CO, losses due to vibrational excitation are substantial. The addition of CO to the 4:1 He:O_2 mixture causes a large decrease in the peak FOP into $O_2(^1\Delta)$, 52% down to 11%. This is due to the large cross-section for CO vibrational excitation [Frolov, 2003]. Figure 3-2 shows the FOP into elastic collisions and vibrational excitation in typical mixtures with He, Ar, and CO. Note that vibrational excitation of CO consumes a large amount of the electron gas power (> 70% at peak) while Ar elastic collisions are insignificant compared to the losses associated with He and CO.
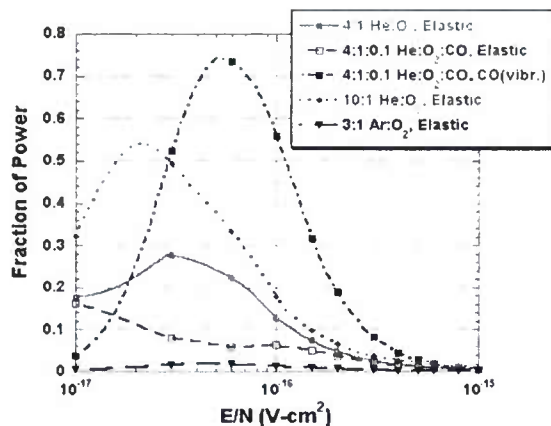
Figure 3–2. Fraction of power devoted to elastic collisions and CO vibrational excitation as a function of E/N for varied oxygen and diluent mixtures.

3.2 Globalkin "Quasi" 1-D Simulation

Globalkin, a time-dependent global plasma kinetics model [Dorai, 2000], was modified to simulate the ElectricOIL discharge as power deposition in a steady-state plug flow. Globalkin consists of three main modules:

1) A reaction chemistry and transport module
2) A Boltzmann equation solver which determines the electron energy distribution
3) An ordinary differential equation (ODE) solver

The EEDF determined from the Boltzmann solver and an electron-impact cross-section database are used to determine electron impact rates as a function of electron temperature. These are used by the chemistry and transport module along with temperature-dependent rates for heavy particle interactions to produce differential equations for the time evolution of each species. The ODE solver is then applied to solve these equations, giving time-dependent results for the various discharge species. The time-dependent model is made quasi 1-D by deriving the position from gas velocity. The change in gas velocity is determined by conservation of mass flux. The reader is directed to Stafford [Stafford, 2004] for a more detailed discussion of the 1-D model.

Application of the 1-D Globalkin model to typical ElectricOIL flow conditions has allowed for numerous studies. These studies include spatial evolution of concentrations in the discharge, the influence and dominance of various kinetics, and the effects of diluents and pressure. Also, the model has been used to develop a scaling law for the dependence of $O_2(^1\Delta)$ on energy deposition.

The 1-D model is primarily useful for predicting the species concentrations produced in the discharge for typical experimental cases. Figure 3-3 shows the concentration of oxygen species as a function of position for a 4:1 $He:O_2$ case at 300 W and 6.5 Torr. Note that the model predicts high concentrations of $O_2(^1\Delta)$ and atoms as well as substantial amounts of $O_2(^1\Sigma)$, $O_2(v)$ and ozone. The metastable $O_2(^1\Delta)$ and O atoms decay very little while $O_2(^1\Sigma)$ decays quickly due to high atom concentration and the energy stored in $O_2(v)$ is converted to gas temperature. Ozone builds up in the afterglow due to three-body reactions with ground state and atoms, rising two orders of magnitude over its value in the discharge region.
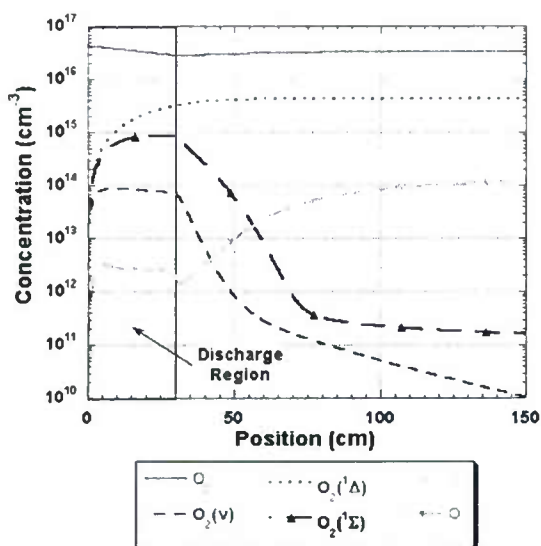
Figure 3–3. Globalkin modeling result of oxygen species concentrations, 4:1 He:O$_2$, 6.5 Torr, 300 W, 30 cm x 4.83 cm I.D. discharge.
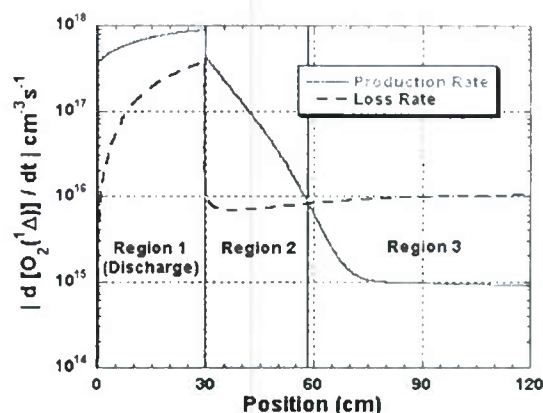
Figure 3–4. Comparison of total O$_2$($^1\Delta$) production and loss rates. 4:1 He:O$_2$, 6.5 Torr, 300 W, 30cm discharge.

Figure 3-4 shows the total O$_2$($^1\Delta$) production and loss rates for the 4:1 He:O$_2$, 300 W case discussed above; characteristic regions of production and loss are labeled. In Region 1, the discharge, production primarily from electronic excitation and O$_2$($^1\Sigma$) quenching dominates loss mechanisms by a factor of 10^{18}. In Region 2, the production primarily from O$_2$($^1\Sigma$) quenching dominates losses by a factor of 10^{17}. In Region 3, O$_2$($^1\Sigma$) is fully quenched and loss mechanisms dominate by only 10^{16}, much lower than the Region 2 and 3 production rates, such that O$_2$($^1\Delta$) density is sustained.

The fastest O$_2$($^1\Delta$) production mechanism inside the discharge is the electron impact excitation of the ground state, O$_2$($^3\Sigma$) > O$_2$($^1\Delta$). The second highest rate is the quenching of O$_2$($^1\Sigma$) by oxygen atoms to O$_2$($^1\Delta$), which is dependent on both the amount of O$_2$($^1\Sigma$) excited, and the degree of dissociation that occurs through the discharge. Both of these mechanisms are responsible for the majority of O$_2$($^1\Delta$) production in this case, with the other "dominant" mechanisms being at least one order of magnitude lower. After the discharge exit, where the electrons are quickly lost to attachment, the O$_2$($^1\Sigma$) deactivation by oxygen atoms becomes the primary production mechanism. Other notable production mechanisms are the super-elastic electron impact with O$_2$($^1\Sigma$), the excitation transfer between O(^{1}D) and ground state oxygen, and the quenching of O$_2$($^1\Sigma$) by ozone. Together, these three mechanisms are responsible for a significant amount of the production. Note that the post-discharge behavior of O$_2$($^1\Delta$) follows the trend of O$_2$($^1\Sigma$) density

The O$_2$($^1\Delta$) loss rates in the discharge are dominated by electron-impact processes (see Table 3-1, rxn. 9-11). The fastest rate is the excitation of O$_2$($^1\Sigma$) from O$_2$($^1\Delta$), which is fast due to a low threshold of 0.65 eV. However, this is not a major concern considering that a significant amount of O$_2$($^1\Sigma$) is converted to O$_2$($^1\Delta$); for instance, in quenching of O$_2$($^1\Sigma$) by O atoms, the assumed

92

branching ratio is 90% in favor of the singlet delta state [Atkinson, 1997]. Super-elastic quenching and dissociation of $O_2(^1\Delta)$ also have considerable rates inside the discharge, but these are one order of magnitude lower than the dominant production rates. Outside of the discharge, the most significant $O_2(^1\Delta)$ loss rate is quenching by oxygen atoms, which is still lower than the combined quenching of $O_2(^1\Sigma)$ to $O_2(^1\Delta)$ by oxygen atoms and ozone.

With insight obtained from basic kinetic studies such as the one above, it was necessary to investigate the effects of varying system parameters and develop a scaling model. Numerous studies with the Globalkin model suggested a scaling parameter based on the energy deposited were input molecule of oxygen.

$$e_{O2} = \frac{TotalEnergyDeposition(eV/cc)}{[O_2]_{total}}$$ (3-1)

Figure 3-5 shows a calculation for maximum $O_2(^1\Delta)$ yield in the reactor afterglow as a function of pressure for varied mixtures and power levels. In the cases used, flow rate varies linearly with pressure. In this chart, each curve has a maximum at which the best efficiency is achieved, corresponding to ~30% $O_2(^1\Delta)$ yield. For the 4:1 helium and 3:1 argon 500 W cases, this occurs at ~2 Torr. When the power level is adjusted to 1 kW for the 4:1 helium case, the optimal pressure rises to ~3.5 Torr. When the power is fixed at 500 W, and the helium diluent ratio raised to 12:1, the optimal pressure becomes ~5 Torr. The reasoning for these behaviors flows from the common sense argument that some optimal energy-to-oxygen partial pressure must be maintained for best performance. Beyond this optimum, energy is lost to dissociation, superelastic collisions, and excitation from singlet delta to other states.

To further investigate the idea of optimal specific energy deposition, various cases which were run were plotted against e_{O2}. The ranges for this parameterization are given in Table 3-2.

Table 3-2. Parameter space investigated in power/mixture/pressure trade study. The discharge volume was held fixed (30 cm length x 4.83 cm I. D.).

Parameter	Minimum	Maximum
Power (kW)	0.01	6
Pressure (Torr)	0.25	29.02
O_2 Mole Fraction	0.02	1
He Diluent Ratio	0:1	50:1
Ar Diluent Ratio	0:1	10:1
CO Diluent Ratio	0:1	1:1

Figure 3-6 plots the maximum yield versus specific energy deposition at exit for the cases investigated in this study. The maximum yield is approximately linear up to ~3 eV/molecule and then begins to saturate and rollover at higher specific energy deposition levels. The best case of this study results in a maximum yield of 32.6 % at ~6.8 eV/molecule, and was for a 12:1 He:O_2 mixture at 13 mmol/s, 15 Torr and 500 W. The spreading of the data points as energy-per-molecule increases is due to the secondary effects of diluent, mixture and pressure, with a key factor being the conversion of $O_2(^1\Sigma)$ to $O_2(^1\Delta)$. The conclusion of this study is that optimal $O_2(^1\Delta)$ production is achieved in the range of 5-8 eV/molecule.
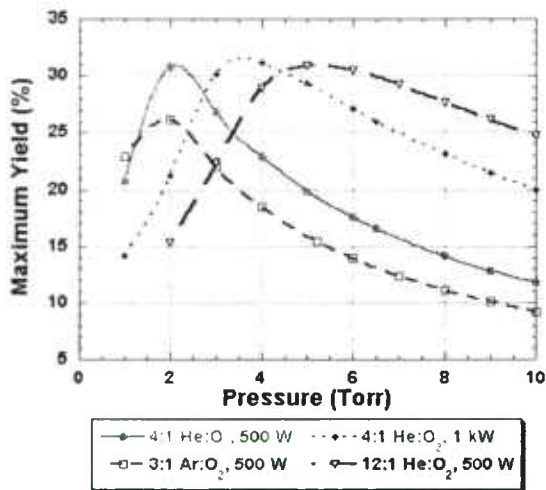
Figure 3–5. Maximum $O_2(^1\Delta)$ yield vs. pressure for varied mixture and power. Flow rate varies linearly with pressure. Cubic splines are used between data points.
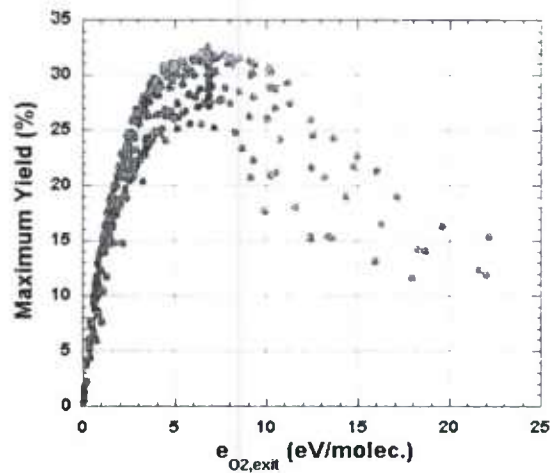

Figure 3–6. Maximum yield versus specific energy deposition for varied mixture, pressure and power. Discharge dimensions are 30 cm x 4.83 cm I.D. for all cases. The maximum temperature is 1500 K.

3.3 1-D Simulation with Axial Transport

Axial transport was modeled by adding the one-dimensional Navier-Stokes equations to the plasma kinetics module of Globalkin. These additional equations account for axial flux of mass, momentum, gas energy, and electron energy. This dimensionally-improved model was used to simulate steady state operation of three power-deposition methods of interest: inductively coupled (ICP), capacitively coupled (CCP), and pulsed power. The ICP model simulates inductive coupling from coils wound directly on the discharge region outer diameter. In this model the power deposition at a point in the discharge is dictated by the sum over all the coils of the magnetic field influence due to the coil current. The CCP model utilizes a transmission line where each cell in the 1-D discretization is represented by its associated plasma resistance and each mesh point has a capacitance based on experimental geometries. The CCP model is visualized in Fig. 3-7. In this model, any axial geometry of capacitive electrodes can be represented, specifying driven electrode regions as a sinusoidal source and the rest of the power deposition region nodes as ground. To model pulsed power, either the ICP or CCP model can be used with a variable duty cycle waveform, specifying pulse period, pulse width, rise and fall times.
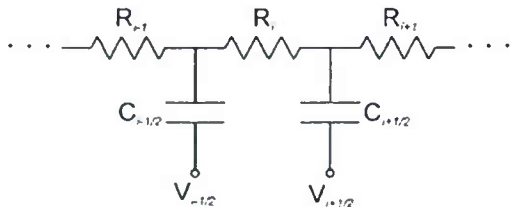

Figure 3–7. Schematic of 1-D CCP transmission line power deposition model.

A key result of including axial transport, is that it predicts the propagation of the plasma upwind of the electrode region similar to that seen in ElectricOIL experiments. Figure 3-8 shows a comparison of ICP and CCP models at 340 W, flowing 16:4 mmol/s $He:O_2$. In this example, the

ICP model consists of 20 coils evenly spaced between 50 and 70 cm, while the CCP model consists of electrodes positioned at 50 and 70 cm. Although the peak electron density is higher in the ICP case, the CCP case achieves a slightly higher density of $O_2(^1\Delta)$. This is due to the CCP case having a lower electron temperature in the bulk plasma. Thus, the use of the CCP method as opposed to ICP results in the inlet flow interacting with more low temperature electrons which are favorable for $O_2(^1\Delta)$ excitation.

The 1-D model with axial transport was also used to obtain quasi-steady state solutions for pulse-sustained discharge methods. The goal in this method is to lower the typical electron temperatures of the continuous-wave discharge from ~2 eV to values more favorable for singlet oxygen production (~1.2 eV). Figure 3-9 shows results for pulsed operation, maintaining conditions similar to those from Fig. 3-8. In this example, a 2.5 kW, 100 ns pulse is used with pulse periods of 1, 2 and 4 μs, and the cw background power is adjusted such that the average power is 340 W. The addition of the ionization pulse results in electron temperatures during the time between pulses lower than those seen in cw operation at the same power level. This leads to an increase in $O_2(^1\Delta)$ excitation, as expected from theory. Also, the lower electron temperature results in less dissociation, another effect of the lowered electron temperature, which might be favorable to ElectricOIL due to the I* + O loss. Furthermore, the $O_2(^1\Delta)$ has saturated at the 2 μs pulse period. This saturation has been confirmed by cases run up to 20 μs, which show no further increases in yield for the applied 2.5 kW, 100 ns pulse.

(a)

(b)

(c)
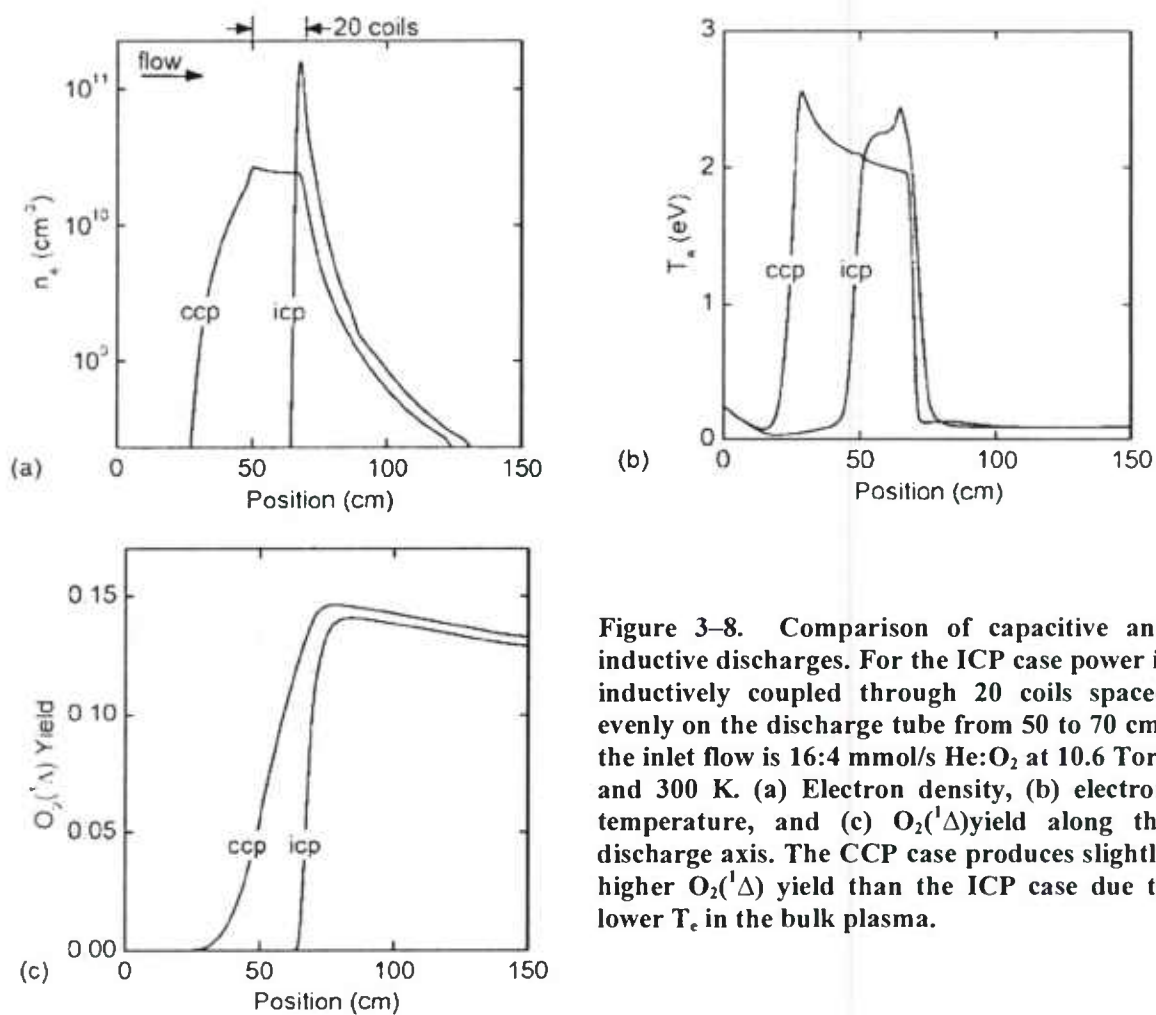
Figure 3–8. Comparison of capacitive and inductive discharges. For the ICP case power is inductively coupled through 20 coils spaced evenly on the discharge tube from 50 to 70 cm; the inlet flow is 16:4 mmol/s He:O_2 at 10.6 Torr and 300 K. (a) Electron density, (b) electron temperature, and (c) $O_2(^1\Delta)$ yield along the discharge axis. The CCP case produces slightly higher $O_2(^1\Delta)$ yield than the ICP case due to lower T_e in the bulk plasma.

(a)

(b)

(c)
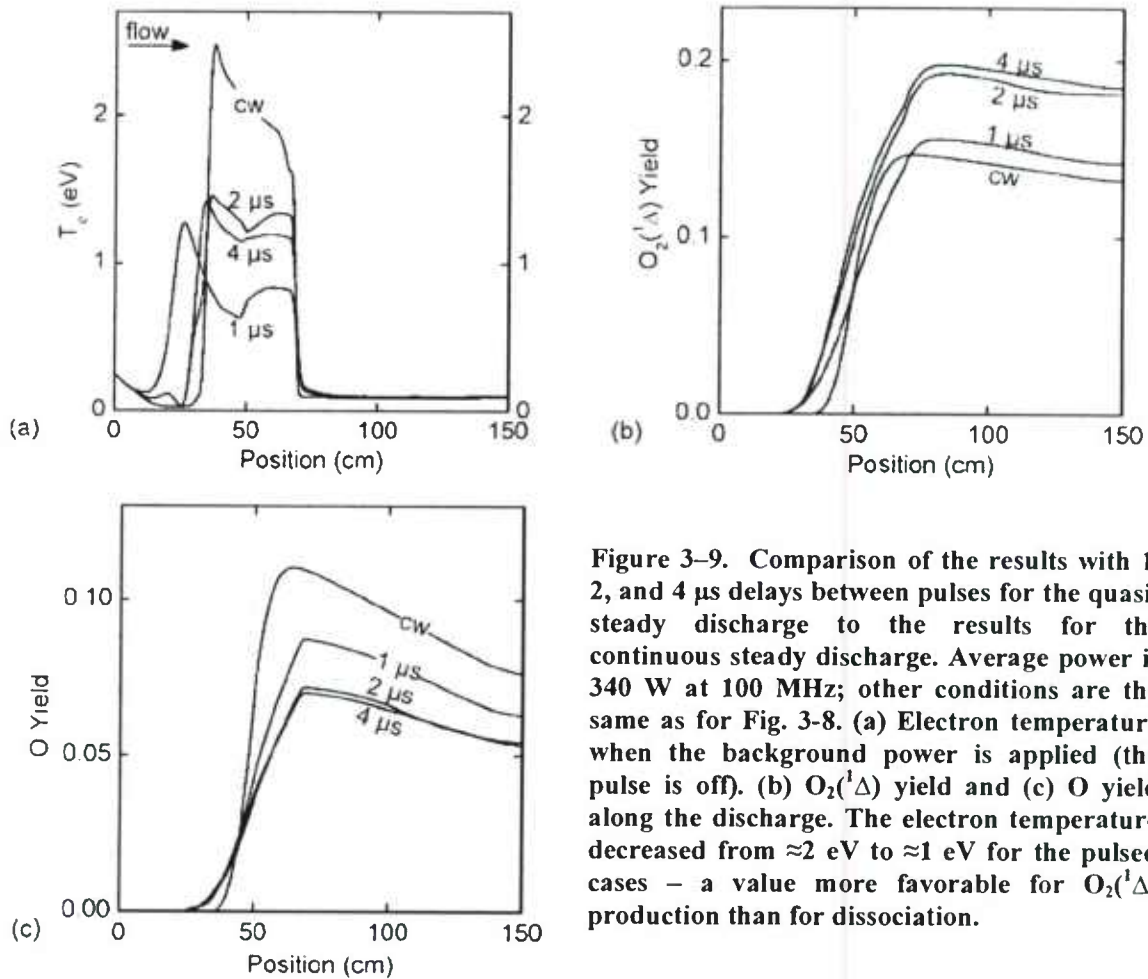
Figure 3–9. Comparison of the results with 1, 2, and 4 μs delays between pulses for the quasi-steady discharge to the results for the continuous steady discharge. Average power is 340 W at 100 MHz; other conditions are the same as for Fig. 3-8. (a) Electron temperature when the background power is applied (the pulse is off). (b) $O_2(^1\Delta)$ yield and (c) O yield along the discharge. The electron temperature decreased from ≈2 eV to ≈1 eV for the pulsed cases – a value more favorable for $O_2(^1\Delta)$ production than for dissociation.

3.4 nonPDPSIM 2-D Simulation

The nonPDPSIM was developed to investigate plasma dynamics at moderate to high pressures in complex geometries. The details of the model are as follows:

- 2-D rectilinear or cylindrical unstructured mesh
- Implicit solution for drift-diffusion for charged particles
- Poisson's equation including volume and surface charge, and material conduction
- Circuit model
- Electron energy equation coupled with the Boltzmann solution for electron transport coefficients
- Optically thick radiation transport with photoionization
- Emission of secondary electrons by impact, thermally enhanced electric field emission, and photoemission
- Surface chemistry
- Monte Carlo simulation for secondary electrons

97

- Navier-Stokes neutrals with individual diffusion speeds (mass, momentum, and thermal energy solutions obtained from unsteady algorithms)

Joining all these components produced a state-of-the-art model of discharge dynamics which more adequately represents the ElectricOIL discharge.

Recently, nonPDPSIM has been modified to address radio-frequency capacitive coupling methods used in ElectricOIL with both continuous wave and pulse-sustainer power deposition. The geometry used is a 6 cm I.D. tube, with 2 cm wide ring electrodes placed 13 cm apart, as shown in Fig. 3-10(a). The electrodes are powered at 13.56 MHz.
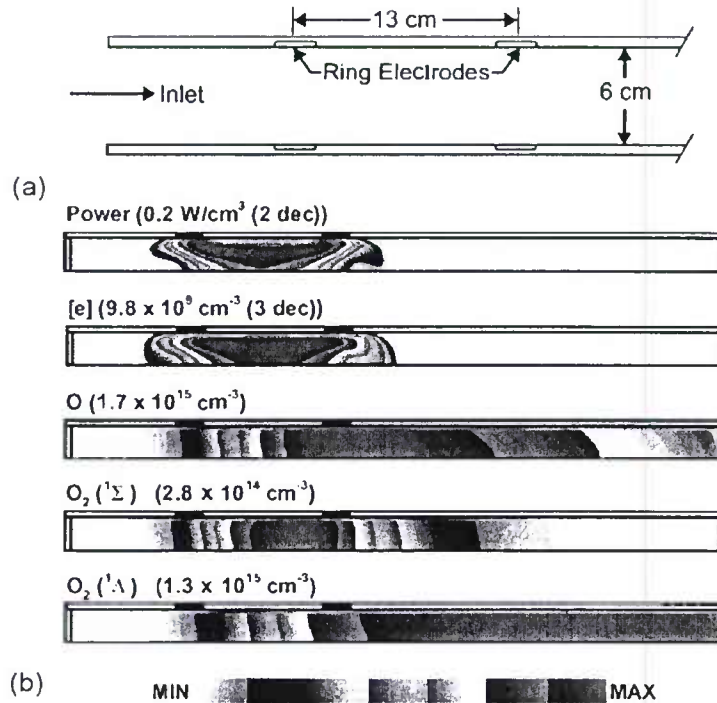
Figure 3–10. Plasma properties for the base case conditions (He/O$_2$=70/30, 3 Torr, 6 lpm, 40 W) when using capacitive coupling at 13.56 MHz. (a) Schematic of the electrodes. (b) Power deposition and densities of electrons O, O$_2$ ($^1\Sigma$), and O$_2$($^1\Delta$). All values are averaged over one rf period. Flow is from the left. Scales are linear with zero minimum values unless the number of decades (i.e., "decs") is indicated for log plots.

Power deposition and densities of electrons, O, O$_2$($^1\Sigma$) and O$_2$($^1\Delta$) are shown in Fig. 3-10(b) for the base case conditions (He/O$_2$=70/30, 3 Torr, 6 lpm, 40 W). Values are shown averaged over the RF cycle. As in the 1-D model with axial transport, the plasma zone extends upstream and downstream of the electrode region, with a semi-uniform distribution of electron density between electrodes. The production of the key plasma species O$_2$($^1\Delta$), O$_2$($^1\Sigma$) and O are fairly uniform through the discharge region, and vary little over the radius of the discharge, with the exception of lowered density near the wall due to deactivation and recombination. Simulating inductively coupled power with nonPDPSIM resulted in similar results to the 1-D model; in particular, the electron temperature and electron density peaked downstream of the center of the coil and the power deposition was less uniform. Since the production of O$_2$($^1\Delta$) is largely a function of total

energy deposition per oxygen molecule for these conditions, the lower local power and electron densities obtained in the capacitive coupling is considered beneficial.

Figure 3-11 shows the combined $O_2(^1\Delta)$ and $O_2(^1\Sigma)$ yields for 5, 20, 40 and 80 W, and the flow conditions in Fig. 3-10. As seen in the lower-dimension models, the yield in the afterglow is approximately linear with power (energy deposition is in the range 0.02-0.4 eV/molecule).
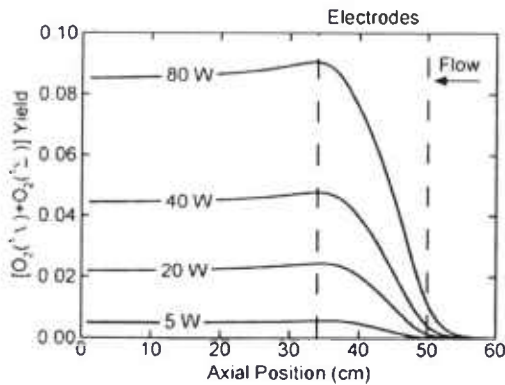
Figure 3–11. Combined yield of $O_2(^1\Delta)$ and $O_2(^1\Sigma)$ on the axis of the tube (He/O_2=70/30, 3 Torr, 6 lpm) with capacitive coupling for different powers.

The dependence of the yield on the RF frequency was also modeled. For example, yields along the axis are shown in Fig. 3-12 for 40 W with continuous wave excitation at 13.56 MHz and 27.12 MHz. Over a wide range of conditions, yields are typically 10-15% higher with the higher frequency. This is due in large part to a larger fraction of the power deposition being dissipated by electron heating as opposed to ion acceleration.
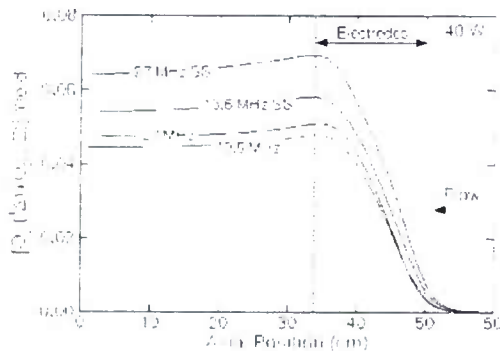
Figure 3–12. Combined yield of $O_2(^1\Delta)$ and $O_2(^1\Sigma)$ on the axis of the tube (He/O_2=70/30, 3 Torr, 6 lpm) with capacitive coupling for 40 W with excitation at 13.56 MHz and 27.12 MHz. Values are shown for continuous wave excitation and pulse-sustainer (denoted by "SS" for spiker-sustainer).

A pulse-sustainer configuration was also investigated. The applied waveform consists of a pulse of applied voltage 2.5 times the amplitude of the background voltage. The pulse is 200 ns wide and applied with a duty cycle of 20% (or a repetition frequency of 1 MHz). Yields along the axis are shown in Fig. 3-12 for 40 W with pulse-sustainer excitation at 13.56 MHz and 27.12 MHz. The total power for the pulsed waveform is 40 W. A 20-40% improvement in yield was obtained with the pulse-sustainer compared to the cw excitation, with the improvement increasing with increasing excitation frequency. These improvements are attributed to a cycle averaged lowering of the electron temperature.

3.5 Electrodynamic Modeling Conclusions

Application of the 1-D and 2-D models to the operating conditions of ElectricOIL has increased understanding of the system's dynamics. Through application of the quasi 1-D model, the key discharge and afterglow mechanisms that affect $O_2(^1\Delta)$ production were identified. In general, the production and loss within the discharge $O_2(^1\Delta)$ is dominated by electron impact, with the prime loss of $O_2(^1\Delta)$ being caused by further excitation [to $O_2(^1\Sigma)$ and dissociation] and superelastic collisions. It was also found that the fraction of electron power into $O_2(^1\Delta)$ is greatly reduced as yield reaches the order of 15%, identifying the limitation of self-sustained discharges. The $O_2(^1\Delta)$ production and loss in the afterglow are due primarily to the deactivation of excited states by atoms.

An energy scaling law was also proposed on the basis of the quasi 1-D model. This law establishes that yield should scale with specific energy deposition (eV per molecule O_2), with secondary scatter due to the effect pressure and diluent ratio on $O_2(^1\Delta)/O_2(^1\Sigma)$ partitioning. The specific energy deposition over a limited operating range at modest densities for best performance (~30% yield) is 5-8 eV/molecule for the self-sustained discharge.

Development of a 1-D steady-state discharge model allowed simulation of some of the geometrical factors observed in the experiment. In particular, these factors were the propagation of the plasma upstream and downstream of the electrode region, and the differences between inductive and capacitive coupling. It also predicted saturation in yield increase as pulse period is increased with the pulse-sustainer power deposition method. Investigation of these factors with the 1-D and 2-D models should help in future design efforts for ElectricOIL discharge development.

The 2-D model was used to model both basic cases and varied power deposition methods. In general, it produced similar results to the 1-D model in terms of species concentrations and energy scaling, and the added dimensionality gave insight into how the electrical and fluid properties interact, and the spatial evolution of species in the discharge. Application of this model to varied RF frequency and pulse-sustainer cases predicts an approximate 40% increase in combined yield. Based on the results seen here, further development of the 2-D nonPDPSIM should be useful when coupled to the models of the laser system, further enhancing understanding of the ElectricOIL system dynamics.

4. LASER SYSTEM MODELING

The GlobalKin model was used to model the discharge physics of the ElectricOIL system. For the laser system we utilize the Blaze II laser simulation code [Sentman, 1977], which contains one-dimensional fluid dynamic equations whose mixing terms were derived from the two-dimensional equations that describe the mixing flow field in a chemical laser cavity. The Blaze model can be used for premixed, axisymmetric mixing and two-dimensional flows and has proven to be a robust and useful modeling tool for 25 years for several different types of gas phase lasers. The use of the Blaze model for oxygen-iodine laser simulations is discussed at length by Carroll [Carroll, 1995].

Because of the more complex kinetics involved with the discharge it was necessary to expand the classic COIL reaction set that is included in the Blaze II code. In addition to the oxygen kinetics associated with O atoms and O_3, discussions with Heaven [Heaven, 2001] suggested the need to incorporate reactions between molecular iodine and atomic oxygen as being an important process. Experiments by the UIUC/CUA group has indicated that the use of NO and/or NO_2 are important for enhancing the production of $O_2(^1\Delta)$ and removing O atoms, respectively. There is also the need to perform and model titrations with molecules such as NO_2 for O atoms and CO_2 for $O_2(^1\Sigma)$. Table 4-1 presents the classic oxygen-iodine gas phase reaction set used in Blaze II, updated to include reactions with Argon, and Table 4-2 presents an expanded mechanism used for the Blaze II modeling of the ElectricOIL system. This mechanism is still in the process of being updated with recent data.

Table 4-1. Classic COIL reaction set. Note: I represents the $I(^2P_{3/2})$ state, I* the $I(^2P_{1/2})$ state, and I_2* is $I_2(v>40)$. Reactions 16-20 were taken from discussions with Heaven, 1996, based upon data from Lawrence, 1997.

k		+		→		+		Rates, cm^3/molecule-s	Ref.
1	$O_2(^1\Delta)$	+	$O_2(^1\Delta)$	→	$O_2(^1\Sigma)$	+	$O_2(^3\Sigma)$	2.7e-17	Perram, 1988
2	$O_2(^1\Delta)$	+	$O_2(^1\Delta)$	→	$O_2(^3\Sigma)$	+	$O_2(^3\Sigma)$	1.7e-17	Perram, 1988
3	$O_2(^1\Sigma)$	+	$O_2(^3\Sigma)$	→	$O_2(^1\Delta)$	+	$O_2(^3\Sigma)$	3.9e-17	Perram, 1988
4	$O_2(^1\Sigma)$	+	H_2O	→	$O_2(^1\Delta)$	+	H_2O	6.7e-12	Perram, 1988
5	$O_2(^1\Sigma)$	+	Cl_2	→	$O_2(^1\Delta)$	+	Cl_2	2.0e-15	Perram, 1988
6	$O_2(^1\Sigma)$	+	He	→	$O_2(^1\Delta)$	+	He	1.0e-17	Perram, 1988
7	$O_2(^1\Delta)$	+	$O_2(^3\Sigma)$	→	$O_2(^3\Sigma)$	+	$O_2(^3\Sigma)$	1.6e-18	Perram, 1988
8	$O_2(^1\Delta)$	+	H_2O	→	$O_2(^3\Sigma)$	+	H_2O	4.0e-18	Perram, 1988
9	$O_2(^1\Delta)$	+	Cl_2	→	$O_2(^3\Sigma)$	+	Cl_2	6.0e-18	Perram, 1988
10	$O_2(^1\Delta)$	+	He	→	$O_2(^3\Sigma)$	+	He	8.0e-21	Perram, 1988
11	I_2	+	$O_2(^1\Sigma)$	→	2I	+	$O_2(^3\Sigma)$	4.0e-12	Perram, 1988
12	I_2	+	$O_2(^1\Sigma)$	→	I_2	+	$O_2(^3\Sigma)$	1.6e-11	Perram, 1988
13	I_2	+	$O_2(^1\Delta)$	→	I_2*	+	$O_2(^3\Sigma)$	7.0e-15	Perram, 1988
14	I_2	+	I*	→	I	+	I_2*	3.5e-11	Perram, 1988
15	I_2	+	$O_2(^1\Delta)$	→	2I	+	$O_2(^3\Sigma)$	3.0e-10	Perram, 1988
16	I_2	+	$O_2(^3\Sigma)$	→	I_2	+	$O_2(^3\Sigma)$	4.9e-12	Heaven, 1995
17	I_2	+	H_2O	→	I_2	+	H_2O	1.7e-11	Heaven, 1995
18	I_2*	+	He	→	I_2	+	He	9.8e-12	Heaven, 1995
19	I_2	+	Cl_2	→	I_2	+	Cl_2	6.3e-12	Heaven, 1995
20	I_2	+	N_2	→	I_2	+	N_2	8.2e-12	Heaven, 1996
21	I	+	$O_2(^1\Delta)$	→	I*	+	$O_2(^3\Sigma)$	7.8e-11	Perram, 1988
22	I*	+	$O_2(^3\Sigma)$	→	I	+	$O_2(^1\Delta)$	1.04e-10*exp(-401.4/T)	Perram, 1988
23	I	+	$O_2(^1\Delta)$	→	I	+	$O_2(^3\Sigma)$	1.0e-15	Perram, 1988
24	I*	+	$O_2(^3\Sigma)$	→	I	+	$O_2(^3\Sigma)$	3.5e-16	Perram, 1988
25	I*	+	$O_2(^1\Delta)$	→	I	+	$O_2(^1\Sigma)$	1.0e-13	Perram, 1988
26	I*	+	$O_2(^1\Delta)$	→	I	+	$O_2(^1\Delta)$	1.1e-13	Perram, 1988
27	I*	+	I	→	I	+	I	1.7e-13	Perram, 1988
28	I*	+	H_2O	→	I	+	H_2O	2.1e-12	Perram, 1988
29	I*	+	He	→	I	+	He	5.0e-18	Perram, 1988
30	I*	+	N_2	→	I	+	N_2	5.0e-17	Deakin, 1972
31	I*	+	Cl_2	→	Cl	+	ICl	5.5e-15	Perram, 1988
32	I*	+	Cl_2	→	I	+	Cl_2	8.0e-15	Perram, 1988
33	I*	+	ICl	→	I_2	+	Cl	1.5e-11	Perram, 1988
34	I_2	+	Cl	→	I	+	ICl	2.0e-10	Perram, 1988
35	Cl	+	ICl	→	I	+	Cl_2	8.0e-12	Perram, 1988
36	2I	+	I_2	→	I_2	+	I_2	3.6e-30	Perram, 1988
37	2I	+	He	→	I_2	+	He	3.8e-33	Busch, 1981
38	2I	+	N_2	→	I_2	+	N_2	4.2e-32	Busch, 1981
39	I* + I	+	I_2	→	$I_2(B)$	+	I_2	3.6e-30	Perram, 1988
40	$I_2(B)$			→	2I			1.0e+6	Perram, 1988

Table 4-2. Incomplete set of ElectricOIL related reactions. Note that the total rate for reactions 63-65 is 6.5e-12*exp(120/T), but the individual branching fractions f_{63}, f_{64}, and f_{65} are unknown but sum to 1.0 (discussed later); the reaction is highly exothermic and the higher excited states arc reasonably likely to occur.

k				→			Rates, cm³/molecule-s	Ref.
41	2O	+	He	→	$O_2(^3\Sigma)$	+ He	$4.5e-34*exp(630/T)$	Herron, 2001
42	2O	+	$O_2(^3\Sigma)$	→	$O_2(^3\Sigma)$	+ $O_2(^3\Sigma)$	$4.5e-34*exp(630/T)$	Herron, 2001
43	2O	+	$O_2(^1\Delta)$	→	$O_2(^3\Sigma)$	+ $O_2(^1\Delta)$	$4.5e-34*exp(630/T)$	Herron, 2001
44	2O	+	O	→	$O_2(^3\Sigma)$	+ O	$4.5e-34*exp(630/T)$	Herron, 2001
45	O + $O_2(^3\Sigma)$	+	He	→	O_3	+ He	$6.0e-34*(T/300)^{-2.8}$	Atkinson, 1997
46	O + $O_2(^3\Sigma)$	+	$O_2(^3\Sigma)$	→	O_3	+ $O_2(^3\Sigma)$	$6.0e-34*(T/300)^{-2.8}$	Atkinson, 1997
47	O + $O_2(^3\Sigma)$	+	$O_2(^1\Delta)$	→	O_3	+ $O_2(^1\Delta)$	$6.0e-34*(T/300)^{-2.8}$	Atkinson, 1997
48	O + $O_2(^3\Sigma)$	+	O	→	O_3	+ O	$6.0e-34*(T/300)^{-2.8}$	Atkinson, 1997
49	$O_2(^1\Sigma)$	+	O	→	$O_2(^1\Delta)$	+ O	$7.2e-14$	Atkinson, 1997
50	$O_2(^1\Sigma)$	+	O	→	$O_2(^3\Sigma)$	+ O	$0.8e-14$	Atkinson, 1997
51	$O_2(^1\Delta)$	+	O	→	$O_2(^3\Sigma)$	+ O	$2.0e-16$	Herron, 2001
52	$O_2(^1\Sigma)$	+	O_3	→	$2O_2(^3\Sigma)$	+ O	$1.54e-11$	Atkinson, 1997
53	$O_2(^1\Sigma)$	+	O_3	→	$O_2(^1\Delta)$	+ O_3	$3.3e-12$	Atkinson, 1997
54	$O_2(^1\Sigma)$	+	O_3	→	$O_2(^3\Sigma)$	+ O_3	$3.3e-12$	Atkinson, 1997
55	$O_2(^1\Delta)$	+	O_3	→	$2O_2(^3\Sigma)$	+ O	$5.2e-11*exp(-2840/T)$	Atkinson, 1997
56	O	+	O_3	→	$O_2(^3\Sigma)$	+ $O_2(^3\Sigma)$	$8.0e-12*exp(-2060/T)$	Atkinson, 1997
57	$O_2(v)$	+	$O_2(^3\Sigma)$	→	$O_2(^3\Sigma)$	+ $O_2(^3\Sigma)$	$4.0e-14$	Atkinson, 1997
58	$O_2(v)$	+	He	→	$O_2(^3\Sigma)$	+ He	$1.3e-13$	Atkinson, 1997
59	I_2	+	O	→	IO	+ I	$1.4e-10$	Atkinson, 1997
60	IO	+	O	→	I	+ $O_2(^3\Sigma)$	$1.5e-10$	Payne, 1998
61	I	+	O_3	→	IO	+ $O_2(^3\Sigma)$	$2.0e-11*exp(-890/T)$	Atkinson, 1997
62	I*	+	O	→	I	+ O	$3.5e-12$	Carroll, 2004
63	O	+	NO_2	→	NO	+ $O_2(^3\Sigma)$	$f_{63}6.5e-12*exp(120/T)$	Atkinson, 1997
64	O	+	NO_2	→	NO	+ $O_2(^1\Delta)$	$f_{64}6.5e-12*exp(120/T)$	Atkinson, 1997
65	O	+	NO_2	→	NO	+ $O_2(^1\Sigma)$	$f_{65}6.5e-12*exp(120/T)$	Atkinson, 1997
66	O	+	NO	→	NO_2		$2.5e-17$	Kaufman, 1958
67	O + NO	+	$O_2(^3\Sigma)$	→	NO_2	+ $O_2(^3\Sigma)$	$1.0e-31*(T/300)^{-1.5}$	Atkinson, 1997
68	$O_2(^1\Sigma)$	+	CO_2	→	$O_2(^1\Delta)$	+ CO_2	$4.1e-13$	Atkinson, 1997

Calculations with Blaze II using the added reaction package, listed in Table 4-2, were performed for some typical flow tube conditions with pure oxygen and oxygen helium mixtures. By comparison to the more detailed mechanism in GlobalKin, it appears that the reduced kinetic package presented in Tables 4-1 and 4-2 is the minimum needed for modeling the oxygen kinetics outside of the discharge region [Carroll, 2003c]. We show the relationships between laser gain and temperature in several places in this report and in more detail in last year's submission.

The question that we have had to answer is, "what routes are available for improving the baseline conditions to produce positive gain from which to perform efficient lasing demonstrations?" There have been several possible approaches:

1) Improve the $O_2(^1\Delta)$ yield entering the mixing zones from the discharge by understanding the plasma chemistry associated with varying discharge compositions and minimize the distances from discharge to cavity so as to reduce the opportunities for deactivation of "a" and "b" states (see Fig 4.1)

    1)   Pre-cool the primary flow so that the mixed stream temperature will also be lowered,

    2)   Provide additional diluent to absorb chemical heat release and lower the temperature,

    3)   Expand the flow supersonically with an optimized supersonic nozzle upstream of the diagnostics/laser cavity.

    4)   Pre-dissociate the iodine molecules prior to injection to eliminate the chemical heat release associated with the I_2 dissociation process and study the complex role of oxygen atoms, and their effects on $O_2(^1\Delta)$, and I* formation,

Combinations of processes $1 - 4$ have been successful in providing improved operating conditions for our initial demonstrations. In addition, pre-dissociation of the iodine was also shown by modeling to be very useful for the supersonic flow situation and provides higher gain than without the pre-dissociation. While all of the processes will be further optimized with our current knowledge of the plasma physics and chemistry, the biggest gains are expected to be made as we bring our new findings regarding non-self sustained discharges to bear on the problem.

Simulations of a supersonic ElectricOIL system with helium diluent indicate that reasonable performance levels can be attained, even at low yield levels of 20% or less [Carroll, 2002]. The presence of O atoms and $O_2(^1\Sigma)$ in the flow very significantly influences the gain by rapidly dissociating molecular I_2 via reactions 12 (Table 4-1), and 59 - 60 (Table 4-2). Our modeling of the experiment also shows that O atoms deactivate I* at a moderate rate so there are deleterious effects to deal with when O atoms are present, Fig. 4-2. The $O_2(a)$ data illustrated in Fig. 2-5 (Section 2.1.2) were converted to yield and Blaze II simulations were run to determine an estimate of the I*+O rate constant, Fig. 4-2. Experimental data were also taken for an over-titrated situation where the NO_2 flow was 0.5 mmol/s (from Sect. 2.1.2, the O atom flow rate for these conditions was approximately 0.32 mmol/s) to simulate the case where the I*+O rate was zero, or equivalently when there are zero oxygen atoms. Figure 4-2 indicates that the rate for I*+O is approximately 3.5×10^{-12} cm^3/molecule-s, which is significantly higher than the upper bound of 2×10^{-12} cm^3/molecule-s estimated by Han et al. [Han, 2004]. Based upon our experiments and analyses (Section 2.1.2, Eqs. 2-5 and 2-6), the rate for I*+O appears to be approximately 5×10^{-12} cm^3/molecule-s. Since the measurement by Han et al. is a more direct measurement of the rate, it is currently believed that the estimate of 8×10^{-12} cm^3/molecule-s determined in this work may be representative of a more global loss mechanism that is still not fully understood. The fact that the Blaze prediction with a zero rate matches the over-titrated data reasonably well supports the conclusion that the presence of O atoms in the flow is not helpful when atomic iodine is also present; however, this still does not mean that the I*+O process, reaction (62), is the only significant loss mechanism. Below we present a study examining the role of Ozone in the sequence of steps in the post discharge flow.
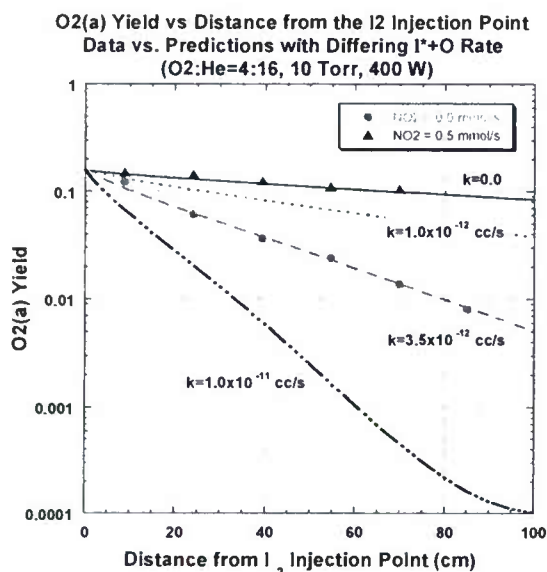
O2(a) Yield vs Distance from the I2 Injection Point
Data vs. Predictions with Differing I*+O Rate
(O2:He=4:16, 10 Torr, 400 W)

Figure 4–1. Blaze II predictions of $O_2(a)$ yield versus distance from the iodine injection point as a function of the I*+O quenching rate constant k_{62}.

A study was performed to determine if the ElectricOIL laser operating conditions with discharge flow rates of $O_2(^3\Sigma)$:He:NO = 10:33:0.15 mmol/s at 16 Torr could be modeled using the Blaze-II chemical laser model. ElectricOIL data was available for $O_2(^1\Delta)$ and $O_2(^1\Sigma)$ yields and flow temperature as a function of distance from the discharge exit and discharge power for the above flow conditions. In these cases, data was not available for the discharge production of atomic oxygen (we have reasonable estimates from related studies) and ozone, two critical species in the kinetics of this flow. Downstream of the electric discharge exit, where $O_2(^1\Sigma)$ concentration is known, $O_2(^1\Sigma)$ is quenched via the following reactions:

$$O_2(^1\Sigma) + M \rightarrow O_2(^1\Delta) + M \tag{4-1}$$

where M may be O, O_3, He, NO or NO_2. At these operating conditions it was calculated that quenching by O_3 is approximately two orders of magnitude more rapid than the next most significant reaction. Blaze-II calculations indicate that $O_2(^1\Sigma)$ quenching by O_3 only occurs when the concentration of O_3 is greater than $\sim 7\times10^{12}$ molecules/cm^3. Calculations also indicate that the primary kinetic mechanism sustaining the concentration of O_3 in this flow is production from atomic oxygen via the following reactions:

$$O + O_2(^3\Sigma) + M \rightarrow O_3 + M \tag{4-2}$$
$$3O \rightarrow O_3 \tag{4-3}$$

where M may be O, $O_2(^3\Sigma)$, $O_2(^1\Delta)$, or He. As a result, it was theorized that the concentration of ozone at the exit of the discharge determines the initial rate of $O_2(^1\Sigma)$ quenching and partially determines the steady-state concentration of $O_2(^1\Sigma)$ (when quenching by O_3 has ceased), Fig. 4-2a, and that the flow rate of atomic oxygen at the exit of the discharge primarily determines the capacity of the flow to sustain the critical ozone concentration, Fig. 4-2b, for $O_2(^1\Sigma)$ quenching and therefore also partially determines the steady-state $O_2(^1\Sigma)$ concentration, Fig. 4-2c.
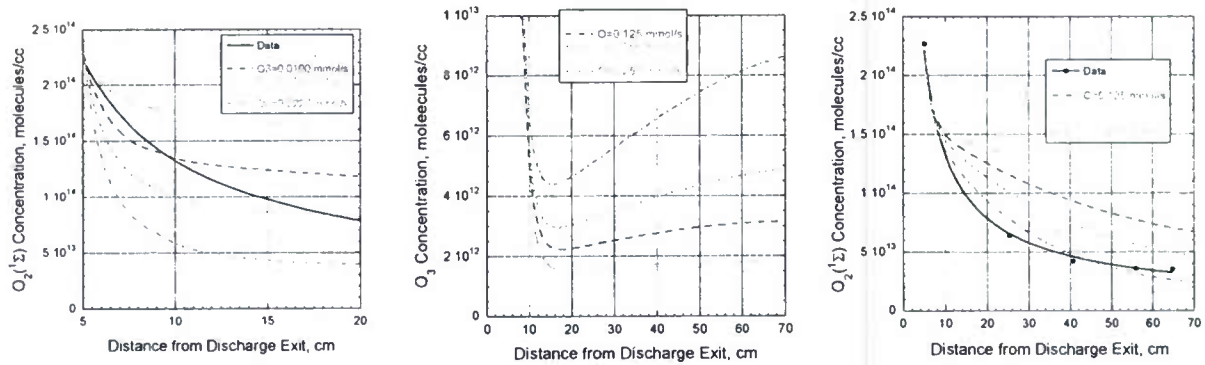
Figure 4–2. (a) $O_2(^1\Sigma)$ concentration as a function of initial O_3 flow rate and distance from the electric discharge exit. (b) O_3 concentration as a function of initial O flow rate and distance from the electric discharge exit. (c) $O_2(^1\Sigma)$ concentration as a function of initial O flow rate and distance from the electric discharge exit.

The calculations indicate that the decay of $O_2(^1\Sigma)$ as a function of distance from the discharge exit is nearly fully determined by the initial flow rates of O and O_3. A parametric study was performed in which the flow tube was modeled for a dense grid of possible combinations of initial O and O_3 flow rates and the resulting $O_2(^1\Sigma)$ decay profiles were compared to data.

The Blaze-II chemical laser model was upgraded to determine the relative agreement of each calculated $O_2(^1\Sigma)$ decay profile with data. The relative agreement [hereafter refered to as fitness] of each calculated profile, F, was determined from $O_2(^1\Sigma)$ concentration data points, D_i, and calculated $O_2(^1\Sigma)$ concentrations, C_i, at five locations downstream of the discharge exit, x_i, using the following method:

$$F = -\sum_i \left(\frac{D_i - C_i}{D_i} \right)^2 \tag{4-4}$$

where a larger F implies greater relative agreement of the calculated $O_2(^1\Sigma)$ decay profile with data. This parametric analysis was performed at rf powers of 100 to 800 Watts at 100 Watts increments in order to determine the correct initial O and O_3 flow rates at each power, Figs. 4-3 (a–b).
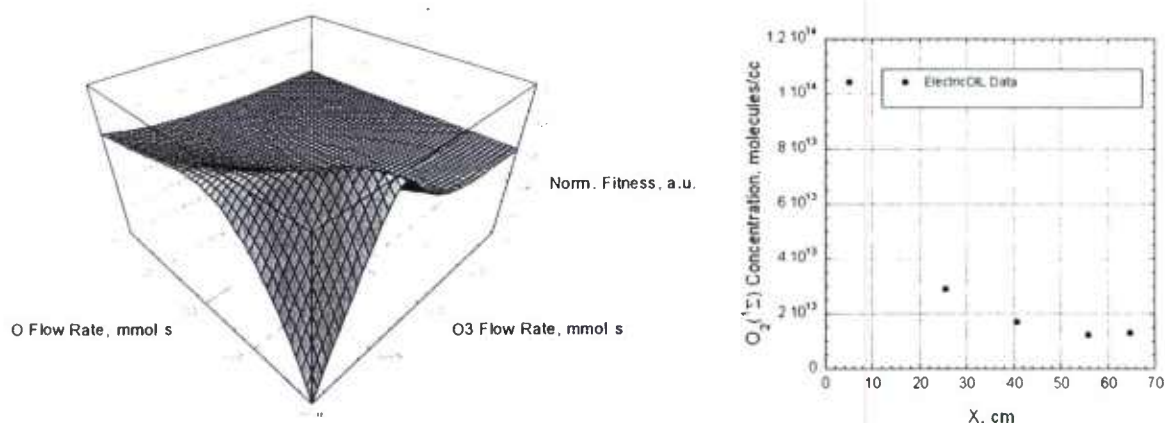
Figure 4–3. (a) Calculated $O_2(^1\Sigma)$ decay profile normalized fitness map for all simulated initial O and O_3 flow rates for ElectricOIL conditions at 300 Watts of rf power. (b) Comparison of calculated $O_2(^1\Sigma)$ decay profile at peak fitness and data.

In addition to performing the analysis at a range of rf powers, a sensitivity analysis was completed to determine the impact of possible error in $O_2(^1\Sigma)$ data on the calculated O and O_3 initial flow rates. The sensitivity analysis was performed by repeating the above analysis at each rf power with the $O_2(^1\Sigma)$ profile data scaled by +25% and -25% which were determined from estimates of $O_2(^1\Sigma)$ measurement error. The complete results of the study and sensitivity analysis are presented in Figs. 4-4 (a–b).
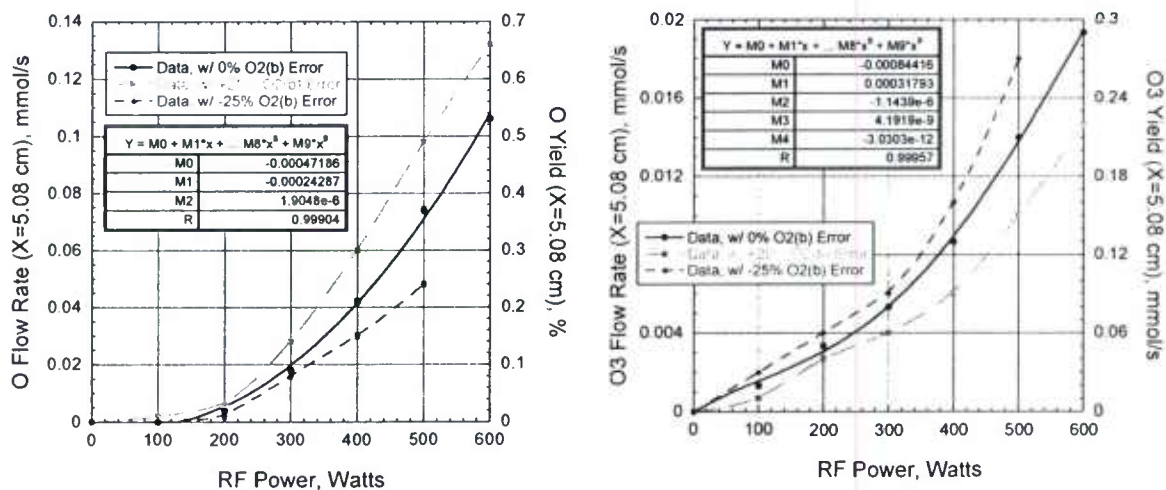
Figure 4–4. (a) Calculated O flow rate and yield near the discharge exit as a function of rf power with sensitivity analysis. (b) Calculated O_3 flow rate and yield near the discharge exit as a function of rf power with sensitivity analysis.

Using the calculated initial O and O_3 flow rates and $O_2(^1\Delta)$ yield, $O_2(^1\Sigma)$ yield, and temperature data at the discharge exit, the $O_2(^3\Sigma):He:NO = 10:33:0.15$ mmol/s, 16 Torr ElectricOIL configuration was modeled and data for $O_2(^1\Delta)$ yield, $O_2(^1\Sigma)$ yield, and temperature as a function of distance from the discharge exit at rf powers of 200, 300, and 550 Watts was accurately reproduced Figs. 4-5 (a–c).

107

Figure 4–5. **(a) Data and calculated $O_2(^1\Delta)$ yield as a function of distance from the discharge exit at rf powers of 200, 300, and 550 Watts. (b) Data and calculated $O_2(^1\Sigma)$ yield as a function of distance from the di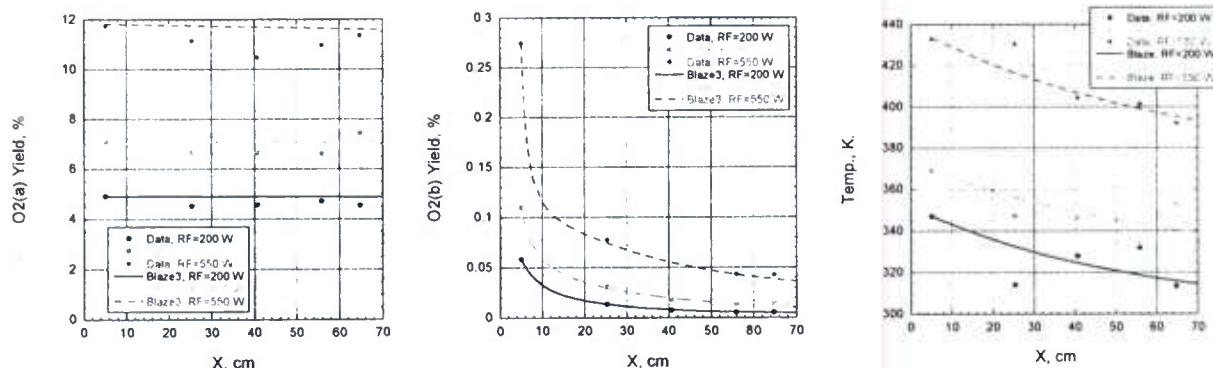scharge exit at rf powers of 200, 300, and 550 Watts. (c) Data and calculated temperature as a function of distance from the discharge exit at rf powers of 200, 300, and 550 Watts.**

Although this method of determining the initial O and O_3 flow rates serves as an excellent means of determining input conditions that cause Blaze-II calculations to be in excellent agreement with data, it should be noted that the actual calculated values for initial O and O_3 flow rates are critically dependent on the accuracy of the kinetics governing the removal of those species from the flow. In particular, an under-representation of reactions of the type:

$$O + NO + M \rightarrow NO_2^{\cdot} + M \tag{4-5}$$
$$O_3 + O \rightarrow 2O_2 \tag{4-6}$$
$$O_3 + O_2(^1\Delta) \rightarrow 2O_2 + O \tag{4-7}$$

where M is $O_2(^3\Sigma)$ or He in particular or any other reactions that remove O or O_3 would cause this method to under-predict initial O and O_3 flow rates. It is however likely that the shape of the O and O_3 profiles as a function of rf discharge power would remain relatively fixed regardless of possible moderate uncertainties in the kinetics. It is, therefore, important that a method for the accurate measurement of O_3 in the ElectricOIL flow tube be conducted

In summary, the Blaze II laser system modeling results are encouraging and many more will be reported in subsequent papers. Further, some of this work has now been repeated with our BLAZE V electrodynamic model, discussed earlier. Based upon theoretical estimates and preliminary laser system modeling, we predict that large scale ElectricOIL devices may be able to deliver electrical efficiencies of over 30%.

5. ADVANCED DISCHARGE TECHNIQUES AND MODELING

The MRl program has had undoubted successes in demonstrating positive gain and lasing with this highly complex system, however, the E/N at which we are presently operating is not optimal. To address this issue the focus of the next phase of the program will be to implement advanced discharge techniques that will control E/N so that theoretical $O_2(a)$ yields of approximately 35% or higher (see Section 3) can be achieved experimentally.

5.1 Review of RF Discharges
There are two basic types of RF discharges: An "E"-discharge and a "H"-discharge – so named for the corresponding primary EM field applied to the plasma. Unfortunately, such historical names tend to obscure the major physical difference and give the erroneous implication that energy is imparted to the electrons by the magnetic field for the H-discharge. In any and all cases, the power transfer is through the electric field alone.

We will use the words "capacitive" and "inductive" to categorize these two types of discharges. A simple circuit representation of each emphasizes the difference between the types.
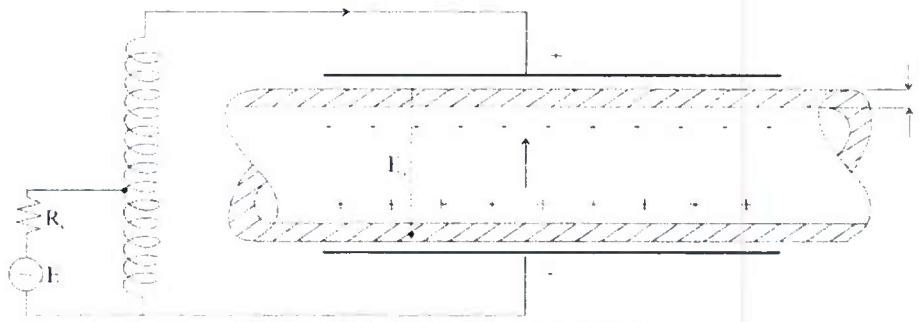
5.1.1 Capacitive RF Discharges

Figure 5–1. Capacitive RF discharge.

Shown here is the case of two external metallic electrodes placed on opposite sides of a glass tube (or they could be 2 cylindrical electrodes separated along the axis of the tube), Fig. 5-1. Clearly, the external current must pass through the glass wall and requires a volt drop across the glass capacitance such that:

$$i = j\,\omega\,\varepsilon_o\,\varepsilon_R\,E_g \tag{5-1}$$

Where $E_g = V_g$ / *thickness of the glass.*

It takes only a few trials to convince oneself that the frequency should be high to carry a significant number density. Example:

Let, $|i| = 10$ mA/cm^2 = 100 A/m^2 = $\omega\,\varepsilon_o\,\varepsilon_R\,E_g$
For, $\varepsilon_R \approx 4$, f = 13.56 MHz (ISM Band);
   $\varepsilon_o = 8.85 \times 10^{-12}$ F/m
Therefore,
   $E_g = 1.33 \times 10^5$ V/m or $V_g = 265$ Volts for 2mm glass thickness.

There are two such capacitances; thus, the applied voltage must exceed 530 volts to put any power into the plasma.

If the metallic electrodes are in direct contact with the plasma, the capacitive voltage drops are not present, but space charge sheaths play a major role, whether or not a non-conducting dielectric is in series or not. This is a subtle but very important point about any discharge. The electrons have a much higher mobility than any of the positive or negative massive ions. Thus a small electric field in the body of the plasma will carry a significant current density.

$$i = n_e \, e \, \mu \, E = n_e \, e \, w_d \tag{5-2}$$

Where n_e = electron density (cm^{-3}), e = electronic charge (coulombs), μ = mobility (cm^2/V-s), and w_d = drift velocity (cm/s).

Note that current must be continuous – a significant problem near the cathode (negative) electrode. Electrons are not emitted from a cold metallic electrode and thus the current must be carried by the ions. The typical voltage drop, due to the space charge of the positive ions is $\approx$ 100-250 volts across the sheath extending a few millimeters from the cathode. Of course, this sheath follows the alternation of the applied voltage. If the frequency is high enough, then the vacuum displacement current can help carry the current to the body of the plasma. At microwave frequencies, for instance, these electrode sheaths play no role. Thus, while the capacitive discharge is the simplest concept, it is very difficult to assign a voltage drop or an electric field to the plasma given the fact that all measurements must be external to the discharge.

The key point about a capacitive discharge is that the current and the applied electric field are parallel to the space-charge fields of the sheaths.

5.1.2 Inductive RF Discharges
An inductive discharge uses a time varying magnetic field to produce an electric field according to

$$\oint \vec{E} \cdot d\vec{l} = -\frac{d}{dt} \iint \vec{B} \cdot d\vec{s} \tag{5-3}$$

The simplest configuration is shown in Fig. 5-2 where a glass tube is surrounded with a few turns of a coil tuned by a shunt capacitor.

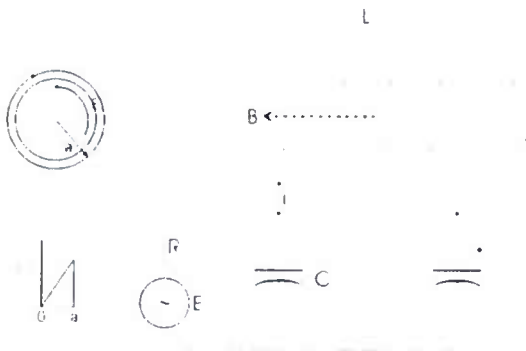Figure 5–2. Simple inductive RF discharge.

Thus the time varying axial magnetic field produces an E_ϕ which is parallel to the tube walls and <u>perpendicular</u> to any space charge sheaths at the walls.

This type of discharge has some distinct advantages over the capacitive one, along with some disadvantages.

Advantages:
- No metallic electrodes are required to be in contact with or even near the plasma container. (Induced diamagnetic currents in a nearby metal are a detriment.)
- Since E_{RF} is perpendicular to any wall sheath, there is never any external induced voltage drops in those sheaths as there is in the capacitive discharge (i.e. cathode fall).
- Since the Electric field is applied parallel to the dielectric walls, there is no voltage drop in walls other than a geometric reduction in E(r) as shown in Fig. 6.

Disadvantages:
- Inductive discharges are sustained by the currents flowing in the coil, i.e., $E_\phi(r=a)$ is proportional to i_{coil}. Thus the I^2R loss in the coil limits the efficiency of power transfer.
- The coupling between the coil current and the diamagnetic current in the plasma is a strong function of the spacing between the coil and the inner wall of the tube. While some imperfect coupling can be tolerated and compensated by circuit design, the geometry must be reproducible.
- All discharges start by a capacitive coupling from the high voltage end of the circuit. Hence there are always some of the problems noted above for the capacitive discharge.

5.2 Non-Self Sustained and Non-Steady State Discharges

A locally self-sustained discharge is one in which there is a local balance (in every dxdydz element of volume) between the pair production from electron collisions with various neutral constituents of the gas and electron losses due to attachment, diffusion, recombination, etc. For instance, a simple steady state rate equation for the electrons could appear as:

$$\frac{dn_e}{dt} = +\alpha\omega_d n_e - a\omega_d n_e \cong 0 \tag{5-4}$$

where α is the first Townsend ionization coefficient (cm^{-1}), ω_d is the drift velocity (cm/s), and a is the attachment rate (cm^{-1}). All three of these terms are a function of E/N, but a steady-state discharge implies a very simple equation for a self-sustained steady state discharge, i.e.,

$$\alpha\,(E/N) = a\,(E/N) \tag{5-5}$$

Without this equality, the steady-state discharge of Eq. (5-1) does not exist. From such an equation one obtains the self-sustaining value of E_{ss}/N. Note also that the equality is independent of electron density and this is a simple explanation as to why the field E is more-or-less constant as one changes the power. The current density i, Eq. (5-2), is established by the circuit driving the discharge.

111

If there is an additional external source of ionization, then (6-4) becomes:

$$\frac{dn_e}{dt} = +\alpha\omega_d n_e - a\omega_d n_e + S \tag{5-6}$$

There are a variety of such sources whose origins may be rather distant from the dxdydz volume element. Common sources are:

1. Energetic electron beam ($\geq$10 keV) injected into the gas container through a thin foil separating the gas region from the vacuum,
2. X-rays or other ionizing radiation
3. External UV light
4. VUV light generated in other parts of the discharge

Under such circumstances, a steady state discharge can exist if:

$$(a - \alpha)\, \omega_d\, n_e = S \tag{5-7}$$

For such conditions, E/N can be less than the self-sustaining value and can be changed by the intensity of the source and the external sustaining circuit. If one does not require a steady-state discharge, one can have many of the features of an externally sustained discharge: an electric field that is lower than the self-sustaining value and controllable by an external circuit. There are at several different approaches to achieving this goal:

I. An added pulsed electric field to a self-sustained discharge, Fig. 5-3. If $\alpha \gg a$ in Eq. (5-4), then the electron density will avalanche to a value limited by the duration of the ionizer pulse, its amplitude, and current capabilities. Such an event creates an electron density that is far greater than that initially sustained by the external circuit of the self-sustained discharge. Thus, in the afterglow of this ionization pulse, both the current and the field produced by the sustainer circuit will change: the current will increase and E/N will decrease. Because of the nonlinear relationship between E/N and ω_d, a simple expression for these changes is not possible. However, it should be clear that if the electron density is to decrease back to the self-sustaining value of Eq. (5-5), then α (E/N) $< a$ (E/N) for the period when the excess electron density exists. After a long enough time, the discharge returns to its self-sustained condition, unless another pulse restarts the avalanches and subsequent afterglow.
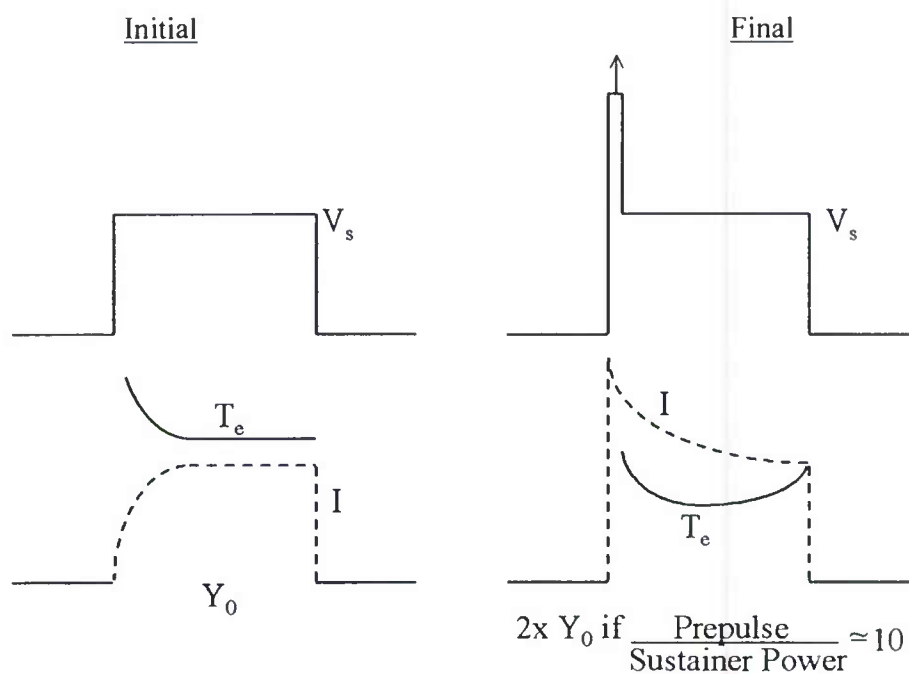
Figure 5-3. Pulse-Sustainer concept I.

II. One could also us an external sustainer field which is <u>less</u> than the self-sustained value. If nothing else is applied, we have no discharge, no current, no nothing. However, if we again <u>add</u> a short intense ionizer pulse, we again have control of the E/N by the sustainer during the afterglow as in (I) above, see Fig. 5-4. Here, however, the discharge would completely disappear if a series of repetitive pulses were not applied. In both (I) and (II), one chooses the repetition rate to keep a time averaged electron density at a mean value of $E/N < E_{ss}/N$. This also means that the electron temperature is less than that of the self-sustained value.

Initial $(V_A \leq V_s)$
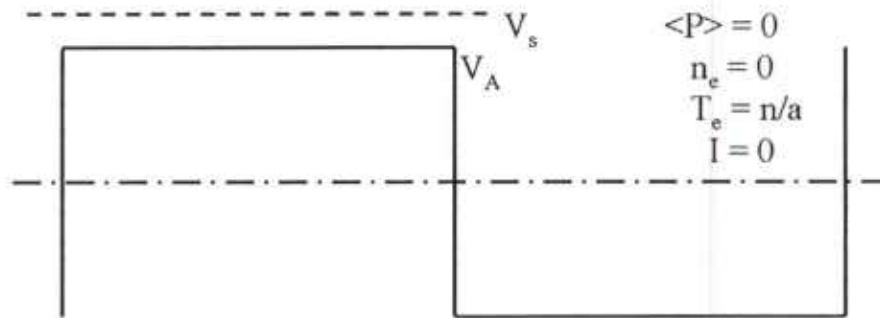
Final $(V_A < V_s)$

Figure 5-4. Pulse-Sustainer concept II.

5.3 Pulse-Sustainer Device and Recent Experiments

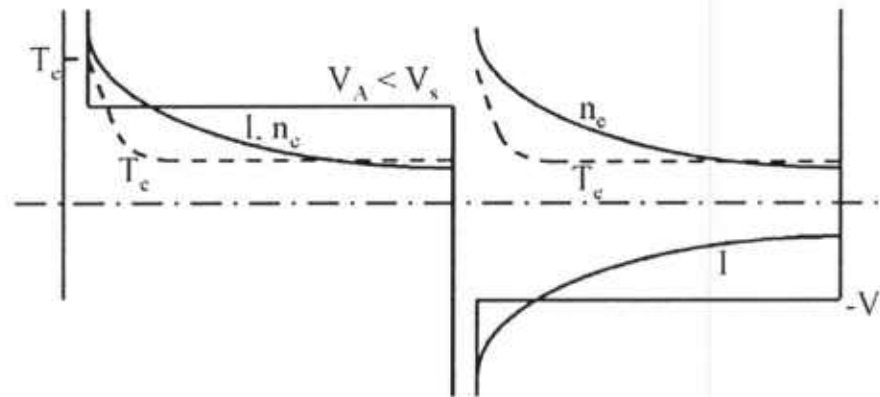A theoretical examination of several types on non-self sustained systems has been conducted (Section 3). These include a pulse added to a square wave discharge system. These initial theoretical results look promising and based on these we are involved in some exploratory pulse-sustainer experiments at lower powers to try to determine the differences in there character versus the partially self-sustained RF systems which we have been investigating in detail.

Several pulse-sustainer circuits were designed by SmartSpark (a local power electronics company at the UIUC campus) and Prof. Verdeyen. The basic circuit is illustrated in Fig. 5-5 and employs HV MOSFETS for switches. One system was designed with the following specifications:

    Pulse circuit
    Transmission line transformer (1:5)
    Pulse width $\geq$ 150 ns
    Rise/fall time $\leq$ 100 ns
    Bipolar at start of sustainer
    Pulse power to 5 kW in small unit
Sustainer circuit
    Transmission line transformer (1:2)

114

Switching rate to 250 kHz
Bipolar square wave output
Power switching > 350 kW @ 2.1 MHz [Jiang et al, Proc. IEEE, 92 (7) 1180 (2004)]
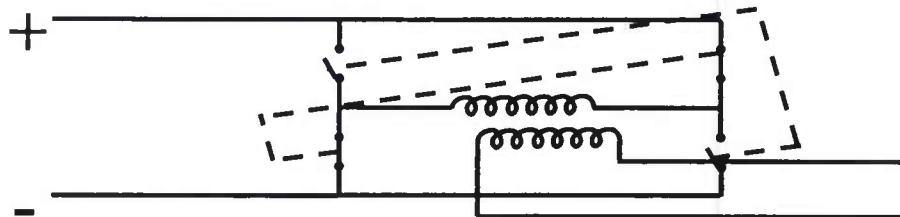
Figure 5-5.   Circuit for Pulse-Sustainer concept.

A small pulse-sustainer was fabricated and is in operation, Fig. 5-6. The unit delivers an average power of 300 W, with a peak power pulse of 5 kW.
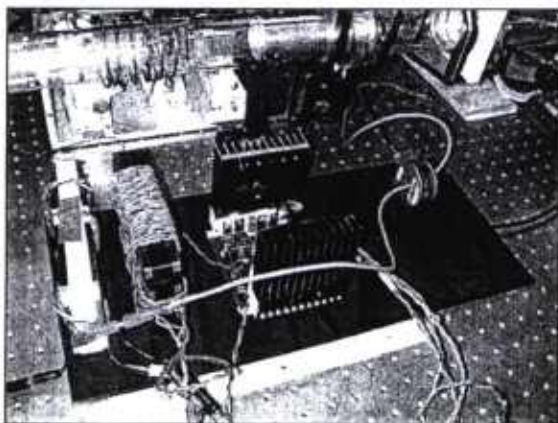
Figure 5-6.   Fabricated circuit for Pulse-Sustainer concept. Note the size of the unit is relatively small due to the use of modern solid-state electronic components.

Testing with the unit at low power were very encouraging and demonstrated a factor of two increase in the singlet-delta signal as the ratio of pulse power to sustainer power was increased, Fig. 5-7 to the limit of the system. Note that this trend is the same as predicted by the theory, Fig. 5-8. It can be shown that $E/N \propto I_{coil}$, therefore as $<E>/N$ decreases, $O_2(a)$ increases.

040930 0.4 µs Pulse Added to 50W Inductive Sustainer
(O2:He = 3:16 @ 3.64 Torr)
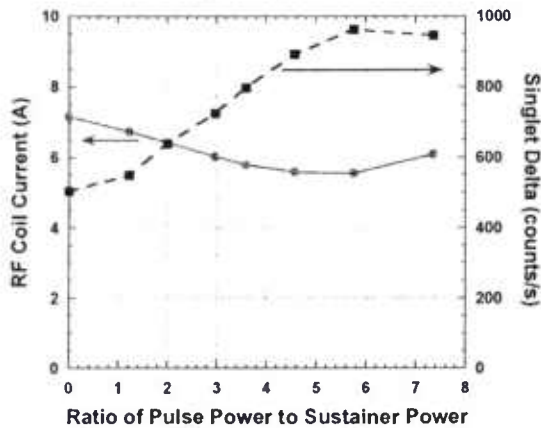
Figure 5-7.   Singlet-delta   signal   and
inductive coil current as a function of the ratio
of pulse to sustainer power.

$([O_2(^1\Delta)] + [O_2(^1\Sigma)]) / eV$
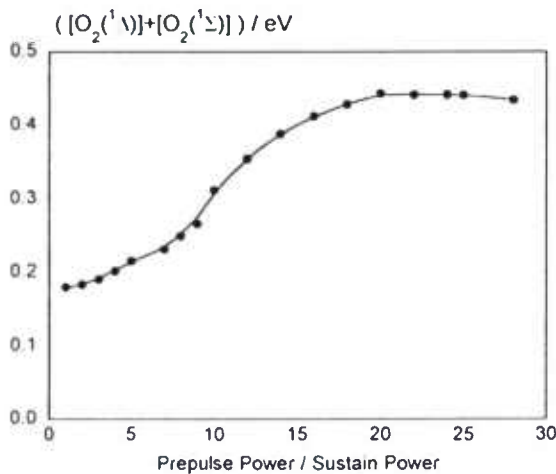
Figure 5-8.   Theoretical   Pulser   Sustainer
performance

Voltage, 1 kV/div	V_s = 697 V, I_s = 900 mA
Current, 0.5 A/div	V_k = 166 V, V_{pc} = 531 V
Capacitive Pickup, 200 V/div	E/N ~ 1.9x10^{-16} V-cm^2, P_p/P_s ~ 5.8
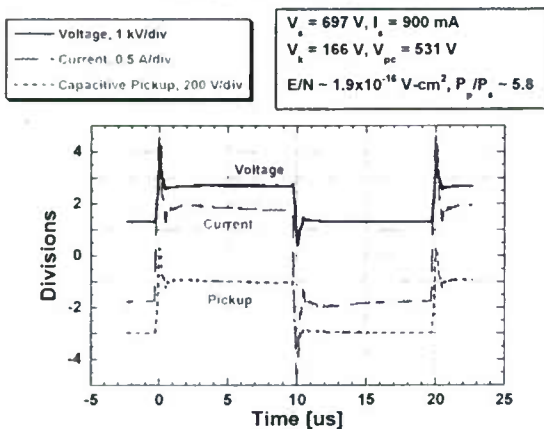
Figure 5-9.   Voltage Current measurements
for pulser-sustainer.

The experimental curves for another of our pulse-sustainer systems are shown in Fig. 5-9, above. We note that the sustainer current rises after the pulse and slowly decreases again until the occurrence of the next pulse. This behavior will modify the average E/N values to lower value in the period between pulses. This behavior then leads to increased performance at higher powers. Figure 5-10 also provides an estimate of the effect of pulse repetition performance and shows

that higher pulse rates also lead to increased performance of the discharge as that variable is increased.

O2(a) Yield vs. Total Pulser-Sustainer Power
[varied sustainer voltage and He:O2:NO, 12.5 Torr]
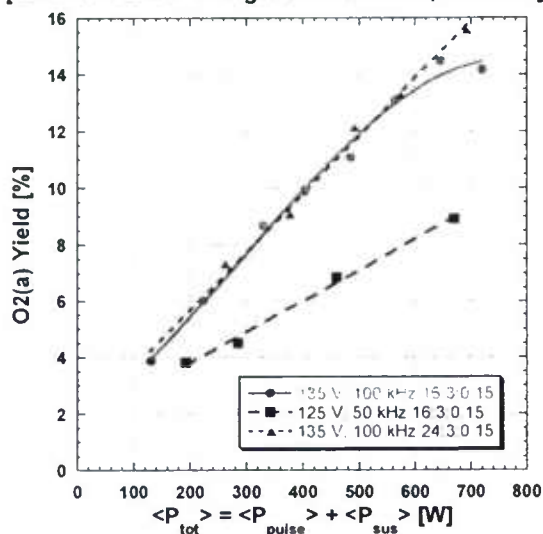
Figure 5-10. Pulser-Sustainer performance as function of pulse repetition rate.

E_{pc}/N vs. Total Power
Pulser-Sustainer v.3, varied sustainer voltage, 100 kHz
24:3:0.15 He:O2:NO, 12.5 Torr
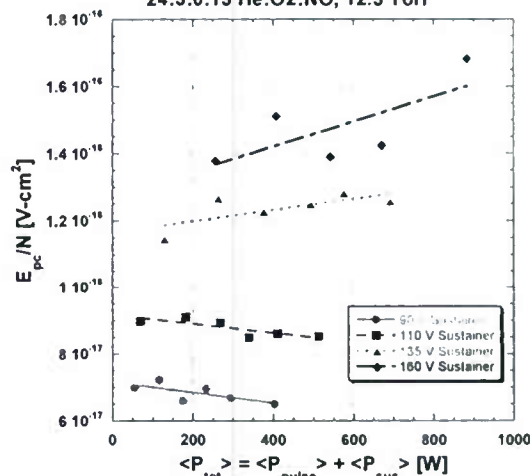
Figure 5-11. E/N measurements for small pulser sustainer.

We have varied a number of parameters with our pulser-sustainer systems in order to gain control over the E/N with some success as seen in Figs. 5-10, 5-11, and 5-12. It is seen in Fig. 5-11 that as we lower E/N (see preceding Figure 3-4) that the rate of production of $O_2(a)$ increases quite dramatically. Our new pulser-sustainer work is designed to take advantage of this dramatic increase in efficiency.

Yield vs. Positive Column Power
Pulser-Sustainer v.3, varied sustainer voltage
24:3:0.15 He:O2:NO, 12.5 Torr
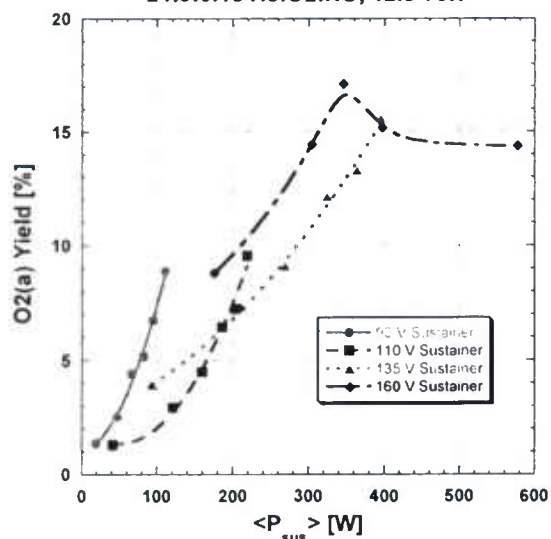
Figure 5-12. Yield vs Power in Pulser sustainer

O₂(a) Signal vs. E_sus/N
Pulser: 100 kHz, V=3.3-4.3 kV
(O₂:He:NO = 3:16:0.15, 16 Torr)
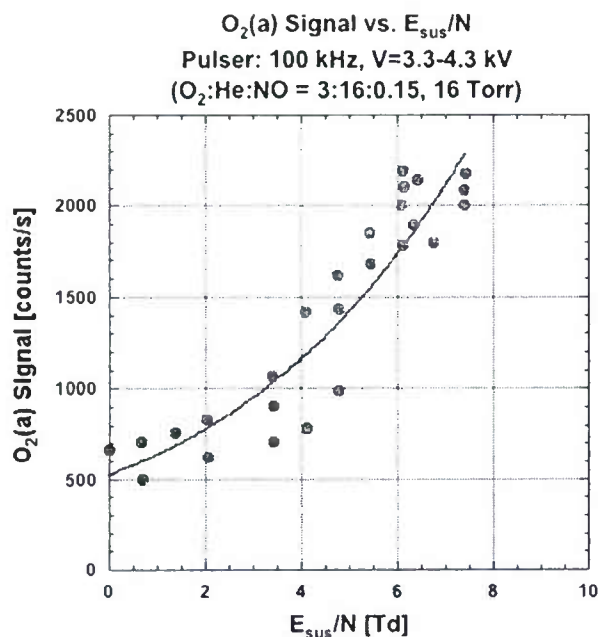
Figure 5-13. At high power higher yields appear at ever higher E/N.
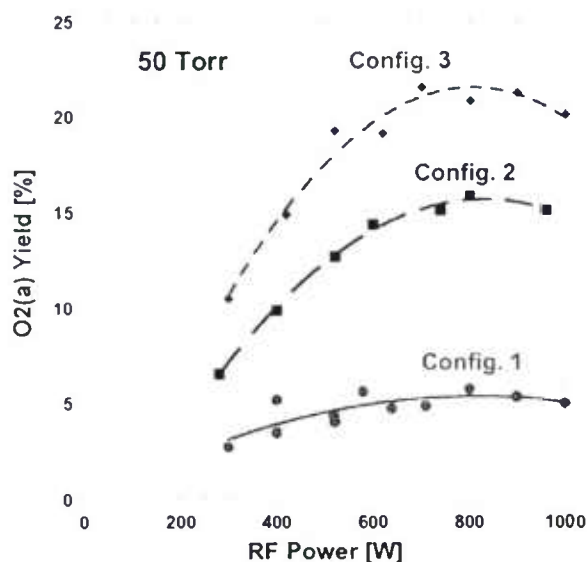
Figure 5-14. High yields with RF Transverse discharges at 50 torr.

For our most recent version of the pulser-sustainer we were able to show that higher yields were obtainable as we drove the system to higher powers at higher E/N's, seen in Fig. 5-13. This is consistent with our most recent theoretical predictions. Even higher yields at high pressure have recently been obtained with our new Transverse RF-discharge shown in Fig. 5-14. Both of these recent data suggest that new combinations of discharges will provide near theoretical quantities (~40-50%) of $O_2(^1\Delta)$ in future experiments. We expect that these results will translate nicely into a scaled laser experiment.

6. SUMMARY AND PERSONNEL

6.1 Summary
The program was initiated in July 2002. Work during this grant resulted over 50 publications in several major breakthroughs by the MRI team: (1) the first measurement of _laser gain_ in a discharge driven oxygen-iodine system was demonstrated in a supersonic flowing cavity; (2) the first measurement of positive gain in a discharge driven oxygen-iodine system was then demonstrated in a subsonic flow tube; (3) the first continuous wave (cw) discharge driven oxygen-iodine _laser_ was demonstrated; (4) Laser gain and power were increased by nearly two orders of magnitude (5) key measurements were made related to ElectricOIL specific kinetics; (6) critical new understanding of the electrodynamic phenomena in a pulse-sustainer type of discharge was attained using a detailed plasma discharge model; and (7) experiments with a pulse-sustainer discharge concept support the intriguing results from the new electrodynamics models. (8) Atomic oxygen was found to play a crucial role in the chemistry of the system in the presence of iodine; it was necessary to titrate the excess O atoms to achieve good gains. NO was found to be beneficial to the performance of the discharge by significantly boosting the production of $O_2(^1\Delta)$. The electrodynamics simulation models were adapted to search the parameter space for appropriate experimental conditions under which more advanced versions of the rf-discharge system could be effective in production rates of $O_2(^1\Delta)$. Based upon electrodynamic model predictions a laser system model was utilized to predict the scalability of the system; results indicate that theoretical electrical efficiencies of 40% into $O_2(^1\Delta)$ may be achievable at very high powers. High pressure experiments with stabilized RF discharges are beginning to approach this theoretical limit.

During the past year the electrodynamics models were improved, a 2-D model was developed and a number of parametric verification studies were conducted at UIUC. The models were adapted to search the parameter space for appropriate experimental conditions under which more advanced versions of discharge systems that could be effective in increasing production rates of $O_2(^1\Delta)$. The studies presented here have shown the effectiveness of the BLAZE -V model being employed for the study of the ElectricOIL discharge. Use of this model has produced further understanding of the discharge kinetics and electrodynamics and has allowed preliminary estimations for the effects of diluent, cooling and geometry changes (changing power density). Modeling results indicate that substantial improvements can be made with a newer discharge models which handle higher level dimensionality. Improvements with the discharge modeling coupled with more in-depth analysis is giving improved understanding of discharge dynamics, providing support for the experimental development of ElectricOIL.

A large body of data was taken to investigate the effect of oxygen with helium diluent as a function of RF power level and axial distance in the flow direction. The partial pressure of oxygen was held fixed at 12 -16 Torr for most of these cases. Differing diluent pressures yielded considerably different behaviors on the $O_2(^1\Delta)$ and $O_2(^1\Sigma)$ levels. Helium provided a very significant decrease in temperature of the flow and an increase in $O_2(^1\Delta)$ signal.

Emory University carried out studies of the highest priority of kinetic rate constants in our ElectricOIL package have been and more are being conducted. New rate constants for deactivation of intermediate species, and I* with various new species involved in electrical

generation were encouraging and no show-stoppers were found. In particular, the interactions involving ground-state O-atoms were examined in their interactions with I and I_2. Results obtained at Emory University give rate constants within the bounds of our upgraded kinetics model and provide confidence in the detailed modeling as it proceeds.

The kinetics package of the Blaze V chemical laser model was repeatedly updated to be appropriate for the evolving ElectricOIL system. The subsequent laser system modeling results were encouraging. Helium diluent appears to be most beneficial to laser gain and performance due to its heat capacity advantages.

PSI has applied the diagnostics for $O_2(a)$, I^*, O, and small-signal gain on the PSI flow reactor at a high level of sensitivity and accuracy, and have assisted with implementation of these methods at UIUC as well. PSI characterized the yields of $O_2(a)$ and O generated by microwave discharge of O_2/Ar mixtures, and demonstrated that large yields of both species can be obtained at low O_2 mole fractions. They applied these results to the investigation of I^* excitation by discharge-generated $O_2(a)$, and they were able to observe positive small-signal gain upon reduction of O concentrations by titration with NO_2. Preliminary kinetics experiments indicate the presence of previously unknown reactions which reduce the efficiency of I^* excitation for these conditions. PSI has conjectured a hypothetical reaction mechanism to account for these effects, and we plan to continue this line of investigation in more detail. They have completed systems for high-sensitivity optical absorption measurements of I_2 dissociation and O_3 formation in both the PSI and UIUC flow reactors. These have been used with great effectiveness. They have conducted a more detailed investigation of the kinetics of the discharge-initiated oxygen-iodine energy transfer mechanism in the PSI flow reactor, in order to more fully characterize and understand the loss phenomena. This will be highly relevant to eventual engineering efforts to design and scale up to prototype discharge-driven laser systems.

AFIT studied the singlet oxygen, $O_2(a^1\Delta, b^1\Sigma)$, produced in a microwave discharge of pure molecular oxygen at modest flow rates provides an initial $O_2(b^1\Sigma)$ concentration that exceeds the steady-state concentration controlled by pooling by more than a factor of ten, reflecting significant discharge yields. When singlet molecular oxygen and atomic oxygen is introduced to the inlet of the second discharge, an increase in $O_2(a^1\Delta)$ is observed immediately outside of the discharge. The kinetic mechanism responsible for this production requires further study. If this production arises from relaxation from higher lying states, then a significant increase in singlet oxygen yield may be obtained if a selective relaxation collision partner were identified. Unfortunately, the sensitivity of singlet oxygen yields from a microwave discharge to the initial excited oxygen inlet conditions is low, suggesting a kinetic limitation to the microwave generator performance. Indeed, the production of $O_2(a, b)$ is likely countered by second order reactions whose rates increase as the singlet oxygen yield increases. In particular, the electron dissociation of $O_2(a, b)$ may be a critical limiting process. Uncovering this limitation will be important to assessing the efficiency and scalability of the proposed ElectricOIL device.

The discharge theory, post-discharge kinetics modeling, experimental plasma measurements and diagnostics measurement was finally put to the test. Yields of $O_2(^1\Delta)$ (up to 28% at low pressures and >20% at moderate pressures) have been confirmed and a careful series of gain surveys were subsequently conducted. Laser gain was realized in both subsonic and supersonic

flows. This was a major program milestone and a major scientific breakthrough. We subsequently procured a set of high reflectivity mirrors and replaced the diagnostics flow cavity in the supersonic flow system with a supersonic laser cavity. Guided by the earlier series gain measurements, our first tests of the system provided laser oscillation. Subsequent testing of the small flow system provided a very stable 200 mWatt 1.314 micron Iodine laser which operated over a wide range of conditions. Improvements to flow and operating conditions have resulted in laser powers of > 5 Watts (Available power is much higher than that extracted in these experiments). As a result, we have in hand the first example of a hybrid electric laser, ElectricOIL, operating at a very important wavelength.

We are in the process of establishing scalability for the ElectricOIL laser system. Over the last year our theorists and electrical engineers have been devising a series of pulse-sustainer discharge and advanced RF experiments to allow us to exploit the recent technology breakthroughs as expeditiously as possible. The theory shows that a pulse-sustainer system is the good way to operate the discharge so as to maximize the $O_2(^1\Delta)$ yield while at the same time minimizing the content of energy sapping species such as oxygen atoms. We now have a much improved RF system which operates stably up to 100 torr. It also allows the system to perform better at lower temperatures. The critical parameters for such discharges have been mapped out. Our preliminary experiments are in concert with the theory and provide substantially increased yields of $O_2(^1\Delta)$. Our program for the out years will emphasize the establishment of scaling laws and engineering parameters for these pulse-sustainer types and high pressure RF discharges. We will improve the theory and improve the science basis for the new laser system to aid in the progress of the experimental program employing pulse-sustainer discharges. We anticipate that increased understanding of the plasma physics and careful experimentation in our laboratories will produce a highly efficient laser system in the most economical fashion. Ultimately, we will demonstrate a lab version of an efficiently packageable high power hybrid laser system.

6.2 Personnel Supported
Partial support was provided to the following personnel during the reporting period:

Profs. Wayne Solomon at UIUC, and Mark Kushner at Iowa State; D. Shane Stafford, Ananth Bhoj, Ramesh Akaroni, Joe Zimmerman, Kirk Kittell, Nathan Richardson, Tyronne Lim and Brian Woodard who are graduate students at UIUC; Jason Amundson and Tyler Field who are undergraduate students at UIUC; Professors. Mike Heaven and Keiji Morokuma at Emory University; Jiande Han, Anatoly V. Komissarov, Scott P. Tinney Samuel Ruffner Leorah Walsh – undergraduate student who are graduate students at Emory University. Professor Glen Perram at AFIT; Mathew Lange, Brian Smith, Greg Pitz - graduate students at AFIT. Dr. Terry Rawlins, Dr. Steve Davis, and Bill Kessler at PSI; Dr. David Carroll, Mr. Darren King, Mr. Joseph Zimmerman, Ms. Julia Laystrom, Mr. Andrew Palla, and Mr. Gabriel Benavides at CU Aerospace. Post Doctoral/Visiting Faculty Fellows include: Valeriy N. Azyazov, Jiande Han, I Dr. Jianjun Liu (Postdoctoral fellow; worked on $O_2 + O_2$ potential energy surfaces) Dr. Yirenf Tzenf (Postdocotoral fellow; worked on time-dependent dynamics code development and calculations) and Dr.Motoichi Tashiro. It should be noted that there was a significant amount of student and faculty interaction and travel between the several laboratories during the conduct of the work in 2004 and 2005.

PSI continues to work with Northeastern University, Boston, MA, to identify talented undergraduate students for work/study cooperative research positions. Northeastern has a very active and successful Co-op program where students work at a company or Federal laboratory for part of their undergraduate term. This requires five years for a BS degree. Since the beginning of this MRI program, we have employed three students who complete internships of several months and are partially supported by this program. They work closely with experienced Ph.D. scientists on duties which include design and assembly of apparatus and sensor components, experimental measurements, and data processing and analysis. While assisting PSI with data collection and analysis, they are learning about chemical lasers, chemical kinetics, optics, and applied spectroscopy, as well as applications of advanced computer techniques to measurements and analysis. This is an excellent educational opportunity for these students, and is consistent with the educational goals of the MRI program.

7. REFERENCES

Allen, M.G., Carleton, K.L., Davis, S.J., Kessler, W.J., Otis, C.E., Palombo, D.A., and Sonnenfroh, D.M., "Ultra-Sensitive Dual-Beam Absorption and Gain Spectroscopy: Applications for Near-IR and Visible Diode Laser Sensors," *Appl. Opt.* 34, 3240 (1995).

Atkinson, R., Baulch, D.L., Cox, R.A., Hampson, R.F. Jr., Kerr, J.A., Rossi, M.J., and Troe, J. (1997). *J. of Phys. and Chem. Ref. Data*, 26, 3, pp. 550-962.

Azyazov, V. N.; Antonov, I. O.; Ruffner, S.; Heaven, M. C. *Proc. SPIE.* 2006, *6101*, 531.

Baulch, D. L.; Cox, R. A.; Crutzen, P. J.; Hampson, R. F.; Kerr, J. A.; Troe, J.; Watson, R. T. *J. Phys. Chem. Ref. Data.* **1982**, *11*, 327.

Bedjanian, Y.; Poulet, G. *Chemical Reviews,* (Washington, DC, United States). 2003, *103*, 4639.

Bemand, P. P., Clyne, M. A. A., Watson, R. T. *J. Chem. Soc. Faraday Trans. 2* **1974**, *70*, 564.

Black, G. and Slanger, T.G., "Production of $O_2(a^1\Delta_g)$ by Oxygen Recombination on a Pyrex Surface," *J. Chem. Phys.* 74, 6517-6519 (1981).

Busch, G.E. (1981). *IEEE J. Quant. Elect.*, QE-17, 6, 1128.

Braginsky, O. V., Kovalev, A. S., Lopaev, D. V., Proshina, O. V., Rakhimova, T. V., Rakhimov, A. T., Vasilieva, A. N., "Pressure scaling of an electro-discharge singlet oxygen generator (ED SOG)." *J. Phys. D.* **40**, 2007.

Braginsky, O. V., Vasilieva, A. N., Klopovsky, K. S., Kovalev, A. S., Lopaev, D. V., Proshina, O. V., Rakhimova, T. V., Rakhimov, A. T., "Singlet oxygen generation in O_2 flow excited by RF discharge: I. Homogeneous discharge mode: α-mode." *J. Phys. D.* **38**, p. 3609-3625, 2005.

Braginsky, O. V., Vasilieva, A. N., Kovalev, A. S., Lopaev, D. V., Mankelevich, Yu. A., Rakhimova, T. V., Rakhimov, A. T., "Singlet oxygen generation in O_2 flow excited by RF discharge: II. Inhomogeneous discharge mode: plasma jet." *J. Phys. D.* **38**, p. 3609-3625, 2005.

Carlos Gomez Martin, J.; Spietz, P.; Burrows, J. P. *J. Photochem. and Photobiology, A: Chem.* **2005**, *176*, 15.

Carroll, D.L. (1995). *AIAA Journal*, 33, 8, 1454.

Carroll, D.L., and Solomon, W.C. (2001) *SPIE* 4184 40.

Carroll, D.L., Verdeyen, J.T., King, D.M., Woodard, B., Skorski, L., Zimmerman, J., and Solomon, W.C. (2002). "Recent Work on the Develoment of an Electric Discharge Oxygen Iodine Laser," Proc. XIX International Symp. on Gas Flow and Chemical Lasers and High Power Laser Conf., Wroclaw, Poland, 26-30 August 2002.

Carroll, D.L., Verdeyen, J.T., King, D.M., Zimmerman, J.W., Laystrom, J.K., Woodard, B.S., Richardson, N., Kittell, K., Kushner, M.J., and Solomon, W.C., "Measurement of Positive Gain on the 1315 nm Transition of Atomic Iodine Pumped by $O_2(a^1\Delta)$ Produced in an Electric Discharge," *Appl. Phys. Lett.* 85, 1320-1322 (2004).

Carroll, D.L., Verdeyen, J.T., King, D.M., Zimmerman, J.W., Laystrom, J.K., Woodard, B.S., Benavides, G.F., Kittell, K., Stafford, D.S., Kushner, M.J., and Solomon, W.C., *Appl. Phys. Lett.* 86, 111104 (2005a).

Carroll, D.L., Verdeyen, J.T., King, D.M., Zimmerman, J.W., Laystrom, J.K., Woodard, B.S., Benavides, G.F., Kittell, K., and Solomon, W.C., *IEEE J. Quantum Electron.* 41, 213-223 (2005b).

Clyne, M.A.A., and Nip, W.S. (1979). *React. Intermed. Gas Phase*, Academic Press, pp. 1-57.

Copeland, R.A., "Laser Double Resonance Study of Collisional Removal of $O_2(A^3\Sigma_u^+,v=7)$ with O_2," *J. Chem. Phys.* 100, 744 (1994).

Cosby, P.C., "Electron-Impact Dissociation of Oxygen," *J. Chem. Phys.* 98, 9560-9569 (1993).

Dai, X.J. 1996). *Aust. J. Phys.* 49 1169.

Davis, S.J. and Hanko, L., "An I_2 Flow Rate Diagnostic for the Oxygen Iodine Laser," Laser Digest, AFWL-TR-79-104, Air Force Weapons Laboratory, Kirtland AFB, New Mexico, 1979.

Davis, S.J., Allen, M.G., Kessler, W.J., McManus, K.R., Miller, M.F., and Mulhall, P.A. (1996) *SPIE* 2702 195.

Deakin, Husain (1972). *JCS Faraday Trans. II*, 68, 1603.

Derwent, R.G. and Thrush, B.A., "Excitation of Iodine by Singlet Molecular Oxygen. Part 2. Kinetics of the Excitation of the Iodine Atoms," *Faraday Discuss. Chem. Soc.* 53, 162-171 (1972).

Dorai, R., and Kushner, M. J. (2001). *J. Phys. D* 34, 574.

Engleman, R., Jr., Palmer, B.A., and Davis, S.J., "Transition Probability and Collision Broadening of the 1.3–µm Transition of Atomic Iodine," *J. Opt. Soc. Am.* 73, 1585-1589 (1983).

Fehsenfeld, F.C., Evenson, K.M., and Broida, H.P., "Microwave Discharge Cavities Operating at 2450 MHz," *Rev. Sci. Instrum.* 36, 294-298 (1965).

Fournier, G., Bonnet, J., and Pigache, D., *J. Physique* 41 Colloque C9, p. 449 (1980).

Franklin, R.N., "The Role of $O_2(a^1\Delta_g)$ Metastables and Associative Detachment in Discharges in Oxygen," *J. Phys. D: Appl. Phys.* 34, 1834-1839 (2001).

Frolov, M. "Electron-Beam Sustained Discharge in Oxygen Gas Mixtures: Electric Properties, Spectroscopy and O2(a1Dg) Yield." AIAA paper, 2003.

Frost, L.S. and Phelps, A.V., "Momentum-Transfer Cross Sections for Slow Electrons in He, Ar, Kr, and Xe from Transport Coefficients," *Phys. Rev. A* 136, 1538 (1969).

Gelb, A.H. and Rawlins, W.T., "Relaxation of Vibrationally Excited Oxygen Molecules by Collision with Oxygen Atoms," Physical Sciences Inc. TR-567, 1986. This unpublished report describes classical trajectory calculations for the $O + O_2(v)$ interaction using the theoretical O_3 potential surface of J.N. Murrell and coworkers: A.J. Stace and J. N. Murrell, *J. Chem. Phys.* 68, 3078 (1978); A.J.C. Varandas and J. N. Murrell, *Chem. Phys. Lett.* 88, 1 (1982).

Grimley, A. J., Houston, P. L. *J. Chem. Phys.* **1978**, *68*, 3366.

Hall, R.I., and Trajmar, S. (1975). *J Phys B* 8 L293.

Han, J., Tinney, S.P., and Heaven, M.C., "I* Kinetics of Relevance to Discharge Driven COIL Systems," Proc. SPIE 5448, 261-268 (2004).

Heaven, M. (1995). *Studies of Energy Transfer Processes of Relevance to Chemically and Optically Pumped Lasers*, Air Force Office of Scientific Research, Bolling Air Force Base, Final Rep. AFOSR-TR-95-0012.

Heaven, M. (1996). Private communication.

Heaven, M. C. *Adv. Series in Phys. Chem.* **2001**, *11*, 138.

Heaven, M. (2001b). *Chemical Dynamics in Extreme Environments*, Advanced Series in Physical Chemistry, Dessler, R.A., ed. World Scientific, Chapter 4, pp. 138-205.

Heaven, M. (2004). Private communication.

Heaven, M. (2005). Private communication.

Heidner, R.F., III, Gardner, C.E., El-Sayed, T.M., Segal, G.I., and Kasper, J. V. V., "Temperature Depedence $O_2(a^1\Delta) + O_2(a^1\Delta)$ and $I(^2P_{1/2}) + O_2(a^1\Delta)$ energy pooling," *J. Phys. Chem.* 74, 5618-5626 (1981).

Heidner, R.F., III, Gardner, C.E., Segal, G.I., and El-Sayed, T.M., "Chain-Reaction Mechanism for I_2 Dissociation in the $O_2(^1\Delta)$-I Atom Laser," *J. Phys. Chem.* 87, 2348-2360 (1983).

Herron, J.T., and Green, D.S. (2001). Plasma Chemistry and Plasma Processing, 21, 3, 456.

Herzberg, G., *Molecular Spectra and Molecular Structure I. Spectra of Diatomic Molecules* (Van Nostrand, New York, 1951).

Hill, A.E (2001). *Proc. of the International Conf. on Lasers 2000*, STS Press, McClean, VA, 249.

Hon, J., Hager, G., Helms, C., and Truesdell, K. (1996). *AIAA Journal*, 34, 8, 1595.

Ionin, A., "Non-self-sustained electric discharge in oxygen gas mixtures: singlet delta oxygen production." *J. Phys. D*, **36**, 982, 2003.

Kaledin, A. L. Heaven, M. C., and Morokuma, *Chem Phys Lett.,* **289**, 110, 1998.

Kaledin, A. L. Heaven, M. C., and Morokuma, *Chem Phys Lett.,* vol. 114, no. 1, pg. 215, 2001.

Kaufman, F. (1958). *Proc. Roy. Soc. A*, 247, 123.

Kaufman, F., "Reactions of Oxygen Atoms," *Progress in Reaction Kinetics* 1, 1-39 (1961).

Kaufman, F., "The Production of Atoms and Simple Free Radicals in Glow Discharges," *Adv. Chem. Ser.* 80, 29-47 (1969).

King, D.M., Carroll, D.L., Laystrom J. K., Verdeyen, J.T., Sexauer, M. S., and Solomon, W.C. (2001). *Proc. of the International Conf. on Lasers 2000*, STS Press, McClean, VA, 265.

Knutsen, K., Dyer, M.J., and Copeland, R.A., "Laser Double-Resonance Study of the Collisional Removal of $O_2(A^3\Sigma_u^+,v=6,7,9)$ with O_2, N_2, CO_2, Ar, and He," *J. Chem. Phys.* 101, 7415-7422 (1994).

Komissarov, A. V., Goncharov, V., and Heaven, M. C., "Chemical Oxygen Iodine Laser (COIL) kinetics and mechanisms," GCL/HPL Conference, 2000.

Komissarov, A. V.; Heaven, M. C. *J. Phys. Chem. A.* **2003**, *107*, 10527.

Krupenie, P.H., "The Spectrum of Molecular Oxygen," *J. Phys. Chem. Ref. Data* 1, 423-534 (1972).

Kushner, M. (2002). Private communication.

Lafferty, W.J., Solodov, A.M., Lugez, C.L., and Fraser, G.T., "Rotational Line Strengths and Self-Pressure-Broadening Coefficients for the 1.27 μm, $a^1\Delta_g$ - $X^3\Sigma_g^-$, v = 0-0 Band of O_2," *Appl. Opt.* 37, 2264-2270 (1998).

Lam, L.; Hastie, D. R.; Ridely, B. A.; Schiff, H. I. *J. Photochem.* **1981**, *15*, 119.

Lawrence, W.G., Van Marten, T.A., Nowlin, M.L., and Heaven, M.C. (1997). *J. Chem. Phys.*, 106, 1, 127.

Lawton, S.A., and Phelps, A.V., "Excitation of the $b^1\Sigma_g^+$ State of O_2 by Low Energy Electrons," *J. Chem. Phys.* 69, 1055 (1978).

Lee, C., Graves, D.B., Lieberman, M.A., and Hess, D.W. (1994). *J. Electrochem. Soc.* 141 1546.

Lee, L.C. and Slanger, T.G., "Observations on $O(^1D\rightarrow^3P)$ and $O_2(b^1\Sigma_g^+\rightarrow X^3\Sigma_g^-)$ Following O_2 Photodissociation," *J. Chem. Phys.* 69, 4053-4060 (1978).

Levitskii, S. M., *Sov. Phys. Tech. Phys.* **2**, 887, 1958.

Marinelli, W.J. and Green, B.D., "Collisional Quenching of Atoms and Molecules on Spacecraft Thermal Protection Surfaces," AIAA Paper 88-2667 (1988).

Marx, W.; Bahe, F.; Schurath, U. *Ber. Bunsenges. Phys. Chem.* **1979**, *83*, 225.

McDermott, W., Pchelkin, N., Benard, D., and Bousek, R. (1978). *Appl. Phys. Lett.* 32, 8, 469.

Meeks, E., Larson, R., Ho, P., Apblett, C., Han, S., Edelberg, E., Aydil, E. (1998). *J. Vac. Sci. Technol. A* 16, 2, 544-563.

Mikheyev, P. A., Shepelenko, A. A., Kupryayev, N. V., and Voronov, A. I., "Excited oxygen in glow discharge afterglow," *SPIE Conf. on Gas and Chemical Lasers and Intense Beam Applications II*, San Jose, CA, Jan, 1999.

Morgan, W.L. and Penetrante, B.M., "ELENDIF: A Time-Dependent Boltzmann Solver for Partially Ionized Plasmas," *Computer Physics Communications* 58, 127-152 (1990).

Newman, S.M., Lane, I.C., Orr-Ewing, A.J., Newnham, D.A., and Ballard, J., "Integrated Absorption Intensity and Einstein Coefficients for the O_2 $a^1\Delta_g$ – $X^3\Sigma_g^-$(0,0) Transition: A Comparison of Cavity Ringdown and High Resolution Fourier Transform Spectroscopy with a Long-Path Absorption Cell," *J. Chem. Phys.* 110, 10749-10757 (1999).

Nishida, S.; Takahashi, K.; Matsumi, Y.; Tanigushi, N.; Hayashida, S. *J. Phys. Chem. A.* **2004**, *108*, 2451.

Palla, A. D.; Carroll, D. L.; Verdeyen, J. T.; Solomon, W. C. *J. App. Phys.*, **2006**, *100*, 023117.

Payne, W.A., Thorn, R.P. Jr., Nesbitt, F.L., and Stief, L.J. (1998). "Rate Constant for the Reaction of O(3P) with IO at T=298 K," *J. Phys. Chem. A*, 102, pp. 6247-6250.

Perram, G.P. and Hager, G.D. (1988). "The Standard COIL Kinetics Package," AFWL-TR-88-50, pp. 7-10.

Perram, G. P. *Int. J. Chem. Kinet.* **1995**, *27*, 817.

Phelps, A.V., private communication, ftp://jila.colorado.edu/collision_data/.

Phelps, A. V., JILA Information Center Report No. 28, 1985.

Piper, L.G., "The Rate Coefficient for Quenching N(^{2}D) by O(^{3}P)," *J. Chem. Phys.* 91, 3516-3524 (1989).

Pritt Jr., A. T., Coombe. R. D., Pilipovich, D., Wagner, R. I., Benard, D., and Dymek, C., *Appl. Phys. Lett.*, vol.31, pp.745-747-1977.

Rapp, D., and Englander-Golden, P. (1965). *J Chem Phys* 43 1464.

Rakhimova, T. V., Kovalev, A. S., Klopovsky, K. S., Lopaev, D. V., Mankelevich, Yu. A., Vasilieva, A. N., Braginsky, O. V., , Popov, N. A., Proshina, O. V., Rakhimov, A. T., "Experimental and theoretical study of a pressure scaling possibility of vhf singlet oxygen generator." *36th AIAA Plasmadynamics and Lasers Conference*, AIAA paper 2005-4918 (2005).

Rakhimova, T. V., Kovalev, A. S., Lopaev, D. V., Proshina, O. V., Mankelevich, Yu. A., Vasilieva, A. N., Braginsky, O. V., Klopovsky, K. S., Popov, N. A., Rakhimov, A. T., Kolobyanin, Yu. V., "Pressure scaling of an electro-discharge singlet oxygen generator (ED SOG)." *Gas Flow, Chemical Lasers, and High-Power Lasers*, SPIE paper 634608-1 (2006).

Rawlins, W.T., Caledonia, G.E., and Kennealy, J.P. (1981). *J. Geophys. Res.* 86, 5247.

Rawlins, W.T., Caledonia, G.E., and Armstrong, R.A., "Dynamics of Vibrationally Excited Ozone Formed by Three-Body Recombination. II. Kinetics and Mechanism," *J. Chem. Phys.* 87, 5209-5221 (1987).

Rawlins, W.T., Lee, S., Kessler, W.J., and Davis, S.J., "Observations of Gain on the I($^2P_{1/2} \rightarrow {}^2P_{3/2}$) Transition by Energy Transfer from $O_2(a^1\Delta_g)$ Generated by a Microwave Discharge in a Subsonic Flow Reactor," *Appl. Phys. Lett.* 86, 051105 (2005).

Rawlins, W.T., Davis, S.J., Lee, S., Silva, M.L., Kessler, W.J., and Piper, L.G., "Optical Diagnostics and Kinetics of Discharge-Initiated Oxygen-Iodine Energy Transfer," AIAA-2003-4032, 34th AIAA Plasmadynamics and Lasers Conference, Orlando, FL, June 2003.

Rawlins, W.T., Lee, S., Kessler, W.J., Oakes, D.B., Piper, L.G., and Davis, S.J., "Spectroscopic Studies of a Prototype Electrically Pumped COIL System," SPIE 5334, Paper No. 12 (2004).

Roszak, S., Krauss, M., Alekeyev, A. B., Lieberman, H. –P. and Buenker, R. J., *J. Phys. Chem A*, vol. 104 pg. 2999, 2000,

Raizer, Yu. P., *Radio Frequency Capacitive Discharges.* Boca Raton, CRC Press.

Schmiedberger, J., Hirahara, S., Ichinoche, Y., Suzuki, M., Masuda, W., Kihara, Y., Yoshitani, E., and Fujii, H. (2001). *SPIE* 4184 32.

Sentman, L., Subbiah, M., and Zelazny, S. (1977). "Blaze II: A Chemical Laser Simulation Computer Program," Bell Aerospace Textron, Buffalo, NY, T.R. H-CR-77-8.

Slanger, T.G. and Black, G., "Interactions of $O_2(b^1\Sigma_g^+)$ with $O(^3P)$ and O_3," *J. Chem. Phys.* 70, 3434-3438 (1979).

Stafford, D.S. and Kushner, M.J., "$O_2(^1\Delta)$ Production in He/O_2 Mixtures in Flowing Low Pressure Plasmas," *J. Appl. Phys.* 96, 2451-2465 (2004).

Stutz, J.; Hebestreit, K.; Alicke, B.; Platt, U. *J. Atmos. Chem.* **1999**, *34*, 65.

Tachibana, K., and Phelps, A.V., "Excitation of the O_2 ($a^1\Delta_g$) State by Low Energy Electrons," *J. Chem. Phys.* 75, 3315 (1981).

Tellingham, J., "Resolution of the Visible-Infrared Absorption Spectrum of I_2 into Three Contributing Transitions," *J. Chem. Phys.* 58, 2821-2834 (1973).

Tellingham, J., "Transition Strengths in the Visible-Infrared Absorption Spectrum of I_2," *J. Chem. Phys.* 76, 4736-4744 (1982).

Upschulte, B.L., Marinelli, W.J., and Green, B.D., "Reactions of $O_2(a^1\Delta_g)$ with O^- and O_2^-," *J. Phys. Chem.* 98, 837-842 (1994).

Vasiljeva, A. N.; Klopovskiy, K. S.; Kovalev, A. S.; Lopaev, D. V.; Mankelevich, Y. A.; Popov, N. A.; Rakhimov, A. T.; Rakhimova, T. V. *J. Phys. D: Appl. Phys.* **2004**, *37*, 2455.

Verdeyen, J.T., King, D.M., Carroll, D.L., and Solomon, W.C. (2002). *SPIE* 4631 154.

Whiting, E. E. "An emprical approximation to the voigt profile." *J. Quantum Spectosc. Radiat. Transfer.*, vol. 8 pp. 1379-1384, 1968.

Yatsenko, N. A., *Zh. Tekh. Fiz.* **51**, 1195, 1981.

Zalesskii, V. Yu., *Zh. Eksp. Teor. Fiz.*, 67, pp. 30-37 (1974) [*Sov. Phys. JETP* 40 (1) 14 (1975)].

Zimmerman, J. W.; King, D. M.; Palla, A. D.; Verdeyen, J. T.; Carroll, D. L.; Laystrom, J. K.; Benavides, G.; Woodard, B. S.; Solomon, W. C.; Rawlins, W. T.; Davis, S. J.; Heaven, M. C. *Proc. SPIE.* **2006**, *6261*, 62611R.

Zolotarev, V. A.; Ishkov, D. V.; Podmar'kov, Y. P.; Frolov, M. P.; Yuryshev, N. N. *Sov. J. Quantum. Electron.* **1991**, *18*, 912.

Zolotarev, V. A.; Kryukov, P. G.; Podmar'kov, Y. P.; Frolov, M. P.; Yuryshev, N. N. *Sov. J. Quantum. Electron.* **1989**, *16*, 1095.

Zolotarev, V. A.; Kryukov, P. G.; Podmar'kov, Y. P.; Frolov, M. P.; Yuryshev, N. N. *Manufacture of singlet oxygen* (P. N. Lebedev Physical Institute, Moscow, USSR). Application: SU 1668288.

8. PUBLICATIONS

The papers which have been presented and published and several more are in review as a result of the last 48 months represent the largest scientific data base in the EOIL area; the partial list follows.

1. A.D. Palla, J.W. Zimmerman, B.S. Woodard, D.L. Carroll, J.T. Verdeyen, T.C. Lim, and W.C. Solomon, "Oxygen discharge and post-discharge kinetics experiments and modeling for the electric oxygen-iodine laser system," *J. Phys. Chem. A*, Vol. 111, pp. 6713-6721 (2007).

2. A.D. Palla, D.L. Carroll, J.T. Verdeyen, and W.C. Solomon, "Effects of mixing on postdischarge modeling of electric oxygen-iodine laser experiments," *Journal of Applied Physics*, Vol. 100, 023117 (2006).

3. G.F. Benavides, A.D. Palla, D.M. King, D.L. Carroll, J.T. Verdeyen, J.K. Laystrom, T.H. Field, J.W. Zimmerman, B.S. Woodard, and W.C. Solomon, "Hybrid ElectricOIL Discharge, Gain, and Power Enhancements," AIAA Paper 2007-4623, AIAA 38th Plasma Dynamics and Lasers Conference, Miami, FL, 25-28 June 2007.

4. A.D. Palla, J.W. Zimmerman, B.S. Woodard, D.L. Carroll, J.T. Verdeyen, T.C. Lim, W.T. Rawlins, S. Lee, S.J. Davis, and W.C. Solomon, "ElectricOIL discharge and post-discharge kinetics experiments and modeling," *Proceedings of Laser Beam Control and Applications Conference*, San Jose, California, 22-25 January 2007, SPIE Vol. 6454, pp. 645419-1-12 (2007).

5. D.L. Carroll, J.T. Verdeyen, D.M. King, A.D. Palla, J.K. Laystrom, G.F. Benavides, J.W. Zimmerman, B.S. Woodard, and W.C. Solomon, "Development of the electric discharge oxygen-iodine laser," Proceedings of the XVI International Symposium on Gas Flow and Chemical Lasers and High Power Laser Conference, Gmunden, Austria, 4 – 8 September 2006, The International Society for Optical Engineering Vol. 6346, pp. 63460H-1-8 (2007).

6. T.V. Rakhimova, A.P. Palov, Yu.A. Mankelevich, N.A. Popov, and D.L. Carroll, "Mixing of post-discharge O_2/He flow with NO_2/He flow: 3D modeling of experimental data," Proceedings of the XVI International Symposium on Gas Flow and Chemical Lasers and High Power Laser Conference, Gmunden, Austria, 4 – 8 September 2006, The International Society for Optical Engineering Vol. 6346, pp. 634622-1-7 (2007).

7. D.M. King, D.L. Carroll, J.T. Verdeyen, J.K. Laystrom, G.F. Benavides, A.D. Palla, J.W. Zimmerman, B.S. Woodard, and W.C. Solomon, "Power Enhancement of the Hybrid ElectricOIL Laser," AIAA Paper 2006-3756, AIAA 37th Plasma Dynamics and Lasers Conference, San Francisco, CA, 5-8 June 2006.

8. J.W. Zimmerman, D.M. King, A.D. Palla, J.T. Verdeyen, D.L. Carroll, J.K. Laystrom, G.F. Benavides, B.S. Woodard, W.C. Solomon, W.T. Rawlins, S.J. Davis, and M.C. Heaven, "Important kinetic effects in the hybrid ElectricOIL system," *Proceedings of the High Power Laser Ablation Conference*, Taos, New Mexico, 8-12 May 2006, The Int. Soc. for Opt. Eng., P.O. Box 10, Bellingham, WA 98227-0010, in press.

9. A.D. Palla, D.L. Carroll, J.T. Verdeyen, and W.C. Solomon, "Effects of mixing on post-discharge modeling of ElectricOIL experiments," *Proceedings of Laser Beam Control and Applications Conference*, San Jose, California, 23-26 January 2006, The Int. Soc. for Opt. Eng. Vol. 6101, P.O. Box 10, Bellingham, WA 98227-0010, pp. 610125-1-12

10. D.L. Carroll, J.T. Verdeyen, D.M. King, J. Zimmerman, J. Laystrom, B. Woodard, G. Benavides, N. Richardson, K. Kittell, and W.C. Solomon, "Studies of CW laser oscillation on the 1315 nm transition of atomic iodine pumped by $O_2(a^1\Delta)$ produced in an electric discharge," *IEEE Journal of Quantum Electronics*, Vol. 41, No. 10, Oct. 2005, pp. 1309-1318.

11. D.L. Carroll, J.T. Verdeyen, D.M. King, J. Zimmerman, J. Laystrom, B. Woodard, G. Benavides, K. Kittell, D.S. Stafford, M.J. Kushner, and W.C. Solomon, "Continuous-wave laser oscillation on the 1315 nm transition of atomic iodine pumped by $O_2(a^1\Delta)$ produced in an electric discharge," *Applied Physics Letters*, Vol. 86, 111104 (2005).

12. D.L. Carroll, J.T. Verdeyen, D.M. King, J. Zimmerman, J. Laystrom, B. Woodard, G. Benavides, K. Kittell, and W.C. Solomon, "Path to the measurement of positive gain on the 1315 nm transition of atomic iodine pumped by $O_2(a^1\Delta)$ produced in an electric discharge," *IEEE Journal of Quantum Electronics*, Vol. 41, No. 2, Feb. 2005, pp. 213-223.

13. D.L. Carroll, J.T. Verdeyen, D.M. King, J.W. Zimmerman, J.K. Laystrom, G.F. Benavides, B.S. Woodard, K. Kittell, and W.C. Solomon, "Recent Experiments with the ElectricOIL Laser System," AIAA Paper 2005-4915, AIAA 36th Plasma Dynamics and Lasers Conference, Toronto, Ontario, Canada, 6-9 June 2005.

14. A.D. Palla, D.L. Carroll, J.T. Verdeyen, and W.C. Solomon, "Post-Discharge Modeling of Recent ElectricOIL Experiments," AIAA Paper 2005-4919, AIAA 36th Plasma Dynamics and Lasers Conference, Toronto, Ontario, Canada, 6-9 June 2005.

15. D.L. Carroll, J.T. Verdeyen, D.M. King, J.W. Zimmerman, J.K. Laystrom, A.D. Palla, B.S. Woodard, G.F. Benavides, K. Kittell, and W.C. Solomon, "Recent Experiments and Post-Discharge Modeling with the ElectricOIL Laser System," Proc. of the ICONO/LAT 2005 Conf., St. Petersburg, Russia, 10-15 May 2005, in press.

16. W.C. Solomon, J.W. Zimmerman, L.W. Skorski, B. Woodard, D.L. Carroll, J.T. Verdeyen, and D.M. King, "Recent Progress in Modeling the ElectriCOIL System," Proceedings of Laser Optics 2003 held in St. Petersburg, Russia, June 30 - July 3, 2003, The International Society for Optical Engineering, P.O. Box 10, Bellingham, Washington 98227-0010.

17. D.L. Carroll, J.T. Verdeyen, J.W. Zimmerman, L.W. Skorski, and W.C. Solomon, "Recent Electrodynamics Modeling of the ElectriCOIL System," AIAA Paper 2003-4030, AIAA 34th Plasma Dynamics and Lasers Conference, June 23-26, Orlando, FL, 2003.

18. D.L. Carroll, D.M. King, J.T. Verdeyen, B. Woodard, J.W. Zimmerman, L.W. Skorski, and W.C. Solomon, "Recent Experimental Measurements of the ElectriCOIL System," AIAA Paper 2003-4029, AIAA 34th Plasma Dynamics and Lasers Conference, June 23-26, Orlando, FL, 2003.

19. J.W. Zimmerman, L.W. Skorski, W.C. Solomon, M.J. Kushner, J.T. Verdeyen, and D.L. Carroll, "Electrodynamic modeling of the ElectriCOIL system," *Proceedings of the Gas and Chemical Lasers and Intense Beam V Conference*, San Jose, California 30 January 2003, SPIE Vol. 4971, pp. 81-86.

20. J. Han, A.V. Komissarov, S.P. Tinney, and M. C. Heaven, "Kinetic studies for advanced iodine laser concepts," *Proceedings of the Gas and Chemical Lasers and Intense Beam V Conference*, San Jose, California 30 January 2003, SPIE Vol. 4971, pp. 45-56.

21. Rawlins, W.T., Davis, S.J., Lee, S., Silva, M.L., Kessler, W.J., and Piper, L.,G. (2003). "Optical Diagnostics and Kinetics of Discharge-Initiated Oxygen-Iodine Energy Transfer," AIAA Paper 2003-4032, Orlando, FL, June 2003.

22. D.L. Carroll, Verdeyen, J.T., King, D.M., Benavides, G., Woodard, B.S., Richardson, N., Solomon, W.C., Rawlins, W.T., Davis, S.J., and Kessler, W.J., "Preliminary yield measurements in the ElectriCOIL system," *Proceedings of the Gas and Chemical Lasers and Applications IV Conference*, San Jose, California 26 January 2004, SPIE Vol. 5334, pp. 79-87

23. D.L. Carroll, J.T. Verdeyen, D.M. King, J. Zimmerman, J. Laystrom, B. Woodard, N. Richardson, K. Kittell, M.J. Kushner, and W.C. Solomon, "Measurement of positive gain on the 1315 nm transition of atomic iodine pumped by $O_2(^1\Delta)$ produced in an electric discharge," *Applied Physics Letters*, Vol. 85, No. 8, pp. 1320-1322 (2004).

24. D.L. Carroll, J.T. Verdeyen, D.M. King, J.W. Zimmerman, J.K. Laystrom, B.S. Woodard, G.F. Benavides, K. Kittell, and W.C. Solomon, "Experimental Effects of Atomic Oxygen on the Development of an Electric Discharge Oxygen Iodine Laser," Proceedings of the XV International Symposium on Gas Flow and Chemical Lasers and High Power Laser Conference, Prague, Czech Republic, 30 August – 3 September 2004, The International Society for Optical Engineering, *The International Society for Optical Engineering Vol.* 5777, pp. 215-220 (2005)..

25. D.L. Carroll, J.T. Verdeyen, D.M. King, J. Zimmerman, J. Laystrom, B. Woodard, G. Benavides, K. Kittell, and W.C. Solomon, "Path to the measurement of positive gain on the 1315 nm transition of atomic iodine pumped by $O_2(^1\Delta)$ produced in an electric discharge," accepted for publication in *IEEE Journal of Quantum Electronics*, 2004.

26. D. Shane Stafford and Mark J. Kushner, "Simulation of O2(1-delta) Yields in Mixtures of O2 and Inert Gases in Low Pressure Plasmas," 56th Gaseous Electronics Conference, San Francisco, CA, October 2003.

27. D.S. Stafford and M.J. Kushner, "$O_2(^1\Delta)$ production in He/O_2 mixtures in flowing low pressure plasmas," *J. of Appl. Phys.* 96 (5) 2451 (2004).

28. D. Shane Stafford and Mark J. Kushner, "Investigation for axially flowing He/O2 plasmas for Oxygen-Iodine lasers," 58th Gaseous Electronics Conference, Bunratty, Ireland, September 2004.

29. . Han, S.P. Tinney, and M.C. Heaven, "I* Kinetics of relevance to discharge driven COIL systems," *SPIE* Vol. 5448, in press.

30. W.T. Rawlins, S. Lee, W.J. Kessler, D.B. Oakes, L.G. Piper, and S.J. Davis, "Spectroscopic studies of a prototype electrically pumped COIL system," *Proceedings of the Gas and Chemical Lasers and Applications IV Conference*, San Jose, California 26 January 2004, SPIE Vol. 5334, pp. 88-99.

31. W.T. Rawlins, S. Lee, W.J. Kessler, and S.J. Davis, "*Observations of Gain on the $I(^2P_{1/2} \rightarrow ^2P_{3/2})$ Transition by Energy Transfer from $O_2(a^1\Delta_g)$ Generated by a Microwave Discharge in a Subsonic Flow Reactor",* submitted for publication in Applied Physics Letters, July 2004.

32. Han, A.V. Komissarov, S.P. Tinney, and M.C. Heaven, "Kinetic Studies for Advanced Iodine Laser Concepts," Proceedings of the XV International Symposium on Gas Flow and Chemical Lasers and

High Power Laser Conference, Prague, Czech Republic, 30 August – 3 September 2004, The International Society for Optical Engineering, in press.

33. S.J. Davis, W.T. Rawlins, W.J. Kessler, S. Lee, M.L. Silva, and P.A. Mulhall, "Next Generation Diagnostics for COIL: New Approaches for Measuring Critical Parameters," Proceedings of the XV International Symposium on Gas Flow and Chemical Lasers and High Power Laser Conference, Prague, Czech Republic, 30 August – 3 September 2004, The International Society for Optical Engineering, in press.

34. S. J. Davis, W.T. Rawlins, S. Lee, M.L. Silva, W.J. Kessler, and P.A. Mulhall, *Advanced Diagnostics for COIL and DOIL*", (SPIE Paper 5448-109, presented at SPIE High-Power Laser Ablation V, Taos, NM, April 2004)

35. M.C. Heaven, J. Han, S.J. Davis, and S. Lee "Re-examination of the role of $O_2(b)$ in the I_2 dissociation mechanism," *Proceedings of the Gas and Chemical Lasers and Applications IV Conference*, San Jose, California 26 January 2004, SPIE Vol. 5334, pp. 53-59

36. Valeriy N. Azyazov and M. C. Heaven, paper 2005-5037 "Investigation of the role of $O2(b)$ and electronically excited I2 in the COIL dissociation process"

37. Azyazov, V.N., Antonov, I.O., Ruffner, S. and Heaven, M.C. (2006a). *Proc. of SPIE*, **6101**, 531.

38. Azyazov, V.N., Kabir, H.M., Antonov, I.O. and Heaven, M.C. (2006b). *J. Phys. Chem. A*, article.

39. Azyazov, V.N., Kabir, H.M. and Heaven, M.C. (2007). *Proc. SPIE* **6454**, 6454-21.

40. J. Liu and K. Morokuma, Ab initio potential energy surfaces of $O_2(X^3\Sigma_g^-, a^1\Delta_g, b^1\Sigma_g^+) + O_2(X^3\Sigma_g^-, a^1\Delta_g, b^1\Sigma_g^+)$: Mechanism of quenching of $O_2 (a^1\Delta_g)$. J. Chem. Phys. 123, 204319/1-10 (2005)

41. M. Tashiro, K. Morokuma, and J. Tennyson, R-matrix calculation of electron collisions with electronically excited O_2 molecules, Phys. Rev. A, 73, 052707/1-8 (2006).

42. M. Tashiro, K. Morokuma and J. Tennyson, R-matrix calculation of differential cross sections for low-energy electron collisions with ground and electronically excited O_2 molecules, Phys. Rev. A 74, 022706/1-8 (2006).

43. N. Yu. Babaeva, R. A. Arakoni and Mark J. Kushner, "Production of $O_2(^1\Delta)$ in flowing plasmas using spiker-sustainer excitation", J. Appl. Phys. **99**, 113306 (2006).

44. J. Han, A. V. Komissarov, S. P. Tinney, M. C. Heaven, S. J. Davis, and S. Lee, Proceedings of SPIE-The International Society for Optical Engineering 5777, 198, (2005) *"Kinetic studies for advanced iodine laser concepts"*

45. M. Lange, B. Smith, and G. Perram, "Kinetics of the Electric Discharge Pumped Oxygen-Iodine Laser", Directed Energy Professional Society 6th Annual Symposium, Albuquerque, NM, October 2003. Matthew Lange, Greg Pitz, Brian Smith and Glen P. Perram, *" Electric Discharge Pumped Oxygen –Iodine Laser Kinetics"* Journal of Directed Energy **1** 219 (2005).

46. G. Pitz, M. Lange, and G. Perram, *"Singlet Oxygen Kinetics in a Double Microwave Discharge"* Proceedings of High Power Laser Ablation V, SPIE **5448** 1039 (2004).

9. INTERACTIONS AND TRANSITIONS

Briefings to the JTO were prepared and delivered in May of 2005 and October of 2004 of 2006 and May 2007. Meetings were held with AFRL personnel in January 2005 and September 2005. Coordination meetings were held with MDA and the Army through the spring and summer of 2005. A briefing for AFRL was prepared and delivered in March of 2005. An EOIL session was sponsored at the DEPS meeting in Fall 2007.

10. PATENT DISCLOSURES, HONORS AND AWARDS

A Provisional Patent Application entitled "Enhanced Electrically Assisted Oxygen Iodine Laser" was filed with the U.S. Patent Office on 15 March 2004.

Wayne Solomon, received the American Institute of Aeronautics and Astronautics, *Plasmadynamics and Lasers Award* for 2005 and was made American Institute of Astronautics, *Fellow* in 2007